AGH UNIVERSITY OF SCIENCE AND TECHNOLOGY

FIELD OF SCIENCE : ENGINEERING AND TECHNOLOGY

SCIENTIFIC DISCIPLINE: AUTOMATION, ELECTRONIC AND ELECTRICAL ENGINEERING

DOCTORAL THESIS

Comprehensive methodology for emission level prediction from magnetically coupled nonlinear circuits in automotive

Author: mgr inż. Grzegorz Oleszek

First supervisor: dr hab. inż. Łukasz Śliwczyński

Second supervisor: dr hab. inż. Cezary Worek, prof. AGH

Completed in: University of Science and Technology AGH, Faculty of Computer Science, Electronics and Telecommunications, Department of Electronics

Krakow, 2021

AGH

AKADEMIA GÓRNICZO-HUTNICZA IM. STANISŁAWA STASZICA W KRAKOWIE

DZIEDZINA : NAUKI INŻYNIERYJNO-TECHNICZNE

DYSCYPLINA : AUTOMATYKA, ELEKTRONIKA I ELEKTROTECHNIKA

ROZPRAWA DOKTORSKA

Metodologia prognozowania poziomu emisji zaburzeń promieniowanych w nieliniowych obwodach sprzężonych magnetycznie dla potrzeb przemysłu motoryzacyjnego

Autor: mgr inż. Grzegorz Oleszek

Promotor rozprawy: dr hab. inż. Łukasz Śliwczyński

Promotor rozprawy: dr hab. inż. Cezary Worek, prof. AGH

Praca wykonana: Akademia Górniczo-Hutnicza AGH, Wydział Informatyki, Elektroniki i Telekomunikacji, Katedra Elektroniki

Kraków, 2021

Acknowledgments

First and foremost, I would like to thank my supervisor, dr hab. inż. Łukasz Śliwczyński for his advice, guidance, and support through the preparation of this work. His knowledge of doing research activities, publishing my work, and dissertation preparation has been valuable to me. A special thanks go to my second supervisor, dr hab. inż. Cezary Worek, prof. AGH for his EMC knowledge he shared with me and provided clarifications for even complicated topics. I want to thank also my technical supervisor, dr inż. Tomasz Klatka for his support and RF guidance. Additionally, my gratitude goes to Aptiv company, allowing me to complete the measurements in their EMC chamber.

Finally, I would like to thank my family for their support, especially my wife, for her patience in the final phase of the preparation of this work.

Grzegorz Oleszek

Abstract

In radiated emission compliance tests of automotive components according to standard CISPR 25, the semi-anechoic ALSE chamber is used. It supports a good correlation with disturbances observed in a vehicle, yet it is expensive and time consuming in use. Therefore, a simple to apply alternative method is expected to provide a reliable assessment of radiated emission levels. This work proposes the comprehensive approach supporting that. This thesis focuses on accurately determining nonlinearities present in the analyzed circuits. Their effects are supposed to be introduced through the inductively coupled coils and observed as radiated disturbances. Firstly, the exact multilayered coil equivalents are introduced, supporting a reliable representation of the mass-produced inductors. Subsequently, the mutual coupling is analyzed for coils freely positioned in space. Next, the excitation voltage supplying a nonlinear part represented by the analog front end circuit is determined. In the following, a spectrum analyzer acting as a high dynamic range null detector supports obtaining its frequency and voltage-dependent impedance, and resulting nonlinearities. Prediction of radiated disturbances utilizes a complete model of the magnetic link. Required nodal quantities as system currents and voltages are obtained on their basis using the harmonic balance method. Finally, they are used in a complete structural model of the CISPR 25 measurement system, supporting estimation of the induced voltage in a rod antenna, the equivalent of radiated emissions. This dissertation extensively uses structural simulations and measurements in the ALSE chamber to verify the proposed methodology's correctness and accuracy.

Streszczenie

Zaproponowana metoda badawcza umożliwia prognozowanie poziomu emisji zaburzeń promieniowanych w nieliniowych obwodach sprzężonych magnetycznie, reprezentowanych przez cewki indukcyjne i współpracujący z nimi układ AFE (Analog Front End) stanowiący obciążenie części wtórnej obwodu. Nieliniowości tego układu analizowano uwzględniając selektywny charakter pracy oraz silne wysterowanie dochodzące do 20 Vpp. Amplitudy i fazy wzbudzonych sygnałów harmonicznych określono w zakresie częstotliwości od 100 kHz do 1,8 MHz wykorzystując dedykowaną metodę kompensacyjną. Na bazie uzyskanych charakterystyk częstotliwościowych, zależnych od aktualnego poziomu wzbudzenia, skonstruowano modele symulacyjne opisane zestawem nieliniowych równań różniczkowych oraz wielkosygnałowymi parametrami X.

Sprzężenie magnetyczne w obwodzie przeanalizowano dla dowolnej orientacji cewek w przestrzeni, w konfiguracji zawierającej cewkę powietrzną oraz cewkę z prętowym rdzeniem ferromagnetycznym. W tym celu skorzystano z metod analitycznych oraz symulacji 3D, których wyniki zweryfikowano wykorzystując dedykowany zestaw pomiarowy.

Stosując analityczną metodę balansu harmonicznych oraz modele cewek i układu AFE wyznaczono planarny rozkład prądów i napięć w obwodzie. Na jego podstawie zdefiniowano korzystny (pod względem poziomu dominującej trzeciej harmonicznej) zakres pracy całego obwodu, który następnie zweryfikowano pomiarami w komorze ALSE. Jednocześnie skonstruowano równoważny model symulacyjny układu pomiarowego zgodnego z normą CISPR 25, na bazie którego estymowano poziom zaburzeń promieniowanych. Finalnie uzyskano zbieżność prognozowanych poziomów z pomiarami lepszą niż ± 6 dB, co stanowi potwierdzenie tezy niniejszej pracy. Przenalizowano również trzy pytania badawcze, z których każde znalazło właściwe umocowanie w wykonanych badaniach i uzyskało potwierdzającą odpowiedź.

Table of Contents

Abbreviations

AF	Antenna Factor
AFE	Analog Front End
ALSE	Absorber-Lined Anechoic Chamber
AM	Amplitude Modulation
AV	Average Value
AWG	American Wire Gauges
BPF	Band-Pass Filter
CISPR	Comité International Spécial des Perturbations Radio
EMC	Electromagnetic Compatibility
EMI	Electromagnetic Interference
EUT	Equipment Under Test
HB	Harmonic Balance
HPC	High Power Computing
IMD	Intermodulation Distortion
IP3	Third-order Intercept Point
LF	Low Frequency
LIA	Lock-In Amplifier
LSOP	Large-Signal Operating Point
LW	Long-Wave
MTL	Multiconductor Transmission Line
MW	Medium-Wave
NB	Narrow-Band
NVNA	Nonlinear Vector Network Analyzer
PA	Power Amplifier
PCB	Printed Circuit Board
PHD	Polyharmonic Distortion
PK	Peak
PWM	Pulse Width Modulation
QP	Quasi-Peak

RF	Radio-Frequency
RFID	Radio-Frequency Identification
SA	Spectrum Analyzer
SG	Signal Generator
SRF	Self-Resonance Frequency
SWR	Standing Wave Ratio
THD	Total Harmonic Distortion
TRC	Three-Reference Calibration
VNA	Vector Network Analyzer

1 Introduction

1.1 Radiated emission from automotive components

An increasing number of electronic modules integrated within a modern vehicle aims to improve energy efficiency, car security, and driving safety. These new features target fulfilling customers' expectations and increasing overall traveling comfort. On the other hand, however, they introduce complexity in their development, as the equipment coexisting in a confined car space can increase the risk of electromagnetic interference (EMI). Disturbances can be considered conducted and radiated emissions, distributed through the cable wiring or directly emitted by the functional modules (i.e., components, according to automotive industry nomenclature). These are simultaneously the paths of injecting disturbances into the sensitive systems (like a radio receiver), mainly when they operate with attached antennas.

A modern car contains numerous electrical and electronic components, which from an emission source perspective can be regarded as disturbance devices. The classic example is the ignition spark system or the electrical brush motor. Similarly, electronic devices are well represented by microcontrollers or switching drivers employing the pulse width modulation (PWM) principle. Electromagnetic compatibility (EMC) related effects of those components can be regarded as unintentional conducted and radiated emission resulting from non-ideal construction and challenging to avoid phenomena (like a PWM bulb control). However, there is also a class of devices, which operating principle requires exciting surrounding magnetic fields. In that case, they can be regarded as narrowband (NB) intentional radiators.

An example is the immobilizer system [1], granting the vehicle's engine starts upon mutual authentication with the security component contained in a key fob. Its role is replaced by the passive entry passive start (PEPS) system supporting hands-free operation in more expensive cars by using multiple antennas.

Another example is the contactless charger of a mobile phone, located in a car interior. All those devices operate in a low frequency (LF) band and show inductive coupling behavior. Despite the role in a car, each above component shall comply with appropriate EMC regulations, which are being verified through dedicated validation procedures.

One of the available methods of lessening the EMC issues in a target vehicle is the component level validation performed with the equipment under test (EUT). In this case, the tested component is considered together with an attached cable bundle, commonly called a harness. The EMC-compliant device is supposed to be immune to disturbances from other components, and, oppositely, its emissions should not disturb the nearby devices. Although passing validation does not guarantee the complete vehicle's compliance with the regulatory limits, early verification can identify associated risks.

Commonly used methods showing a good correlation of the component-level disturbances with the car's emission behavior are tests performed according to the CISPR 25 [2] standard in an absorber-lined anechoic chamber (ALSE). A complete validation approach defines unified methodology, specifies a measurement setup, and provides compliance limits. Due to the confirmed reproducibility of the recorded disturbances, various car manufacturers adopted that regulation as fundamental of their internal procedures. However, due to different level classes defined in the standard (as a function of the frequency), the vehicle manufacturer and the component supplier shall agree on that level before a validation. For example, considering LF operation within the long-wave (LW) and medium-wave (MW) bands, the defined levels are shown in Table 1.

Table 1 CISPR 25 limits for radiated disturbances, ALSE method [2]

Band	**Frequency (MHz)**	**Levels in dBµV/m**														
		Class 5			**Class 4**			**Class 3**			**Class 2**			**Class 1**		
		PK	**QP**	**AV**	**PK**	**QP**	**AV**	**PK**	**QP**	**AV**	**PK**	**QP**	**AV**	**PK**	**QP**	**AV**
LW	0.15 to 0.3	46	33	26	56	43	36	66	53	46	76	63	56	86	73	66
MW	0.53 to 1.8	40	27	20	48	35	28	56	43	36	64	51	44	72	59	52

Presented limits reflect emission levels determined using a peak (PK), a quasi-peak (QP), and an average (AV) detector. Using different detectors is appropriate for capturing of the strength of signals that are activated only periodically. Hence, in the case of the unmodulated continuous sine wave, those detectors should indicate a similar level, according to CISPR 16-1-1 [3]. That observation can lead to compatibility issues when a continuous operation is the main operating mode of the device. In that case, the excited harmonic spurs should stay all the time below the predefined limits to assure compliance with the standard. A situation further complicates when the particular limits are reduced (like in the case of the automotive specification FMC1278 [4] expecting a maximum of 20 dBµV/m PK and 12 dBµV/m AV within the 0.53 to 1.7 MHz band). Such levels are only slightly above the typical noise floor recorded in the ALSE chamber [5]. Therefore, to allow accurate determination of low-level disturbances with a presence of a relatively high ambient noise, mentioned standards [2, 4] allow the use of the reduced measurement bandwidth (from default 9 kHz or 10 kHz to 1 kHz) in the LF. In that case, the peak values remain unchanged, yet the monitored noise floor is lowered. An example of the radiated emission spectrum of an NB intentional radiator system is shown in Figure 1.1.

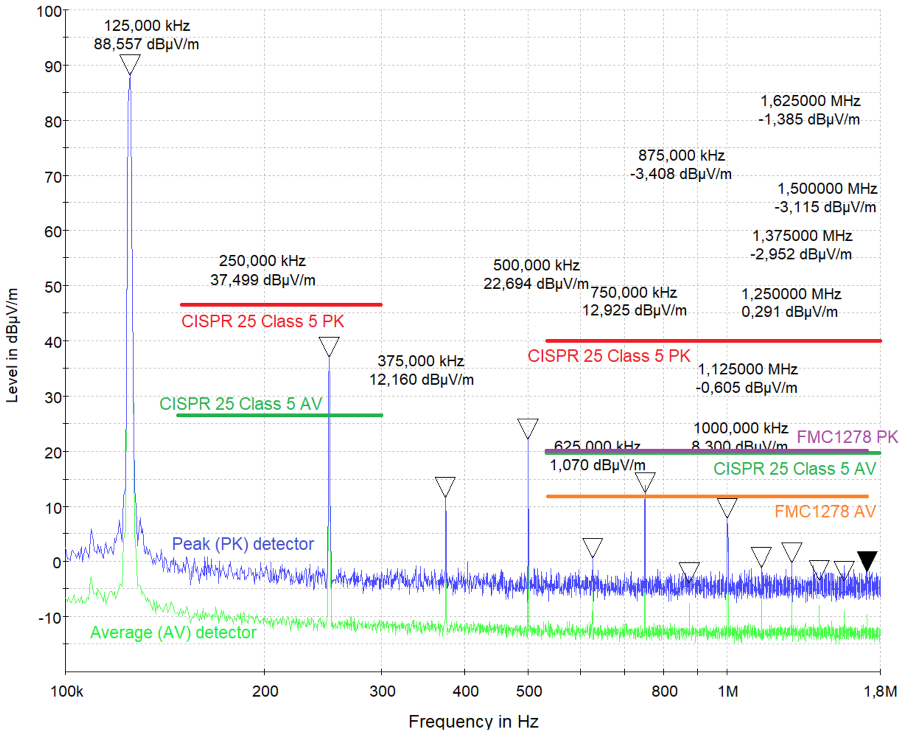

Figure 1.1 The NB system radiated emission spectrum example [5]

The EUT testing, according to the CISPR 25 (or any similar specification), requires access to specialized equipment (like an EMI receiver, antennas, ALSE chamber). Although car manufacturers typically own a full-sized anechoic chamber to conduct compliance testing, EMC validation is always a costly process. Component suppliers can find it even more demanding in their budgets and usually cannot afford complete test equipment. Moreover, the associated development cost can be inadvertently increased when the EUT repeatedly fails to comply with regulations. Therefore, alternate methods capable of predicting disturbance levels are required.

1.2 Prediction of radiated disturbances in a low frequency band

Although the NB inductive components mentioned above are different, some common features can be identified. Typically, the magnetically coupled system contains the onboard transmitting station, represented in Figure 1.2 by the primary coil inductance L_p, the harmonic excitation source U_{src}, and the impedance Z_{src}. The receiving part, considered a secondary circuit, includes the coil inductance L_s with a ferromagnetic core and the capacitor C_r supporting the NB operation. The secondary coil is loaded by the nonlinear impedance Z_{AFE}, representing the front-end circuit described in the following. The mutual inductance M represents the dominating magnetic coupling between primary and secondary coils. Commonly, the position of the primary coil is fixed, while the secondary can have some movement freedom. Therefore, the system currents I_p and I_s, and voltages U_p and U_s vary depending on the secondary coil's actual position. Those nodal quantities contain the effects of nonlinearities introduced by the impedance Z_{AFE} and the response to a pure harmonic excitation. The operation at relatively high voltage levels (~10 .. 20 V_{pp}) can add content to the frequency spectrum (like core-related spurs), which needs to be considered. The overall system is considered as a low-power in this work, with a primary current $I_p = 0.1$ A peak.

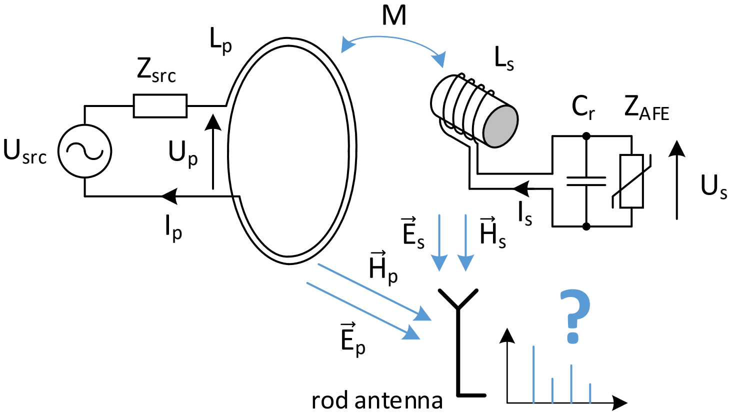

Figure 1.2 Radiated emission prediction problem

To assure compliance against particular specifications [2, 4], the magnetically coupled system considered as the EUT is then validated in the ALSE chamber. The actual level of disturbances is monitored by the rod antenna being part of the measurement setup. On that result, the compliance (or non-compliance) is finally determined.

Now the question arises – is it possible to accurately predict the level of introduced radiated disturbances? There were already attempts to answer that.

The first group of methods supposes that it is possible to estimate the equivalent field strength at the monitoring antenna position (hence the induced voltage in a rod) from the exciting magnetic and electric fields. These can be obtained analytically, by structural simulation, or using intermediate near-field measurements. Except for the latter, those methods commonly simplify radiation sources to the elementary forms (like a straight wire) to achieve results within a limited timeframe and at a reasonable cost. On the other hand, an alternative approach utilizing a detailed multiwire harness model is analytically complex. Moreover, it usually employs multiconductor transmission line theory, which is inefficient for fast estimation.

Similarly, attempts to accurately represent the radiation mechanism of the full-sized twisted wire cable increased the required computational resources significantly. Complementary near-field measurements performed in front of radiating sources over the Huygens' surface [6] demonstrated satisfying results for the MHz-range frequencies. However, they were regarded as less accurate [7, 8] for the lower bands due to typically neglecting magnetic fields.

The second group of methods allowing to predict radiated disturbances is those based on the so-called transmission factor concept. The idea reflects determining the antenna induced voltage ratio to the exciting nodal quantity (i.e., particular node voltage or current) versus frequency. In the case of a multiwire harness, the common current of the complete cable bundle is measured first and then referenced to the rod voltage. For simpler structures like a twisted cable, the common voltage is determined typically by an oscilloscope-based measurement. The quasi-static interaction with a rod antenna is typically assumed [9], which allows determining induced voltage directly from the electrostatic fields. However, those methods typically neglect the inductive coupling with the remaining setup parts, which is a deficiency of such approach.

The thesis proposes a simplified yet still accurate approach oriented especially to fulfill the strict needs of the automotive industry. Within the considered low frequency band, all the dimensions of circuit components and the measurement setup, including ALSE chamber, can be regarded as much shorter than the largest considered wavelength. It allows taking them (i.e., the EUT and the setup parts) as lumped circuits and using their mutual capacitances and inductances as coupling equivalents. The necessary nodal currents and voltages can be determined using circuit theory (i.e., the Kirchhoff's laws) from identified system nonlinearities.

1.3 Motivation and aims

The development of electronic modules typically requires many verification steps during a design process and not only the final validation at the end-stage. With limited time and access to the laboratory resources ensuring EMC compliance is challenging. Having an alternate method capable of predicting radiated disturbances at the early development phase reliably and at a reasonable cost is thus necessary.

The discussed method is not willing to replace the verifications at all as only the measurements can provide a realistic view of the actual level of introduced disturbances. However, the robust methodology allowing the assessment of the radiated emission spectrum can be regarded as an essential supporting tool during the component development.

The method should utilize the available design resources used during the car's development cycle as much as possible. Commonly, the structural model of the vehicle (called a *digital twin* [10]) is prepared, which example is shown in Figure 1.3, presenting the car interior with the considered immobilizer system near the steering wheel [11].

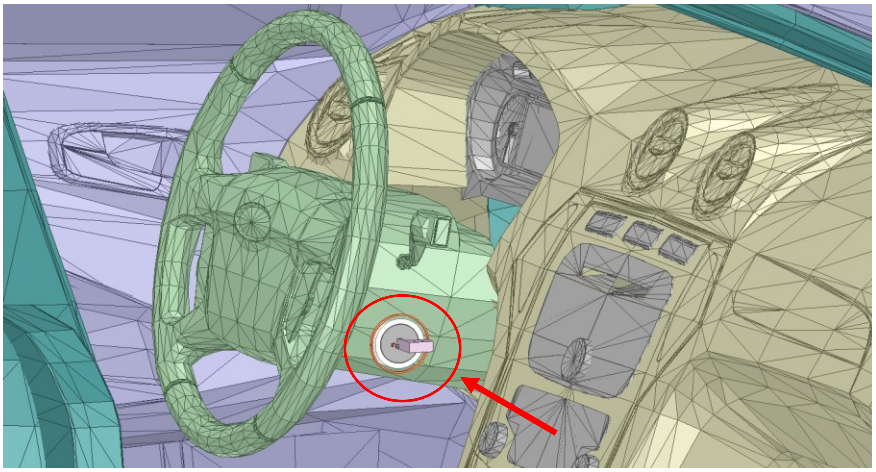

Figure 1.3 Structural model of a car interior with an immobilizer system [11]

In that case, the features of the component (like dimensions and material data) are copied to the simulation model representing it within a measurement setup equivalent, similarly to measurement in the ALSE chamber. The primary and secondary coils consisting of the magnetic link shown in Figure 1.2 are used for that purpose, on which basis their respective currents and voltages are determined. As a result, the radiated emission spectra obtained on their basis can serve as predicted disturbance levels from the given component. The implementation-specific parts like a mechanical lock or a metal key are excluded from below analysis, although their presence can be introduced to the simulation model when needed, as in [11, 12].

The method should support estimations at least within the LW and MW bands, considered together as the LF band. However, to not limit the method usability, it is expected to describe emission spectra within the continuous band starting from 100 kHz to 1.8 MHz. In addition, the frequency range extension can describe radiated mechanisms from inductive circuits operating below the 150 kHz limit, whose effects are observed within CISPR 25 bands. That case is shown in Figure 1.1, where the carrier signal at 125 kHz excited additional spurs due to system nonlinearities.

Therefore, this thesis proposes a comprehensive approach to the problem of predicting radiated disturbances from the magnetically coupled nonlinear circuit operating in the low-frequency band to support similar evaluations.

The methodology considers inductively-coupled coils freely positioned in space, for which their mutual inductance is determined analytically. The work proposes an approximation of the coil winding as a circular ring of a rectangular cross-section. To prove the applicability of such an approach, a structural simulation model using the filamentary method was applied. Additionally, the effect of a ferromagnetic core within one of the coils is analyzed. Its scope is extended to angular and radial displacements, typically omitted in referenced approaches [13-15]. The proposed evaluations are oriented on determining the induced voltage in the core-based coil, connected directly to the nonlinear part.

The coil load is represented by the low-power component acting as an analog front end (AFE) circuit [5, 16]. The AFE typically exists in NB inductive links, thus also in the examined immobilizer system, where it operates as a matching interface to the rest of the circuitry. Typically, the AFE integrates an input rectifier [17, 18], which operation is expected to introduce dominant nonlinearities. That frequency-dependent behavior is analyzed in a wide voltage range, resulting from variable coupling conditions between the coils. The AFE's complex impedance (i.e., including the magnitude and phase) at the carrier frequency and the excited harmonic spurs (both magnitude and phase) need detailed characterization to describe the nonlinear behavior correctly. Practical implementations use a signal generator with the following power amplifier [19] and a bandpass filter for component excitation [17]. The frequency-dependent gain-phase characteristics are obtained using a directional coupler [20, 21] or an oscilloscope [17], yet with a typically reduced dynamic range. Therefore, the compensation method using a spectrum analyzer as a null detector is proposed to overcome that limitation.

Identified nonlinearities allow determining the distorted currents using the equivalent AFE model. Various approaches have been proposed for similar cases, starting from linearization methods [22], Volterra series extension [23, 24], or frequency response functions [25]. However, all those methods either oversimplify the problem [22, 26] or introduce too much complexity [27, 28] and, in practice, are often not feasible for reliable and fast estimations. Therefore, measurement-based modeling implementing gray-box or black-box approach is used instead. Finally, the required nodal quantities (i.e., system currents and voltages) are determined using the harmonic balance method.

Prediction of radiated disturbances needs to be aligned with the practical methodologies used in the EMC laboratory, hence having to include the measurement setup's accurate model. In some works [6, 29], it is usually reduced to the harness only, on which basis the radiated emissions were estimated. However, with the presence of the inductive coils, such simplification is no more valid. Furthermore, both inductive and capacitive couplings with a rod antenna need to be considered, as they can determine the overall disturbance level.

1.4 Research questions

As described above, obtaining the radiated emission spectrum is a complex task involving many intermediate steps. Therefore, the first question addressing the proposed prediction methodology is how accurate it is and does it fit the automotive industry demands.

Another important aspect is the consideration of magnetically coupled coils in the simplified form as circular rings. Because the induced voltage follows the mutual inductance determined on their basis (and thus the disturbance level), the question is if those forms accurately describe the coupling mechanism for various positions and coil types in proximity.

The third research question put in this work is the possibility of determining circuit nonlinearities in a wide excitation range with the support of a spectrum analyzer and an external, dedicated test setup. Does elementary instrumentation allow obtaining the complex impedance accurately in the considered band?

These questions are going to be answered in this work.

1.5 Work thesis

The CISPR 16-4-1 document [30] specifies the methodology determining overall uncertainty in standardized EMC tests. The uncertainty sources, summarized in Figure 1.4, are supposed to reflect the EUT influence, the used measurement setup, impacts from the measurement procedures and instrumentation, and the environmental factors. All the sources together are considered using a type B uncertainty approach [31], on which basis the expanded uncertainty is obtained (using typical value of the coverage factor $k = 2$).

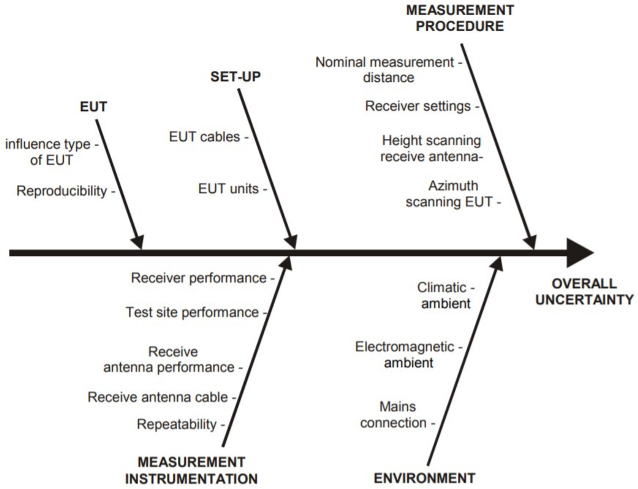

Figure 1.4 Uncertainty sources in radiated emission measurements [30]

The above specification expects the EUT's set-up and cabling reproducibility as a dominating problem during the EMC tests compared to those induced by the instrumentation and the test procedure. Typically, the environmental factors during the tests are of less influence due to generally low variations. Most commonly ± 6 dB of the expanded uncertainty is assumed by the EMC laboratories as reliable determination of the resulting levels, including the impact from the EUT.

Therefore, this work argues that the proposed methodology of predicting the radiated emission levels satisfies the ± 6 dB limit for the carrier signal and the dominant harmonic spurs within the LF band.

1.6 Structure of the work

This dissertation is structured as follow:

- Chapter 1 introduces the work and proposes the work thesis and the three main research questions that should be answered through this dissertation.
- Chapter 2 describes the main issues related to modeling the actual coils and proposes the geometry equivalent representing the coil impedance reflecting the manufacturing capabilities.
- Chapter 3 analyzes the mutual inductance of coils freely positioned in space, including the frequency influence and the presence of the ferromagnetic core in a coil.
- Chapter 4 evaluates the nonlinearities of the coupled circuits using the compensation method operating with high excitation levels.
- Chapter 5 introduces the nonlinear coupling model and determines the frequency spectra of coil currents using the harmonic balance method.
- Chapter 6 analyzes the coupling mechanisms present in the CISPR 25 setup and validates the predicted radiated disturbances through the measurements in the ALSE chamber.
- Chapter 7 concludes this work and gives an outlook.
- Chapter 8 includes the supportive data collected through this work.

2 Coil model

This chapter on wire loops covers methodology details of building an equivalent circuit of coreless and ferromagnetic core inductors used in automotive as loop antennas. The chapter begins with the analysis of material and winding properties, on which basis the new geometry model supporting manufacturing limitations is proposed. Its formulation reflects existing deformations of the winding structure identified during the inspection of the actual coils.

The following section concentrates on defining a frequency-dependent circuit model representing coil operation up to the self-resonance frequency. A model preparation starts with a short review of the associated phenomena, including skin and proximity effects and the ferromagnetic core losses. Then, the issue of radiated resistance in the LF band is highlighted. Finally, taking applicable effects into account, the complete structure containing the equivalent inductance, resistance, and capacitance is presented.

In the following, the proposed geometry model is used to obtain variations of lumped parameters of the coils. The compact engineering formulae are supplemented by 2D simulations, together reliably determining model parameters. Conclusively, obtained model data are compared with actual characteristics collected from vector measurements of designed coil prototypes.

2.1 Coil geometry model

This section aims to derive electrical equivalents of multilayer coil dimensioned in Figure 2.1 left. It is assumed that knowing wire properties, winding structure, and data of the optional core, the resulting impedance can be accurately determined. The presented structure shows the expected orthocyclic winding type [32], in which tightly wound wire turns provide the highest filling ratio [33]. The coil winding is externally limited by the bobbin's diameter D and axial length l, while the radial height h results from the actual turns placement.

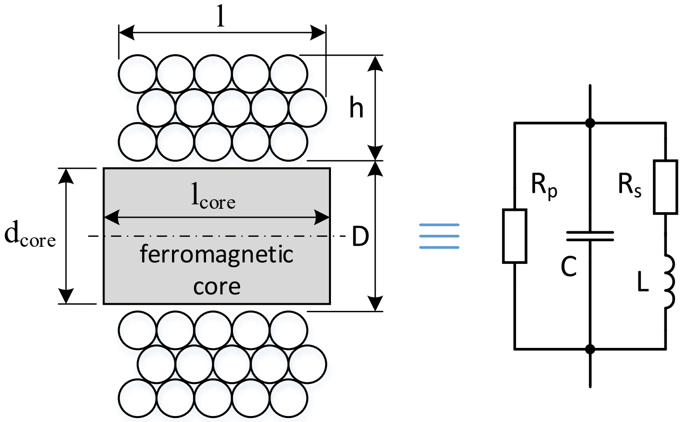

Figure 2.1 Multilayer coil dimensions (left) and coil electrical equivalent (right)

Both coreless (or simply air) and ferromagnetic core inductors are analyzed. The second case is limited to miniature coils containing a rod core (of diameter d_{core} and length l_{core}) and acting as receiving antennas. In particular, the scope of their analysis is limited to conditions in which hysteresis and saturation effects are negligible due to the low strength of an associated magnetic flux.

In this section, the new coil geometry model is introduced. It reflects the existing imperfections indicated from the inspection of the winding structure regarding turns placement and wire characteristics.

The need for a more accurate winding model

The idealized winding presented in Figure 2.1 is challenging to keep in reality. Mass-produced coils can significantly violate the idealized configuration by the winding structure and properties of magnet wire. A brief review of the manufacturers' capabilities was applied to identify applicable limits, summarized in the following. The realistic structure of winding was inspected by preparing the section view of exampled coils wound by AWG33 and AWG40 wires, which is shown in Figure 2.2.

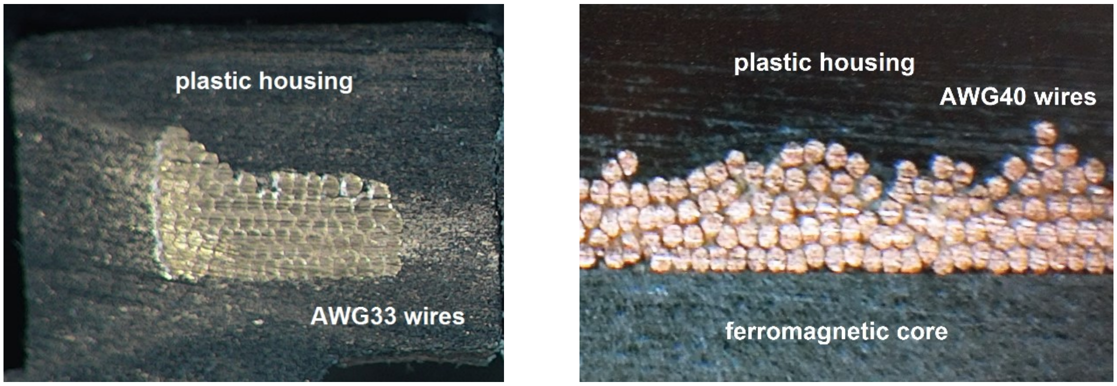

Figure 2.2 Section view of the air (left) and ferrite-core (right) coils

The section views of both coils indicate layered structure, at least from the initial inner layer. However, as observed in both pictures, the first layer deviates from the nominal horizontal orientation, and radial displacement is locally visible. This disturbance remains through all turns, resulting in significant deformation of the outer layer.

Another observation is that not all wires are tightly coupled to neighbor ones. This phenomenon arises if the wire's position is far from the first layer. The turns are floating on the outer external layer, thus indicating significant axial and radial displacements from expected positions.

The recognized number of layers for both coils is imprecise. For example, for an air coil case, one could count it from 6 to 10 and ferrite from 4 to 6. In this case, it can assume that considered coils represent a quasi-layered structure. In particular, such coils are the subject of analysis in this chapter.

2.1.1 Material and manufacturing capabilities

This section briefly reviews the base parameters of the magnet wire and the associated winding process. These are assumed as manufacturing capabilities, defining the achievable quality of wound coils.

Magnet wire

The enameled copper wires AWG33 and AWG40 are commonly used to construct air and ferromagnetic core coil windings in automotive applications. Table 2 summarizes data characterizing both radius r and insulation thickness t of the magnet wire types [34, 35] selected for further study.

Table 2 Summary of AWG33 and AWG40 wire data [34]

	Parameter	Value		
		minimal	typical	maximal
AWG33	Wire radius, r	88,9 µm	90.2 µm	91.4 µm
	Thickness of wire insulation, 2t, single type	12.7 µm	17.8 µm	22.9 µm
	Thickness of wire insulation, 2t, heavy type	25.4 µm	33 µm	40.6 µm
	Thickness of wire insulation, 2t, triple type	43.2 µm	50.8 µm	58.4 µm
AWG40	Wire radius, r	38.1 µm	39.4 µm	40.6 µm
	Thickness of wire insulation, 2t, single type	5.1 µm	8.9 µm	12.7 µm
	Thickness of wire insulation, 2t, heavy type	15.2 µm	17.8 µm	20.3 µm
	Thickness of wire insulation, 2t, triple type	22.9 µm	26.7 µm	30.5 µm

The diameter of conducting core of AWG33 wire indicates a possible change from nominal value $2r$ = 180.4 µm by ± 1.4 %. For AWG40 wire, this parameter varies from nominal $2r$ = 78.8 µm by ± 3.2 %, so both of them are assumed as quite accurate.

The insulation layer thickness t is characterized by greater variability. Depending on insulation type – single, heavy or triple, it can vary up to ± 28.5 % for AWG33 and up to ± 42.8 % for AWG40, for the most common single insulation. These ranges directly influence external wire diameter d_w, calculated as:

$$d_w = 2(r + t)\ . \tag{1}$$

Consequently, external dimensions of AWG33 remain in a range d_w = [190.5 .. 205.7] µm (198.6 µm nominal), which is around ± 4 % for the single insulation type. Similarly, AWG40 diameter stays in a range of d_w = [81.3 .. 93.9] µm (87.7 µm nominal), up to 7.3 % for single insulation. This range is surprisingly higher than typically one may assume. To compensate for this effect, the coil manufacturers occasionally introduce a redrawing process – Figure 2.3; the aim is to get the same outer diameter among coil lengths. However, during the wire processing, the conducting core exhibits additional shrink due to mechanical stress, resulting in diameter and conductivity variations.

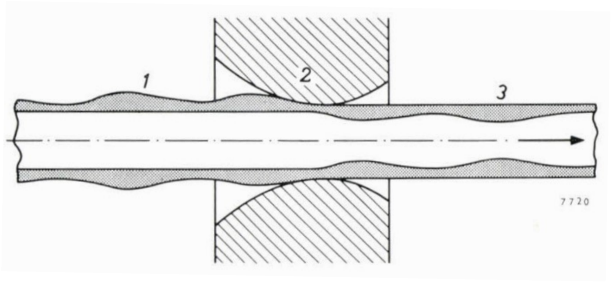

Figure 2.3 Wire redrawing process, adapted from [36] (not in scale)

The wire material used for a conducting core also has its own variation. The reported conductivity of copper used as a wire conductor [37, 38] indicates a shift from a mean value of $5.69 \cdot 10^7$ S/m by

± 0.26 %. Observed change arises primarily due to the uncontrolled addition of other elements like aluminum and process variation, mostly annealing. It is worth mentioning that electromagnetic field simulators (like Ansys Maxwell 2D/3D [39]) by default assume other conductivity values, typically $5.80 \cdot 10^7$ S/m. Without appropriate adjustment (even estimated), the obtained results may indicate an initial offset of nearly ± 2 %.

The relative permittivity ε_r of wire coating material is frequency-dependent in a considered low frequency band. For a polypropylene (PP) insulation investigated here ε_r = [2.0 .. 2.25] and loss tangent is 0.02 .. 0.06 % within 50 .. 10^6 Hz band [35, 40].

Although the above materials can exhibit drifts due to temperature change, the controllable laboratory conditions (typically 20 .. 25 ºC) allow assuming their effects as minor. That approach is typical for EMC-related tests, where tests majority are completed at the nominal temperature. Thermal effects in the automotive industry are commonly considered part of the worst-case circuit analysis, which is excluded in this study. Additionally, plastic housing's electrical and magnetic properties are not analyzed, assuming they are insignificant within a considered frequency range.

Winding process

A specific range of repeatability characterizes the winding process [32, 36, 41, 42]. The direct reason for the inaccuracy is the machinery and process parameters, thus winding jump, rotational speed or acceleration of the coil body, layer jump, and the caster angle of the wire guide [32, 43] [42, 44]. Additionally, the tension applied during the winding plays a significant role by influencing the deformation of the wire [32]. The other factor is the contact behavior between wire and coil body and wire self-contact, including friction [32, 36]. The critical phenomenon remains the deformation of coil winding, resulting from multiple layers, coil dimensions, relaxation of tension, and possible stretching or compression during the housing injection process.

All the above parameters were considered in recent works as constant factors representing axial ea and radial er displacements. However, as indicated above, these parameters cannot be fixed, and the existing approaches can provide only a rough estimation of their effects. As variables (depending on turn number or position), one can evaluate their individual impacts on the coil's resulting properties (i.e., inductance, resistance, and capacitance components). Furthermore, they can support the analysis of optimal coil design, which has been addressed in [45, 46].

The existing constraints described in this section are considered to be the basis for creating the coil winding model proposed below.

2.1.2 Realistic winding model

The proposed structure of more realistic, orthocyclic winding is presented in Figure 2.4. Supplemental to referenced evaluations [32, 47], the flexibility of analysis of non-tight winding is introduced by varying the axial ea and radial er parameters. As clearly pointed out in works [32, 42, 44], turns located on the initial layer have a dominant impact on the rest of the winding quality, thus positions of upper turns. Even if they are expected to be spaced by a pitch p distance, the following layers' turns fall into the grooves below due to a wire's initial tension. However, if the tension is not constant, the wire may get relaxed, which is not supported by the latest winding models [48, 49], although observed in reality. Therefore, the flexibility supported by ea_i and er_i parameters for i-th turn allows the more accurate prediction of the next position of each turn and, in practice, supports the estimation of the actual winding process more correctly.

Given wire position is identified by radius a_i and distance from coil side l_i for each considered i-th turn. The number of layers N_L with the same number of turns N_V and number of turns on outer layer N_E define together a total number of turns N_T, according to formula (2). The index within each turn in Figure 2.4 identifies winding order, thus a turn number itself.

$$N_T = N_L \cdot N_V + N_E \,. \tag{2}$$

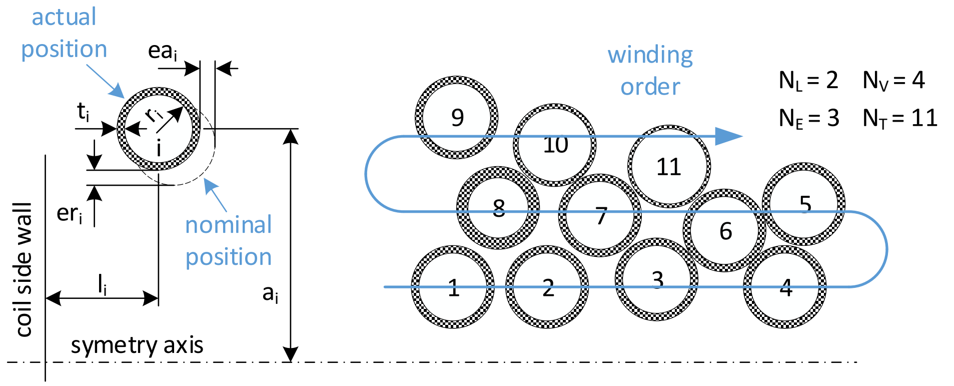

Figure 2.4 Definition of i-th turn position (left) and turns numbering rule (right)

To make the proposed geometry model flexible, the specific radius of conducting core r_i and the insulation thickness t_i of a given i-th turn is kept. However, it is assumed that those parameters remain constant within a given turn, which is reasonable for the considered class of miniature coils.

The presented geometry shows relations between individual turns in a simplified way. The exact dependencies should base on a conical structure, on which the start and end radii of a given turn can be different. However, such degree of details may lead to a significantly extended geometrical analysis that is not the aim of this work. By estimating winding turns as a set of circular rings, the required accuracy is still adequate, as confirmed in several works [47, 50-55].

The introduced model supports the required flexibility in analyzing the influence of material and dimensional variations, which can reasonably be expected in the case of mass production (see section 2.1.1 for typical parameter tolerances). In particular, it is possible defining the position of the individual turn from the cases shown in Figure 2.2, for which the layered structure described by the formula (2) cannot be appropriately assigned.

Examples of the virtual “wound” air coils of the nominal (i.e., $ea = er = 0$ mm) and disordered (or spread) winding with ea and er parameters uniformly distributed in the intervals [-0.05 .. 0.05] mm and [0 .. 0.05] mm respectively, are shown in Figure 2.5. Turns distribution shown in the right picture is assumed representative for disordered cases collected during the evaluation described in section 2.3. It reflects the highest difference of the coil impedance components (i.e., R_s, R_p, C, L) compared to their nominal values.

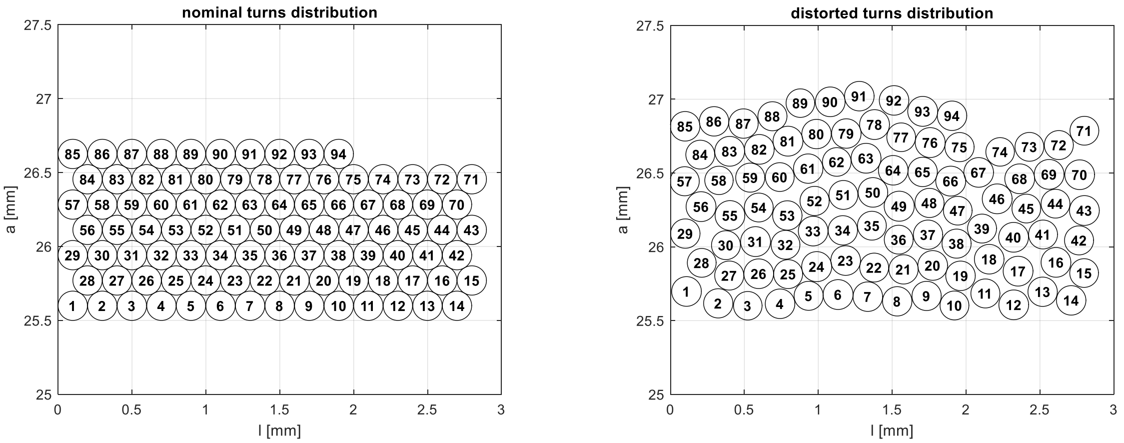

Figure 2.5 Nominal (left) and disordered (right) geometry of the air coil, with $D = 51$ mm, $l_p = 2.9$ mm, $p = 0.2$ mm, $N_L = 6$, $N_V = 14$, $N_E = 10$, $N_T = 94$, $h_{nom} = 1.22$ mm, $h_{dis} = 1.61$ mm

Appendix 8.1 provides further details of the proposed geometry model. In the following section, the changes of the coil impedance components are obtained on its basis.

2.2 Coil impedance modeling

This section aims to define a compact yet fully functional circuit representing coil equivalent up to the first self-resonance frequency (SRF). Beyond this limit, the inductor can act as capacitance, and the presented model may not support such behavior accurately [56].

Before describing circuit model in detail, an overview of related physical phenomena is presented.

2.2.1 Equivalent resistive losses

The selected loss mechanisms of a multilayer coil within a low-frequency band are presented here. On their basis, it is possible to quantify frequency-related effects as equivalent resistive parts or as multiplication factors. That way, their consideration within a complete lumped circuit model is possible.

Skin and proximity effects

The alternating current flowing through the conductor tends to penetrate a volume only up to a certain depth. Consequently, the current density is not uniform and shows a higher value close to the conductor surface. This phenomenon, called the *skin effect*, is dependent on both the frequency and material properties. The work of Wheeler [57] indicated it as a reduction of equivalent area conducting current with frequency increase. An accurate evaluation of this problem is found in Lammeraner [58] and Smythe [59] books, relating it to the longitudinal magnetic field in a wire.

If the source of a magnetic field is an alternate current flowing in a nearby conductor, the associated phenomenon is called the *proximity effect*. To account for it, the impact of a transversal magnetic field is considered. If the source of it is a coil winding, the individual contribution from each turn needs to be evaluated. The famous Dowell's formula (3) [60, 61], quoted herein as a reference, assumes a quadratic dependency from a number of layers N_L, with optional scaling by a porosity factor [62]. However, having a well-defined position of each turn described by the winding model, a more accurate assessment of the proximity effect is possible using structural simulations. Furthermore, as reported in several works [62-64], Dowell's formula tends to increase an overall proximity effect, which suggests using field solvers like Ansys Maxwell 2D/3D [39] for more accurate studies.

The skin and proximity effects are recognized externally as an increase of the apparent resistance, together with a simultaneous decrease of the reactance part of wire impedance. The factors quantifying this process as F_{Rskin} and F_{Rprox}, and F_{Lskin} and F_{Lprox} [62, 65], respectively, are frequency, material, wire shape, and turns' position dependent and typically estimated using hyperbolic or Bessel functions [62, 66].

Because of the orthogonality of skin and proximity effects [65] (see also Appendix 8.2), the relevant impacts can be directly summed up as a common factor (see formula (22) as an example), resulting with [61, 64]:

$$F_R = F_{Rskin} + F_{Rprox} = A\left[\frac{sinh(2A) + sin(2A)}{cosh(2A) + cos(2A)} + \frac{2(N_L^2 - 1)}{3}\frac{sinh(A) - sin(A)}{cosh(A) + cos(A)}\right], \qquad (3)$$

where parameter A normalizes wire radius to skin depth δ_{cond} [61] and compensates it due to winding pitch p as:

$$A = \frac{r}{\delta_{cond}}\sqrt{\frac{2\pi r}{p}}. \qquad (4)$$

The similar to the above formula yet addressing F_L factor can be found in [64, 67, 68].

The impact of a dominant proximity effect is not uniform along coil winding and strongly depends on wire location. Therefore, in analyzing disordered turns' distribution like in Figure 2.5 right, the 2D simulation is useful due to the flexibility in defining turns positions. Even so, there are attempts to estimate it as a random winding [69] or unevenly spaced turns [70]. However, these methods cannot handle *any defined* position of the coil turns; therefore, the 2D simulation is preferred. It results in the current density distribution shown in Figure 2.6 within the considered air coil winding.

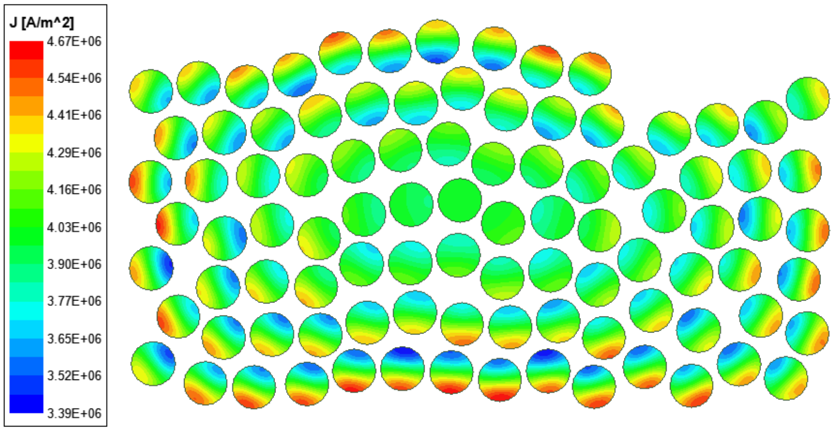

Figure 2.6 Simulated skin and proximity effects within air coil winding, I_p = 100 mA, f = 125 kHz

The same net current is used for each turn to obtain the above data. However, due to longitudinal (i.e., resulting from own wires' currents) and horizontal and vertical magnetic fields (i.e., of neighbor wires' currents), the given wire's current distribution is not uniform. Therefore, it results in a more increased density on the outer side of the winding, simultaneously with nearly equal distribution in its central positions. As each turn's current density distribution contributes to the overall resistive loss [71], the resulting winding's AC resistance is determined with higher accuracy. The simulated factors for the above case were $F_R = 1.35$ and $F_L = 0.99$.

Ferromagnetic core losses

The coil power losses, associated with a presence of a ferromagnetic material nearby the winding, resulting from the used core's material and shape, the strength of coupled magnetic flux, and the operating frequency. Although it is possible to quantify their individual impacts as resulting from the eddy currents [72-75], hysteresis [72, 74, 76], Barkhausen effect [77], or residuals [78], the typical approaches [14, 75] employ simplified methods for a low magnetic field case.

Experimental formula

The power dissipated within a core volume V_c, neglecting individual phenomena of the complicated ferrite physics, can be estimated using the experimental Steinmetz formula [75, 76] as:

$$P_{core} = P_v V_c = k f^a B_m^b V_c \,, \tag{5}$$

where k, a, b are the coefficients identified for a given material and shape, and B_m is the peak value of the magnetic field [79].

Knowing the root-mean-square current I_{rms} flowing through the coil, the equivalent resistance R_{core} summarizing overall core losses is defined as:

$$R_{core} \approx \frac{P_{core}}{I_{rms}^2} = \frac{2P_{core}}{I^2} \,. \tag{6}$$

However, according to supplier notice [79], the calculated loss resistance might be inaccurate using the considered rod core (i.e., $d_{core} = 1.5$ mm, $l_{core} = 10$ mm) of MnZn 3C90 material [80]. A direct reason is very low power loss density P_v as 0.94 mW/mm^3 @ 125 kHz, for which the equation (5) was not optimized. The calculated loss equivalent was $R_{core} = 0.33\ \Omega$ and assumed $B_m = 2.3$ mT (i.e., field intensity in a core center caused by coil current $I = 1$ mA, data obtained from 2D simulation).

Loss tangent method

Alternate method [81] supports calculation of core losses using a complex permeability characteristic identified for a given rod core design. Similarly, the equivalent resistance R_{core} is defined, yet aligned with a coil inductance L containing ferromagnetic core, as:

$$R_{core} = \frac{\omega \mu'' L}{\mu'} = \omega L tan(\delta_m) \,, \tag{7}$$

where μ' and μ'' result from the complex permeability μ of a ferromagnetic material defined as:

$$\mu = \mu' - j\mu'' = \mu_0(\mu_r - j\mu_r'') \,, \tag{8}$$

and δ_m is called magnetic loss tangent.

The estimation of core loss using 3C90 material of permeability data shown in Figure 2.7 left, together with core effect considered in section 3.1.2, results in $R_{core} = 0.095\ \Omega$ @ 125 kHz assuming $L = 1.64$ mH. This loss increases up to $R_{core} = 29.24\ \Omega$ @ 1 MHz and remains in line with the 2D simulation – see in Figure 2.7 right.

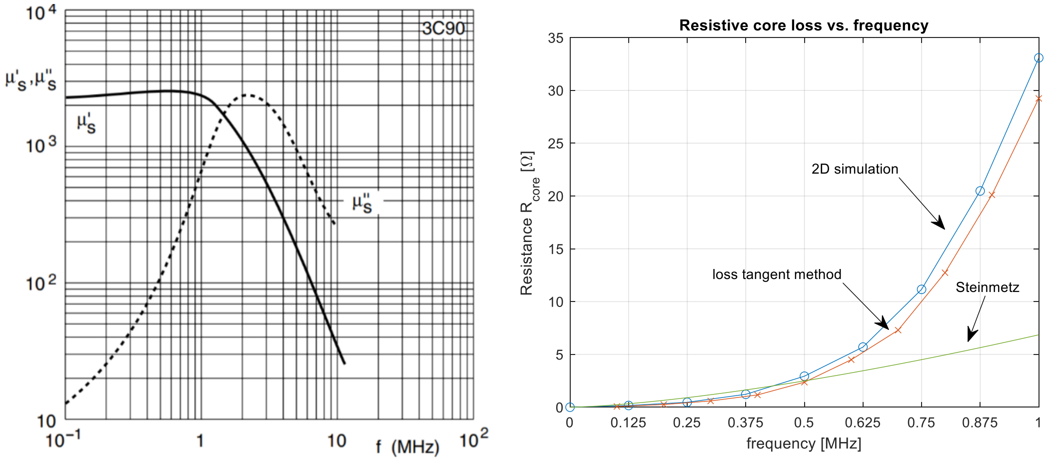

Figure 2.7 Complex relative permeability data of 3C90 material (left) [80] and resulting core loss equivalent (right)

The value of R_{core} is very low within a considered LF band and remains minor (i.e., 1.2 % @ 125 kHz) compared to total coil resistance (see Figure 2.10). However, it increases with a frequency due to higher loss caused by induced eddy currents and reaches 16.1 % of the total resistive loss at 1 MHz.

Radiation resistance

The last phenomenon reviewed in this section is radiation resistance, which describes electrical power transmitted (or received) by the loop antenna. The associated power loss can be described by integrating the real part of the complex Poynting vector over the spherical surface, following normalization to the square current [82, 83].

The presence of a ferromagnetic core of effective relative permeability μ_{eff} increases radiation resistance due to a square law relation, according to Balanis formula [82]:

$$R_{rad} = \left(\frac{8\mu_0\mu_{eff}^2\pi^5}{3c^3}\right) r_{avg}^4 N_T^2 f^4 \,, \tag{9}$$

where c is the speed of light, and r_{avg} is an average coil radius. However, regardless of core impact, the resulting radiation resistance remains very low (i.e., ~10^{-12} Ω range) and, therefore, is neglected in further analysis.

Knowing the individual contributions from the above phenomena, makes it possible to combine a complete lumped coil model consisting of equivalent impedance parts.

2.2.2 Model structure

The proposed equivalent circuit for both air and ferromagnetic-core coils, which has already been shown in Figure 2.1 right, assumes its use for a quasi-harmonic analysis considered in this work. This condition reflects the applied frequency-dependence of the R_{ac} and L parts as individual factors, accurately determined only at the fundamental frequency and its harmonics. Hence, the more accurate ladder structure [84-88] can be used for the time domain analysis.

The used circuit model consists of the coil's inductance L and parallel capacitance C coarsely defining the angular frequency ω_{SRF} of first resonance. It is supplemented by the coil resistance R_s, lumping together the DC resistance, skin and proximity effects, and optional core losses.

Parallel resistance R_p is optional; however, it supports the unique mapping of the measured impedance to the model parameters near the SRF. Additionally, it allows consideration of a dielectric loss [71], which cannot be modeled using the R_s. As long as R_p is determined in a range above hundreds of kΩ, it can be omitted without significantly affecting the overall model's accuracy.

The L, C and R_s parameters in a general case are frequency-dependent, yet for notation simplicity, their dependencies (ω) are omitted. The R_p is assumed fixed as determined only at the SRF. Anyhow, it is still possible to estimate its value as resulting from the turn-to-turn leakage, similarly as in [56].

The admittance Y of circuit from Figure 2.1 right in terms of lumped parameters is described as:

$$Y(\omega) = \frac{1}{R_p} + \frac{1}{R_s + j\omega L} + j\omega C = \frac{1}{R_p} + \frac{R_s}{R_s^2 + \omega^2 L^2} + j\omega\left(C - \frac{L}{R_s^2 + \omega^2 L^2}\right). \tag{10}$$

In parallel resonance, the imaginary part vanishes, which determines the equivalent capacitance as:

$$C = \frac{L}{R_s^2 + \omega_{SRF}^2 L^2}. \tag{11}$$

Parallel resistance R_p results from the remaining impedance Z_{SRF} indicated at SRF, as:

$$R_p = \frac{1}{\frac{1}{|Z_{SRF}|} - \frac{R_s}{R_s^2 + \omega_{SRF}^2 L^2}}. \tag{12}$$

The angular frequency ω_{SRF} is derived from (11), clearly indicating the reduction of the self-resonance frequency due to coil losses [89].

$$\omega_{SRF} = \frac{1}{\sqrt{LC}}\sqrt{1 - \frac{CR_s^2}{L}} . \tag{13}$$

The above relations allow coil analysis as a lumped circuit, of which individual parts are described below.

2.2.3 Inductance

In the literature, many formulae exist for the calculation of coil inductance in various configurations. Starting from Rosa [90], Snow [91], Nagaoka [51], or Wheeler's [52] works, numerous attempts have been made over decades to provide accurate equations in a compact form. In recent years, evaluations mainly addressed structural approach [88], finite element methods [92], or 2D/3D simulations [93], on which base the achieved inaccuracy as low as 0.02 % is possible [88]. However, the high level of detail may lead to convergence issues (see 3.1.5) and significantly extended simulation time [94]. The methodology presented below, originating from Maxwell's work [95], assumes inaccuracy 1 .. 2 %, which is considered adequate in analyzed cases.

The same net current *I* is assumed for serially connected coil turns. Therefore, the total inductance *L* of the multilayer coil calculated near DC is a sum of internal L_{INT} and external L_{EXT} self-inductances and mutual inductance L_{MUT} of coil rings, according to:

$$L = L_{INT} + L_{EXT} + L_{MUT} . \tag{14}$$

Internal self-inductance L_{INT}

The internal part of self-inductance of wire with length equal circumference of a given *i*-th ring, having internal radius a_i, is calculated as:

$$L_{INT} = \sum_{i=1}^{N_T} L_{INT_i} = \frac{\mu_0\mu_{cond}}{8\pi}\sum_{i=1}^{N_T} 2\pi a_i = \frac{\mu_0\mu_{cond}}{8\pi} W_l , \tag{15}$$

where $\mu_0 = 4\pi 10^{-7}$ H/m, and μ_{cond} and W_l are a relative permeability and a total length of wire conductor, respectively. Typically, the internal self-inductance is negligible as remaining in the nH range. However, it can provide a measurable impact in a low number of turns and a high root diameter. Therefore, this and the following contributions are examined concerning a particular coil configuration presented in section 2.3.

External self-inductance L_{EXT}

The external part of self-inductance, L_{EXT}, is geometry-dependent and reflects the mutual inductance of segments within same circular ring. Following [96], it can be calculated as:

$$L_{EXT} = \sum_{i=1}^{N_T} L_{EXT_i} = \mu_0\mu_{ext}\sum_{i=1}^{N_T}\sqrt{a_i(a_i - r_i)}\left[\left(\frac{2}{k_i} - k_i\right)K(k_i) - \frac{2}{k_i}E(k_i)\right], \tag{16}$$

where μ_{ext} is relative permeability of medium surrounding wire, $K(\cdot)$ and $E(\cdot)$ are complete elliptic integrals of the first and second kind, respectively, and k_i is defined as:

$$k_i = \frac{2\sqrt{a_i(a_i - r_i)}}{2a_i - r_i}. \tag{17}$$

Mutual inductance L_{MUT}

The calculation of a mutual inductance part of the multilayer coil follows the observation that i-th and j-th circular rings are coaxially oriented, with axial distance $|l_i - l_j|$. Thus based on [96], L_{MUT} calculates as:

$$L_{MUT} = \sum_{i=1}^{N_T} \sum_{j=1, j\neq i}^{N_T} L_{MUT_i} = \mu_0 \mu_{ext} \sum_{i=1}^{N_T} \sum_{j=1, j\neq i}^{N_T} \sqrt{a_i a_j} \left[\left(\frac{2}{k_{ij}} - k_{ij} \right) K(k_{ij}) - \frac{2}{k_{ij}} E(k_{ij}) \right], \tag{18}$$

where k_{ij} is defined as:

$$k_{ij} = 2\sqrt{\frac{a_i a_j}{(a_i + a_j)^2 + (l_i - l_j)^2}}\,. \tag{19}$$

Having the flexibility in describing the turn position by a_i and l_i, together with wire radius r_i, the more general evaluations are possible.

The frequency-dependence of a coil inductance is obtained from the 2D simulation, which allows analyzing the disordered winding structure.

2.2.4 Resistance

Without external alternating magnetic fields, the winding losses are identified with Joule energy dissipated in a conductor due to a current flowing through the turns. In the case of operating frequency approaching DC, the sole source of losses is the resistance R_{dc} of the coil windings, calculated as:

$$R_{dc} = \frac{W_l}{\pi r^2 \sigma_{cond}}, \tag{20}$$

where σ_{cond} is the conductivity of wire material.

More accurate formula

The assumption of representing coil turns as circles of constant radii simultaneously neglects a conical winding structure. To account for its contribution, the accurate length formula $W_{lcon}(\cdot)$ is derived in Appendix 8.3. Using it, together with an individual wire radius of a given turn, it is possible to express R_{dc} more accurately as:

$$R_{dc} = \frac{1}{\pi \sigma_{cond}} \sum_{i=1}^{N_T} \frac{W_{lcon}(a_i, l_i)}{r_i^2}, \tag{21}$$

The difference (yet still minor) is observed only regarding the AWG40 wire used for the miniature coil due to a lower D/p ratio. Comparing the results of both equations (20) and (21), these numbers were 10.2792 Ω and 10.2804 Ω, respectively. Definitely, the indicated difference of 0.012 % allows using a simplified formula (20) in practical cases.

Total resistive loss

As presented in section 2.2.1, the impacts of the skin and proximity effects can be summed up following their orthogonality. Hence, the total equivalent series resistance R_s within the coil model is calculated as:

$$R_s = R_{ac} + R_{core} = R_{dc}F_R + R_{core}\,, \tag{22}$$

where the presence of the last part follows the existence of a ferromagnetic core. Due to frequency dependence, the coil resistive loss needs estimation at the points of interest (like spurs harmonics) using formula (3) or more accurate 2D simulation.

2.2.5 Capacitance

Self-capacitance of the coil referred to as parasitic, stray, distributed, or internal capacitance, results from the nonzero voltage across coil connectors, thus the electric field between turns. This field depends on a voltage distribution among coil winding and, except for some cases like a flyback winding type [97-99], is not uniform as visible in Figure 2.8. As the charge on the conductor surface changes from turn to turn, the apparent capacitance seen between coil feeds (i.e., marked as 1 and 94) is not straightforward to calculate, even using the charge distribution-based model [100]. Therefore, the approximation methods [101, 102] are typically used to overcome this complexity.

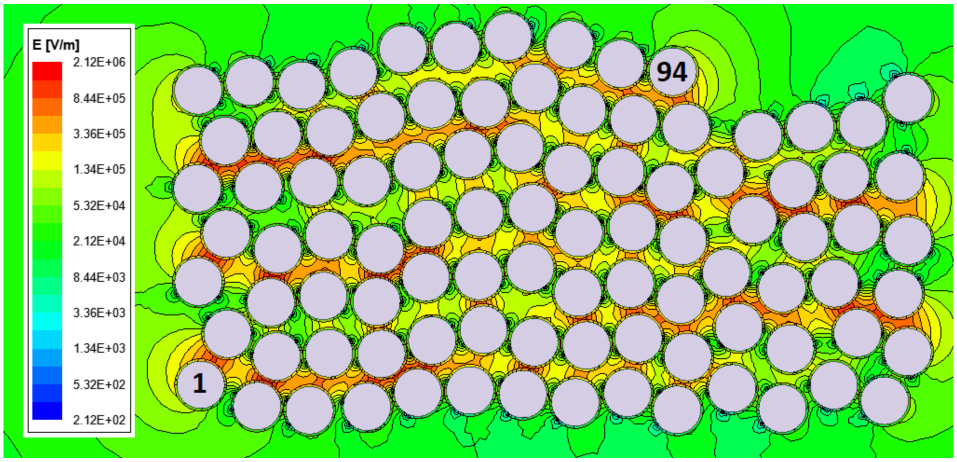

Figure 2.8 Electric field intensity within disordered coil winding, $V_{coil} = 70$ V

The most common approach uses the electrostatic model [102-107] to obtain the coil capacitance. The basis of the analytical method lies in the assumption that the equivalent turn-to-turn and the resulting layer-to-layer capacitance C_{LL}sufficiently estimates capacitance distributed between coil turns. Simultaneously, capacitances other than reflecting a direct connection to a considered turn are neglected due to minor contributions. Therefore, the estimation of resulting capacitance can utilize elementary capacitor concepts like parallel [101] or cylindrical [108] plates, parallel wires [109], or basic cell [99, 109]. Each of them provides a solution for C_{LL}, which allows an estimation of a total coil capacitance [99] as:

$$C = 2\frac{\left(\frac{N_E}{N_V} C_{LL,N_V-1}\right) \cdot N_E^2 + \sum_{k=1}^{N_L-2} C_{LL,k} \cdot N_V^2}{\left((N_L-1) \cdot N_V + N_E\right)^2}, \tag{23}$$

where $C_{LL,k}$ represents a capacitance between two consecutive layers (i.e., k and $k+1$).

For a quasi-layered winding structure, the solution can utilize a concept of a mean layer radius [47] or apply the efficient 2D simulation as in [48, 101, 110, 111]. In the second case, the equivalent capacitance is determined accurately using the total energy E_E stored in the electrostatic field [48, 97, 107, 112] as:

$$C = \frac{2E_E}{V_{coil}^2}, \tag{24}$$

where V_{coil} is the voltage applied to the coil terminals.

A significant part of works addressing capacitance modeling [89, 99, 101, 109] assume it as invariant in the LF band. This approach is correct until permittivity of wire insulation remains constant or, more generally, the indicated changes allow neglecting them. Notwithstanding, knowing the actual variation of the material permittivity, the more accurate evaluations are possible. In this case, the ε_r value is usually indicated as a complex number, of which the imaginary part is associated with absorption losses [108]. This kind of loss, however, is typically neglected considering low-power operations. As verified, the consideration of a permittivity variation (i.e., decrease with a frequency rise for the polypropylene material [40]) helped to describe coil behavior near the SRF more accurately. Beyond this limit, the capacitive part starts to dominate, and the coil operates more as a lossy capacitor.

2.3 Coil model evaluation

The model evaluation aims to provide a comprehensive approach in analyzing a similar class of coils regarding their frequency dependence and parameters tolerances. The initial evaluation steps are similar for the air and ferromagnetic-core-based coils and consist of a nominal geometry definition with the following estimation of equivalent parameters using the presented engineering formulae (like (3), (20), (23)). Then, the 2D simulations are applied, allowing comparison with the calculated values. The evaluations within this step are referenced to the nominal turns reflecting Figure 2.5 left data.

The second step aims analysis of disordered coils (like shown in Figure 2.5 right) and employs hybrid evaluation using Matlab and Maxwell 2D simulator. The typical variations of ea, er, r and t parameters (see [47] and Table 2) are used for that purpose, on which base the Matlab tool generates the disordered geometry (i.e., described by the set of a_i and l_i coordinates). Instead of using the maximum limits of all parameters (which is not realistic), the random values from defined distributions are used (i.e., uniform for ea and er, normal for r and t). The coil geometry is then imported into the Maxwell 2D environment as a script-defined model. On this basis, two independent simulations are run. The first extracts the R_s and L components and is performed up to 1 MHz (supposed as SRF range) using the eddy current solver. Simultaneously for a case of a ferrite coil, the equivalent loss in a core volume is calculated. The second simulation determines coil capacitance C using pre-calculated voltage distribution along coil turns, employing the same geometry model but using the electrostatic solver. The above Monte Carlo approach repeats 500 times to obtain a reliable statistic [113]. Due to an extended simulation time (~25 minutes each step on a typical PC computer), the evaluations used the high power computing (HPC) platform employing 24 CPU cores and 1 TB RAM [114]. Finally, the results are exported back to Matlab for data postprocessing.

Supplementary to the above evaluations, the ea and er parameters' individual impacts are determined, assuming other parameters as nominal. On their basis, the influence of a manufacturing equipment capabilities is estimated.

Finally, the simulations are referenced to the measurements results obtained for sample coils prepared by the author exclusively for that purpose.

2.3.1 The frequency dependence of coil impedance

Using 2D simulations helped collect model variations regarding R_s, L and C parameters and their frequency dependence for coreless and ferrite core coils. Although the collected impedance data are different for both coil types, the observed variations show similar behavior. Therefore, the following subsections present more detailed results only for the air coil (the summary for a ferrite-core coil is shown in Appendix 8.4).

The presence of the rod core is analyzed as a separate section 2.3.2.

Inductive component

The simulated frequency dependence of the L component is shown in Figure 2.9. The reduction of the inductance part at the nominal frequency (i.e., 125 kHz) is negligible and calculated as less than 0.05 % for both turn distributions shown in Figure 2.5. However, the inductance decreases for higher frequencies, approaching around -2 % at 1 MHz. This change is attributed to reducing the wire volume conducting AC current and dominates in the self-inductance part of a coil.

The effect of winding spreading is recognized here. The increased distances between loops lead to a mutual coupling reduction, assumed as a dominant inductance part of a multilayered coil. Therefore, the coil inductance near DC is bigger for a case of the nominal coil with tightly packed turns compared to disordered ones ($L = 1.0057$ mH and $L = 0.9937$ mH, respectively). Nevertheless, that change is relatively low and quantified as -1.2 % using simulation data.

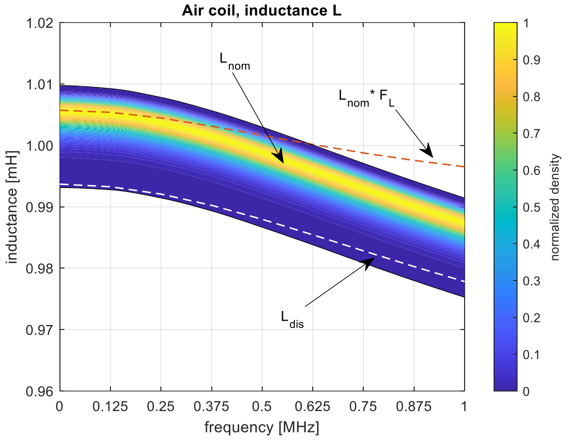

Figure 2.9 2D simulated frequency dependence of air coil inductance L, referencing nominal and disordered turns shown in Figure 2.5

The asymmetrical distribution of inductance values shown in Figure 2.9 results from the tight coupling of turns, possible to shrink more only due to reduced wire diameter and insulation thickness. The lower values follow the opposite behavior (i.e., diameter and insulation increase), yet axial, and radial relaxations can extend it further.

The F_L factor reflects correctly the frequency dependence only up to a few hundreds of kHz. Above, the 2D simulation provides a more accurate estimation due to reflecting wires' current densities on a mutual inductance [85].

Resistive component

The resistance variation that can be inferred from Figure 2.10 shows increasing R_{ac} from a minimal value of 10.7 Ω near DC to 14.4 Ω @ 125 kHz and 154 Ω @ 1 MHz (i.e. more than 14 times). These numbers were 10.8 Ω, 14.0 Ω, and 139 Ω (i.e., nearly 13 times) for a disordered case, respectively. Therefore, the spreading of coil winding reduces the resulting loss despite slightly higher (i.e., by 0.84 %) initial DC resistance. This spreading thus decreases the overall proximity effect.

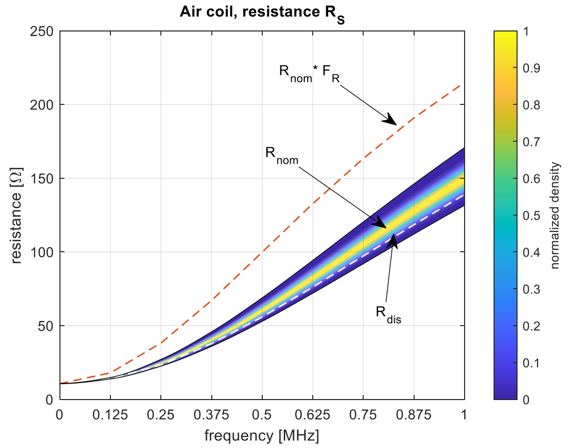

Figure 2.10 2D simulated frequency dependence of air coil resistance R_s, referencing nominal and disordered turns shown in Figure 2.5

The upper and lower resistance values are defined mainly by the wire diameter; therefore, they are nearly symmetrical. However, they change with frequency - smaller R_{ac} is observed as following the reduced coupling between turns. To quantify that effect, the F_R factor provides some estimation, yet accurate only for low frequencies.

Capacitive component

The frequency dependence of winding capacitance was estimated using the relative permittivity data of the PP material [35, 40] shown in Figure 2.11 right. It is the straightforward yet still satisfying method indicating the direction of change qualitatively. Referencing it with an assumed more accurate evaluation employing the AC conduction solver, results in similar ones observed in Figure 2.11 left. The efficient way of making such a comparison is relating the capacitance matrices [103, 108] obtained from both solvers. The difference obtained that way was less than 0.12 % and, therefore, negligible, so the faster method (i.e., electrostatic) was used in the subsequent 2D simulations.

The capacitance values determined in a way similar to inductance (or resistance) are shown in Figure 2.11 left. The upper values are practically defined by the tight (i.e., nominal) turns coupling, while the bottom extends below the disordered case. With a reasonably high number of simulations, the obtained range can be assumed as fully determining the confidence interval [113].

As expected, the spreading of coil turns leads to reducing equivalent capacitance. However, the observed change as -56.5 % is significant, compared to the minor variations of L and R_S. The main reason is the reduced turn-to-turn capacitance, which is inversely proportional to the distance between neighbor turns assuming the elementary parallel plate capacitance model [101].

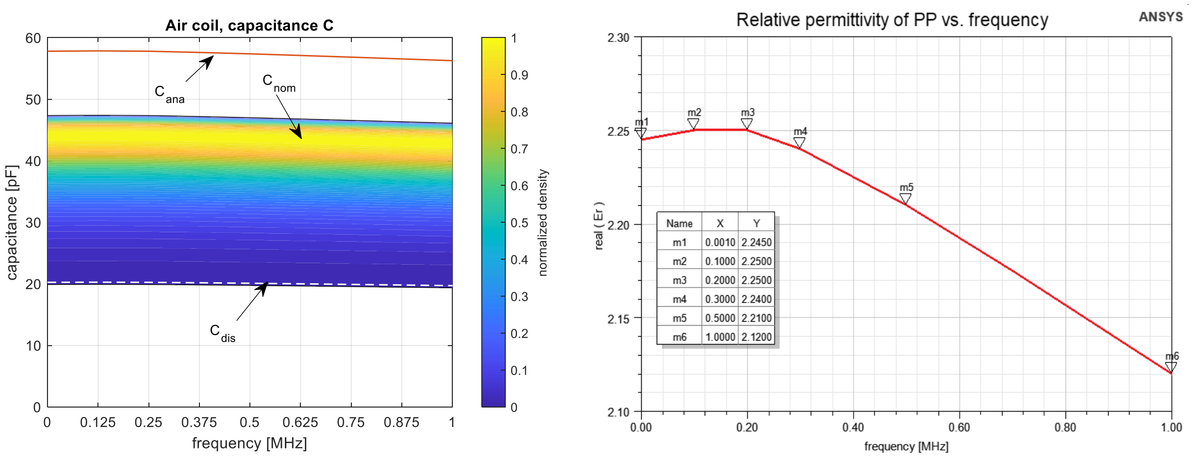

Name	X	Y
m1	0.0010	2.2450
m2	0.1000	2.2500
m3	0.2000	2.2500
m4	0.3000	2.2400
m5	0.5000	2.2100
m6	1.0000	2.1200

Figure 2.11 2D simulated frequency dependence of air coil capacitance C (left) referencing nominal and disordered turns shown in Figure 2.5. On the right, the change of the real part of ε_r assumed for simulations [35, 40]

The considered range of ea and er parameters defined in section 2.1.2 stays in line with Martinez's work [47], simultaneously extending now the capacitance analysis within their range up to 50 μm. It is supposed that equivalent capacitance will be reduced more for displacement higher than the 5 μm limit used in the referenced work. As frequently reported, the capacitance estimations [98, 101, 103, 105] are accurate only considering tight turns coupling; for a higher distance, the mismatch can easily reach 60 % [99, 115].

Further consideration of capacitive component

The influence of individual parameters can be unintentionally masked using simultaneous randomization of all geometry factors. For example, reducing insulation thickness and increasing the wire diameter will not modify turns placement, although it increases the resulting capacitance. Such a case is shown in Figure 2.12 analyzing nominal and disordered windings within allowed range of r and t parameters.

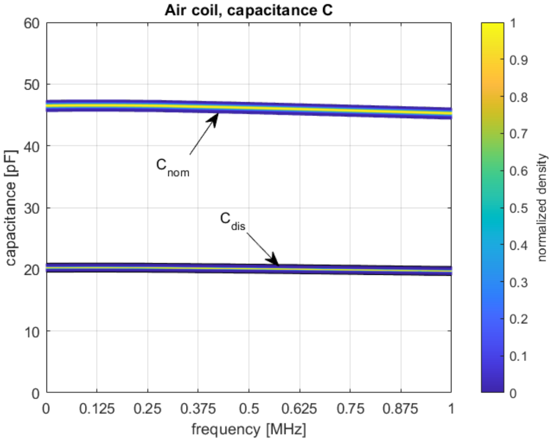

Figure 2.12 Summary of the capacitance variation (left) and selective impact of wire data (right)

The coil capacitance generally follows the changes of the relative permittivity value. However, the relationship is not directly proportional because the presence of a surrounding material (like air or plastic case) further modifies the equivalent permittivity value [56, 106].

Similar relations can be considered for the inductance and resistance parts, but the expected impacts are low. In either case, the proposed model fully supports such evaluations if extended studies are needed.

Impedance data

The coil impedance data, resulting from the individual L, R_s, C contributions described in section 2.2, represents the typical frequency behavior observed for small-sized low-power inductive components. The magnitude and phase characteristics shown in Figure 2.13 clearly indicate the self-resonance frequency and are consistent between measured and simulated values. The laboratory measurements of coil samples used as a reference are described in section 2.3.4 and summarized in Appendix 8.4.

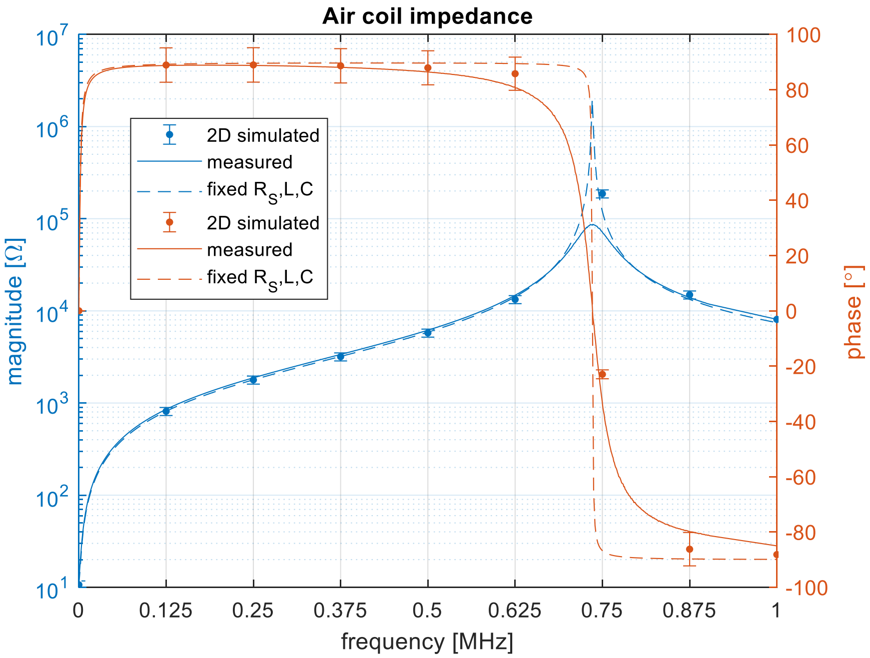

Figure 2.13 Summary of measured and simulated impedance of the air coil, compared to simplified model using frequency independent (i.e., fixed) L, R_S, and C components

Notwithstanding adequate representation of the coil impedance by the frequency-dependent L, R_S, and C components, there is still an option to reduce the model's complexity with a potentially low loss of overall accuracy. For that, assuming coil operation far below ω_{SRF}, the impedance parts can be assumed fixed, resulting in only minor mismatch up to the 3rd harmonic spur (i.e., 375 kHz), as observed in Figure 2.13. Furthermore, the accuracy can be increased by optimizing resistance R_p, yet this approach was not evaluated and can be considered as an extension of this work.

2.3.2 Influence of a ferromagnetic core

Considering a low-power operation of a coil containing a ferromagnetic core may suggest neglecting the core losses. As indicated in section 2.2.1, the equivalent resistance R_{core} is less than 5 % of either R_{dc} or R_{ac} @ 125 kHz values. Comparing core losses with power dissipated in the coil winding suggests neglecting it entirely, as their impact contribution to the overall coil losses is only minor (i.e., 1.23 % @ 125 kHz).

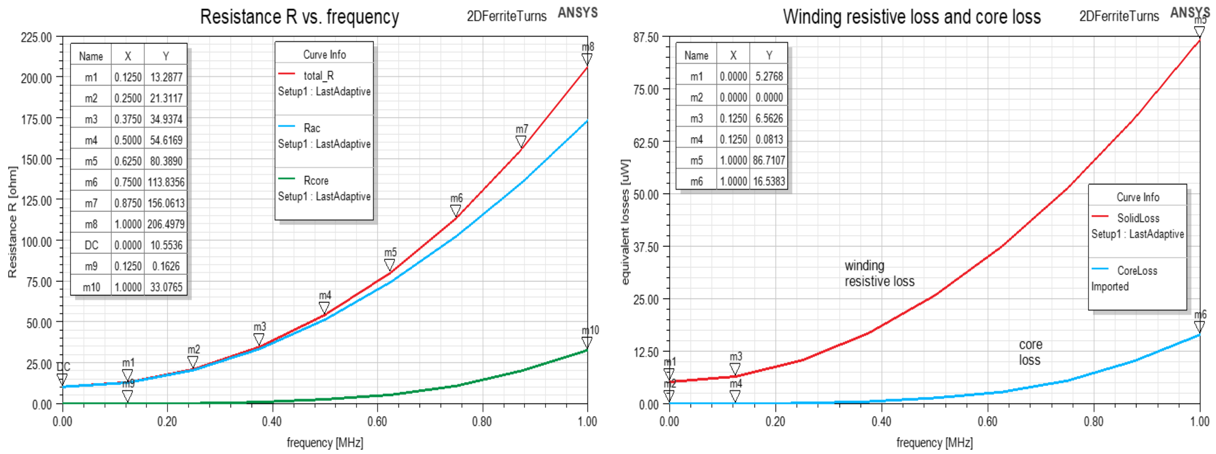

Name	X	Y
m1	0.1250	13.2877
m2	0.2500	21.3117
m3	0.3750	34.9374
m4	0.5000	54.6169
m5	0.6250	80.3890
m6	0.7500	113.8356
m7	0.8750	156.0613
m8	1.0000	206.4979
DC	0.0000	10.5536
m9	0.1250	0.1626
m10	1.0000	33.0765

Name	X	Y
m1	0.0000	5.2768
m2	0.0000	0.0000
m3	0.1250	6.5626
m4	0.1250	0.0813
m5	1.0000	86.7107
m6	1.0000	16.5383

Figure 2.14 Equivalent resistance R_s of the ferrite-core coil (left) and simulated power losses (right)

However, core losses increase with frequency, as it is shown in Figure 2.14. The main reason for that is core material properties (see Figure 2.7 left), showing fast growth of the imaginary part of the complex permeability μ approaching the frequency of 1 MHz. As a consequence, the observed core loss reaches 19 % of winding loss @ 1 MHz, which can no longer be neglected.

Therefore, using core equivalent loss needs to reflect the actual operating condition of a given coil, mainly the range of excitation frequency and its harmonics. If it approaches the coil's self-resonance, including core losses is necessary.

2.3.3 Impact of manufacturing capabilities

In this section, the inductance L and resistance R_{dc} of the air coil are evaluated regarding manufacturing limitations.

Impact of the axial displacement parameter *ea*

A usable feature of having individual ea_i (or er_i) parameters are the possibility of analyzing the impact of individual i-th turn on resulting coil impedance. Although it is expected that a single turn does not contribute much to the final data, the group of them (like the ones located on the initial inner layer) can dominate obtained characteristic. Therefore, to analyze such an effect, the parameter ea_i is related to the considered layer by the equation (25) as:

$$ea_i = \begin{cases} ea_{inner}, i \leq N_V \\ ea_{outer}, i > N_V \end{cases}, \tag{25}$$

where ea_{inner} and ea_{outer} define turns placement accuracy on the initial or other layers, respectively.

Two cases of the ea parameter are considered now, in which $ea_{inner} = ea_{outer}$ (case 1) and $ea_{inner} = 0$ mm (case 2). Such assignment aims to observe a given impact of the initial layer's placement accuracy, assuming other parameters as nominal. The range of ea_{outer} is selected as $[-0.05\,..\,0.05]$ mm and analyzed with 0.01 mm granularity. The resulting variations are presented in Figure 2.15 and Figure 2.16, following the Monte Carlo simulations using 1000 runs at each ea grid limit value.

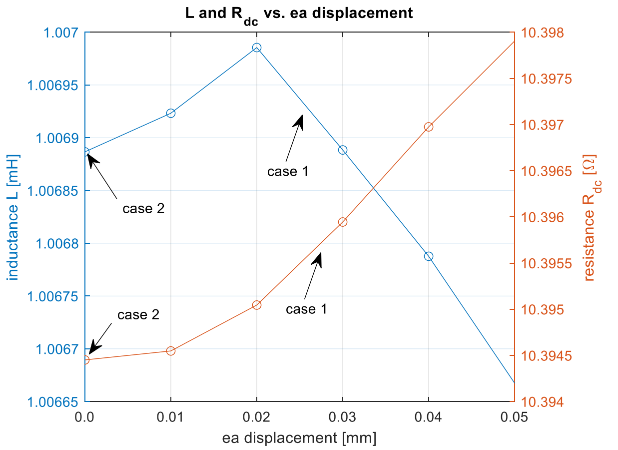

Figure 2.15 Air coil inductance L and resistance R_{dc} dependence on ea parameter

The dot marked points represent respective L either R_{dc} values with the highest occurrence. These can be assumed as expected values for a given ea displacement limit. Although the indicated changes are minor, they show directions of impedance variation resulting from the axial shift. Analyzing the first case, in which ea limit is assumed same for each layer, the inductance L is reduced with increased pitch, reflecting an increase in the coil length. The small peak around 0.02 mm results from the used coil topology, in which same minor turns' freedom was assumed (i.e., $d_w = 0.1803$ mm, p = 0.2 mm, see eqn. (1)). The change of resistance R_{dc} directly follows elongation of wire, which is caused by the axial movement of turns.

The second case's important observation is that assumption of $ea_{inner} = 0$ mm led to the nominal winding structure, despite the possibility of axial movement of turns on the higher layers (i.e., $i > N_V$). This happened because those turns had only a possibility to drop into the grooves created by the lower layers, without any radial freedom (i.e., due to $er_i = 0$ mm). Therefore, as it was stated in subsection 2.1.2, the turns' placement on the inner layer predominates the overall winding structure.

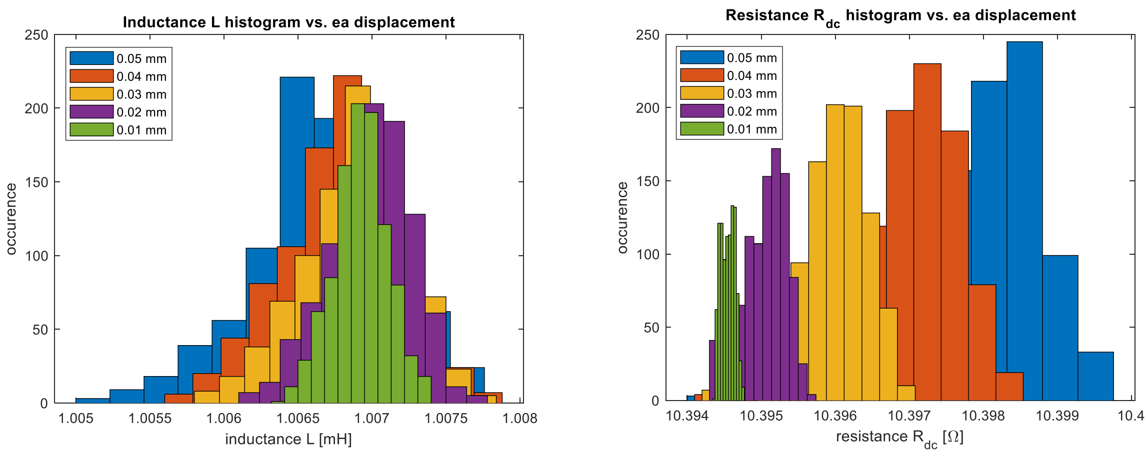

Figure 2.16 Histograms of the air coil inductance L (left) and resistance R_{dc} (right) dependence on ea parameter

Analyzing histograms from Figure 2.16 it is observed, that increasing the axial displacement simultaneously increases the dispersion of both L and R_{dc} components, which is an expected behavior. The asymmetrical distribution in the case of the resistive part results from the limited movement towards a tight winding, with a freedom in the opposite direction.

The proposed methodology can be used for analyzing the influence of the other parameters (like er_i, d_w, t) or even complex relations between coil parameters and, therefore, creates a flexible tool for analyzing multilayer coils in further works.

2.3.4 Coil prototypes

Several prototype coils were built to obtain the most accurate units. Initially, the nominal coils' configurations were determined using formulae presented in section 2.2. Next, the coils were carefully wound to reflect the nominal orthocyclic structure as accurately as possible. Although this manual process was not straightforward, requiring lots of effort and microscope support, it was finally possible to obtain acceptable samples after a few trials. In the last step, the samples representing tight and neat winding were selected for subsequent evaluations.

Coreless air coil

The sample air coil was designed to fit in an existing immobilizer circuit [116], expecting an inductance close to 1 mH. The summary of coil prototype data is shown in Table 3.

Table 3 Summary of air coil design using AWG33 wire

Parameter	D	l_p	p	h_p	N_L	N_V	N_E	N_T
Value	51 mm	2.9 mm	0.2 mm	1.22 mm	6	14	10	94

The number of turns on the outer layer N_E was adjusted to obtain a nominal value close to $L = 1$ mH.

Ferrite-core coil

The ferrite coil contained a magnetic rod core made from MnZn 3C90 material, which is optimized for low-power operation under the LF band. Although the selected small dimensions of rod and used wire diameter did not help to prepare coil prototypes, those characteristics were appropriate to the sample coil presented in Figure 2.2 right.

Table 4 Summary of ferrite-core coil design using AWG40 wire

Parameter	d_{core}	l_{core}	D	l_s	p	h_s	N_L	N_V	N_E	N_T
Value	1.5 mm	10 mm	1.5 mm	8.8 mm	0.09 mm	0.38 mm	5	98	0	490

The pictures of both coil prototypes, together with evaluation summary data, are shown in Appendix 8.4. These units were used for inductance measurements, and the following verification completed in the ALSE chamber (discussed in chapter 6).

Chapter summary

In this chapter, the new geometry model reflecting the process of coil winding was introduced. The proposed approach filled the existing gap of defining positions of the floating turns, which are observed in practice, yet have not been considered in existing works. Such disordered structures were found by making section cuts of the mass-produced automotive coreless and ferromagnetic-core coils. Supplementary to the recent models from literature, the flexibility in defining individual displacements of given turns was introduced. It allowed the more accurate prediction of the coil deformation propagated from the initial layer.

The introduced geometry model was used for the extended hybrid evaluations employing the 2D Maxwell simulator and Matlab tools. The accurate determination of coil impedance was possible using it for both nominal and disordered turns placement. Such detailed structural simulations, rarely found in existing papers, allowed prediction of coil impedance, simultaneously reflecting manufacturing and material capabilities. Supplementary to that, the existing closed-form formulae weaknesses were indicated, satisfying only the nominal, challenging to achieve in reality idealized conditions. It was shown that widely used Dowell's equation provides only a coarse estimation of the proximity effect. In practice, the existing form cannot be used for disordered turns in multilayered coils at higher frequencies due to limited accuracy. The presented solution employing 2D simulation showed a satisfactory correlation with the measured impedance of the coil samples on the contrary.

END OF CHAPTER 2

3 Magnetic coupling

This chapter presents practical methods for determining the magnetic coupling between coils, expressed by the mutual inductance and the coupling factor. On the example of coils freely arranged in space, appropriate methodologies are presented, while reducing existing limitations in this respect. In particular, the accuracy of the analytical solution is verified by spatial measurement of the configuration consisting of the air and ferromagnetic core coils, which is not yet available in a range covering angular and radial displacements. To support that, the dedicated measurement setup is designed, allowing the spectrum analyzer to measure the mutual inductance. The two-dimensional coupling map is captured on its base, together with constructed non-magnetic stand for coils positioning. It enables further evaluation of the nonlinearity introduced by the magnetically linked circuits.

The coupling behavior is evaluated from the proximity standpoint, in which the possible simplification of the multilayer coil winding model to the equivalent solid turn is presented. To confirm that, the magnetic flux density maps are obtained for both approaches, on which base the approximation error is derived. The forms of achieved equivalent coils enable a significant reduction of the simulation time of 3D models while still supporting the required level of accuracy.

3.1 Magnetically coupled coils

Let us consider two loop coils with sinusoidal low-frequency currents I_p and I_s, presented in Figure 3.1. The primary coil of radius r_p is located in the origin $O(0,0,0)$ of XOY coordinate system, laying in the XOY plane, symmetrically along z-axis. The plane $X'CY'$ of the secondary coil, having its center located in $C(x_c, y_c, z_c)$ and radius r_s, is inclined with respect to the plane of the primary coil. In a general case, such an elementary form of coupled filamentary circuits should reflect any desired position and is used as a base for the following evaluations.

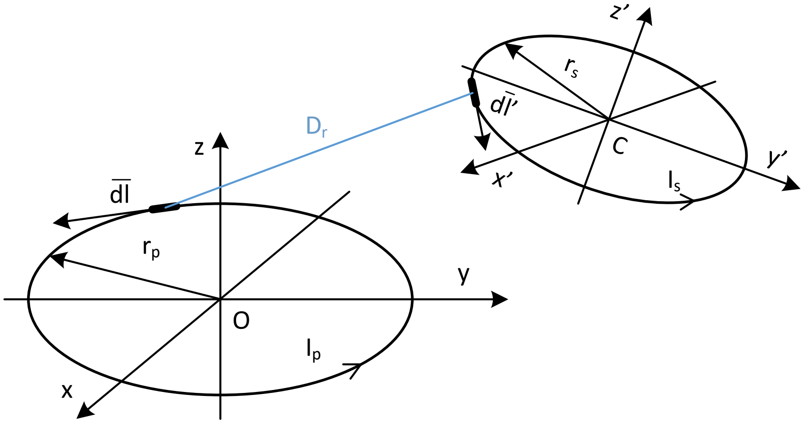

Figure 3.1 Loop coils in a general orientation case

Although it is a classical problem and partially investigated by Maxwell [95] and Neumann [117], the complete analyses of such general cases are limited in the literature. The work of Butterworth [118] provided a solution of parallel coils' axes, where the distance D_r between the coils is less than any of radii. Snow [50] solved the problem for a larger distance, but the obtained form of the solution was reported as difficult for computation [119]. A general orientation was analyzed by Groover [119], although the tabulated form of the solution is complicated in use. The concept of separation to lateral and angular cases was proposed by Soma [120] and used through the years with moderate accuracy [54, 55, 121, 122]. The alternative to Groover's method was proposed by Babic *et all* [123]. However, it provides an unsolved singularity problem when secondary coil touches the origin O. Recent works on mutual inductance involve the use of inverse Mellin transform for non-coaxial Bitter coils [124] and propose to combine field and circuit equations for an accurate coupling analysis [125]. Supplementary, for a fast approximation of the mutual coupling, the work [126] suggests behavioral modeling, satisfying an overall accuracy no worse than 15 %, although only for the restricted sets of misaligned coils.

The additional complexity to the above-coupled set of air coils is introduced by a ferromagnetic core in one of the coils. The problem of such an analysis resulted from the rod core's anisotropy and was investigated for cylinders by Bozorth [127] and Chen [13]. On that base, the effect of mutual coupling between air and core coils was evaluated by Theilmann [14], although only in the simplest, coaxial orientation. Similarly, the work [15] analyzed the coupling factor with small core coil by effective permeability method in the same, coaxial position.

Ultimately, there is no definite proof of the accuracy of mutual inductance and coupling factor formulae, simultaneously embedding ferromagnetic rod core in one of the coils. This knowledge is essential for predicting the induced voltage in a coupled circuit in any position. Therefore, it can serve as a method to estimate the level of disturbances introduced by connected nonlinear circuits through such a magnetic link.

3.1.1 Analytical methods for air coils

Following [96], the mutual inductance in free space, expressed in terms of current sources is:

$$M = \frac{\mu_0}{4\pi I_p I_s} \int\limits_{V_1} \int\limits_{V_1} \frac{\boldsymbol{J}' \cdot \boldsymbol{J}}{D_r} dv' dv \,, \tag{26}$$

where V_1, V_2 are conductor volumes of primary and secondary circuits, respectively, and primes are used to distinguish the secondary source point current element $\boldsymbol{J}'dv'$ from the unprimed field point element of the primary. This equation assumes knowledge of the current distribution in wires and, therefore, may accurately describe the value of the mutual inductance and its change due to material, frequency, skin, and proximity effects. However, for practical considerations of multiturn, multilayer coils this method is inefficient due to complicated form, involving the use of volume integrals. To simplify it, if the distance between the coupled circuits is significantly larger than the wires' radii, the current distribution in the wires may be assumed as uniform, when considered in a low-frequency band [53]. For that purpose, the mutual inductance is calculated efficiently based on the coils' shapes instead of volumetric current densities.

Flux linkage method

Given the known distribution of a magnetic flux density, the mutual inductance can be evaluated by the flux linkage method. The procedure relies on integrating magnetic flux on the coupled coil area and then taking into account the current, which excited it. This methodology allows calculation of both coupled and leakage fluxes and, therefore, may provide more knowledge about coupling between circuits.

In practice, the flux linkage method is used with known currents distributions or assuming their uniformity. The selection of appropriate approaches depends on frequency, coil shape, and circuit linearity. With the condition, when the wire cross-section is assumed as infinitesimal, and any nonlinearities of coupled magnetics are neglected, the Neumann's formula can be used instead.

Neumann formula

Reflecting notations from Figure 3.1, the mutual inductance between circuits of filamentary currents I_p and I_s can be calculated by Neumann's formula:

$$M = \frac{\mu_0}{4\pi} \int_{l_1} \int_{l_2} \frac{d\boldsymbol{l}' \cdot d\boldsymbol{l}}{D_r}, \tag{27}$$

where l_1 and l_2 are integration contours of primary and secondary circuits, and D_r is the distance between infinitesimal lengths dl' and dl of both contours. Despite its pure form, this double integral is not trivial to calculate analytically, even for generic structures [122, 128]. Following that, the already mentioned work of Babic [53] addressed this problem, providing a unified solution for each coils' orientation from Figure 3.1. The obtained equation (28), corroborated with other works [119, 128, 129], is used here for the calculation of the mutual inductance between filamentary loops.

$$M = \frac{\mu_0 r_s}{\pi} \int_0^{2\pi} \frac{(p_1 cos\phi + p_2 sin\phi + p_3)\Psi(k)}{k\sqrt{V_0^3}} d\phi\,, \tag{28}$$

where the meaning of each parameter is explained in reference [123] and summarized in Appendix 8.5. The mentioned computation singularity can be workaround by a minimal shift of the position of the coils and redo the calculation, although, this problem never occurred in analyzed configurations.

3.1.2 Effect of a ferromagnetic core

With the ferromagnetic core embedded inside a secondary coil, the resulting mutual inductance M_{core} is:

$$M_{core} = M \cdot FF\,, \tag{29}$$

where, FF is the ferrite factor, effectively increasing observed coupling. Following Theilmann [14], the effect of a ferromagnetic rod of radius $r_{core} = d_{core}/2$, length l_{core}, and relative permeability μ_r is summarized as:

$$FF \equiv \left(1 - \frac{r_{core}^2}{r_s^2}\right) + \sqrt[3]{\frac{l_{core}}{l_s}} \cdot \frac{\mu_r}{1 + D_{fc}(\mu_r - 1)} \cdot \left(\frac{r_{core}}{r_s}\right)^2, \tag{30}$$

where l_s is the length of the secondary winding. The demagnetization factor D_{fc} calculates as:

$$D_{fc} = D_{fe} \cdot 0.755 \cdot \left(\frac{l_{core}}{d_{core}}\right)^{0.13}, \tag{31}$$

where D_{fe} for rod cylinders of $l_{core}/d_{core} > 1$ calculates as:

$$D_{fe} = \frac{2r_{core}^2}{l_{core}^2} \cdot \frac{1}{e^3}\left[ln\left(\frac{1+e}{1-e}\right) - 2e\right]. \tag{32}$$

The e parameter defines as:

$$e = \sqrt{1 - \left(\frac{d_{core}}{l_{core}}\right)^2}. \tag{33}$$

It is important to note, that the original formula (10.c) from [14] has typo error, corrected above by (32).

The presented solution is only an approximation of the actual core effect. Because of the magnetic flux leakage from rod ends, the flux density in a cylindrical core volume is not constant, as assumed during derivation of the above formulae in [14]. Due to the rod's non-negligible dimensions, the flux density is also not constant along the coil's length, especially at angular displacement, which can lead to an additional discrepancy of the solution. In particular, the evaluation of the accuracy of equation (30) together with a method allowing estimation of the mutual coupling in any desired position is the subject considered here.

3.1.3 Frequency impact on mutual inductance

As presented in chapter 2 employing equation (8), the permeability of a ferromagnetic material is the complex number, depending among others on the frequency. Following that, the FF factor expressed by (30) also has complex and dispersive behavior, which can be linked with a mutual inductance (real part) and the core loss (imaginary part). By observing Figure 2.7 left, the variation of μ_r' within considered LF band is minor, resulting in $Re\{FF\}$ = 18.24 .. 18.26, so the mutual inductance can be assumed as fixed. To prove it, the completed measurements addressed and confirmed such assumption. Similarly, μ_r'' changes only slightly and its influence on overall coupling budget between coils due to the core loss is low. For the consistency of the proposed approach, section 5.3 summarizes all these factors in a standard lumped model of the magnetic link.

In the following subsections, the accuracy of the magnetic coupling, neglecting the frequency impact, is considered. Despite the skin and proximity effects, resulting in the change of the current density of a wire, the magnetic coupling remains nearly constant in LF, and therefore it is assumed as dependent only on coils' dimensions and positions.

3.1.4 Approximation of the winding structure

Most realistic coils have more than one turn, which in the case of components discussed in chapter 2 results with tens or even hundreds of turns. Under such conditions, external dimensions of coils are not negligible, and to keep the use of the filamentary approach, the discretization of the winding is needed. However, such a process cannot be directly applied to the discontinuous cross-section of the coil winding, because turns do not fill it.

In this and following subsections, it is shown how to simplify multiturn winding to the single-turn form of approximately the same external magnetic field [130], and then correctly apply a filamentary method for calculating the mutual inductance and following coupling factor. According to the Author's knowledge, there is a gap in the available literature describing achievable accuracy, simplifying the winding turns.

The winding equivalent of the air coil

The equivalence of the single turn with a rectangular section shape is analyzed in regards to the multilayer air coil structure of the same external dimensions, as presented in Figure 3.2.

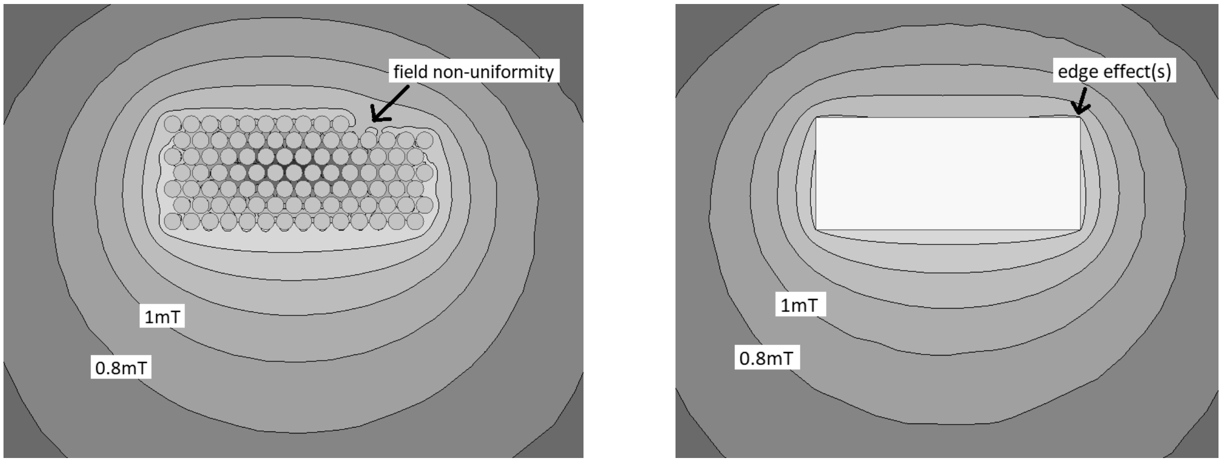

Figure 3.2 Air coil, B field of nominal (left) and simplified (right) winding, near turn(s) view

It is visible that the edge effect of the proposed equivalent form distorts the field distribution in the area near the winding. However, with increased distance from the turns, the field level becomes more accurate. The longer distance is being considered, and it can be said, that the magnetic field outside an air coil is more similar to one created by the simplified, solid turn of rectangular shape, as presented in Figure 3.3. With that observation, the magnetic field can be assumed equivalent in both cases, with the accuracy presented in Figure 3.4. For the considered case, this error is never higher than 1 % in either direction, except the area near turns, where it could reach tens or even more percent. However, this area could be excluded from practical cases, because realistic coils are typically embedded in a housing and/or assembled on a dedicated printed circuit board (PCB) [116], which additionally extends the distance between them. The overall accuracy can be further improved if the simplified turn would have rounded corners, which is visible in left Figure 3.2. Similarly, filling the external layer by missing turns might introduce additional uniformity of the field, although in this case, topology adaptation (i.e., N_V, N_L, N_E) is needed to obtain required inductance value.

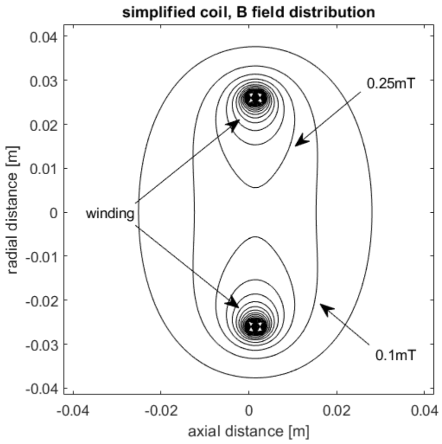

Figure 3.3 Air coil, distribution of magnetic flux density, ± 40 mm either direction from the coil center

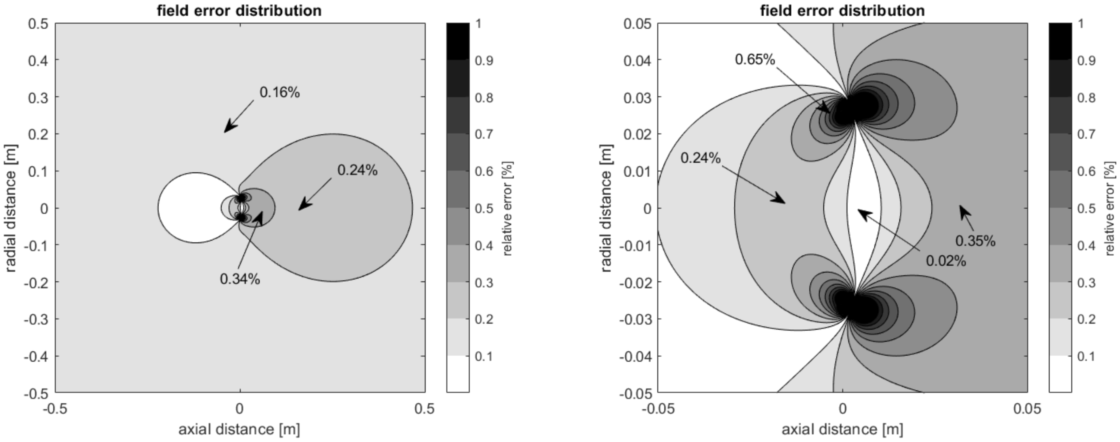

Figure 3.4 Air coil, distribution of relative error, ± 500 mm and ± 50 mm

Because each part of the winding section contributes to the overall external magnetic field, the mutual inductance calculation should reflect the total current flowing through all the turns. In this case, by replacing the winding made of multiple turns with the single rectangular turn with equivalent ampere-turn current, the magnetic coupling calculation is still possible with accuracy better than 2 .. 5 %.

The winding equivalent of the ferrite coil

The simplification of the winding of the secondary coil, embedding a ferromagnetic core, is managed similarly. Due to the higher number of turns compared to the air coil, the distribution of the magnetic field is more uniform and less sensitive to local perturbations, introduced by missing turns or edge effect. The presence of the core additionally smooths the magnetic field inside the winding, which results in increased accuracy of the proposed equivalent.

Figure 3.5 shows the distribution of the magnetic flux density and the relative error introduced by the equivalent winding of the secondary coil embedding ferromagnetic core. It could be concluded that for any distance referenced from the coil center and larger than its length, the introduced error is always lower than 0.5 % in any direction.

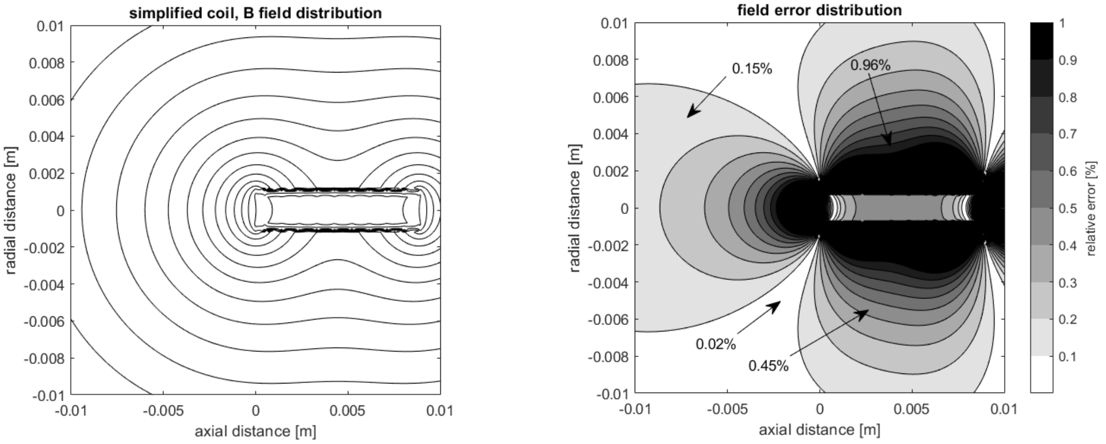

Figure 3.5 Ferrite coil, distributions of the magnetic field density (left) and relative error (right), utilizing the equivalent winding, ± 10 mm range

3.1.5 3D simulation model

As a result of the above evaluations, the 3D model used in Ansys Maxwell 3D environment was prepared. It contains the primary air coil and a ferromagnetic core-based secondary coil - presented in Figure 3.6, both approximated as having a single turn of solid cross-section.

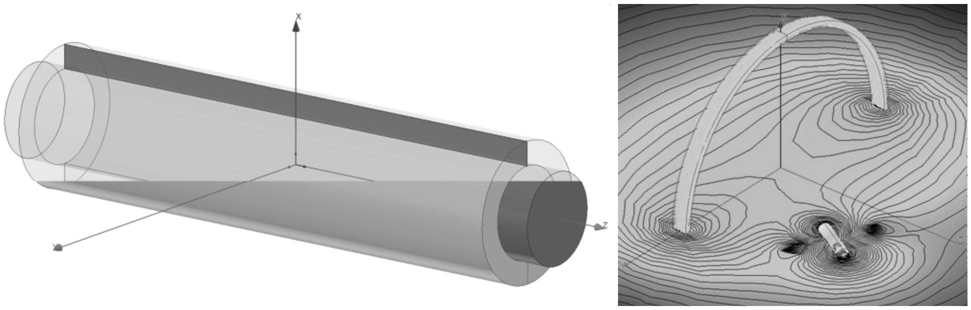

Figure 3.6 3D model of the secondary coil (left) and Maxwell 3D model (right)

This simplified model aims to have the capability to quickly assess the magnetic coupling between the coils for any required position in space, especially with the presence of surrounding objects like a metal housing or key insert near the coil winding. The effect of the reduced turns' model is immediately observed as a significant reduction of the computational time. With the proposed structure, the coupling calculation in any spatial position takes less than 5 .. 8 minutes, typically on a standard PC platform, embedding i5 4-core CPU with 16 GB RAM. The attempts to simulate the complete multiturn windings consumed more than 22 .. 28h, with frequent issues related to the convergence of calculations. To overcome this limitation as assumed resulting from the system's resources, the supercomputer Prometheus trial within the PLgrid infrastructure [114] was made. Using a computational slot consisting of 24 cores and dedicated 1 TB memory, the results were obtained after 7 hours and 20 minutes. This observation directly points that simulations based on complete windings are not applicable for fast and efficient evaluations. The quick yet accurate estimations can still be collected using standard tools and the proposed single-turn model.

3.1.6 Filamentary analysis

To apply the filamentary method to a solid conductor turn, the coil's cross-section is virtually divided into several smaller rectangular subsections, assuming the same current flowing through each filament. Such a discretization process is presented in Figure 3.7. In practice, the number of discretization cells is limited by the required accuracy, which increase is not observed for a significantly extended resolution. For typical cases, it is enough to use up to 9-25 subdivisions [53, 129].

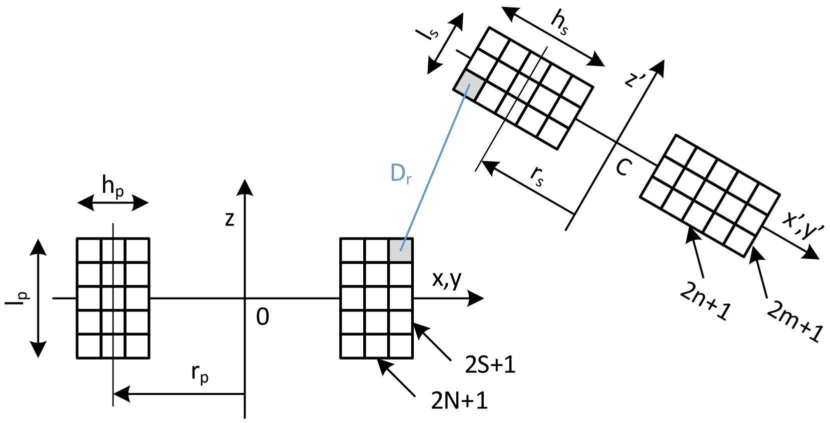

Figure 3.7 Discretization of coil sections – remastered from [53]

To calculate the mutual inductance on the base of the method presented in [53], rectangular sections of primary and secondary coils are discretized into $(2N+1)\times(2S+1)$ and $(2n+1)\times(2m+1)$ subsections. Subsequently, the mutual inductance between each subsection of primary and secondary coils is calculated using (28), observing radial and axial change of coordinates. Within the last step, individual contributions are summed up, scaled by the number of discretization cells, and multiplied by the number of turns N_p, N_s. The below formula explains this process:

$$M = N_p N_s \sum_{g=-S}^{S} \sum_{h=-N}^{N} \sum_{p=-m}^{m} \sum_{q=-n}^{n} \frac{M(g,h,p,q)}{(2S+1)(2N+1)(2m+1)(2n+1)}. \tag{34}$$

The exact form of parameters used by the nominator of (34) is presented in [53] and detailed in Appendix 8.5.

3.1.7 Accuracy evaluation

To evaluate the accuracy of (34), the comparison with 3D simulation and spatial measurement was completed using representative coils identified in chapter 2. The selection criteria were as follows: the correlation with serially produced types, availability of manufacturing limits (i.e., tolerance, drifts), and the reference to the completed evaluations, which proceeded with this work [5]. However, due to the model's flexibility, the proposed approach can also be applied to other configurations, as presented in a work summary.

The evaluation setup

The primary coil, reflecting notation from Figure 3.1, was arranged with $N_p = 94$, $h_p = 1.2$ mm, $l_p = 2.8$ mm, and $r_p = 26.1$ mm. The secondary coil used $N_s = 490$, $h_s = 0.4$ mm, $l_s = 8.8$ mm, and

r_s = 0.95 mm. The core effect was evaluated by use of the ferromagnetic rod from Ferroxcube, type ROD 1.5/10-3C90, of radius r_{core} = 0.75 mm, length l_{core} = 10 mm, and μ_r = 2300 ± 20 %, which was embedded in a secondary coil. For this core data, the ferrite factor calculated according to (30) is FF = 18.24 ± 0.05.

The number of subdivisions used in (34) was set as 9, thus $N = S = m = n = 4$. Three movement cases of the secondary coil were evaluated: the axial displacement within 0 .. 100 mm range, the lateral displacement 0 .. 100 mm, and the angular rotation in 0 .. 60° range with the radius r_p, as clarified in Figure 3.8. Simulations were carried out with condition f = 1 Hz to compare them with results obtained by using (34) and supplemented at f = 125 kHz as a reference for measurements. Both air and core configurations were investigated, using the interface detailed in the next paragraph. The displacement between the coils was determined by the dedicated non-magnetic stand – Figure 3.8, enabling a linear resolution ± 1 mm and an incremental rotation by 5°. The placement repeatability, resulting from the accuracy of a laser-cut process for stand preparation, is approximated as ± 0.15 mm.

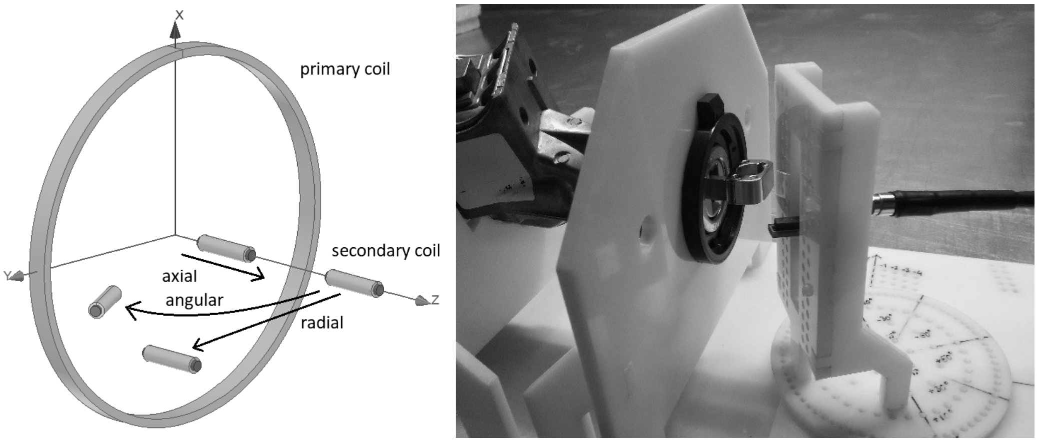

Figure 3.8 Movement definition (left) and setup used for coils positioning (right)

The interface used for measurement of mutual coupling in LF band

For the measurement of the mutual inductance, the method originating from [93] is used, with adaptation allowing the use of the spectrum analyzer as a level indicator, utilizing the interface presented in Figure 3.9.

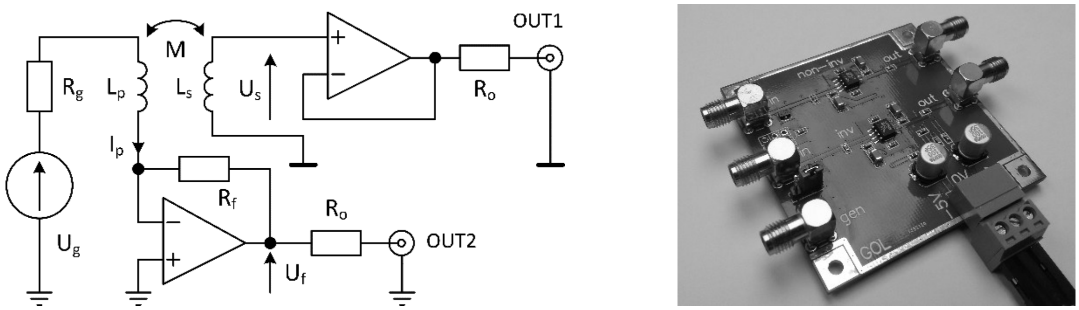

Figure 3.9 Interface used for the measurement of a mutual inductance

The primary coil is connected to the signal source, providing sinusoidal excitation U_g of a frequency f. If the analyzer has a tracking generator capability, it can be used here for this purpose. On the opposite side of the coil, the impedance converter is connected, realized with the operational amplifier with the feedback resistor R_f, delivering signal U_f proportional to the coil current I_p. The secondary coil induces voltage U_s, which is equivalent to the coupled magnetic flux and thus directly related to the current in a primary coil. This signal is buffered to allow proper driving of a low impedance input of the analyzer, typically 50 Ω.

Neglecting load added by a buffer input to the secondary coil, the magnitude of U_s can be derived as:

$$|U_s| = |j\omega M \cdot I_p| = \omega|M| \cdot |I_p| = \omega|M| \cdot \left|\frac{-U_f}{R_f}\right|. \quad (35)$$

Therefore, the magnitude of the mutual inductance is calculated as:

$$|M| = \frac{R_f|U_s|}{2\pi f|U_f|}. \quad (36)$$

Because there is no need to observe phase relation between U_f and U_s, the analyzer input can be toggled between two outputs OUT1 and OUT2, allowing reliable measurement with a one port analyzer. However, phase information is useful for detecting the sign change of a mutual inductance, which exists for angular displacement and was confirmed during a measurement. This phenomenon, indicated as a phase reversal, may simplify the overall analysis, so the multiport analyzer's use is preferred. In this case, the short introduced between grounds – Figure 3.9, does not violate accuracy within the considered LF band, as verified during the evaluation.

There are alternative methods [131-133], which can be used for the measure of a mutual coupling. However, the proposed method reflects the current flowing through the primary circuit and therefore includes the impact of a coil resistance at a given operating frequency, which is mostly neglected in other methods. Additionally, due to the selective measurement with a high dynamic range provided by a spectrum analyzer, the range of measurable couplings extends significantly, compared to typical voltmeter-based methods.

The estimated uncertainty of M is estimated conservatively as ± 100 nH for coupling lower than 5 μH, and ± 1 μH for higher coupling values.

Evaluation results

The goal of completed assessments is to determine the accuracy of equation (29) in most practical orientations of the coils (i.e., having axial, radial, and angular displacements) of used setup, followed by the effect of the ferromagnetic core, according to (29). To achieve this, two independent measurement configurations are realized – on the base of coils without cores and utilizing a core embedded in a secondary coil.

The figures below summarize analytically collected, simulated, and measured data of the real coil samples.

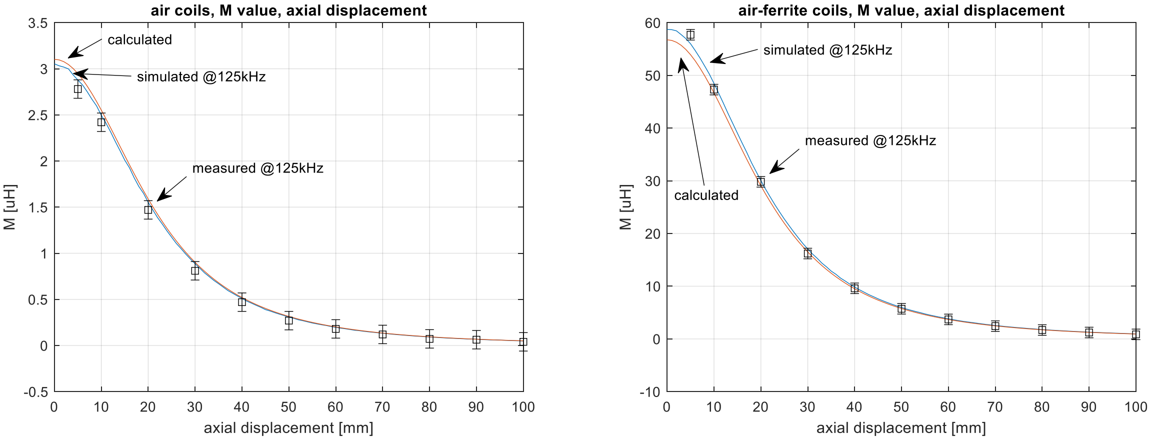

Figure 3.10 Comparison of calculated, simulated and measured data for axial displacement of the secondary coil without (left) and with the ferromagnetic core (right)

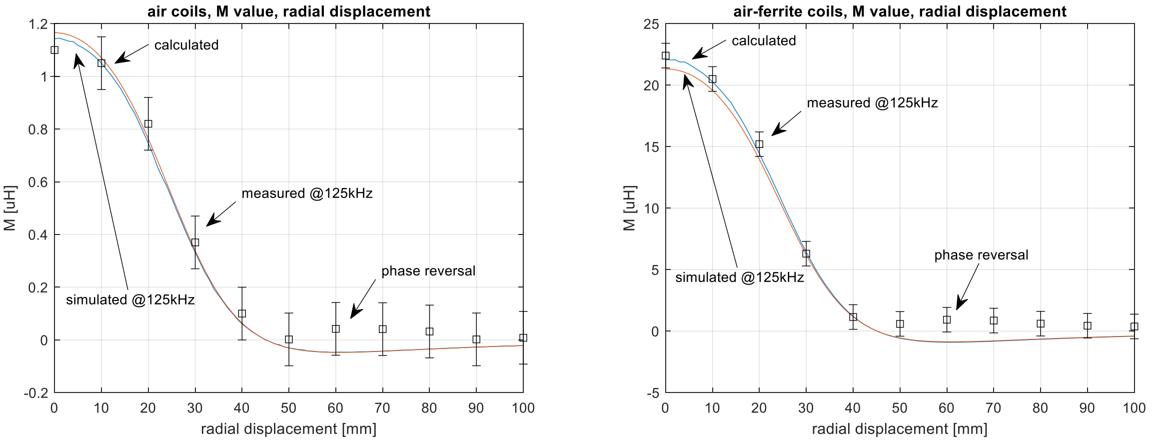

Figure 3.11 Comparison of calculated, simulated and measured data for a radial displacement of the secondary coil without (left) and with the ferromagnetic core (right)

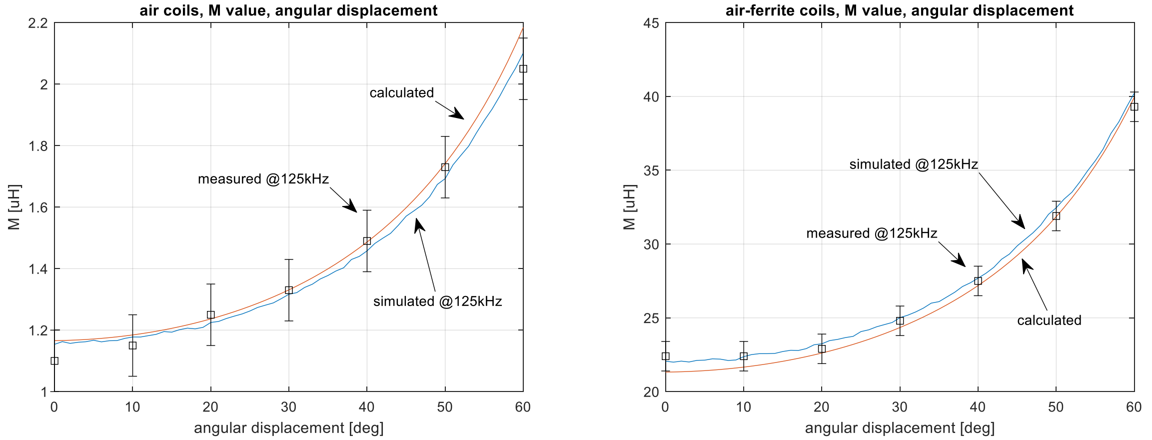

Figure 3.12 Comparison of calculated, simulated and measured data for angular displacement of the secondary coil without (left) and with the ferromagnetic core (right)

The first important observation is that operation at low frequency does not impact the behavior of mutual inductance in a considered LF band, which confirms initial assumptions. Additionally, simulations made for complete winding and simplified by a single turn, provide nearly identical results, which allows the use of such a simple model for an accurate coupling definition. Subsequently, comparing coupling values obtained analytically, and by simulation for air coils, the difference is less than 1.6 %, 2.1 %, and 3.9 % for each considered orientation, respectively, which leads to the acceptable accuracy of equation (34) for this case.

The introduction of a ferromagnetic core increases mutual inductance more than predicted using (29). The difference is nearly 3.7 % for coaxial orientation, which points to the influence of the core length, which was suggested before. Even higher discrepancies were reported by [94], which shows the limited precision of (29), utilizing a demagnetization factor concept. Comparing it to the simulated and measured values as 19.1 and 20.3, respectively, it concludes, that the analytical method correctly describes coupling behavior, but with a gain error. This observation immediately suggests using a hybrid approach, in which the analytical method references the simulation or a single point measurement. In this case, the mutual coupling calculates with increased accuracy by using the following formula:

$$M_{core} = M \cdot FF \cdot C_{cal} \, , \tag{37}$$

in which calibration factor C_{cal}, together with FF defines the actual effect of a ferromagnetic core.

If the simulated value as FF = 19.1 (thus C_{cal} = 1.047) will be used for coupling definition, the overall accuracy will be no worse than 2 .. 4 % for any considered coil orientations, including air and ferromagnetic core coils. Such an approximation level satisfies most practical cases and guarantees a fast evaluation of various coil sets. The present findings seem to be consistent with other research, simultaneously providing a higher level of accuracy, not possible to reach by direct application of the analytical formulae.

3.2 Coupling factor

For a comparative study between coils in different positions, it is convenient to link the mutual and self-inductance by unitless magnetic coupling factor k, calculated as:

$$k = \frac{M}{\sqrt{L_p L_s}} \, . \tag{38}$$

By analyzing the above definition formula, the value of a coupling factor depends indirectly on the coils' spatial orientation (because of M changes with their locations) and properties of the surrounding medium (which influences the strength of a magnetic flux approaching coupled coil). The typical approach [125] is that air variation can be neglected in cases, in which the magnetic link is considered in open space. Therefore, a coupling factor is independent of the frequency in the considered band [134], and only the orientation of the coils defines its value.

2D distribution map

The coupling factor's spatial distribution can provide relevant knowledge about the magnetic link properties and the possible regions of anomalies, indicated as a distortion of the magnetic field uniformity [5, 135]. To give an illustration of such analysis, data collected similarly to plots of Figure 3.10 .. Figure 3.12 are used here for the determination of the plane distribution of a coupling factor. Two cases – parallel orientation of coil axes and angular rotation of the secondary coil by 45° on *XOZ* plane are analyzed, within range, *XYZ* = [-100:100, 0, 0:100] mm, for results in Figure 3.13.

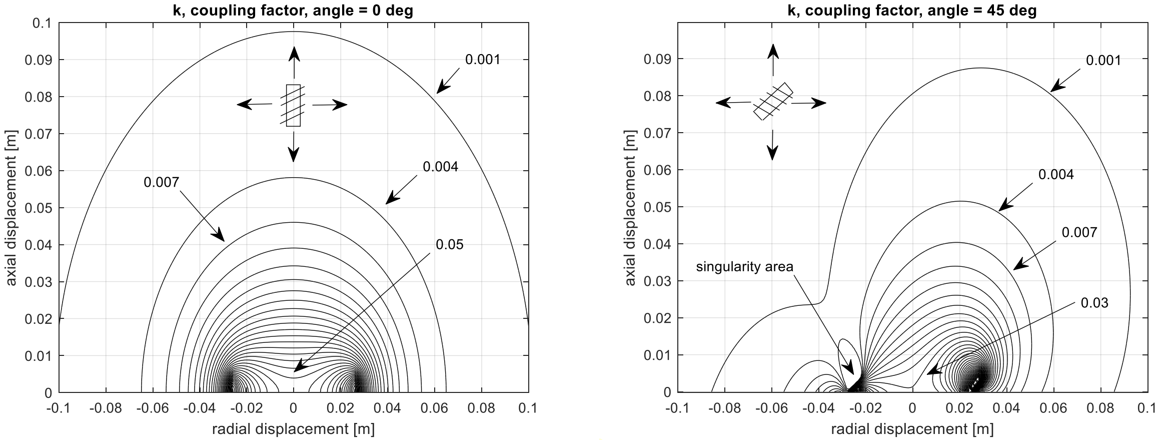

Figure 3.13 Distribution of a coupling factor, parallel axes of coils (left) and a secondary rotated by 45° (right)

Comparing the obtained distribution maps of the coupling factor, the occurrence of areas in which values vary significantly is noticed. This drop is seen in the right figure, in which the rotation of the secondary coil results in nulling of the coupling, despite the proximity to the primary coil winding. This phenomenon is present because part of the magnetic flux on the left, outer side of the primary coil has a different direction than the flux inside the coil. The integral nature of the long winding of the secondary coil, enhanced by a ferromagnetic core, means that the resultant value of the magnetic flux within this coil can be null.

On the contrary, in the left figure presenting the axial coupling, there is practically no area where coupling between coils can fade completely. This fading is only possible for more considerable distances where the field decays to minimal values, which is the typical and expected behavior of the coil.

The presented distribution maps of the coupling factor will be used to analyze nonlinear phenomena in the following chapters.

Chapter summary

In this chapter, the behavior of the mutual inductance between magnetically coupled inductive coils was considered. Firstly, the analytical methods used for calculating the mutual inductance were presented, indicating the possibility of using the filamentary method to analyze the complex, multilayered coil structures in a low-frequency band. To support such evaluations, the analysis of the equivalent single turn concept was presented. On its basis, it was confirmed, that the simplified coil can provide approximately identical distribution of the magnetic field, allowing faster, but still accurate simulations.

Secondly, the effect of the presence of the ferromagnetic core inside a coil was reviewed. It was highlighted that mutual inductance would change due to the core material and core dimensions, although existing rod anisotropy may influence the overall accuracy of the analytical solution. In particular, the comparison of the solutions based on the simulation, calculation, and measurement were analyzed as follows.

Thirdly, to allow an accurate indication of the mutual coupling, a practical measurement interface using low distortion operational amplifiers was designed and tested. With a spectrum analyzer, this practical tool enables a measurement of the mutual inductance in a wide range extending 80dB, which is very difficult to achieve with a conventional, voltmeter based method. To accurately correlate coil positions with the indicated coupling, the dedicated non-magnetic stand was built. On its basis, the repeatable misalignments were defined, allowing linear and angular displacement of the analyzed set of coils.

Finally, the last part of this chapter focused on the derivation of the two-dimensional map of the coupling factor, allowing further consideration of the nonlinearity introduced by the magnetically linked circuits, which follows in the next chapter.

END OF CHAPTER 3

4 Magnetic link nonlinearities

The methodologies presented in the previous chapter allow accurate determination of the voltage induced in the magnetically coupled secondary coil. Applying such voltage to the load circuit (typically connected directly to the coil terminals) causes the load current flow. Depending on the load type, which is assumed to be nonlinear in a general case, this current may have distorted form, despite being excited by a clean, harmonic voltage source.

This chapter identifies and summarizes the origins of such behavior. Nonlinearities' contributions are recognized resulting from the source driving the primary coil, a ferrite core of the secondary coil, and the dominant one – the AFE circuit. The full-wave AFE's rectifier (i.e., functional block typically present within the input structure of integrated circuits supplied inductively from a magnetic field) is evaluated using a compensation method based on a spectrum analyzer, dual channels signal generator, and a dedicated 4-stage bandpass filter with a transformer circuit. This approach overcomes constraints related to the classical lab instruments that provide only a low level of the excitation signal. Compared to the usual techniques, the one presented in this chapter introduces significant simplification of the filter design without compromising the overall performance.

The equivalent nonlinear capacitance and resistance of the load circuit were obtained using the proposed methodology at the fundamental frequency (or in a short, a carrier). Then, they were referenced to the RLC bridge measurement, proving solution correctness. Next, the individual spurs up to 11th order were identified, both phase and amplitude, and compared with the lock-in amplifier (LIA) results as a reference. The I/U characteristics for different excitation levels were collected in the last step, clearly determining the current threshold, above which the significant distortions arise.

4.1 Contributors of nonlinearities

The general view on the magnetic link - Figure 4.1, focusing on sources of distorted currents I_p and I_s, identifies them as a circuit driving the primary coil called a transmitter (TX), a ferrite core of the receiving coil L_s, and the load's AFE circuit. The fourth part - the primary loop L_p, can be excluded from the analysis when driven by the low current in consideration due to its coreless design.

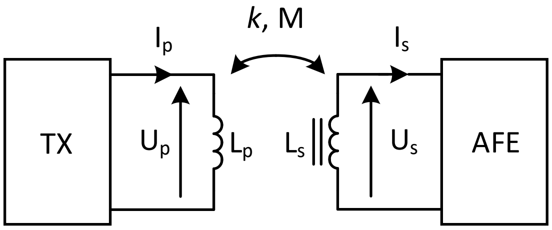

Figure 4.1 The general view on the magnetic link

4.1.1 The transmitter

The transmitter in the cases analyzed in this work operates as a voltage source U_{src} with the internal impedance Z_{src}. In general cases, these two parts do not need to be considered as purely linear components. They can implement even complicated variations due to the actual voltage, current, or frequency of operation. An example shown in Figure 4.2 can present them as amplitude modulated (AM) sources with the following lowpass filter (LPF) and the impedance matching (IM) section, typically existing in such topologies.

However, the consideration only of the specific driver's structure, capability, or selected modulation type can significantly focus the analysis on the particular case(s), which is not preferred. A more helpful approach would reflect pure harmonic voltage excitation, on which base magnetic link nonlinearities can be clearly recognized among those supplied by the signal source. In practical cases, this procedure can provide additional benefits, as the effects of a distorted source (or being intentionally modified) can be immediately referenced to the clean excitation. Such methodology will be presented in chapter 5, dealing with the equivalent link's model and practically verified during measurements in the anechoic chamber (summarized in chapter 6).

This work aims to concentrate on distortions introduced by the nonlinear load and focuses on the phenomena relevant to the magnetic link. However, the proposed approach does not limit the method's universality, as it can utilize any form of U_{src} and Z_{src}. On their base, most of the practical cases can be simulated, while the identification of nonlinearities considered here can utilize undistorted sources.

Therefore, it is assumed in further considerations that the voltage source provides a pure harmonic signal only. This important presumption will be verified and clearly pointed-out when applicable. The source's impedance Z_{src} can be adjusted in a wide range, although it is useful to reference it to the typical measurement scenarios, in which Z_{src} = 50 Ω.

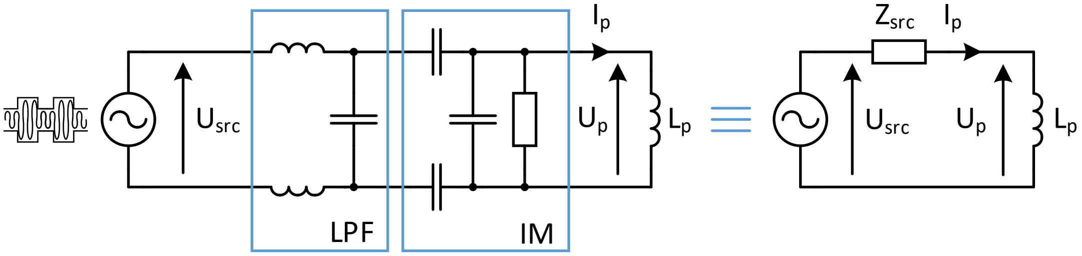

Figure 4.2 Typical transmitting path (left) and its equivalent (right)

The load current observed on the primary side due to the coupled coils' transformer-like operation can be considered a reflected load [136, 137] using the Thevenin theorem. However, this approach is applicable only to a class of linear circuits or assuming small signal operation around the operating point. Thus a usual design constraint is limited only to the value of the current flowing through the primary coil of the transmitter circuit, i.e., I_p. Depending on the application needs the peak current ranges from 70 mA to 100 mA, which is assumed to be the maximum intensity at the carrier frequency, typically 125 kHz. Other harmonics, which can arise in the frequency spectrum, and result from nonlinearities considered below, are not counted-in to this limiting value.

4.1.2 Ferrite-core based coil

The receiving coil L_s embeds the ferromagnetic rod core, which prime purpose is increasing the coil's initial inductance. When this coil locates in the center of the primary loop, the magnetic flux density in its proximity, following the Biot-Savart law, is:

$$B = \mu_0 N_p \frac{I_p}{2r_p}, \tag{39}$$

which calculates to $B = 0.23$ mT, using $I_p = 100$ mA assumed above. Indeed, it is a low value, difficult to locate on the *B-H* curve of the 3C90 core material [80] and indicate its possible hysteresis [138], neither accurately calculate nonlinear effects.

Therefore, it is proposed to utilize a common approach [139], neglecting core distortions for the low magnetic fields. Nevertheless, as this part was identified as a potential source of the harmonic spurs, the following measurements will address this point (see in 4.3.2).

4.1.3 AFE circuit

The load's analog front end (i.e., AFE) circuit plays a significant role in the magnetic link. It includes an analog conditioning circuitry, whose main function provides a known impedance to the receiving side. For the case of inductively coupled coils, it also supports the input rectifier, capable of supplying the remaining sections of the load [17]. Typically, it is supplemented with the protection component (like a bi-directional clamping diode), minimizing an overvoltage or ESD stress.

The AFE circuit's behavior strongly depends on the voltage observed on its terminals, and hence is identified from the magnetic coupling between the coils. On its basis, the equivalent nonlinear circuit reflecting impedance between the AFE's pins is proposed.

Open circuit voltage

Magnetically coupled coils are characterized by both mutual inductance *M* and the unitless coupling factor k, analyzed in chapter 3. The common formula (40) linking coils' voltage with k is:

$$k = \frac{U_s}{U_p}\sqrt{\frac{L_p}{L_s}}, \tag{40}$$

where U_s is the voltage of interest, observed on the open terminals of the secondary coil.

The U_p voltage on the primary inductance L_p results from coil's reactance and current. Therefore, U_s calculates as:

$$U_s = \frac{kU_p}{\sqrt{\frac{L_p}{L_s}}} = kI_p 2\pi f L_p \sqrt{\frac{L_s}{L_p}} = kI_p 2\pi f \sqrt{L_p L_s}\,. \tag{41}$$

From the results presented in Figure 3.13, one can read max $k = [0.08 .. 0.1]$ in the area near the primary coil's winding. Therefore, using $f = 125$ kHz, $L_p = 1$ mH, $L_s = 1.64$ mH (i.e., inductances of coils considered in chapter 2), and $I_p = 100$ mA, the peak voltage at open terminals is U_s = [8.04 .. 10.05] V. The actual measurement shows a value of 9.62 V, which correlates well with this range.

AFE's equivalent circuit

The standard approach defining AFE behavior [5, 17, 21, 140] presents it as a parallel connection of the equivalent resistance and capacitance for a given excitation level - Figure 4.3. Although requiring dedicated identification methodologies presented in the next subsection, this method allows accurate representation of large and small signals' circuit operation [20, 141]. Therefore, as outlined in works dealing with behavioral modeling of nonlinear RF circuits [142-144], the model's quality is essential for the adequate reproduction of the observed phenomena, particularly the rise of distortions for higher excitations.

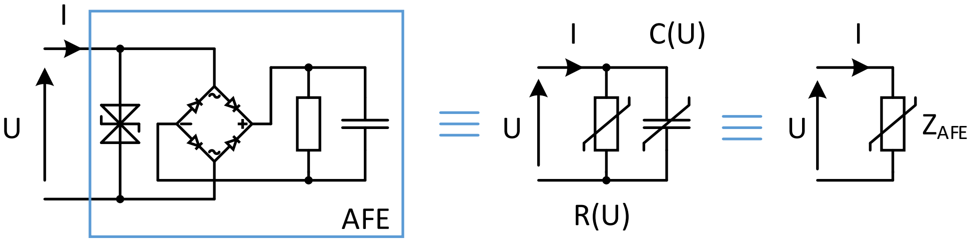

Figure 4.3 The equivalent *R*, *C* model of AFE circuit

The equivalent *R*, *C* components are determined for the excitation levels, which cannot be provided by typical laboratory instruments (discussed in subsection 4.2.1), but are observed at the carrier's frequency (that is $f = f_0$ = 125 kHz) directly on AFE terminals, i.e., up to ± 10 V. Simultaneously, the harmonic spurs excited by the AFE's nonlinear effects are monitored, so the complete spectral data are collected, including phase information. The appropriate methodologies allowing the capture of these data are presented below.

4.2 Measurement methodologies

The topic considered in this section was already highlighted in former works addressing nonlinear impedance and intermodulation measurements.

The solution provided by Gvozdenovic [17] utilized an external RF amplifier and a dedicated low-pass filter to measure distortions introduced by AFE of the RFID circuit in the HF band, together with an equivalent chip impedance. He proposed two separate setups, employing VNA to measure harmonics' amplitude and using the oscilloscope for a phase determination. However, the filter data, which affects overall performance, was not detailed. Gebhart [20] suggested using a simple RLC meter for excitations below 2 V; above, an RF amplifier and a directional coupler were employed, similarly to Rizkala's work [21], to indicate AFE impedance and monitor distortions.

The idea to use a step-up transformer for high power measurements below 30 kHz and analysis of up to 11th harmonic spur was proposed by Faifer [19]. The setup embeds simultaneous sampling on both pins of the equipment under test (EUT), provided by 16-bit digitizers, together with the synchronous generation of the excitation signal. The phase and magnitude information were extracted using the following FFT. However, with this approach, the power amplifier and transformer's nonlinear artifacts cannot be canceled out, as the Authors claimed.

Harmonic distortion measurement proposed by Komuro [145] used a 20-stage bandpass filter (BPF) for carrier signal cleanup and a 5-stage band elimination filter for carrier removal from the analyzed spectrum. Despite achieved -120 dBc system performance, reported difficulties suggest consideration of alternative or simplified solutions, which in prime should address filter design.

There is clearly no standard methodology, which can universally apply to assess magnetically coupled circuits' nonlinear behavior. For each specific case, a dedicated and optimized setup is usually proposed instead. An overview of the instrumentation usable for such analyses is described below.

4.2.1 Lab tools capabilities

A brief overview of standard laboratory instruments' capabilities is present in the following.

Impedance measurement at carrier frequency

Classical lab-class instruments like impedance analyzer HP 4294A or RLC meter HP 4284A provide high accuracy within a wide frequency range, simultaneously supporting voltage or current bias options. Despite low-level voltage excitation (up to 1V only) or coarse frequency tuning, their limitations can be partially overcome using a current excitation and performing approximate measurement at the closest frequency. Notwithstanding low availability, these instruments maintain reference quality for the impedance characterization.

Direct reflection-based measurement of the S_{11}, provided by the vector network analyzer (VNA) in a shunt mode (and the following translation to the equivalent impedance), characterizes a measurement range typically limited to 10 Ω .. 1 kΩ. This restriction reduces using thru or shunt-thru method, relying on the higher dynamic range during the S_{21} measurement. However, the instrument's excitation source provided to the EUT rarely exceeds + 10 dBm @ 50 Ω, limiting its use to low excitation only.

Spur phase and magnitude measurement

The identification of EUT's harmonics (both phase and magnitude) requires a frequency shift, unfortunately not a standard analyzer's feature. Using an instrument embedding the 2nd mixer like a nonlinear vector network analyzer (NVNA) can be a workaround, but this option is rarely available at low frequencies [141]. An alternative can be using the multiport analyzer and an external splitter [146, 147], but this solution further extends complexity and cost.

Knowledge of the EUT behavior enables the prediction of the frequencies at which disturbances arise. In this case, using a lock-in amplifier (LIA) [148] provides high usability as this tool offers both phase and level information at each known frequency. The only limitation in its use may be the unavailability of this kind of device, as periodically experienced during laboratory work. Nevertheless, the results obtained with this tool serve as references to validate the presented methodology.

Excitation source

The standard low-frequency signal generator (like Keysight 33220A) gives harmonic excitation tunable in amplitude, phase, and frequency with the satisfying resolution and accuracy. However, it provides a harmonic distortion level of -60 dBc for a moderate power +18 dBm @ 50 Ω (5 V_{pp}), which further significantly degrades when increasing the load, as presented in Figure 4.4.

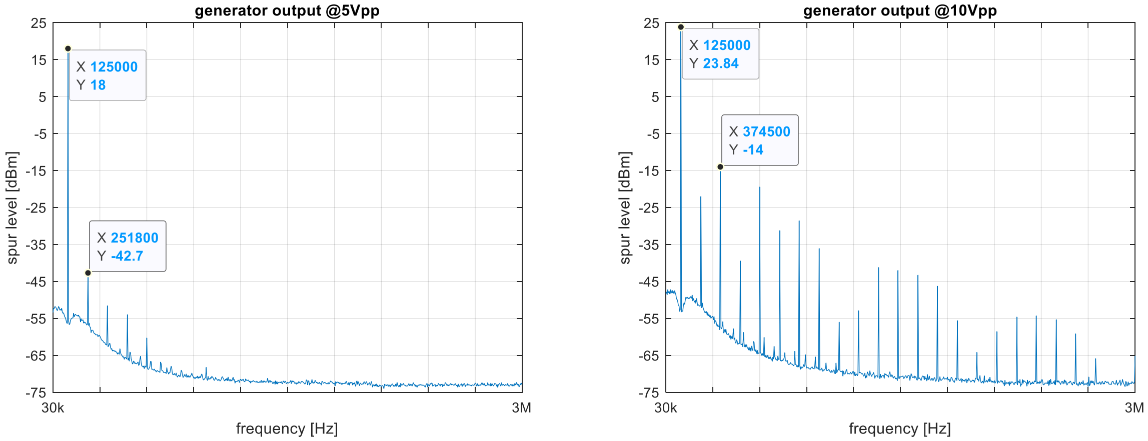

Figure 4.4 Keysight 33220A harmonics, 5 Vpp @ 50 Ω (left) and 10 Vpp @ 50 Ω (right)

A similar to the above limitation exists with VNA and SA excitation sources. An attempt using it together with an external amplifier forces implementation of a bandpass filter in a power path, as suggested in [17]. For that case, the required filter's roll-off results from the source spectrum [149]. Therefore, it shall stay in a 50 dB/octave range for the examples above to attenuate 2^{nd} and 3^{rd} harmonics to a satisfactory level.

The use of an additional RF amplifier can be reconsidered when the power delivered to the EUT is relatively low. Already mentioned references [17, 21] reported peak power dissipated within AFE as high as 380 mW and 200 mW, respectively. However, low power AFE examined in this work and operated under LW/MW bands consume less than 100 mW. Therefore, they are within typical generator capability (+24 dBm or 250 mW), which suggests an external RF amp is unnecessary.

Nonlinear characterization need under LF

The standard laboratory instruments [150] are optimized for a low voltage, fundamental frequency characterization of the EUT. The excitation source capabilities, like the output voltage swing of the tracking source (i.e., embedded within a spectrum or vector analyzer) and its spectral purity at higher loads, limit an attempt to use them during large-signal characterization (up to ± 10 V). The standard approach utilizes an external power amplifier to overcome such limitations, which is, however, abundant for low-power circuits. Typically, its presence forces using a sophisticated BPF capable of achieving an expected distortion level better than -70 dBc, which introduces additional complexity.

An essential and not fully solved topic is also a low-frequency vector characterization (i.e., both magnitude and phase) at a frequency different than fundamental. The existing instruments (like NVNA) typically cover sub-GHz bands or are very rare in the laboratory (like LIA). This constraint seems to be a general limitation, as a common practice is to use a proprietary or in-house developed instrumentation to solve that.

Summarizing the above limitations, there is an actual demand to develop a unified solution for the high-level nonlinear characterization of the low-power devices under low-frequency.

4.2.2 Proposed methodology

The measurement setup providing capabilities of impedance characterization and identification of EUT's nonlinear effects is presented in this section. It employs a compensation method, together with a selective spur cancellation by a synchronized voltage source. The complicated bandpass filter used to limit the source's distortions is reduced to four stages only. The band elimination filter, typically following the measured component, is avoided here as the injected compensating signal replaces its role. The required voltage excitation of the EUT supports a matched step-up transformer, eliminating an additional power amplifier. Supplementary, the system supports the collection of current-voltage trajectories using only the minor modification of the circuit. The structure of the proposed setup presents Figure 4.5.

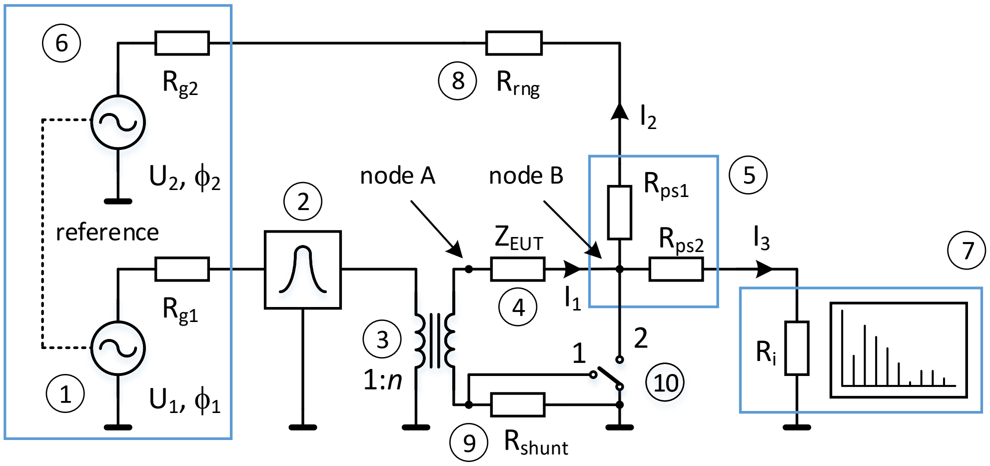

Figure 4.5 The proposed measurement setup

The setup consists of the main harmonic generator ①, characterized by its output voltage U_1 and phase ϕ_1 (assumed for simplicity as zero). Next, the bandpass filter ② is located, whose prime function is reducing of source's distortions. The step-up transformer ③ increases an excitation voltage to the level required by the following EUT ④. Next in the measurement path, the power splitter ⑤ shares EUT's current I_1 with the out-of-phase current I_2 (supplied by the compensating harmonic generator ⑥), and current I_3 flowing into the spectrum analyzer ⑦ input. Both sources, ① and ⑥ (realized as a dual-channel signal generator) are synchronized in phase by the use of a common reference signal, so the accurate phase tuning of ϕ_2 versus ϕ_1 is possible. The spectrum analyzer operates either as a selective null detector or measures carrier and its harmonics levels, depending on the measurement mode. Optional range resistor R_{rng} ⑧ allows identification of higher impedances. The shunt resistor R_{shunt} ⑨ introduces a possibility to independently verify actual current flowing through the EUT, usually indicated by the analyzer ⑦. Finally, the switch ⑩ selects the actual measurement mode of the setup (described later).

The presented setup is optimized to accurately measure EUT's current, following the assumption of its dominant contribution to the distortions observed within the radiated emission spectrum [116] considered later in this work. Therefore, identifying the voltage across EUT pins is less critical. It can be estimated with enough accuracy from the measured current and source's equivalents, presented in the following.

4.2.3 System calibration

The instrumentation impedances within circuit are reduced to resistances (nominally 50 Ω, except R_{shunt} and R_{rng},), because of the low-frequency operation. However, during a measurement, some residuals resulting from used components (i.e., transformer leakages), wiring (i.e., cable capacitance), and non-nominal system gains (i.e., filter's insertion loss, actual transformer's winding ratio) are present. While it is expected that these factors can be neglected, it is proposed to check the system's accuracy prior to and after applied calibration.

Base system calibration

A two-step calibration process (evaluated in section 4.3.1) is proposed here. It consists of the main generator's voltage U_1 sweep at fixed frequency f_0 in the first step, using known references as Z_{EUT}. During this step, the linearity and gain of signal path are indicated up to 10 V. The primary purpose of doing that is to estimate the voltage across EUT pins resulting from U_1. This voltage is expected to be lower than nominal, mainly due to the filter's insertion loss in a passband.

In the second step, the compensating generator's signal phase ϕ_2 is preset as π (i.e., 180º), while the output voltage U_2 is tuned to achieve the minimum level indicated by the analyzer. If there is an un-negligible phase shift in the measurement path (resulting mainly from the filter characteristic either transformer capacitance), the following correction of phase ϕ_2 is required. This step ends when changes of U_2 neither ϕ_2 do not further reduce analyzer readout. The actual difference (i.e., $\phi_2 - \pi$) indicates the phase-related residuals at a carrier frequency. It can be used directly as a phase correction or recalculated as a reactance part's contribution.

Extended TRC calibration

The single-value calibration method presented above can be extended in a way similar to the common open-short-load principle. However, instead of open and short conditions, it is more beneficial to provide reference values representing the expected maximum and minimum impedances of the tested EUT. In this case, such references do not need to be pure resistive and can consist of the reactance part. The three-reference calibration (TRC) method proposed in [151, 152] reflects this approach. It utilizes three RC circuits, which actual values are close to the limiting and mid-scale impedances of the EUT (marked as Z_{min}, Z_{max}, Z_{mid}, respectively). On their base using equation (42), the Z_{EUT} can be obtained more accurately as:

$$Z_{EUT} = Z_{min}\frac{(Z_{EUT\_U}-Z_{mid\_U})(Z_{EUT\_U}-Z_{max\_U})}{(Z_{min\_U}-Z_{mid\_U})(Z_{min\_U}-Z_{max\_U})} + Z_{mid}\frac{(Z_{EUT\_U}-Z_{max\_U})(Z_{EUT\_U}-Z_{min\_U})}{(Z_{mid_U}-Z_{max\_U})(Z_{mid\_U}-Z_{min\_U})} + Z_{max}\frac{(Z_{EUT\_U}-Z_{min\_U})(Z_{EUT\_U}-Z_{mid\_U})}{(Z_{max\_U}-Z_{min\_U})(Z_{max\_U}-Z_{mid\_U})}, \tag{42}$$

where Z_{min_U}, Z_{max_U}, Z_{mid_U}, Z_{EUT_U} are limiting, mid-scale and EUT impedances, respectively, measured using the considered, uncalibrated setup.

Out-of-band calibration

A similar calibration process at frequencies different than f_0 is possible. However, the primary expectation from the setup, in this case, is accurate indication of the EUT's excited spurs using the fundamental current as a reference. For that, only the identification of the phase shift at a given frequency is needed. The constant path gain supports the proper selection of the filter type and the following transformer's wideband matching. Indeed, keeping a low value of SWR towards the main generator helps to achieve that. The following subsections will address this point.

4.2.4 Operating modes

The proposed system supports three measurement modes using a common setup.

Mode 1 - EUT impedance characterization at carrier frequency

The measurement of the EUT impedance implements the compensation method. An accurate cancellation of EUT’s current I_1 by I_2 requires the analyzer’s input current I_3 to be null. To achieve that, the voltage U_2 and phase ϕ_2 of the compensating source follow the instrument’s readouts in a way to achieve the equilibrium state, i.e., $I_1 \approx I_2$. The tuning process, implementing the LMS algorithm [153] in Matlab, ends when the analyzer’s current I_3 reaches a pre-defined level (-60 dBc, i.e., 1/1000-th of I_1) or analyzer’s noise floor. In this state $I_3 \approx 0$ and node B becomes a virtual ground, so the following compensation formula applies:

$$Z_{EUT} = \frac{U_{EUT} \cdot \left(2R + R_{rng}\right)}{U_2}, \qquad (43)$$

where U_{EUT} is the voltage over unknown impedance Z_{EUT} and R is the system impedance, typically 50 Ω. The angle of Z_{EUT} is accurately described at equilibrium as $\phi_2 - \pi$ (after path calibration).

The U_{EUT} follows main generator’s voltage U_1, transformer’s turn ratio n, and reflects overall path loss, summarized as Z_{exc}. The equivalent excitation circuit covering these parts is shown in Figure 4.6.

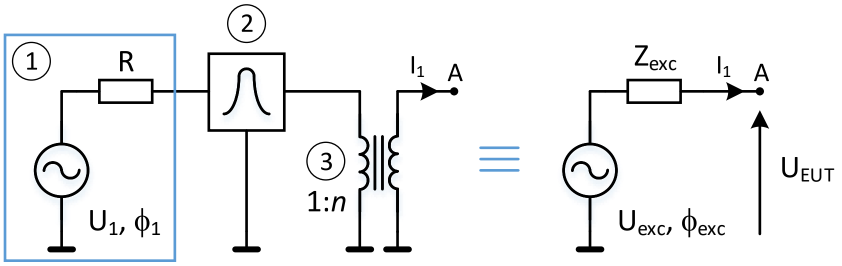

Figure 4.6 Equivalents of the excitation source path

Therefore, assuming simplified relations $U_{exc} \approx nU_1$ and $Z_{exc} \approx Rn^2$, the unknown impedance Z_{EUT} calculates using (44) as:

$$Z_{EUT} = \frac{U_{exc} \cdot \left(2R + R_{rng}\right)}{U_2} - Z_{exc}\,. \qquad (44)$$

The overall accuracy is further improved by a calibration process covering the filter’s insertion loss and transformer’s leakages, as presented in section 4.3.1.

It is important to note that currents' cancellation occurs at the excitation frequency, so the condition $I_1 \approx I_2$ is valid only for the f_0 component in this mode.

The R_{shunt} resistor is not used in this mode (i.e., switch in position 1).

Mode 2 – spur phase and magnitude measurement

Because the sources ① and ⑥ are synchronized, the frequency of the compensating generator can be tuned exactly to multiples of the carrier's frequency f_0, that is $2f_0 \,..\, Nf_0$, where N is the order of spur. In this case, the analyzer identifies firstly the power of the N-th spur as P_N by the direct measurement with the condition $U_2 = 0$. Due to a bypass behavior of the compensating generator (i.e., I_1 is equally shared as I_2 and I_3, R_{rng} is not used in this mode), the result is multiplied by two to obtain total current supplied by the EUT at a given frequency.

Therefore, the current of the N-th spur I_N is:

$$I_N = 2\sqrt{\frac{P_N}{R}}. \tag{45}$$

In the second step, the compensating generator is tuned to the frequency of the N-th spur, and then cancels it out in the same way as it was during the impedance characterization. The difference is, that nulling process occurs at spur's frequency, not carrier's. The angle of the fully compensated spur's current is similarly $\phi_2 - \pi$.

In this mode, the switch remains in position 1.

During the measurement, the carrier to spur power ratio shall be monitored to remain within a dynamic range of the analyzer (typically 80 .. 130 dB). If this is a case (although not observed during tests), a second power splitter and the 3rd synchronized generator shall be inserted into a measurement path and remove (or reduce) the carrier's signal. The potential risk of injection of additional disturbances is low because compensation of the maximum EUT's current (i.e., ten mA range) requires only + 7 dBm power from the 3rd generator, which it could deliver with negligible distortions.

Up to 25 harmonics were identified in related works [19, 143, 154-157], but this number strongly depends on the nonlinearity of the tested EUT and the analysis needs. Practically, up to 11 dominant spurs were excited from 125 kHz carrier for the considered cases and thus assumed for the following studies. Notwithstanding, an indication of higher harmonics is still possible until the used transformer type supports the wideband operation.

Mode 3 – I(U) monitoring

Assessing the current-voltage trajectories is optional, although they can provide further information about the circuit (like hysteresis or behavior during an overdrive), which cannot be easily identified from the frequency spectra. For that reason, direct observation in the time domain using an oscilloscope is necessary [17, 141]. To achieve that, the output pin from the EUT, i.e., node B, is grounded (switch in position 2), which provides an extra benefit in the noise immunity. The current signal is captured across R_{shunt} terminals, while the EUT voltage is measured between node *A* and the ground. That way of current monitoring introduces phase inversion, further corrected in control software. The results gathered this way are presented further in section 4.3.5.

4.2.5 Important setup components

The methodologies outlined above support the fundamental evaluation needs and implement well-established practices. However, the essential components in the measurement path: the bandpass filter and the step-up transformer, are considered below, as they determine an overall setup performance.

The passband filter

The main expectation from the filter (together with a narrow-band operation) is that its output impedance (i.e., one seen from the EUT towards the generator) remains close to the characteristic system's impedance in a broadband sense, not only in a passband. If this condition remains satisfied (i.e., SWR ≤ 1.5 broadband), the spurs introduced by the EUT (which are out-of-band by nature) will see nearly constant impedance, which improves accuracy of the measurement [145]. Otherwise, the spur's current magnitude (indicated as equivalent dBm power by the spectrum analyzer) will be significantly attenuated due to a high output impedance of the filter in the out-of-band range. In practice, nonlinearity measurement under such conditions will not be possible without a dedicated buffer circuit (which should, however, be avoided [158]). Therefore, the preselection of the filter's structure was primarily driven by the matching quality. Additional criteria (i.e., insertion loss and ripple in a passband, out-of-band attenuation) were assumed as possible to support by a path calibration and the use of multiple filter stages.

It was attempted to use the commercial 125 kHz passband filter FN-564 manufactured by Filtronetics for this purpose. Despite acceptable transfer characteristics, this filter's output SWR does not provide expected broadband matching, as shown in Figure 4.7. The flat-top filter type supports reasonable SWR around the center frequency 125 kHz; however, the SWR significantly increases in a stopband, and such feature is not preferred.

The author decided to build a dedicated filter fulfilling design expectations having difficulties finding a ready-to-use filter on the market.

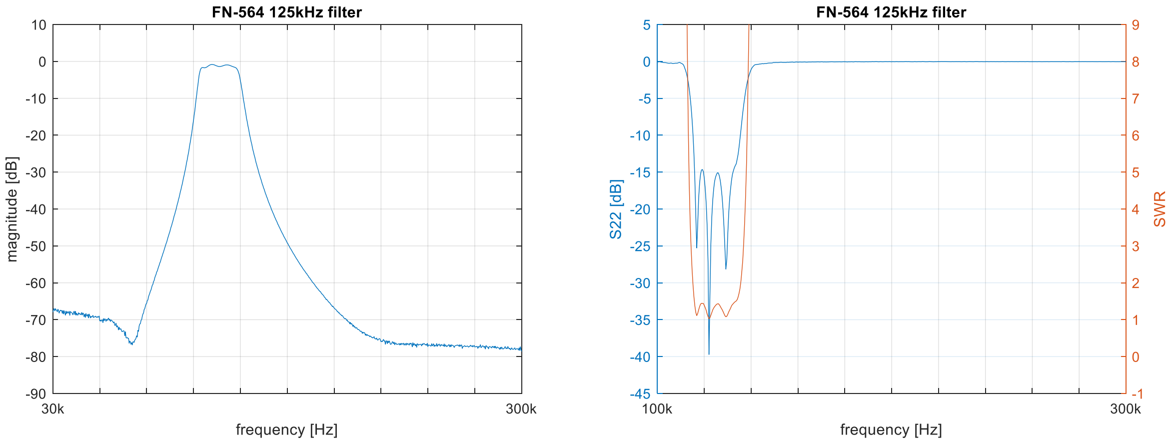

Figure 4.7 Commercial filter FN-564 transfer data (left) and its output port matching (right)

The RLC bridged-T or, in short, the tee filter shown in Figure 4.8 was selected and used as a passband filter for the following evaluations. Among other filter topologies [145, 159], the implemented one serves possible high return loss, cascading ability, and bandwidth scalability.

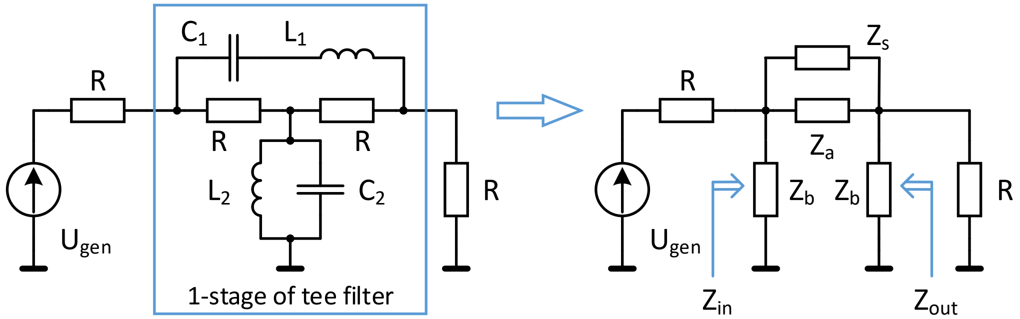

Figure 4.8 Structure of the single stage tee filter (left) and its equivalent (right)

Two design equations – (46) and (47), determine the passband center frequency f_0 of the tee filter and the relation of its components to the typical resistive system impedance R.

$$f_0 = \frac{1}{2\pi\sqrt{LC}}, \tag{46}$$

$$L = CR^2 . \tag{47}$$

In principle, the inductances and the capacitances within the filter stage do not need to be equal. It is possible to introduce a passband width parameter B and, therefore, adjust filter selectivity. Resulting components' equations will be [160]:

$$L_1 = \frac{R}{2\pi B}, \tag{48}$$

$$L_2 = \frac{BR}{2\pi f_0^2}, \tag{49}$$

$$C_1 = \frac{B}{2\pi f_0^2 R}, \tag{50}$$

$$C_2 = \frac{1}{2\pi BR}. \tag{51}$$

By introducing equivalent series and parallel impedances (denoted as Z_s and Z_p), and equivalent impedances obtained from star to delta conversion (i.e., Z_a and Z_b – Figure 4.8), the input and output impedances of the filter (Z_{in} and Z_{out}, respectively) can be obtained as follow:

$$Z_s = j\omega L_1 + \frac{1}{j\omega C_1}, \tag{52}$$

$$Z_p = j\omega L_2 || \frac{1}{j\omega C_2}\,, \tag{53}$$

$$Z_a = R + R + \frac{R \cdot R}{Z_p} = 2R + \frac{R^2}{Z_p}\,, \tag{54}$$

$$Z_b = R + Z_p + \frac{R \cdot Z_p}{R} = R + 2Z_p\,, \tag{55}$$

$$Z_{in} = (R\|Z_b + Z_s\|Z_a)||Z_b = R\,. \tag{56}$$

Because of the filter symmetry and equal source and load resistances, the following observation applies:

$$Z_{out} = Z_{in} = R\,. \tag{57}$$

Indeed, the tee filter presents resistive impedance from both ends, constant throughout the entire frequency range, including also the out-of-band range. In theory, it is equivalent to the all-band matching and no insertion loss in the passband. In practice, due to the nonzero resistance of the inductor windings, the filter introduces around 1 dB loss, as presented in Figure 4.9 (right). However, before the measurement, it can be corrected by the calibration process.

Due to the fixed resistive impedance, the direct connection between subsequent stages is possible without affecting their transfer characteristics. In theory, the four segments are enough [149] to attenuate the 2nd and 3rd harmonics by 58 dB and 77 dB, respectively – see in Figure 4.9 (left).

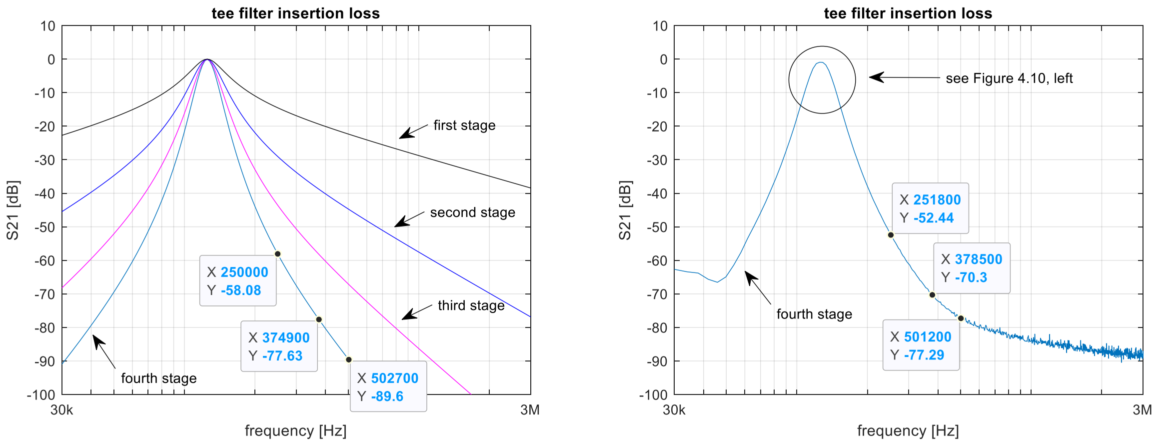

Figure 4.9 Theoretical (left) and measured (right) insertion loss of the designed 4-stage filter, note $IL = -S_{21}$

The filter implementing the elementary structure, presented in Figure 4.8, was realized as a cascade of four identical stages and assembled on a common printed circuit board. To obtain 125 kHz filter's center frequency and close to 50 Ω impedance, the following component values were calculated: $R = 49.9\ \Omega$, $L_1 = 220.6\ \mu\text{H}$, $L_2 = 18.3\ \mu\text{H}$, $C_1 = 7.35$ nF, $C_2 = 88.6$ nF for $B = 36$ kHz. The nearby to nominal capacitances were obtained by the parallel connection of the two standard values. Supplementary, the selection of inductors was applied, which helped to achieve the desired level of out-of-band attenuation. The resulted filter performance is shown in Figure 4.9 (right) and below.

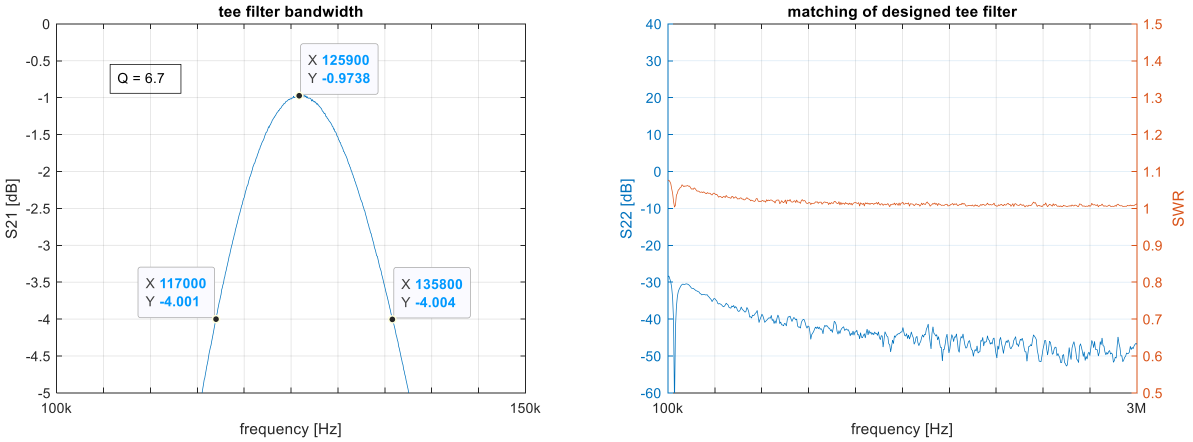

Figure 4.10 Measured Q-factor of constructed 4-stage filter (left) and filter's output port matching (right)

Step-up transformer

The transformer's primary purpose is to increase n times the excitation voltage supplied by the signal generator, where n is the winding turn ratio. As a general requirement, the step-up transformer shall give a relatively flat frequency response [155, 161] and provide a substantial matching within the considered band (i.e., from f_0 to Nf_0). The constructed unit, using EFD15 transformer from Wurth having six identical windings (1+1 on the primary, 1+1+1+1 on the secondary) satisfied 3 dB bandwidth @ 100 mW load up to 15.3 MHz – see in Figure 4.11 (left), and 0.3 dB flatness within 100 kHz .. 3 MHz band. The return loss is better than 23 dB for frequencies higher than 100 kHz, as illustrated in Figure 4.11 (right). The transfer characteristics were collected using two-port matching, utilizing actual transformer ratio $n = 2$. The return loss within the analyzed spectrum results mostly from the transformer's main and leakage inductances; however, it was not further improved (by the optional matching circuit [162]) and assumed as satisfying design needs.

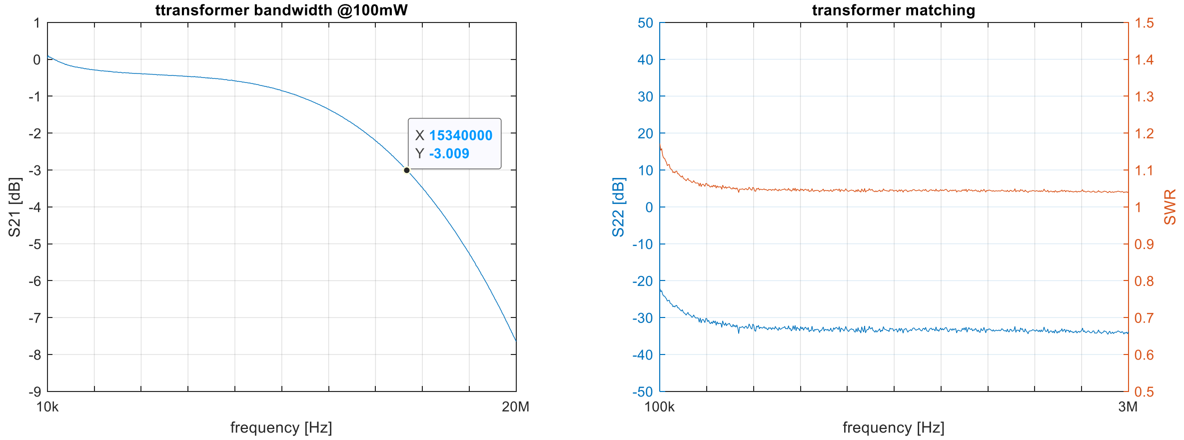

Figure 4.11 Measured transformer's bandwidth (left) and return loss (right), note $RL = -S_{22}$

Alternatively to the type proposed above, the transformers commonly used within xDSL networks can be considered. These designs are optimized for sub- and MHz ranges, for both the power efficiency and the level of introduced disturbances [163]. This approach will be proposed as an extension of this work.

Discussion of the measurement setup

An essential factor addressed during the evaluation was the placement of the filter within a measurement path. Putting it directly after a signal source provides the expected attenuation of generator harmonics; however, it does not reduce optional distortions introduced by the transformer. Conversely, locating a passband filter after the transformer can minimize distortions from both sources. However, it will require changing the filter's characteristic impedance, which needs to be adapted to the actual transformer's winding ratio. Additionally, the increased excitation voltage provided to the following filter input may introduce nonlinear distortions by the filter's components [164], which cannot be further removed.

The selected configuration, experimentally verified for a broad range of excitations up to ± 18 V on EUT pins, showed the best performance when placing the filter directly after the signal source. In this case, the transformer circuitry capable of power transfer as of 2 W nominal, when loaded up to 100 mW, introduced negligible distortions (less than -74 dBc) compared with ones excited by the EUT.

The measurement path can be further simplified by removing the power splitter. However, this additional resistance provides extra protection of the analyzer input, simultaneously introducing only a minor attenuation [165], and hence used for the below evaluations.

In addition, the range resistor R_{rng} could be replaced by an attenuator, maintaining constant resistance towards the compensating generator (although such an option was not tested).

4.3 Evaluations

There were several checks executed with a proposed setup before using it for the characterization of the nonlinear circuits. These are described below.

4.3.1 Setup accuracy

Base calibration

Firstly, the measurement path's initial accuracy was investigated with a set of known impedance loads, previously measured with a precise RLC bridge HP 4284A. The indicated residual phase shift in a passband was 0.72°, and a parasitic capacitance at node B was estimated as < 12 pF. The main source's path gain (measured as 1.83), including filter's insertion loss and transformer's winding ratio, remained constant for a whole excitation range, confirming high setup's linearity. Using these offset data as a base calibration showed a maximum relative error for 200 kΩ || 100 pF impedance (+ 5.4 % module, - 1.3 % phase, R_{rng}= 1000 Ω in this case).

Extended calibration

The TRC calibration procedure presented in section 4.2.3 was applied in the next step.

The representative measurement of the EUT circuit, provided by 2 kΩ || 470 pF, is presented in Table 5. The relative error referred to the bridge measurement was < 4 % before calibration and better than 2.5 % after it. Considering these values in the logarithmic scale, it results with 0.35 dB and 0.22 dB, respectively. It is more than satisfactory for the unoptimized prototype setup and fully supports evaluation needs. As the calibration process does not improve the accuracy significantly, it is proposed to omit it in future use. However, in this case, a more detailed uncertainty assessment of the measurement path is needed. It is presented in the last section of this chapter.

Table 5 Impedance measurement accuracy, 125 kHz, @1 V

Configuration	**Parameter**			
	|Z| [Ω]	**Angle [°]**	**R [Ω]**	**C [pF]**
RLC bridge results, basic accuracy ±0.2 %	1601.0	-36.70	1996.8	475.3
This setup, before TRC calibration	1609.4	-35.42	1974.4	458.3
This setup, after TRC calibration	**1613.1**	**-35.97**	**1993.3**	**463.6**
Initial error referred to RLC bridge	0.52 %	3.48 %	-0.67 %	-4.01 %
Final error referred to RLC bridge	0.75 %	-1.98 %	-0.17 %	-2.46 %

Spurs measurement accuracy

The measurement of the magnitude and phase of spurs referred to the results obtained with the commercial lock-in amplifier (LIA) SR860 was made in the following. The reference signal was brought to the LIA from node *A* (to skip phase shift and loss introduced by the filter and transformer), while EUT's response was observed at node *B*. As EUT, the ordinary silicon diode LL4148 was used, as suggested in [166]. The results of the comparison are summarized in Table 6, indicating good agreement between both approaches (i.e., < 1.5 dB of magnitude and < 1° of phase).

Table 6 Silicon diode spurs, referenced to carrier's current, 125 kHz, 2 V_{pp}

Parameter	**Spur number**							
	Magnitude [dBc]				**Angle [°]**			
	2	**3**	**4**	**5**	**2**	**3**	**4**	**5**
LIA SR860 results, basic accuracy ± 2 %	-2.62	-7.59	-16.83	-39.53	+90.05	-179.92	-90.12	+178.19
This setup	**-2.58**	**-7.44**	**-16.55**	**-38.19**	**+90.13**	**-179.77**	**-89.46**	**+177.54**
Delta referred to LIA	0.04	0.15	0.28	1.34	0.08	0.15	0.66	-0.65

I/U path residuals

Finally, the measurement path was investigated for the potential offsets and phase shifts, which cannot be corrected during the collection of the current-voltage trajectories. The low inductance 1 kΩ resistor was used as EUT to observe that. The results shown in Figure 4.12, confirm low residual phase shift (estimated here as 0.35°) and negligible offsets. This measurement was completed on the secondary side of the transformer. It helped to indicate impacts from both transformer's output capacitance and winding resistance. It was assumed that these factors could be neglected during high-level characterization in Mode 3, and no further corrections of collected trajectories are needed. Observing Figure 4.12 right data, the measurement system supports 1:1 V/mA scaling ratio using a 1 kΩ shunt resistor. It points to the minor voltage drop introduced by the secondary winding resistance.

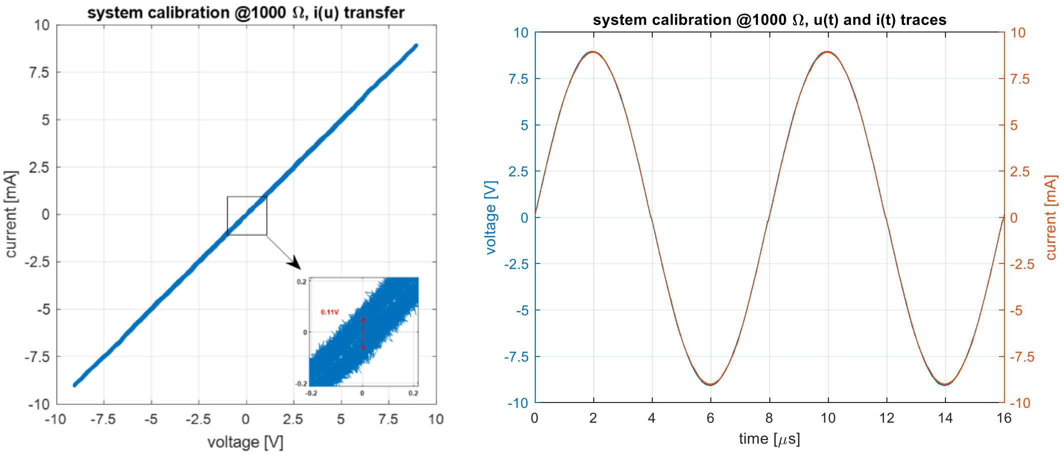

Figure 4.12 Voltage and current signal paths, *i(u)* transfer (left), and *u(t)* and *i(t)* traces (right)

4.3.2 Investigation of core distortions

The assumption made in section 4.1.2 neglecting the secondary coil core distortions needs to be indeed verified. The secondary coil L_s = 1.64 mH (described in chapter 2), in series with 1 nF mica capacitor, were put in place of EUT to prove that. Both components created a resonance circuit with the impedance minimum near f_0 = 125 kHz. The coil current with excited spurs was measured utilizing the setup operating in Mode 2, resulting in Figure 4.13 (left). For this exercise only, the comparable measurement with a direct connection from the same generator to the analyzer input was made (i.e., in a thru mode). In this case, it results in a slight increase of 4th and 5th harmonics level (by 2 .. 3 dB) – see Figure 4.13 (right), which can be attributed to the driving generator.

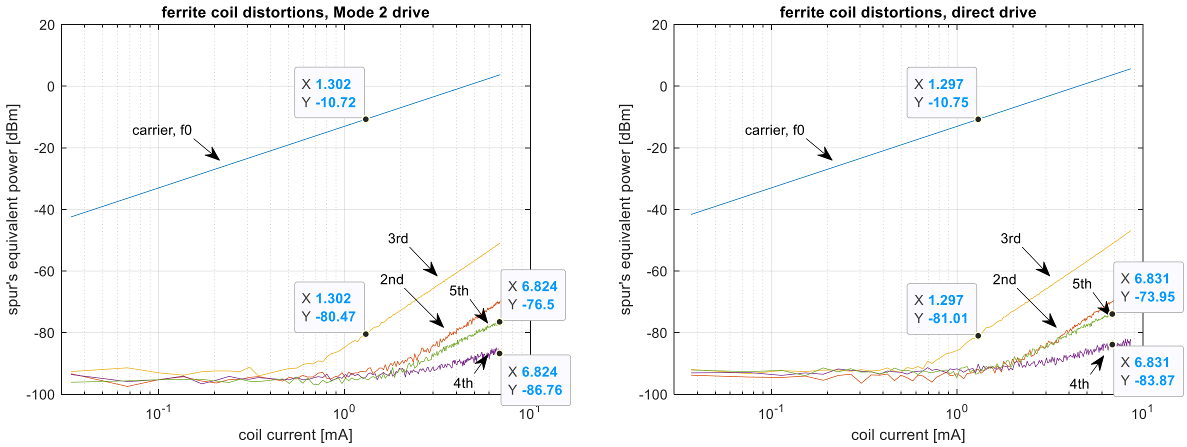

Figure 4.13 Harmonics of the ferrite coil, Mode 2 measurement (left) and direct thru mode (right)

The distortion-free operation (i.e., defined as less than - 70 dBc for a dominant harmonic spur) is possible for coil currents up to 1.3 mA, which is limited by the level of 3rd harmonic. With a quasi-linear behavior of the following AFE circuit up to 0.1 .. 0.2 mA only (see Figure 4.16), the ferrite-core coil distortions are lower by more than 25 dB compared to the dominant 3rd harmonic of AFE. This margin further extends up to 65 dB @ 1 mA, and slightly reduces to 43 dB @ 7 mA. Therefore, the neglection of core distortions is valid compared to ones introduced by the AFE circuit.

4.3.3 Nonlinear AFE impedance

The AFE circuit was put in place of EUT, where impedance Z_{AFE} was indicated firstly in a low span (< 1 V), in which it was possible to compare results of Mode 1 with ones from the RLC bridge - Figure 4.14 (left). Next, the full span was captured, in which AFE operated up to 10 mA (voltage excitation < 9 V), assumed as a non-destructive limit. The shaded area shows an uncertainty range assessed using the method proposed in section 4.3.6, with the following base calibration.

Equivalent impedance of AFE

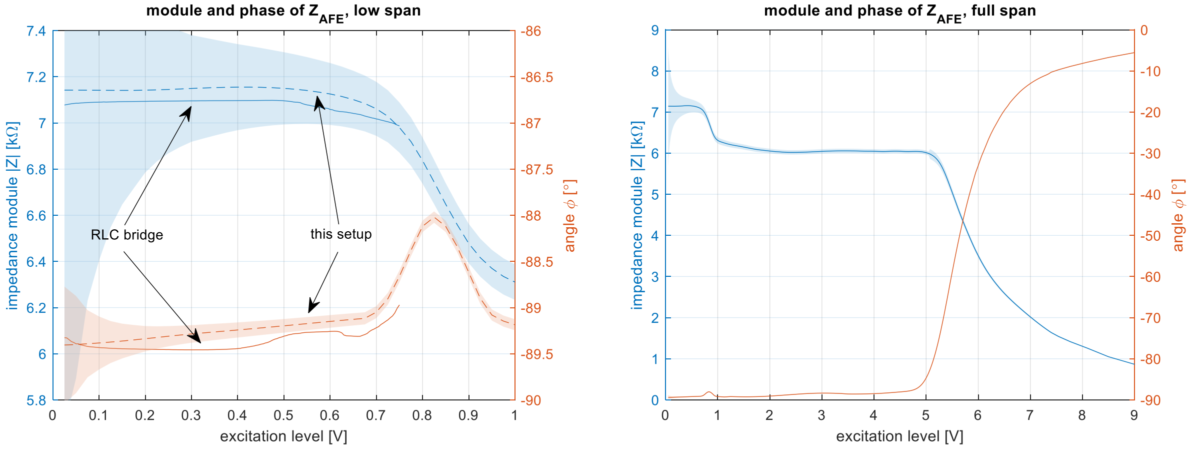

Figure 4.14 Equivalent AFE impedance, low span < 1 V (left), full span (right)

The AFE circuit represents a lossy capacitor for the low excitations, which further degrades at higher levels. It starts to act more as a resistance above 5 V due to activation of the internal clamping circuit.

Equivalent resistance and capacitance parts of AFE

On the base of impedance data captured above, the equivalent resistance and capacitance parts are calculated at carrier's frequency. Their dependencies on the excitation voltage are shown in Figure 4.15.

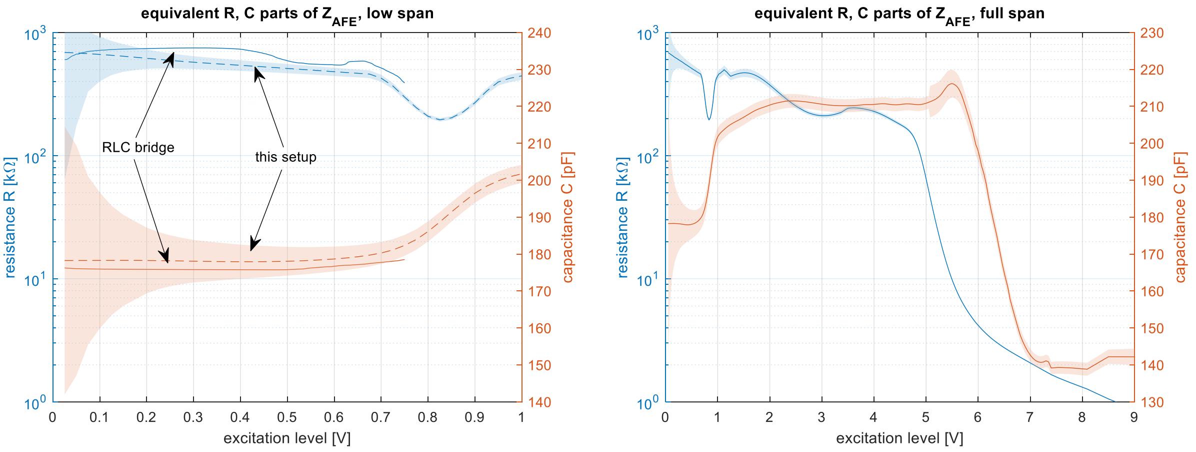

Figure 4.15 Equivalent AFE resistance and capacitance, low span < 1 V (left), full span (right)

Resistance R and reactance X parts of the parallel network (see Figure 4.3) were obtained from impedance data (i.e., module $|Z_{AFE}|$ and phase angle ϕ) as:

$$R = |Z_{AFE}| \frac{1}{cos(\phi)}, \tag{58}$$

$$X = -|Z_{AFE}| \frac{1}{sin(\phi)}. \tag{59}$$

Therefore, resulting equivalent capacitance C is:

$$C = \frac{-sin(\phi)}{2\pi f_0 |Z_{AFE}|}. \tag{60}$$

Typically, R and C equivalents' recalculation results in increased uncertainty when the indicated impedance's angle is higher. These values were assessed in section 4.3.6 as 3.9 % and 4.7 %, respectively, for a selected case as an example.

4.3.4 AFE harmonics measurements

Utilizing setup operating in Mode 2, both spur’s power and phase were collected. The results are presented in Figure 4.16 and Figure 4.17. It is helpful to define regions in which specific operation of AFE circuit is observed. Although there is no standard rule for making such a selection, it is proposed to use excited spurs’ levels and associated current values for that purpose.

The low excitation range is defined for AFE’s currents less than 0.07 mA (0.1 mA_p), in which it assumes operation with negligible distortions (i.e., lower than - 70 dBm for a dominant spur).

Within the high excitation range, AFE’s distortions increase nearly simultaneously with the carrier signal f_0, keeping spurious-free dynamic range on the level 35 .. 40 dBc. It is valid for currents up to 0.6 mA (0.85 mA_p).

Activation of the internal clamping structure (observed above 0.6 mA) forces a substantial increase of spurs’ levels, dominated here by odd ones. This range, named overdrive, extends up to 10 mA, assumed in 4.3.3 as a non-destructive limit.

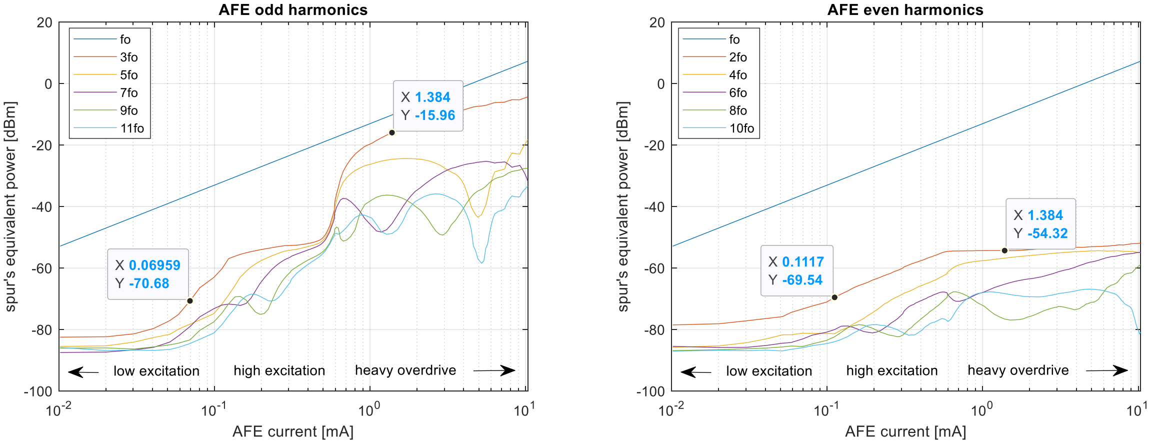

Figure 4.16 Power of the 11 initial harmonics of the AFE circuit, odd (left) and even (right)

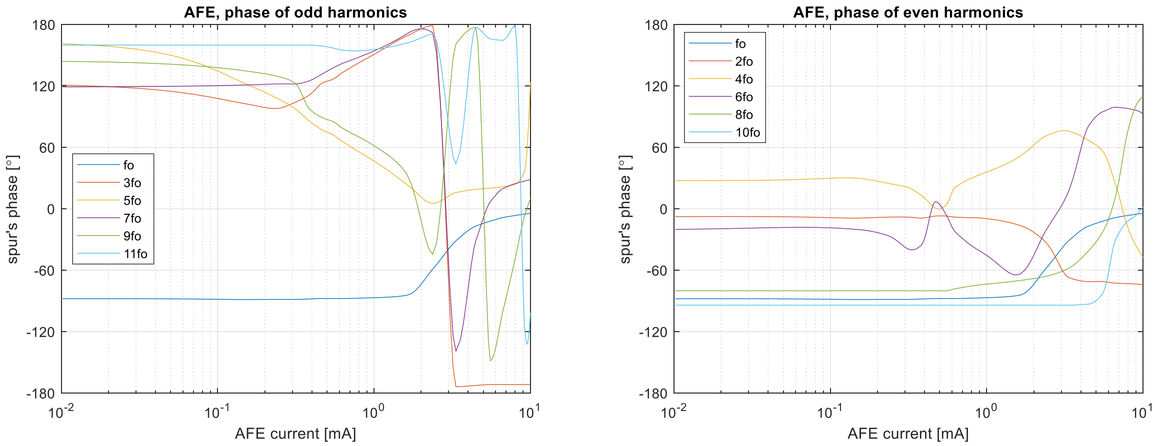

Figure 4.17 Phases of the 11 initial harmonics of the AFE circuit, odd (left) and even (right)

The highly nonlinear character of AFE circuit predicted in section 4.1 is now confirmed. The changes are significant – from kindly 700 kΩ down to 1 kΩ for the equivalent resistive part, and by 140 .. 215 pF for the capacitive, as shown in Figure 4.15. This undoubtedly can impact proper resonance matching with L_S coil, which will be analyzed in the next chapters.

The dominance of 3rd harmonic is recognized during an overdrive, analyzing Figure 4.16 data. For the lower levels, the 2nd spur shall be further observed, as it follows the full-wave rectifier behavior of AFE.

4.3.5 I/U trajectories

The regions of low and high excitations defined in Figure 4.16, and overdrive are visible also on the scope traces. The distortion-free area can be outlined briefly within ± 0.7 V and ± 0.1 mA, as observed in Figure 4.18. In this range, AFE operates with minor distortions, which correlates well with Figure 4.16 data.

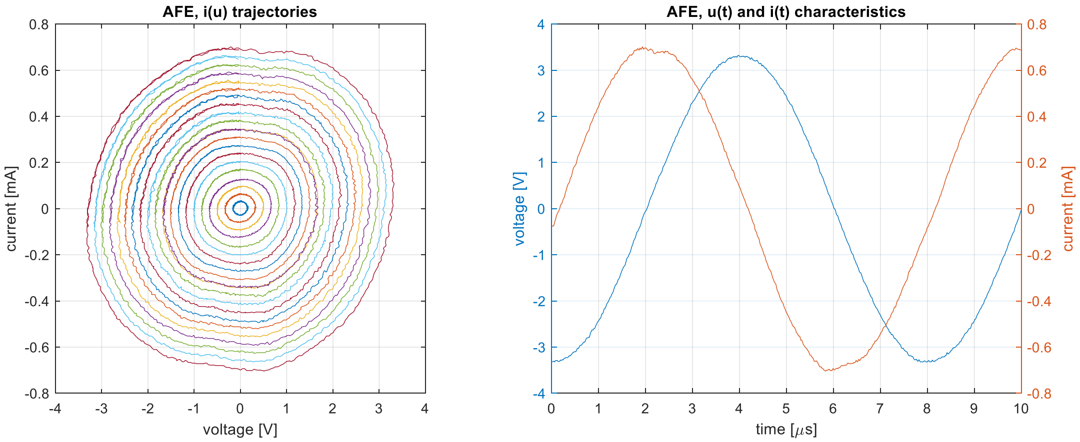

Figure 4.18 AFE at low excitation, $i(u)$ trajectories (left) and $u(t)$, $i(t)$ @max level (right)

Increased voltage along AFE pins starts to supply its internal circuitry, up to roughly ± 4 V, when the internal clamping protection activates, as observed in Figure 4.19. The significant part of the

AFE current flows now through the protection circuitry, which implies highly distorted waveforms, also observed in a frequency domain in Figure 4.16.

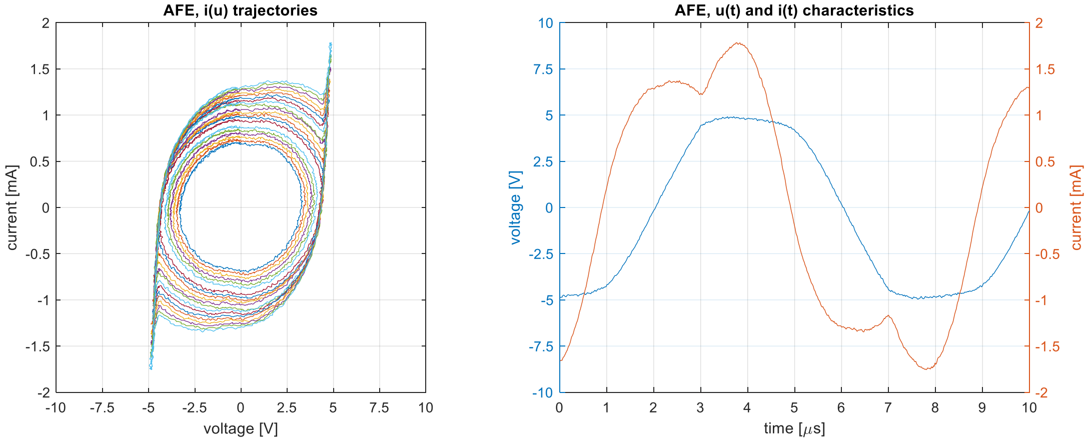

Figure 4.19 AFE at high excitation, $i(u)$ trajectories (left) and $u(t)$, $i(t)$ @max level (right)

The overdrive state is characterized mostly by resistive character of the AFE. Therefore the predominant current flows during the clipping phase - Figure 4.20.

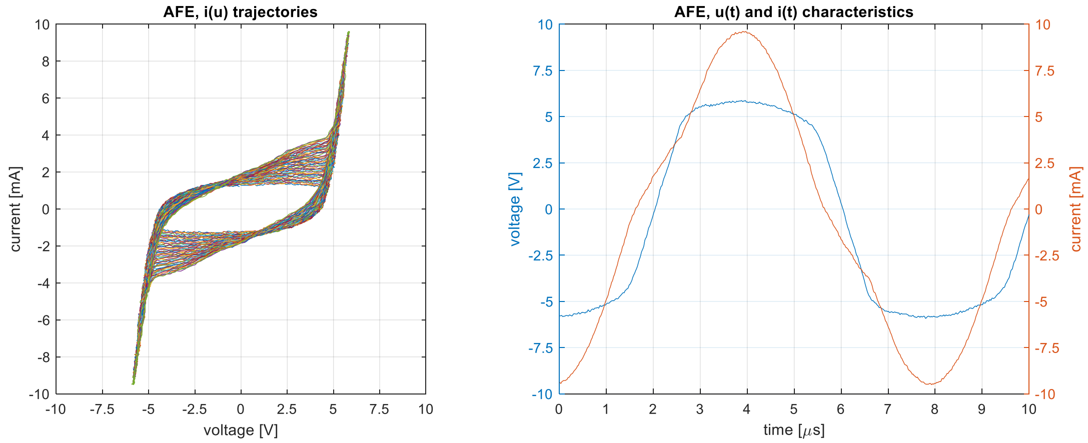

Figure 4.20 AFE at overdrive, $i(u)$ trajectories (left) and $u(t)$, $i(t)$ @max level (right)

Both states - high excitation and overdrive shall be avoided due to the high nonlinearity. This limitation will be considered in the next chapters.

4.3.6 Uncertainty assessment

This section shows the simplified metrological analysis of the setup presented in 4.2.2. The results obtained here will allow to define the measurement uncertainty while performing impedance characterization at the carrier's frequency.

Measurement path

Without loss of the overall setup functionality, it could be simplified to the form presented below.

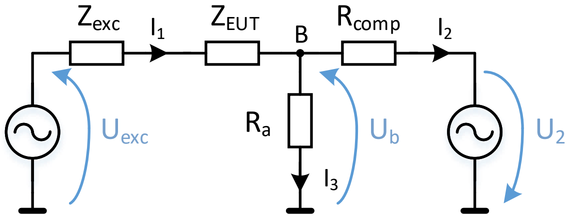

Figure 4.21 Simplified measurement paths

The unknown impedance Z_{EUT} is calculated from the equation (61), considering the nonzero analyzer's current I_3 (thus node's B unbalance voltage $U_b \neq 0$). On the base of Figure 4.21, the Z_{EUT} calculates as:

$$Z_{EUT} = \frac{-U_b\left(R_a R_{comp} + R_a R_{exc} + R_{comp} R_{exc}\right) + U_{exc} R_a R_{comp} - U_2 R_a R_{exc}}{U_b(R_a + R_c) + U_2 R_a}, \qquad (61)$$

where R_{comp} summarizes path towards compensating generator (i.e., of a power splitter R_{s1}, range resistor R_{rng}, and internal resistance R_{g2}), and R_a simplifies analyzer's path (including part of power splitter R_{s2} and instrument input R_i). As a quick check, the above formula reduces to (44) for $U_b = 0$ (i.e., during fully compensated state).

The excitation voltage considers the main generator's voltage U_1, transformer winding ratio n, and the filter's insertion loss IL. The phase shift consists of generator phase ϕ_1 and a sum of filter and transformer phases expressed as ϕ_{flt}. Therefore, the resulting excitation voltage U_{exc} is:

$$U_{exc} = nU_1 \cdot IL \cdot e^{-j(\phi_1 + \phi_{flt})}. \qquad (62)$$

Combined standard uncertainty

The following equation is the definition of combined standard uncertainty $u_c(y) = u_c(Z_{EUT})$, which includes uncertainties of the above components, assuming the mathematical model is of the form $y = f(x_1, x_2, .. x_N)$:

$$u_c(y) = \sqrt{\sum_{i=1}^{N} \left(\frac{\partial f}{\partial x_i}\right)^2 u^2(x_i) + 2 \sum_{i=1}^{N-1} \sum_{j=i+1}^{N} \frac{\partial f}{\partial x_i} \frac{\partial f}{\partial x_j} u\left(x_i, x_j\right)}. \qquad (63)$$

The partial derivative of $f(\cdot)$ concerning the x_i, together with standard uncertainty $u(x_i)$, defines the independent contribution of x_i. Supplementary, $u\left(x_i, x_j\right)$ estimates the covariance associated with x_i and x_j, introduced due to an existing correlation between a dual-channel generator's output signals.

Uncertainty contributions

Above formulae (61)..(63), together with (58) and (60), were applied in Matlab using an uncertainty toolbox (AUT) [167] to obtain individual contributions (evaluated below for the impedance 2 kΩ || 470 pF). Initially, the setup budget was estimated for this case (summarized in Table 7), reflecting instrumentation capabilities and unbalance level, assumed as equilibrium state.

Table 7 Uncertainty budget of the setup

Quantity	Estimated value	Standard uncertainty	Probability distribution
	x_i	$u(x_i)$	
U_b (equivalent power)	-60 dBm	1 dBm	normal
U_1	10 V	0.001 V	normal
ϕ_1	0º	0.01º	normal
U_2	1.127 V	0.001 V	normal
ϕ_2	32.61º	0.01º	normal
R_{s1}, R_{s2}, R_{g1}, R_{g2}, R_i	50 Ω	0.1 Ω	normal
n	2	0.01	normal
IL	1	0.01	normal
ϕ_{flt}	0º	0.35º	normal
R_{rng}	0 Ω	0.1 Ω	normal
f_0	125 kHz	1 Hz	normal

Next, the nonzero correlation was defined between U_1 and U_2, taking into account their dependencies from internal voltage reference (however with some freedom due to different loads), set obligatory as $cor(U_1, U_2) = 0.5$. The effect of a common reference clock was assumed as $cor(\phi_1, \phi_2) = 0.9$.

Using the above data, the module and phase angle of Z_{EUT}, together with equivalent R and C parts were calculated. Applying the suggested GUM notation [31], they were respectively: 1609(19) Ω, 36.44(39)º, 2000(26) Ω and 470.0(7.3) pF.

Finally, the uncertainty contributions were indicated. Influences smaller than 1E-3 times the max value were omitted for clarity. These evaluations are summarized in Figure 4.22 below.

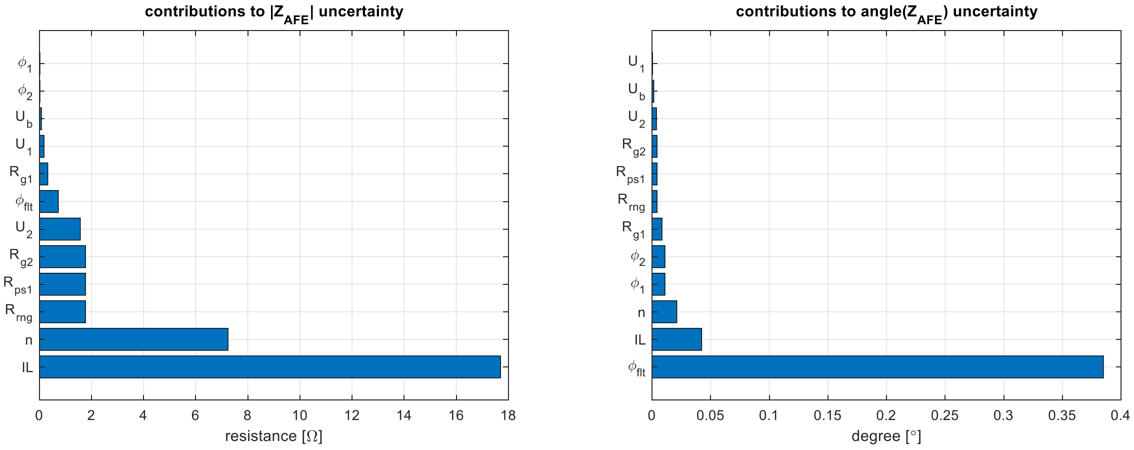

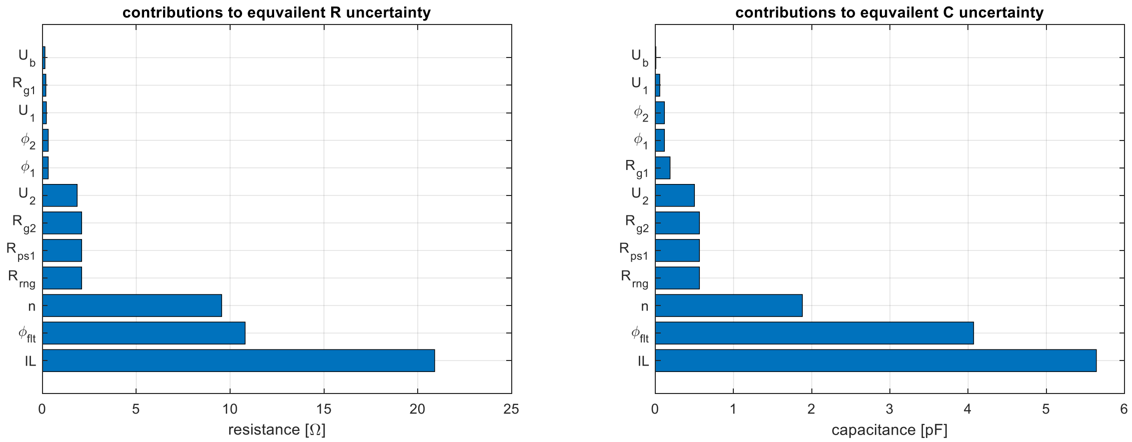

Figure 4.22 Uncertainty contributions of Z_{EUT} and equivalent R, C parts

The dominance of IL, ϕ_{flt}, and n factors are clearly indicated by observing the above data. They together define an overall uncertainty level, leaving other contributions as less critical. Therefore, the proposed in section 4.2.2 base calibration shall primarily focus on the accuracy while obtaining these values.

A standard approach of using uncertainty $u_c(y)$ is to multiply it by a coverage factor k = 2 .. 3, which is chosen according to the desired confidence level. Therefore, assuming k = 3 (i.e., confidence greater than 99 %), the relative expanded uncertainty defined as:

$$U_r(y) = \frac{ku_c(y)}{|y|}, \tag{64}$$

results with the following uncertainties: $U_r(|Z_{EUT}|)$ = 3.6 %, $U_r(\angle Z_{EUT})$ = 3.2 %, $U_r(R)$ = 3.9 %, and $U_r(C)$ = 4.7 % for the case considered above.

Calibration effect

The recognition of actual uncertainty of dominant contribution can be applied to improve overall setup accuracy. As an example, the more accurate estimation of uncertainty $u(\phi_{flt})$ from coarse 0.35 to possible 0.01 can provide significant improvement, as presented in Figure 4.23. Such identification can be achieved during the base calibration process and is suggested here.

The visible step-change follows the use of a range resistor R_{rng} = 1000 Ω below 5 V limit. This value could be further increased to improve overall accuracy below 2 V. However, this option was not examined, assuming that the low excitation range is supported by typical instrumentation, or by the optional TRC calibration.

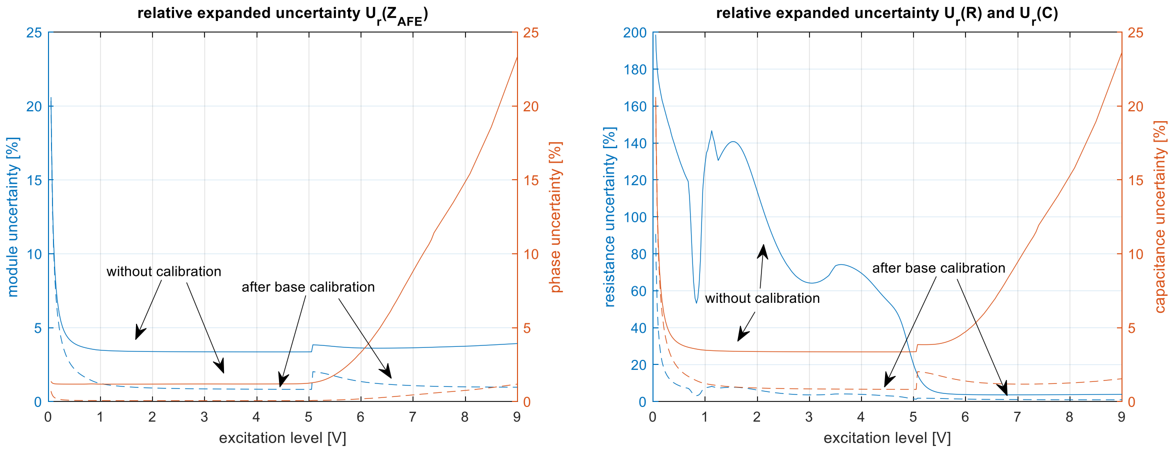

Figure 4.23 Effect of base calibration ($u(\phi_{flt})$ = 0.01) to relative expanded uncertainty

Chapter summary

This chapter has been devoted to the recognition and characterization of the nonlinearities present in the magnetic link. It was found by analyzing individual components' individual influences on the observed level of harmonic distortion that the AFE block plays a dominant role in this process. The impact of the remaining parts was neglected (like an air coil and transmitter), or it was much lower than the dominant contribution (in the case of a ferrite-core inductor).

The predominant AFE block was characterized in both frequency and time domains. Firstly, the applicable measurement methods were reviewed. It was shown that there is a gap in the instrumentation operating within LF band, concerning ,in particular, the signal purity, excitation levels, and the capability of phase measurements. Therefore, the dedicated setup was proposed and validated. It implemented an accurate compensation method, using two synchronized generators to cancel out excited spurs selectively and a dedicated matched bandpass filter, providing constant impedance to the tested unit. Supplementary, the step-up transformer was introduced, simultaneously eliminating the need for an external RF amplifier for testing low-power devices in LF band. The setup's uncertainty was analyzed in the last section, clearly indicating dominant contributions, which were recognized as the main generator path's loss and filter's phase shift in a passband. It was shown that applying a base calibration process can significantly improve the overall system's accuracy.

The proposed methodology allowed the characterization of unknown AFE impedance in a wide range, together with an accurate measurement of excited spurs' magnitudes and phases. It showed that equivalent resistive and capacitive parts could vary significantly within a possible operating range, impacting the circuit's resonance behavior analyzed in the next chapter.

END OF CHAPTER 4

5 Nonlinear analysis of linked circuits

This chapter summarizes methods of numerical modeling of the magnetic link, on which base the distorted currents are identified. The chapter starts with an overview of the standard behavioral models, followed by a brief presentation of the nonlinear frequency-domain analyzing methods.

The magnetic link's core component, recognized in the previous chapter as the AFE circuit, is modeled in more detail. Two different structures are proposed to reflect its operation, following formulation by the set of nonlinear differential circuit equations and, alternatively, as the one-port device. Both forms result from methodologies described in section 4.2.2 and allow obtaining simulated spectrum data well aligned with completed measurements. These evaluations end with estimating phase and magnitude uncertainties propagated from the complex impedance characterizing the AFE component.

Next, the complete magnetic link is modeled as a lumped circuit, containing equivalents of the primary and secondary coils, mutual inductance, and the AFE circuit. The two-dimensional distortion map is created on its base, clearly identifying regions of increased spurs' magnitudes.

In the last step, the effect of the secondary side circuit's nonlinearities is recognized as a resonance frequency shift using the proposed model. This phenomenon known to RF circuit designers is now presented in a wider context, providing additional benefits in evaluating coupled nonlinear circuits.

5.1 Nonlinear behavioral modeling in the frequency domain

The large-signal characterization of active components commonly assumes nonlinear relations between input and output signals [168, 169]. This approach is typical for simple components (like diodes, transistors, etc.) and complex structures (as amplifiers, mixers, etc.). Therefore, the identification of an actual level of nonlinearity is a prime target during such circuit evaluation. Although this process is well recognized and quantified (as IMD, IP3, THD, etc.), the concise and useful description of a real input-output relationship in the frequency domain remains complicated [23, 24]. The difficulty reflects frequency spectrum dependency on the excitation level and its harmonic content, including an interaction between output spurs [144]. Therefore, an accurate capturing of all these effects requires an appropriate methodology selection (i.e., the model and methods), which a short overview is outlined below.

5.1.1 Behavioral modeling concepts

The analysis of the nonlinear devices requires the selection of a dedicated class of models capable of predicting circuit behavior correctly. The classical methods [22] employ simplification and linearization at the operating point; however, this approach may fail when considering a large-signal operation. The attempt to accurately describe nonlinear circuits can lead to complex analysis or complicated extraction of the needed parameters. An example is the Volterra series analysis, which was reported in some works [24, 170, 171] as complicated for the higher order kernels (i.e., above 3) and having no physical interpretation of the indicated parameters. The methods originating from the above, like the generalized frequency response function (GFRF) [25, 172] and the nonlinear output frequency response functions (NOFRF) [25], suggest the same observations. Despite the mathematical elegance [24], the above methods are not recognized as intuitive, fast, and easy to apply [22, 144].

Therefore, straight-forward measurement-based modeling, directly employing observed behavior, becomes preferred in engineering practice [22, 173]. This approach supports instinctive recognition of the predominant components (like equivalent capacitance or resistance) and circuit operation (like clipping), which significantly reduces the extraction time of the required parameters [172]. However, with limited knowledge of the circuit's structure, this approach – proposed also in this study, should not over-simplify the model. This topic, in particular, was addressed in the subsequent sections in more detail.

5.1.2 Nonlinear harmonic analysis methods

A characteristic feature of the nonlinear operation is introducing additional frequency content to the output, which was not present in the input stimulus. This effect exists for single and multitone excitations and typically intensifies with the input level. It is observed in a time domain as possible signal clipping, or, generally~~,~~ signal distortion. Considering it in a frequency domain allows recognition of the additional spurs introduced to the output signal.

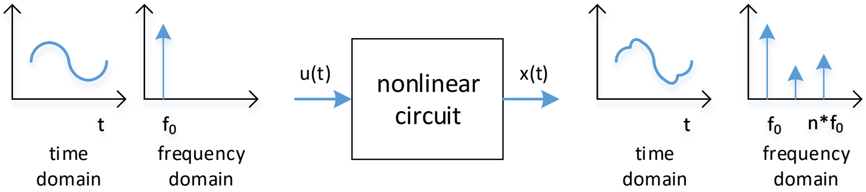

Figure 5.1 Nonlinear circuit operation

There were already developed several nonlinear methods to capture these phenomena. Starting from the mentioned Volterra series [174, 175], through neural networks [176], or hybrid ones [177] to list a few. Since each method has its features, it should be properly selected in advance. Useful selection criterion can be the operating mode of the nonlinear circuit. Considering it, e.g., as a quasi-static operation (i.e., employing time-invariant components), the harmonic analysis neglecting the transient state is highly usable.

The commonly used method addressing RF circuits is the harmonic balance (HB). This method is well fitted to the broad class of nonlinear components [166, 178], including nonlinear resonators [179, 180], Duffing oscillator [180], and the full-wave rectifiers [181]. It also supports the memory effects of nonlinear RF circuits, identified as the additional phase shift of the spectral products, as in [182, 183]. The HB method is currently recognized as a leading solver in commercially available applications targeting RF analyses [173, 184]. The basis of the HB method extensively used in subsequent analyses is presented below.

Harmonic balance (HB) method basics

Considering the nonlinear circuit operating in a steady-state under harmonic excitation can present it as a real-valued nonlinear equation in a form:

$$\dot{x}(t) = X(x(t), t), \tag{65}$$

for a periodic function $x(t)$.

The harmonic balance method adopts the solution as the Fourier series limited to the order N, expressed in a form

$$x(t) \approx x_N(t) = \frac{a_0}{2} + \sum_{k=1}^{N}(a_k \cos(k\omega_N t) + b_k \sin(k\omega_N t)) , \quad (66)$$

with amplitudes a_k, b_k unknown for all $k \leq N$.

In practical cases, due to typically complicated nonlinear system of equations, the solution is obtained using numerical methods. The calculation process is performed in both time-domain, where the nonlinear effects are evaluated, and in frequency-domain, where the response of the linear part of the circuit is obtained. The nodal quantities (i.e., currents or voltages) from both domains should compensate (or better - balance) each other for each harmonic order when the solution is found. The HB method by the principle allows the use of multiple excitation sources in various forms (as AM, FM, PM modulated signals, etc.); therefore, analyses of intermodulation distortions or even complicated test scenarios [183] are supported. Further details of the HB method and its variants can be found in related works [184, 185].

The HB method is used in this chapter for obtaining currents' spectral response from the equivalent lumped circuit model of the magnetic link. The simulation model of the AFE circuit, which is an integral part of the discussed link, is presented first.

5.2 Nonlinear AFE model

This section introduces the nonlinear AFE model, allowing the prediction of the harmonic spurs using the HB method.

The need for the AFE model

Obtaining the behavioral AFE model, on which base it is possible to derive the frequency spectrum for different working conditions (including mutual coupling, load value, etc.), provides a significant advance compared to recent works. Kronberger [140] identified chip impedance to match it with the antenna for an optimum power transfer. In [21], researchers have evaluated nonlinear impedance in compliance with the ISO14443 standard, primarily addressing achievable bit rates for a given H-field intensity. The dependence of introduced harmonic distortions on the chip excitation level was proposed in work [17]. However, the authors used the identified impedance mainly to recognize the actual operating mode of the chip, including clipping regions. The attempt to correlate AFE impedance with the introduced disturbances was proposed in Author's work [5], analyzing two elementary types of analog front-end circuits. The evaluations presented herein follow the suggested concepts and fill the existing gap in more detailed modeling of nonlinear circuits.

Shared gray-box model

The AFE circuit is an essential part of the magnetic link. It was characterized using multiple approaches as a nonlinear impedance (using equivalent resistance and capacitance parts), a frequency spectrum (both in magnitude and phase), and current-voltage trajectories. Generally speaking, these characteristics were obtained using a common setup, however operating in three different modes. Therefore, it is reasonable to observe how these results correlate with each other using a shared AFE model. This topic is addressed in section 5.2.1 when the gray-box modeling approach is proposed.

One-port black-box model

The supplementary black-box model concept of the AFE circuit is presented in section 5.2.2. It increases the flexibility in analyzing nonlinear devices existing in the magnetic link when only the frequency response measured during a large signal excitation is available. On its basis, the concept of using X-parameters [173, 186] for one-port devices is proposed in section 5.2.3, following the formulation of a harmonic distortion model. It completes the recent technology approach widely used within GHz bands for nonlinear characterization but applied here in LF.

An overview of the above modeling concepts is shown below.

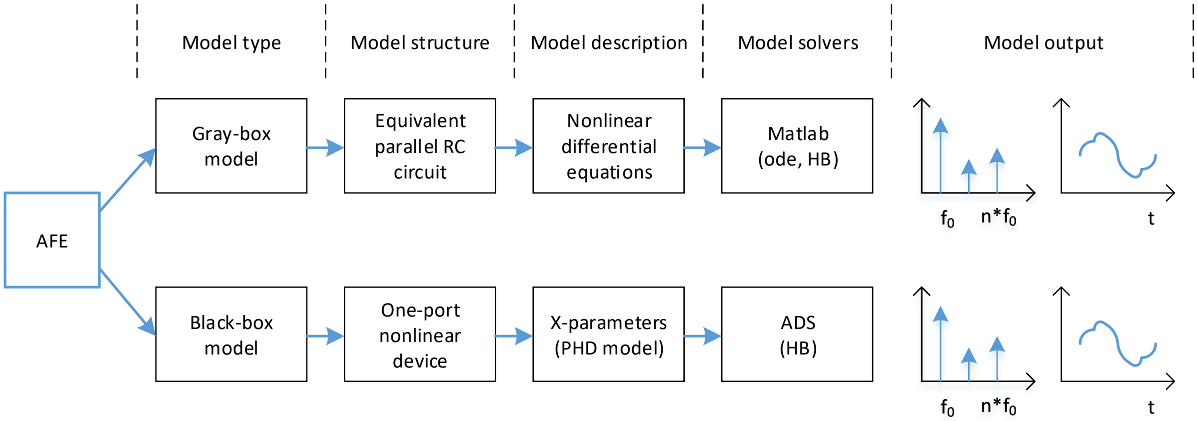

Figure 5.2 AFE modeling concepts

The following sections present the proposed approaches in regards to the AFE circuit.

5.2.1 Gray-box AFE model

In this section, the compact, nonlinear model of the AFE circuit is composed and verified. It is described by the set of nonlinear differential equations obtained from the simplified structure of the measurement setup shown in Figure 5.3. The selected form of the model, among other possible [22], provides a clear and natural representation of the impedance part as R and C components. It is also well fitted to the gray-box modeling approach when only a limited knowledge about the internal structure is given.

The $i(u)$ trajectories and time waveforms $i(t)$ and $u(t)$ are obtained using the proposed AFE model based on $R(U)$, $C(U)$ equivalents' data and paired with those collected in section 4.3.4. In a second step, the frequency response of the AFE circuit is obtained using the HB method. Next, it is compared with the results presented in section 4.3.3, which describe magnitude and phase for different excitation levels. Conclusively, the model's applicability and existing limitations are presented.

Model formulation

The AFE model is derived using a simplified form of a measurement setup operating in Mode 1 (i.e., in which the equivalent circuit's impedance at the carrier frequency is identified). Considering the measurement path in a fully compensated state is shown in Figure 5.3:

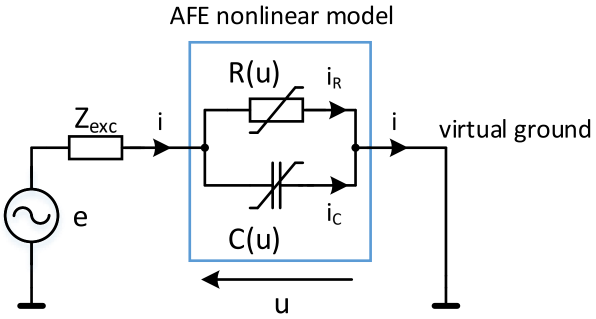

Figure 5.3 The measurement path in a fully compensated state

The voltage source e, together with the source's impedance Z_{exc}, represents the excitation of the AFE circuit (shown as a parallel connection of the voltage-dependent resistance $R(u)$ and capacitance $C(u)$ parts).

The Kirchhoff's voltage law (KVL) of the circuit from Figure 5.3 in a time domain is described as:

$$e(t) - i(t) \cdot Z_{exc} - u(t) = 0, \tag{67}$$

where the net current $i(t)$, assuming $R(u(t))$ >0, calculates from the voltage $u(t)$ over a time-invariant nonlinear part of the circuit as:

$$i(t) = i_C(t) + i_R(t). \tag{68}$$

The orthogonal currents $i_C(t)$ and $i_R(t)$ calculates as:

$$i_C(t) = C\big(u(t)\big) \cdot \frac{du(t)}{dt}, \tag{69}$$

$$i_R(t) = \frac{u(t)}{R\big(u(t)\big)} = G\big(u(t)\big) \cdot u(t)\,. \tag{70}$$

Therefore, putting (67) .. (70) together shows

$$e(t) - \left[u(t) \cdot G\big(u(t)\big) + C\big(u(t)\big) \cdot \frac{du(t)}{dt}\right] \cdot Z_{exc} - u(t) = 0. \tag{71}$$

Then, after re-arranging above, it results with a differential equation of the form:

$$C\big(u(t)\big) \cdot Z_{exc} \cdot \frac{du(t)}{dt} + \left[G\big(u(t)\big) \cdot Z_{exc} + 1\right] \cdot u(t) - e(t) = 0. \tag{72}$$

The excitation $e(t)$ has a form of single tone harmonic signal so, assuming $\varphi_{exc} = 0$:

$$e(t) = U_{exc} sin(\omega t). \tag{73}$$

The model equations (68) .. (70) together with circuit's formula (67) describes the nonlinear behavior of the AFE circuit.

Time-domain simulations

Based on the AFE model defined above, the current-voltage trajectories and time waveforms were obtained using a nonlinear solver *ode45* from Matlab. Next, they were referenced to the low, high, and overdrive excitation conditions and, finally, shown in figures below.

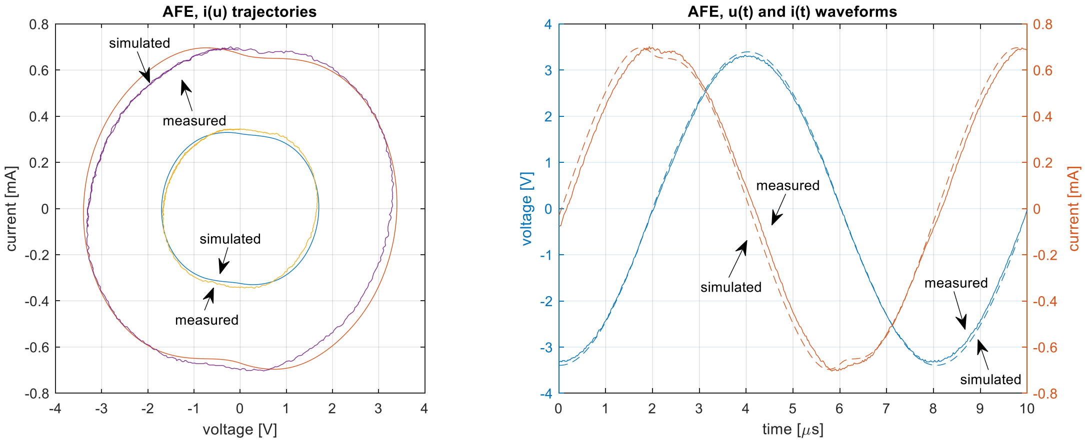

Figure 5.4 Simulated and measured $i(u)$, $u(t)$ and $i(t)$ waveforms, low excitation

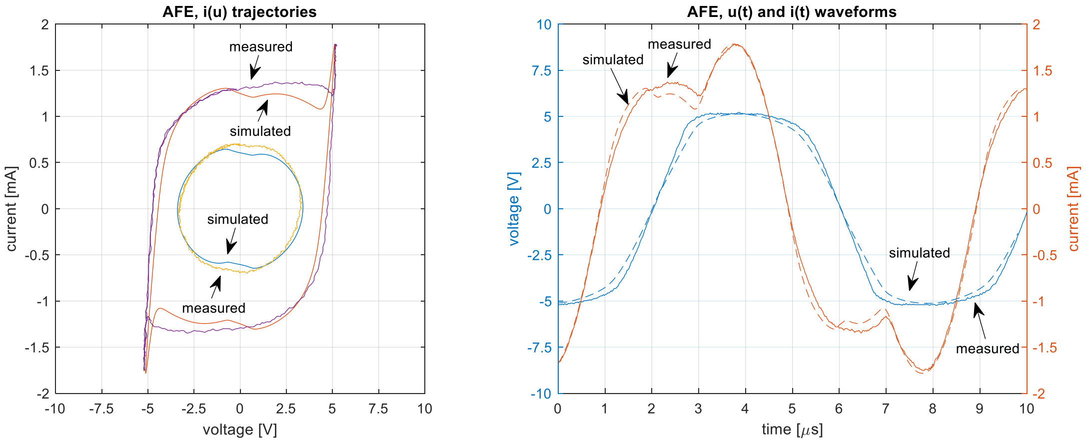

Figure 5.5 Simulated and measured $i(u)$, $u(t)$ and $i(t)$ waveforms, high excitation

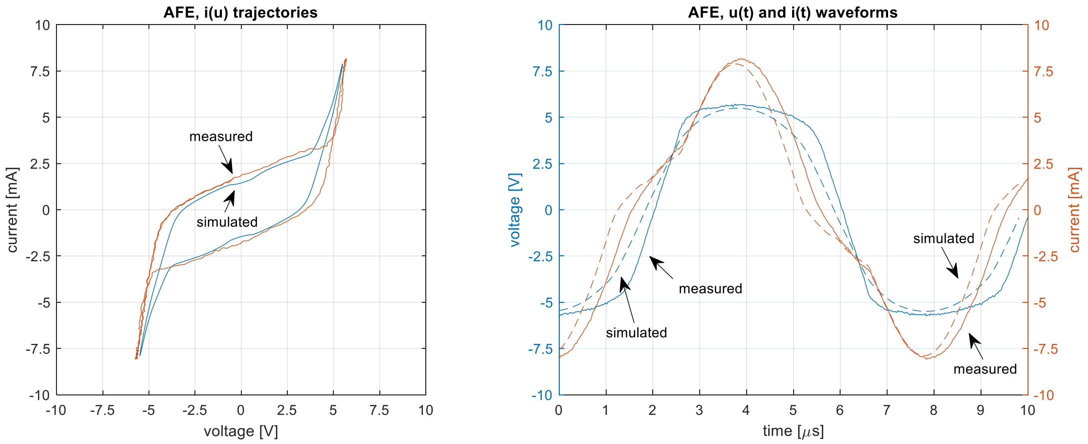

Figure 5.6 Simulated and measured $i(u)$, $u(t)$ and $i(t)$ waveforms, overdrive

The reproduction quality of $i(u)$ trajectories from the $R(U)$ and $C(U)$ equivalents are satisfactory, the same as of time waveforms. The proposed model correctly describes AFE's operation in a time domain within each of the considered excitation ranges, including accurate representation of the peak values (i.e. with the magnitude error typically less than 5 %). The existing imperfections can be attributed to the simple form of the model, consisting only of the two components. For improved quality (if required), the model can be extended to the lagged form [187]; however, more sophisticated measurements are necessary in this case.

Frequency domain model consideration

The AFE circuit can also be considered in the frequency domain using the proposed nonlinear impedance model. The measurement circuit shows high similarity to the one presented above and analyzed in the time domain. Notwithstanding, it is described below for clarity.

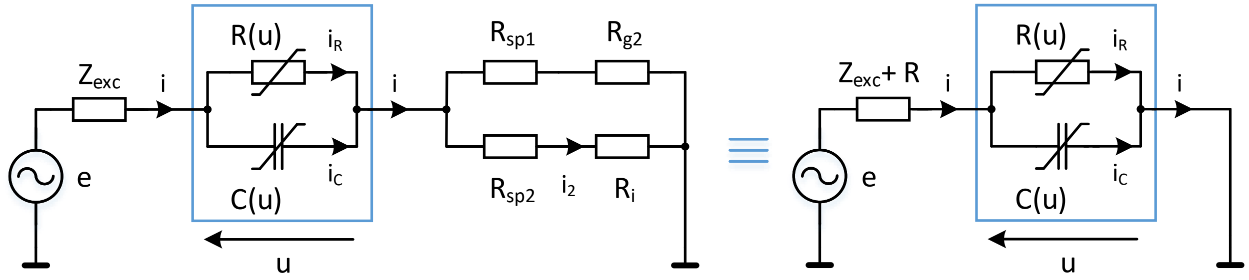

Figure 5.7 The measurement setup operating in Mode 2

In section 4.2.3 it was assumed (see also Figure 4.5), that the power splitter resistances, compensating generator's internal resistance, and analyzer input are equivalent to the system resistance R, thus $R_{sp1} = R_{sp2} = R_{g2} = R_i = R = 50\,\Omega$, respectively. Accordingly, the measurement path of the setup operating in Mode 2 (i.e., allowing spur's phase and magnitude identification) is simplified to the form presented in Figure 5.7 right, where the above components reduce to a single part.

The differential equation describing the above circuit is therefore similar to (72):

$$C\big(u(t)\big)\cdot(Z_{exc}+R)\cdot\frac{du(t)}{dt}+\big[G\big(u(t)\big)\cdot(Z_{exc}+R)+1\big]\cdot u(t)-e(t)=0. \qquad (74)$$

The frequency spectrum of AFE's current $i(t)$ is calculated using the HB method implemented in Matlab as *NLvib* library [188].

Simulated spur magnitudes

The simulation results presented below were collected for the same excitation range as during the measurements (i.e., up to 10 mA), which were summarized in section 4.3.3.

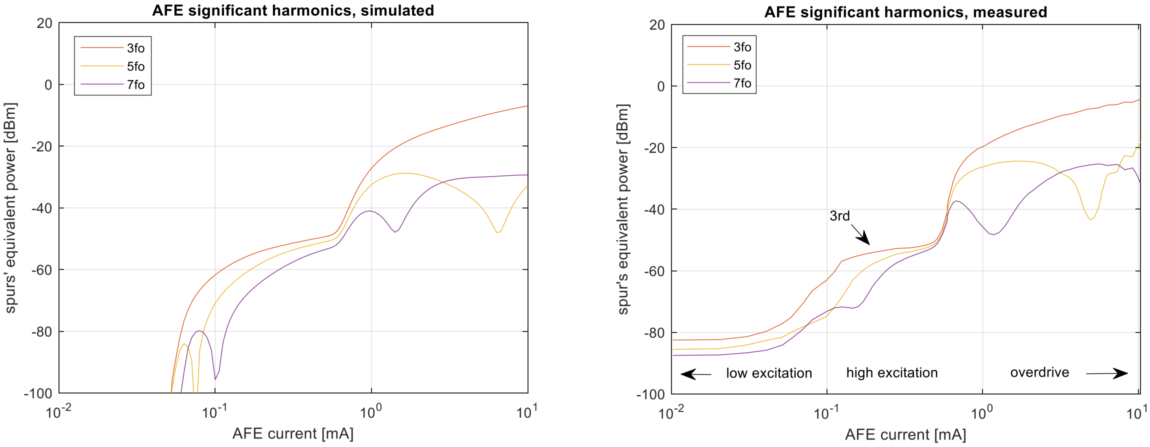

Figure 5.8 Simulated (left) and measured (right) power of the significant harmonics of the AFE circuit

The first observation addresses the low excitation range, in which the simulated magnitudes are significantly smaller than measured ones. It has a direct explanation because the proposed model does not include AFE's equivalent noise sources. The limitations of used instrumentation (as a noise floor of analyzer and setup) are also neglected during a simulation. It is typical for nonlinear circuits that reducing excitation level leads to lower distortions, while the actual measurements tend to reach the system's noise floor. Therefore, it is supposed that the simulation correctly describes noiseless AFE, while the setup capabilities in this range dominate the measured spectrum.

The next remark reflecting both measured and simulated data is that 3^{rd} harmonic spur dominates each operating region. It follows the symmetry of the tested AFE circuit, in which even harmonics are always significantly smaller (typically by 10 .. 45 dB) compared to the odd ones. Without loss of model's functionality, the even harmonics can be neglected in a considered case.

The following note points to an acceptable representation of the dominant (i.e., 3^{rd}) spur magnitude, with a maximum error of - 6 dB observed around 1 mA. This error follows the assumed modeling approach, in which spectrum data are restored from the measured impedance. Because of the uncertainty propagation in complex value numbers (analyzed in the following), the magnitude accuracy is affected by the initial identification process. However, it is still possible to apply a correction to the simulation results using measured spectrum data as a reference.

Conclusively, the behaviors of simulated and measured odd harmonics' magnitudes are very similar, except for some small regions during an overdrive. However, in this state, the dominant third spur accurately determines the remaining quantities and can be taken as the most significant model's parameter.

Simulated spur phase

Phase information obtained from the gray-box simulation and referenced to the measurement is shown in Figure 5.9. The representation of the carrier component is correct as reproduced directly from the measured impedance data. Phases of the dominant 3rd and 5th spurs also have the proper behavior, although they were calculated indirectly from the model. This observation immediately points to the suitable form of the relatively simple yet fully functional gray-box representation of the AFE circuit.

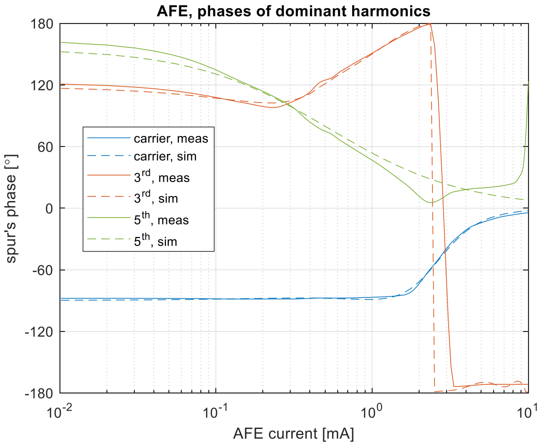

Figure 5.9 Simulated and measured phases of carrier and dominant 3rd and 5th spur

Presented above evaluations implementing gray-box model confirm consistency with the measurement results. Despite limited knowledge of the internal structure of the AFE circuit, represented by the equivalent nonlinear capacitance and resistance parts, the achieved model quality is fully satisfying.

The following section considers the case where the information of the internal circuit structure is not available.

5.2.2 Black-box AFE model

The black-box modeling approach assumes the unknown (i.e., IP-protected, hidden, etc.) structure of the considered AFE circuit. By the principle, such behavioral modeling provides the possibility of identifying a broad class of unknown circuits [27, 173] by observing only its external signal relationships [189, 190].

AFE as the one-port nonlinear device

The analyzed AFE circuit can be regarded as the one-port nonlinear device operating under a large sinusoidal excitation. In this case, the incident a and reflected b waves [168, 189] can be considered using voltage U and current I present on the AFE terminals as:

$$a := \frac{U + Z_{exc} I}{2\sqrt{Re(Z_{exc})}} = \frac{E}{2\sqrt{Re(Z_{exc})}}, \tag{75}$$

and

$$b := \frac{U - Z_{exc}^{*} I}{2\sqrt{Re(Z_{exc})}} = \frac{E - 2Z_{exc}^{*} I}{2\sqrt{Re(Z_{exc})}}. \tag{76}$$

Due to existing device nonlinearities, the response of the circuit is a periodic signal with harmonic spurs, as presented in Figure 5.10.

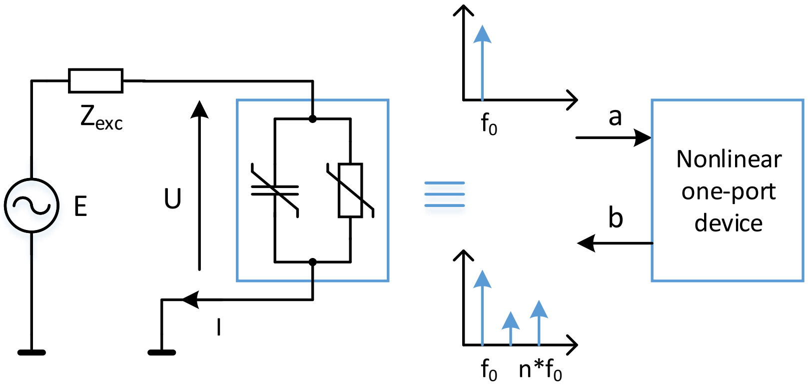

Figure 5.10 The AFE circuit considered as the one-port device

The above circuit's behavior considered in a more general case assumes that device operation can be defined by the nonlinear describing function F, linking a and b waves as:

$$b = F(a)\,. \tag{77}$$

Obtaining the analytical form of the $F(\cdot)$ in most practical cases is either difficult or impossible [22, 172, 181]. Therefore, certain simplifications are typically applied using different modeling approaches [22, 174, 189], in which the polyharmonic distortion (PHD) method is usually preferred [28, 173].

The polyharmonic distortion (PHD) model concept

The PHD model assumes that describing function can be linearized around the large-signal operating point (LSOP) [173, 189], defined by the response b_0 to the large excitation a_0. Therefore, the complete circuit's response b includes the response Δb to the small-signal excitation Δa (superimposed on a_0), using the below formulation:

$$b = F(a_0 + \Delta a) \xrightarrow{PHD} b \cong b_0 + \Delta b = b_0 + \left(\frac{\partial b}{\partial a}\right)_{LSOP} \Delta a, \tag{78}$$

where the set of partial derivatives $\left(\frac{\partial b}{\partial a}\right)$ is derived under LSOP.

There is an extension of the PHD model considering a second-order linearization, called quadratic PHD (QPHD) [169, 191]. In this case, the spectral linearization principle introduced by equation (78) also includes higher terms, resulting in greater accuracy by the cost of increased measurement setup and method complexity.

The general form of the PHD model, as presented by equation (78), allows the estimation of the circuit's response using various excitation sources. It could be a single-tone (i.e., the one studied in this work, thus $\Delta a = 0$) or superimposed with a narrow-band sideband signal (i.e., $\Delta a \neq 0$). Consideration of Δa excitation as the harmonics of a_0 allows formulation of the X-parameters [166, 186] using the proposed PHD model structure. This approach for a one-port device is presented below, following an overview of the X-parameters concept.

5.2.3 PHD model as X-parameters of one-port device in LF

A typical way of using X-parameters [166, 192, 193] assumes the excitation of the multiport nonlinear component (i.e., amplifier, BJT, mixer, etc.) by the large, dominant signal, together with its small harmonic spurs. Because of the PHD linearization concept around the operating point, predicting the selective harmonic interaction from each input spurs to the output spectrum on a given port is possible.

X-parameters overview

Considering k-th output harmonic on p-th output port, according to the X-parameter notation [186], gives:

$$\begin{aligned} b_{p,k} = X^{F}_{p,k}(|a_{1,1}|)P^{k} + \sum_{q=1}^{q=Q}\sum_{l=1}^{l=L} X^{S}_{p,k;q,l}(|a_{1,1}|)\, a_{q,l}P^{k-l} \\ + \sum_{q=1}^{q=Q}\sum_{l=1}^{l=L} X^{T}_{p,k;q,l}\,(|a_{1,1}|)a^{*}_{q,l}P^{k+l}\,, \end{aligned} \tag{79}$$

$$(q,l) \neq (1,1), \tag{80}$$

where q and p are the input and output port number, respectively, l and k are the input and output harmonics, respectively, Q is a number of input ports, and L is a number of considered input harmonics. The $X^{F}_{p,k}$ is a response to a sole, large-signal excitation $a_{1,1}$, while $X^{S}_{p,k;q,l}$ and $X^{T}_{p,k;q,l}$ defines a harmonic mapping of incident wave and its conjugate, respectively. The parameter P creates the reference plane for the harmonics and is calculated as:

$$P = \frac{a_{1,1}}{|a_{1,1}|} = e^{jArg(a_{1,1})}. \tag{81}$$

Its meaning reflects the reference delay of the input signal $a_{1,1}$, which is equivalent to the linear phase shift (i.e., proportional to the frequency) in a frequency domain (thus power factors in formula (79)).

Similar to the PHD model, the X-parameters can be extended to the higher terms X^U, X^V, and X^W (indexes omitted for clarity) [169], but this case is not considered here. For a high variation of a connected load, the X-parameters can also be analyzed regarding matching conditions as in [193, 194].

The identification procedure of $b_{p,k}$ simplifies for the one-port device, which is presented below for the two practical cases.

Single-tone excitation case

For the case of the one-port device (i.e., Q = 1) driven by the single-tone signal (i.e., L = 1), the formula (79) reduces to:

$$b_{1,k} = X^F_{1,k}\left(\left|a_{1,1}\right|\right)P^k. \tag{82}$$

The complete response b_1 is thus equal to the sum of k large-signal responses, as:

$$b_1 = \sum_{k=1}^{k=K} b_{1,k}\,, \tag{83}$$

where K is a number of considered output harmonics.

Multi-tone excitation case

A consideration of $L > 1$ input harmonics around a large excitation $a_{1,1}$ allows distinguishing of their selective contributions to each k-th harmonic spur $b_{1,k}$. Therefore, using a formula (79), k-th output spur is now the sum of the response to the large excitation, supplemented by the impacts from up to L small harmonics, as:

$$b_{1,k} = X^F_{1,k}\left(\left|a_{1,1}\right|\right)P^k + \sum_{l=2}^{l=L} X^S_{1,k;1,l}\left(\left|a_{1,1}\right|\right)\, a_{1,l}P^{k-l} + \sum_{l=2}^{l=L} X^T_{1,k;1,l}\left(\left|a_{1,1}\right|\right)\, a^*_{1,l}P^{k+l}. \tag{84}$$

The above formula estimates a contribution from l-th input harmonic to k-th output spur as $X^S_{1,k;1,l}$ and $X^T_{1,k;1,l}$ coefficients. This process is repeated (L - 1) times and results with single $b_{1,k}$ response. The complete response b_1, therefore, requires a similar repetition for each considered k-th spur as in (83).

Offset-phase estimation method

The required steps to estimate complex $X^S_{1,k;1,l}$ and $X^T_{1,k;1,l}$ coefficients, assuming their mapping around LSOP, are as follows. First, the large-signal contribution $X^F_{1,k}\left(\left|a_{1,1}\right|\right)$ to considered k-th harmonic spur is measured, using pure $a_{1,1}$ stimulus (DC is not present here). Next, the small signal $u_{1,l}$ (typically 2 .. 5 % of $\left|a_{1,1}\right|$) with known phase shift is superimposed with $a_{1,1}$, on which base the temporary response Y^S_l is obtained. The related small signal $u_{2,l}$ yet shifted by $\frac{\pi}{2}$

(comparing to $u_{1,l}$) is supplied in the following, resulting in the response Y_l^T. Finally, the following equation is created [172]:

$$\begin{bmatrix} Y_l^S - X_{1,k}^F \\ Y_l^T - X_{1,k}^F \end{bmatrix} = \begin{bmatrix} u_{1,l} & u_{1,l}^* \\ u_{2,l}^* & u_{2,l} \end{bmatrix} \begin{bmatrix} X_{1,k;1,l}^S \\ X_{1,k;1,l}^T \end{bmatrix}, \tag{85}$$

where the Y_l^S and Y_l^T responses are biased due to LSOP.

Representative ADS examples

The following examples implement the X-parameters within the ADS environment [195], utilizing the aforementioned method for the AFE circuit driven by the monochromatic signal.

Example 1 – mapping spurs' data

The first step to get the circuit's response is to determine the incident wave for a given excitation level, using the equation (75). Next, utilizing spurs' magnitude and phase data (shown in Figure 4.16 and Figure 4.17), the reflected wave is calculated employing formulae (76) and (82). Such waves' data are identified up to 24 dB @ 50 Ω and include considered 11 harmonics. The X-parameters are constructed implementing GMDIF format [195] as *x_afe_gen.xnp* file. This file is then used as an input to the X1P component, which primary function is to handle waves' data from the measurement as a one-port large-signal nonlinear device.

The response of the AFE circuit during exampled overdrive condition implementing X-parameters and applying the HB method is presented in Figure 5.11. The V_AFE signal is assumed as a voltage difference between A and B nodes.

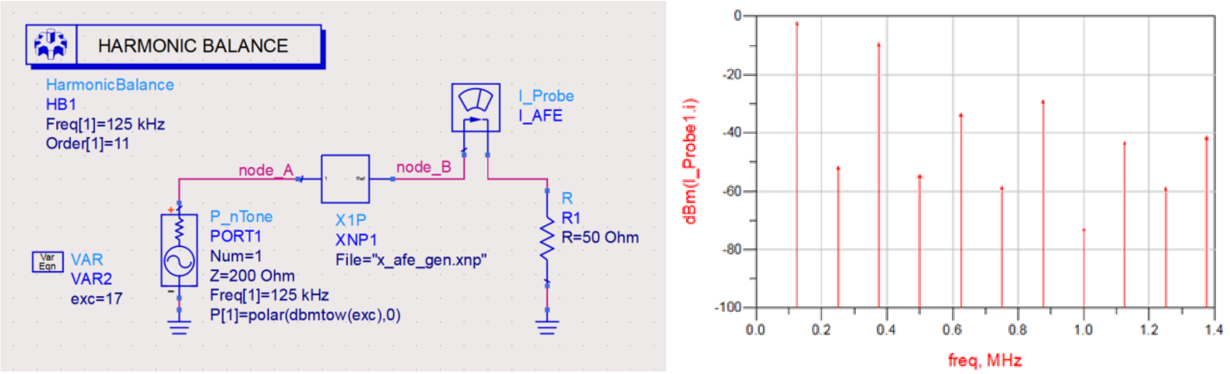

Figure 5.11 The simulation circuit used by ADS tool (left) and spur magnitude obtained using X-parameters (right)

The proposed approach allows accurate representation of circuit nonlinearities based on the measurement data by creating their compact representation as X-parameters. In this case, the magnitude and phase for each harmonic spur within the model's response are determined by the measurement, which provides a consistent representation of the actual circuit.

Example 2 – generation from impedance model

The X-parameters can also be generated using impedance equivalents instead of measured spur data. For this case, the dedicated simulation circuit shown in Figure 5.13 is composed.

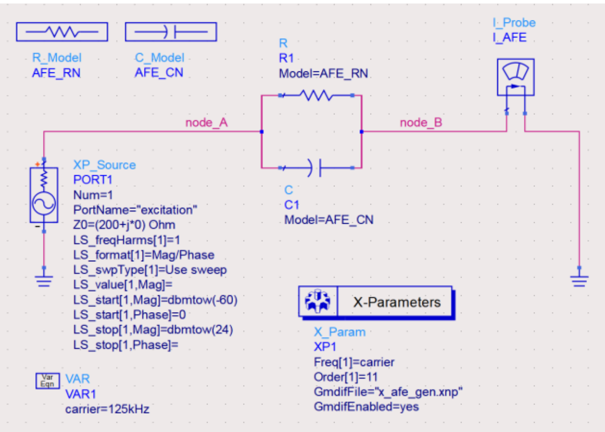

R_Model
AFE_RN

C_Model
AFE_CN

R
R1
Model=AFE_RN

I_Probe
I_AFE

XP_Source
PORT1
Num=1
PortName="excitation"
Z0=(200+j*0) Ohm
LS_freqHarms[1]=1
LS_format[1]=Mag/Phase
LS_swpType[1]=Use sweep
LS_value[1,Mag]=
LS_start[1,Mag]=dbmtow(-60)
LS_start[1,Phase]=0
LS_stop[1,Mag]=dbmtow(24)
LS_stop[1,Phase]=

C
C1
Model=AFE_CN

X_Param
XP1
Freq[1]=carrier
Order[1]=11
GmdifFile="x_afe_gen.xnp"
GmdifEnabled=yes

VAR
VAR1
carrier=125kHz

Figure 5.12 The AFE simulation circuit used to generate X-parameters

The strongly nonlinear characteristics of $R(U)$ and $C(U)$ were adopted in ADS tool as R_MODEL and C_MODEL components, implementing the polynomial representation, in the following manner:

$$R(V) = \frac{R}{(1+r_1V+r_2V^2+\cdots+r_mV^m)} \equiv \frac{R}{G(V)}, \tag{86}$$

where r_1, $r_2, \ldots, r_m$ are the coefficients of the m-order polynomial approximation of $R(U)$, and V is the actual voltage provided to the R_MODEL component.

Similarly, the voltage dependence of capacitance within C_MODEL is calculated as:

$$C(V) = C(1 + c_1V + c_2V^2 + \cdots + c_nV^n), \tag{87}$$

where c_1, $c_2, \ldots, c_n$ are the coefficients of the n-order polynomial approximation of $C(U)$, and V is similarly component's voltage.

The approximation orders are limited in practice to low numbers ($m = 5$, $n = 7$) because increasing their values led to the simulation convergence issues (due to poor scaling of polynomial coefficients) and raised phase error.

Once the X-parameters are generated as *x_afe_gen.xnp* file, they can be used for the determination of excited harmonics using the circuit presented in Figure 5.11. It is also possible to extract the time waveforms and current-voltage trajectory, similarly to the actual measurement. The example of such, derived under a high excitation state, is shown in Figure 5.13.

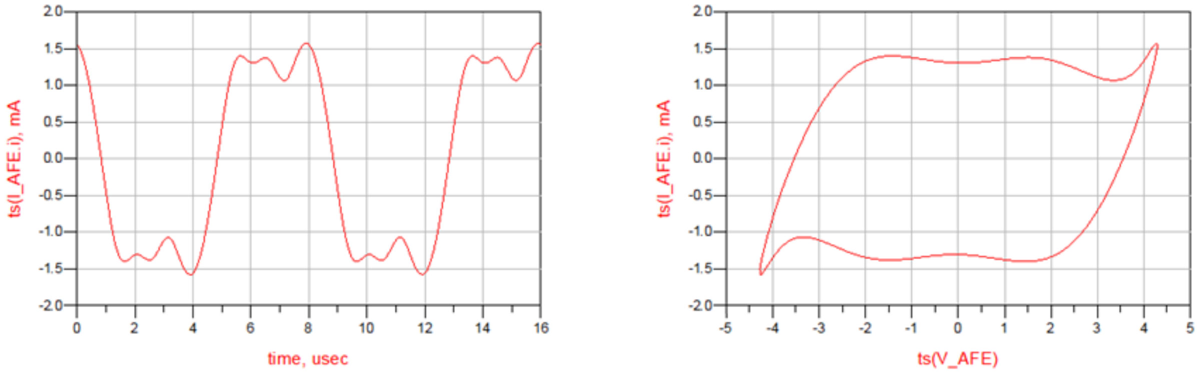

Figure 5.13 Current waveform (left) and current-voltage trajectory (right) obtained from generated X-parameters

The complex impedance model employing parameters generated from a polynomial representation of R and C parts provides less accuracy than the spur's mapping option. There are few reasons for that. Firstly, the capacitance and resistance equivalents derived as a separate measurement process inadvertently propagate their inaccuracy through the model to the output spectrum. Section 5.2.5 addresses this topic in more detail. Next, the curve fitting step supported by the R_MODEL and C_MODEL components significantly simplifies the actual $R(U)$ and $C(U)$ characteristics because of a reduced order of approximation. And lastly, the elementary (yet still functional) model form consisting of the complex impedance introduces additional simplification, which is observed in the output response. Notwithstanding, comparing the corresponding data from Figure 5.13 and Figure 4.19, the discrepancy is less than 10 .. 20 %, which is still acceptable for most practical cases .

5.2.4 AFE models summary

In this section, the conclusions about AFE models are summarized. The review starts with comparing the magnitude and phase results, followed by presenting existing models' limitations. The supplementing evaluation of the gray-box model's uncertainty propagation is shown as a separate section next.

Models comparison

The responses collected from AFE models as spurs' magnitude and phase are compared here.

Figure 5.14 summarizes AFE responses from the gray-box and black-box models, obtained under excitation U_{exc} = 7 V. Both approaches to X-parameters are presented, utilizing spectrum mapping and generation from nonlinear R, C equivalent models.

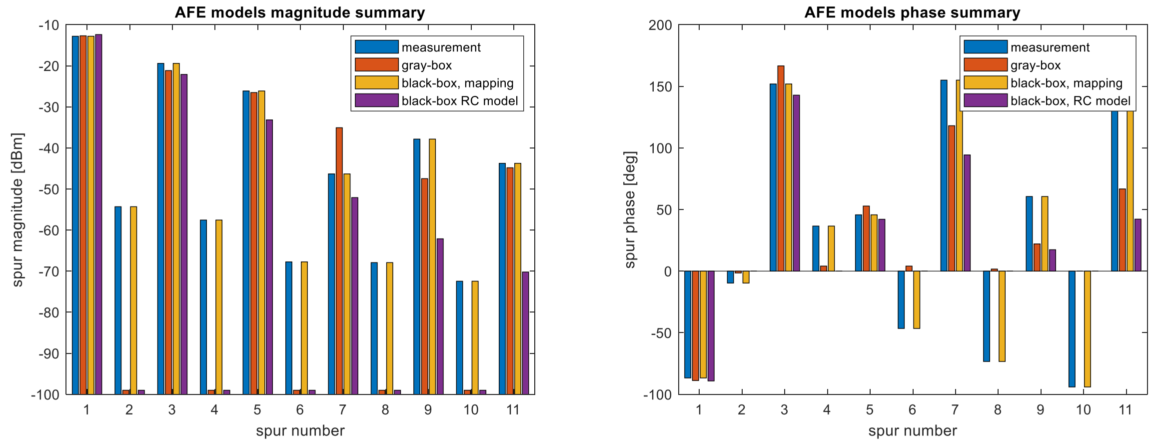

Figure 5.14 Summary of spurs' magnitude (left) and phase (right)

The accurate representation of the actual AFE behavior provides the black-box model, in which a direct spectrum mapping is implemented. Using it, both even and odd harmonics are correctly reproduced, similarly in magnitude and phase. This pure behavioral model, wholly based on the measurement data, supports a large-signal operation in every state where it was prior characterized. It is *de facto* a table-based model, adapted into the simulation environment as a one-port device.

The gray-box model and X-parameters model based on R , C equivalents satisfy proper representation of the dominant harmonics. They are recognized as odd ones; therefore, the proposed methods are also well suited here. Both models assume symmetrical R, C relations to the negative and positive voltage along with AFE pins. In practice, they are represented as absolute value functions. The odd-like behavior is expected for the symmetrical rectifiers, of which the analyzed AFE circuit is an exact example.

Analyzing AFE's frequency spectrum suggests the conclusion that 3rd harmonic spur predominates the circuit's response. That statement stays in line with a similar observation provided in a recent work of Vera [196] and his associated paper [197], considering the RFID structures. Moreover, this direction seems attractive from the modeling standpoint (due to lower demands for higher-order harmonics) and the identification process (fewer spurs to measure). Notwithstanding, such a decision always needs additional evaluation (like EMC compliance review) and will follow in the next chapter.

In conclusion, selecting the most appropriate model structure depends primarily on the circuit operation, which is recognized by quickly identifying the exciting spectrum content. Assuming dominant spur as a 3rd harmonic only, all the above-presented models are well applicable.

Model applicability

The proposed AFE models have certain features, which are presented here.

Considering the large-signal operation of the AFE circuit allows neglecting the noise sources, which are dominant for the low levels only. This approach justifies omitting them without the loss of the method's universality.

The DC operating point dependency is also skipped, as the considered circuit's principle reflects only the AC excitation. The voltage supplying the AFE circuit comes from the secondary coil, which is assumed as a DC-free source, which linearity was additionally verified in section 4.3.2.

The temperature dependency of AFE is omitted entirely. The impedance identification, time-domain behavior, and frequency spectra are all collected under controlled laboratory conditions. The same applies to the EMC chamber measurements, where the model's predicted currents were verified. Notwithstanding, the temperature dependency can be added when needed in the gray-box model and the X-parameters [198].

Completing the AFE evaluations, the uncertainty analysis of the output spur is presented below.

5.2.5 Uncertainty propagation in complex-valued variables

In this section, an uncertainty propagation topic is considered. It evaluates the output variance in regards to the complex input data. The following analysis takes input variables as resistance and capacitance parts of the AFE circuit employing the gray-box model. A similar approach can utilize X-parameters from the black-box model. However, a recent work of Stant [199] presented it already in a somewhat similar context and, therefore, it can be used for such reference.

Uncertainty propagation method

The covariance Σ^x matrix of the complex input, assumed as bivariate $\boldsymbol{x} = [\boldsymbol{R}, \boldsymbol{C}]$, is constructed from variances σ_R and σ_C, together with covariances $\sigma_{R,C}$ and $\sigma_{C,R}$, determined from resistance *R* and capacitance *C* statistics, respectively. Therefore, it can be presented as:

$$\Sigma^x = \begin{bmatrix} \sigma_R^2 & \sigma_{R,C} \\ \sigma_{C,R} & \sigma_C^2 \end{bmatrix}. \tag{88}$$

The output $\boldsymbol{S}$, consisting of spur's magnitude $\boldsymbol{S}_m$ and phase $\boldsymbol{S}_p$, is defined accordingly to (77), thus:

$$\boldsymbol{S} = [\boldsymbol{S}_m, \boldsymbol{S}_p] = F(\boldsymbol{x}) = [|F(\boldsymbol{x})|, \angle F(\boldsymbol{x})], \tag{89}$$

where F is a complex function, mapping the input $\boldsymbol{x}$ to $\boldsymbol{S}_m$ and $\boldsymbol{S}_p$, through the modulus $|F(\cdot)|$ and phase $\angle F(\cdot)$ functions, respectively.

With the assumption of a possible local linear approximation of *F*, the resulting uncertainty of output $\boldsymbol{S}$ is, following [25], equal to:

$$\Sigma^S = \boldsymbol{J} \Sigma^x \boldsymbol{J}^T, \tag{90}$$

where $\boldsymbol{J}$ is the Jacobian matrix given by:

$$\boldsymbol{J} = \begin{bmatrix} \frac{\partial |F|}{\partial R} & \frac{\partial |F|}{\partial C} \\ \frac{\partial \angle F}{\partial R} & \frac{\partial \angle F}{\partial C} \end{bmatrix}. \tag{91}$$

The partial derivatives are obtained at a given excitation level, for which output $\boldsymbol{S}$ (i.e., harmonic spur) is determined. These were derived in [25] as:

$$\frac{\partial |F|}{\partial \theta} = \frac{1}{|F|} Re\left(F^* \frac{\partial F}{\partial \theta}\right), \tag{92}$$

$$\frac{\partial \angle F}{\partial \theta} = \frac{1}{|F|^2} Im\left(F^* \frac{\partial F}{\partial \theta}\right), \tag{93}$$

assuming $\theta = \{R, C\}$, respectively. These forms were used in the following example to calculate the uncertainty of the spur's magnitude and phase.

Uncertainty propagation example

The uncertainty estimation based on the measurements and the subsequent simulations were completed using the AFE circuit and its gray-box model.

Uncertainty estimation

A large number (actually N = 1640) of impedance measurements was completed to obtain the basic statistics of resistance and capacitance parts, according to (88). It was assumed that R and C components are not independent variables; therefore, their covariance can be estimated from the common measurement. Simultaneously, maintaining the same excitation level of the AFE circuit, the magnitude and phase of the exciting 3rd harmonic spur were recorded. This procedure allowed obtaining the complex input and output variables related through the nonlinear mapping $F(\cdot)$.

The following statistics, collected under excitation U_{exc} = 5.25 V, estimate the covariance matrix Σ_{meas}^{x} as:

$$\Sigma_{meas}^{x} = \begin{bmatrix} (0.21)^2 & 0.013 \\ 0.013 & (0.30)^2 \end{bmatrix}. \tag{94}$$

Accordingly, the uncertainty of the output variable (i.e., current magnitude and phase of the 3rd spur) were obtained from the measurements as:

$$\Sigma_{meas}^{S} = \begin{bmatrix} (0.18)^2 & -0.04 \\ -0.04 & (0.42)^2 \end{bmatrix}. \tag{95}$$

Obtained representations of bivariate input and output uncertainties are shown in Figure 5.15. There is visible granularity following the compensating generator's voltage and phase resolutions (0.01 V and 0.1°, respectively) and overall system drift during a long measurement cycle (actually 14 hours).

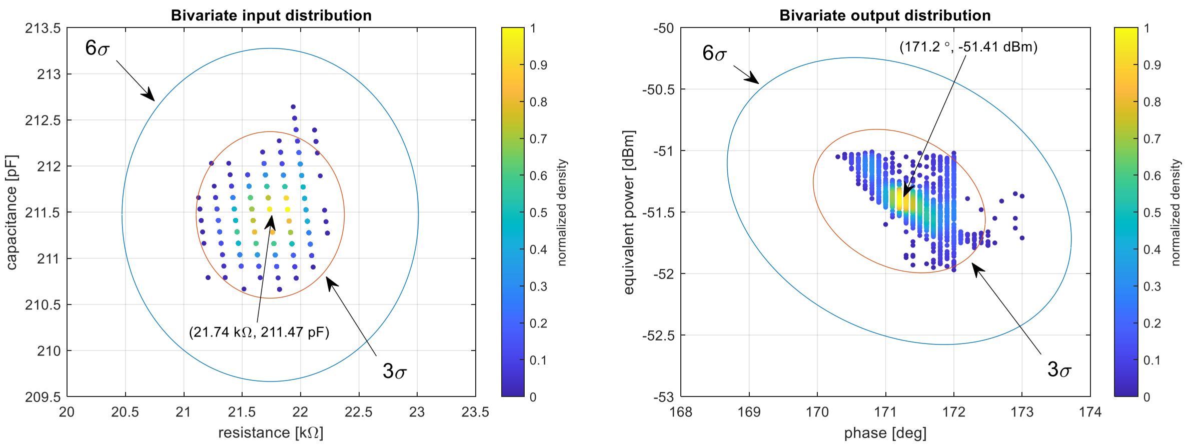

Figure 5.15 Measured bivariate input (left) and output (right) distributions with marked confidence areas

Uncertainty simulations

The Monte Carlo simulation (16400 runs) was used in the next step to predict spur's complex uncertainty from the AFE model. Compared to measurements, the increased number of runs allowed more accurate determination of the input and output values with the highest occurrence, presented as a normalized density. The excitation source was characterized for simulation needs as $\mu_{exc} = 5.25$ V and $\sigma_{exc} = 0.001$ V, reflecting the generator's short-term variance data. The remaining uncertainties (i.e., system tolerances and drifts) were neglected for simplicity. The nominal values of the resistance and capacitance parts were indicated from the nonlinear voltage dependency curves as 22.2 kΩ and 212.7 pF, respectively. The covariance matrix of such a complex input was assumed as equal to (94).

The calculation of Jacobian matrix employed the method proposed above and resulted in:

$$\boldsymbol{J} = \begin{bmatrix} 0.29 & 0.39 \\ -1.72 & 0.0 \end{bmatrix}. \tag{96}$$

Therefore, the uncertainty of considered 3rd harmonic spur, using the gray-box AFE model, was estimated as:

$$\Sigma_{sim}^{S} = \begin{bmatrix} (0.14)^2 & -0.033 \\ -0.033 & (0.37)^2 \end{bmatrix}, \tag{97}$$

and it appears to be very similar to (95) (i.e., the one obtained from the measurement).

Figure 5.16 shows simulated distributions for a single excitation case. A minor shift exists between the mean values of spur's magnitude and phase (0.9 dBm and - 2.0º) when comparing them to measurements. Such differences can be neglected in most cases, especially taking into account simulations advantages (i.e., shorter evaluation time, flexibility in changing values of parameters and external conditions, etc.) and understanding their limitations.

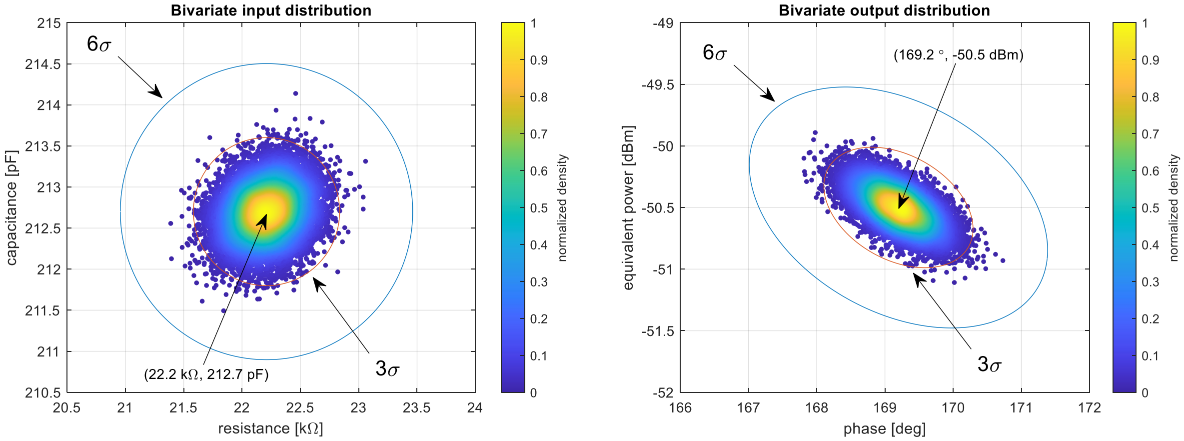

Figure 5.16 Simulated bivariate input (left) and output (right) distributions with marked confidence areas

Summarizing this subsection, the compact gray-box model supports a short evaluation time (less than 5 minutes for the above case) and the accurate representation of exciting harmonic spurs. This model will serve in the determining of a planar disturbance map, considered in the next section.

5.3 Lumped model of the magnetic link

In this section, a lumped model of the magnetic link is proposed. It contains components presented in previous chapters: the primary and secondary coil, the transmitter and the AFE circuits. It is supplemented by the parameters describing magnetic coupling, thus the mutual inductance and a coupling factor. The primary and secondary coils' currents of the linked circuits are determined using the proposed lumped model. They are supposed to provide knowledge of the radiated disturbance level, which is considered in the next chapter.

5.3.1 Model structure

The general model of the magnetic link extended by the coils' models is shown in Figure 5.17. The assumed structure allows modeling in a wide frequency range and identification of the spurs up to the self-resonance frequency of the coils. The circuit is supplemented by the capacitor C_r, enabling initial tuning to the resonance frequency f_0.

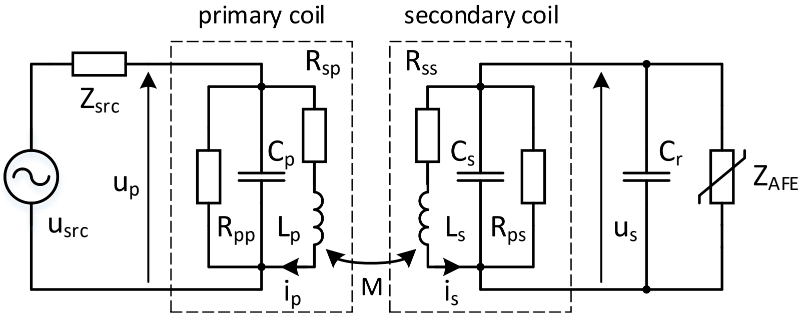

Figure 5.17 Detailed model of the magnetic link

The detailed circuit formulae, shown in Appendix 8.6, describe the operation of the magnetic link. On this basis, the circuit variables (i.e., i_p, i_s, u_s) are determined using numerical methods described in section 5.1.2. The source impedance Z_{src} is considered equal to the system resistance R in a final formula (176). In some cases, it can be supplemented by a series resonance capacitor, as explained in the following.

Applying HB method efficiently

To take advantage of the harmonic balance method in a shorter evaluation time (compared to integration-based methods like *ode* solver), the circuit from Figure 5.17 is split into linear and nonlinear sections. Only the AFE circuit is considered nonlinear, which was confirmed in the previous chapter.

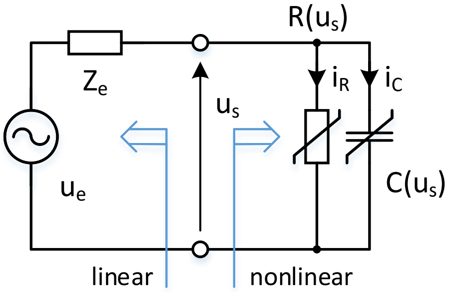

Figure 5.18 Circuit split into linear and nonlinear sections

The circuit's decomposition supports accurate and fast localization of the cases with an increased disturbance level. Therefore, the voltage u_s representing a low excitation range (defined in section 4.3.4) is assumed as the analysis threshold, and such range is excluded from the consideration. It was observed that u_s voltages smaller than ± 3 V on AFE's pins lead only to the negligible harmonic distortions.

Equivalent linear section

The group of linear components can be combined as the equivalent Thevenin or Norton source following the circuit theory. Selecting the first form is more usable in the considered cases due to voltage output of the signal generator used for comparative verifications. The equivalent voltage u_e and impedance Z_e of the Thevenin source are indicated in a usual way [200]. As a part of this transformation process, the impedance present on the primary side of the coil transformer (i.e., consisting of inductances L_p, L_s, and M) is reflected on the secondary side as:

$$\frac{\omega^2 M^2}{j\omega L_p + Z_p}, \tag{98}$$

where the primary side's impedance Z_p is defined from Figure 5.17 as:

$$Z_p \equiv \left(Z_{src} \,||\, R_{pp} \,||\, C_p\right) + R_{sp}\,. \tag{99}$$

The equivalent source impedance Z_e can be pre-calculated at the considered frequencies (i.e., carrier and spurs) and given mutual coupling of the coils. This approach additionally shortens the evaluation's time, which scope is presented in the following subsection.

5.3.2 Model evaluations

The compact model of the magnetically linked nonlinear circuits introduces a possibility to evaluate a broad spectrum of associated phenomena. The first and the natural one is an option to indicate the conditions allowing the achievement of a high figure-of-merit of the complete circuit. These can be identified as selecting the components' values satisfying the high efficiency of the power transfer, as in [201]. The next is analyzing the existing topologies, for which the critical factors (like mutual coupling state) can be obtained by simulations using the equivalent model [22]. Eventually, it is an option of localization of a mutual resonance dip [5], supporting the determination of coils' positions with the most robust coupling.

In the author's work [5] the two-dimensional distortion map was first proposed. Using this approach, it was possible to locate the clipping regions and the areas of the dominance of odd and even harmonics. These results, obtained for the elementary rectifier types (i.e., based on diodes and MOSFET structures), provide significant support in spurs predicting from the linked nonlinear circuits. However, only the air coils were used there, considered under the limited axial and radial displacements, which created a gap in a more generalized view.

The following evaluation attempts to complete that. Firstly, the coupling between the air coil and the ferrite core-based coil, reflecting the results from section 3.1.7 considering the magnetic coupling, is introduced. Similarly, the angular displacement is supported, utilizing a 2D coupling map of a rotated secondary coil, derived in section 3.2. All these together support a calculation of a map of distorted currents, following the initial tuning of the model.

Initial tuning

The excitation source and a nominal value of the resonance capacitor were defined before running simulations.

Excitation source

The primary coil's current I_p in a typical application can reach 100 mA at the carrier frequency, as mentioned in section 4.1.1. Achieving such level using inductance L_p = 1 mH requires the excitation voltage U_{src} as:

$$U_{src} \approx 2\pi f_0 L_p I_p = 78.5\ V. \tag{100}$$

That level is impractical during measurements; however, still feasible during simulation. Practical cases support it by adding a series capacitor C_{res} or, in general, a dedicated matching circuit. It effectively reduces path reactance and allows achieving the same I_p current using a smaller excitation voltage. However, it creates a resonance circuit and, therefore, alters the primary current's frequency spectrum. Thus, the two different excitation sources, summarized in Table 8, were considered initially. Both were defined for the uncoupled state (i.e., M = 0 H), assuming carrier frequency f_0 = 125 kHz.

Table 8 Summary of excitation source, supporting I_p = 100 mA

Excitation mode	R	C_{res}	U_{src}
Direct mode	50 Ω	n/a	79.1 V
Resonant mode	50 Ω	1612 pF	8.9 V

Compared to (100), the higher level during a direct mode results from the system resistance and coil parasitic.

The completed evaluations did not indicate significant differences between these two excitation modes. A strong dominance of a carrier signal on the primary side was observed, following a pure harmonic drive provided by the voltage source u_{src}, and a relatively weak magnetic coupling between the coils. Therefore, the nonlinear portion of the secondary current I_s reflected on the primary side was minor. On the secondary side, the voltage induced on the coil L_s and resulting from the spectral content of the primary current I_p is pre-dominated by the carrier. Therefore, both excitation modes are similar for the considered case, and hence the resonant mode was selected as more convenient to further compare with measurement data.

Nominal value of a resonance capacitor C_r

In theory, the capacitor C_r defines a resonant operation of the connected AFE circuit. However, due to existing nonlinearities, the resonant peak shifts depending on the voltage level, as explained in the following. To achieve a resonance state (i.e., operation at the peak of u_s voltage), the C_r capacitance was calculated as 752 pF for a weak (i.e., k = 0.001) coupling condition. This value was used for further consideration, as reflecting the most linear reference state.

2D distortion map

This section aims to describe a two-dimensional map, containing the frequency spectra of currents flowing in coupled coils. On its base, the level of radiated disturbances is derived within the next chapter. The results shown below implement coupling data from Figure 3.13 right, yet limited to range *XYZ* = [-50 .. 50, 0, 0 .. 50] mm, a more suited to considered cases of coupled coils considered in relevant works [5, 116].

Figure 5.19 summarizes the frequency spectra for both currents, depending on the distance from the center of the primary coil, along its symmetry axis. Compared to the carrier frequency, only the minor level of 3rd harmonic spur for the primary current is observed in the left picture. The reason for that is the resonance behavior of the secondary side of the circuit in which the higher harmonics introduced by the AFE circuit are significantly filtered out [197]. Therefore, the secondary current reflected on the primary side results only with the negligible level, comparable with the gray-box model residuals (i.e., < - 80 dBc). For the secondary current on the right, the dominance of the 3rd spur is noticed, as it was indicated in the previous sections.

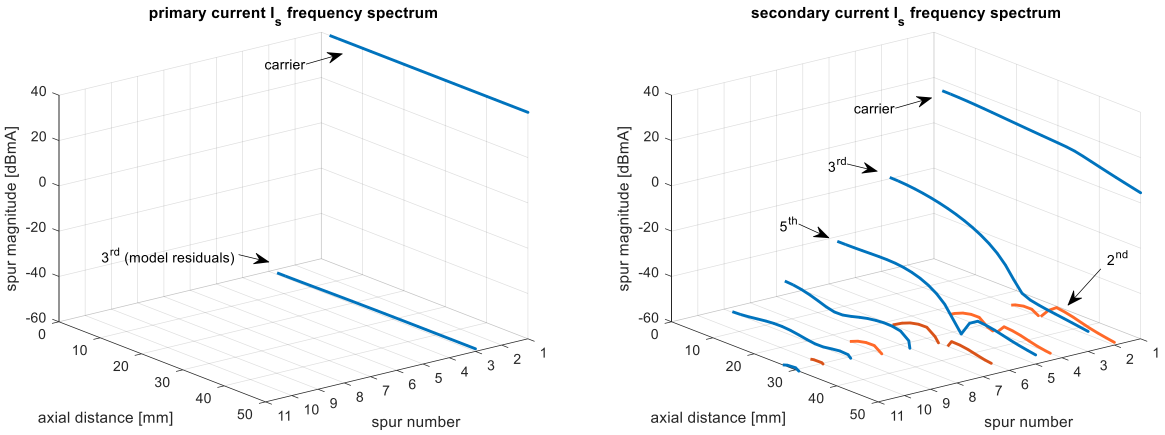

Figure 5.19 Frequency spectra of the primary (left) and the secondary (right) currents

The planar representation of the secondary voltage U_s and the dominant third harmonic spur of the secondary current I_p is presented in Figure 5.20. These two variables quantify the overall nonlinearity. The first is identified as a supply of the secondary side, leading to the operation of the AFE circuit in a low, high, or overdrive condition (as defined in section 4.3.4). Therefore, its actual level can be assumed as a threshold parameter, as it is presented in the following. The second one – a 3rd harmonic spur, is recognized as dominant along the whole considered area.

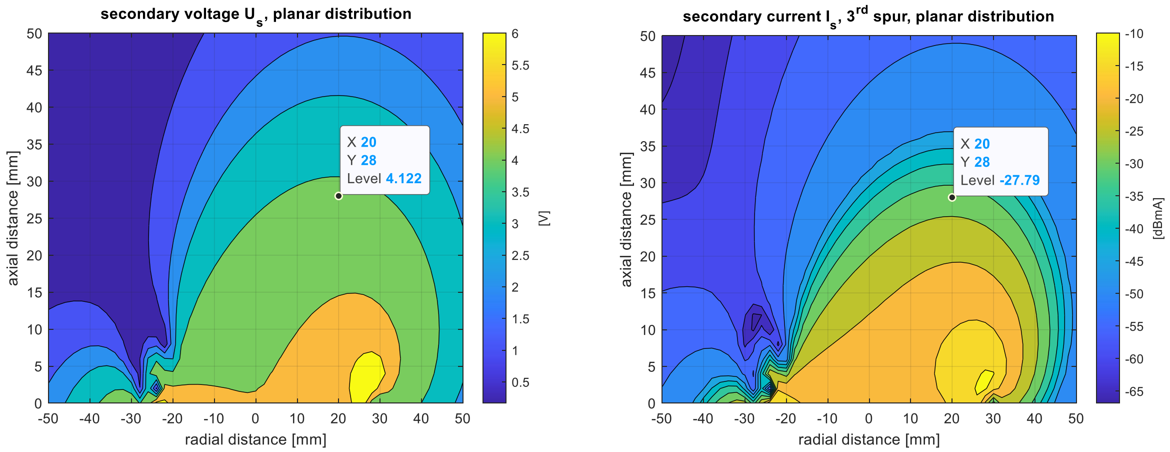

Figure 5.20 Planar representation of the secondary voltage (left) and 3rd spur (right) of the secondary current

As it is observed in Figure 4.15 right, the equivalent resistance and capacitance parts remain nearly constant within $U_s = 2 .. 4.7$ V. Therefore, that range is assumed as the expected operating condition, in which the internal clamping structures are not yet activated. As a result, the indicated level of a dominant third harmonic spur is assumed as the threshold parameter here, below which the overall distortions are still acceptable. Its level is defined initially as - 20 dBmA; however, the more detailed considerations in the next chapter can adjust it according to the allowed radiated emission level. The coincidence of these two conditions is presented in Figure 5.21 as a white-marked area. The visible sharp edges resulted from the simulation steps (actual 2 mm each direction).

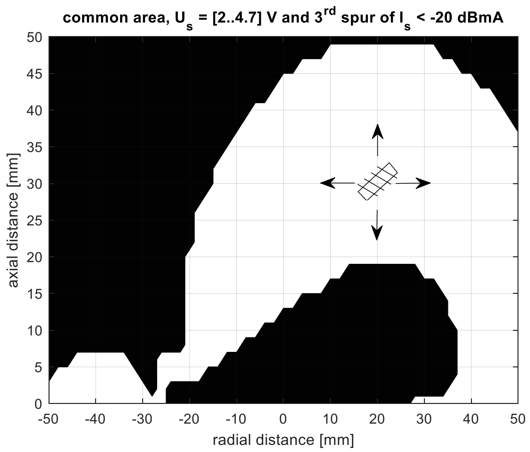

Figure 5.21 Area (marked white), assuring $U_s = [2\,..\,4.7]$ V and 3rd spur $I_s < -20$ dBmA

The meaning of this area is essential for further studies, defining allowed locations of the secondary coil in respect to the primary, as highlighted in the first chapter. There is flexibility in selecting the target position as other limitations (like mechanical dimensions or influence of surrounding parts) also exist. Therefore, the proposed position as $r = 20$ mm and $a = 28$ mm is assumed only as a starting point for further assessment. There is still a flexibility to adjust it in some range – for that, data correlating the coil movement with the level of a third harmonic spur are shown in Figure 5.22. In general, increasing the axial distance reduces distortion level, similarly to side shifts from the above-defined point.

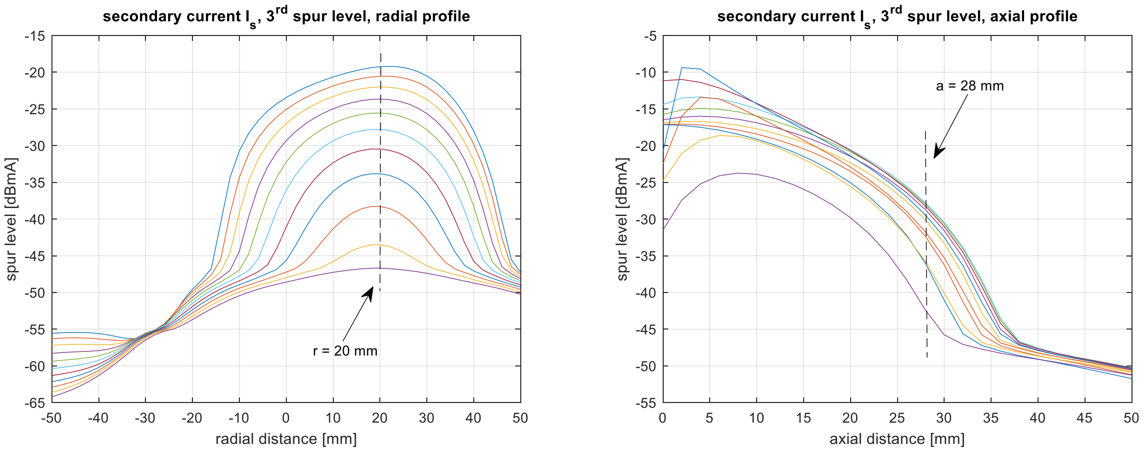

Figure 5.22 Radial (left) and axial (right) profiles of 3^{rd} spur level of I_s, referenced to position $r = 20$ mm and $a = 28$ mm

Besides the harmonic spurs' planar mapping presented above, the presence of a nonlinear circuit introduces other interesting phenomenon presented below.

Nonlinear resonance effect

The voltage-dependent AFE circuit attached to the secondary coil changes the resulting resonant characteristics, assumed here as a nonlinear resonance effect. Its measurable indication is a frequency shift of the peak voltage excited on the secondary coil terminals. That effect strongly depends on the excitation level and is typically higher for bigger nonlinearities. In the considered cases shown in Figure 5.23 left, the simulated down-shift reached 3.4 kHz for a high excitation and nearly 9.4 kHz during an overdrive. Referencing it to the center frequency f_0 = 125 kHz gives 2.7 % and 7.5 % relative shift, respectively.

Simultaneously with the peak shift (indicated as a black curve linking dot marked maxima), the resonance circuit's bandwidth extends significantly. It is a consequence of reduced equivalent resistance of the AFE circuit, following the increase of the U_s voltage. Starting from 22 kHz (Q = 5.6) for low-levels, it extends above 100 kHz (Q = 1.25) for highest excitations. Such a range significantly degrades the selectivity (even not too high initially), typically expected from the resonant circuits. In practice, during high excitation and overdrive conditions, the whole circuit shall be considered as broadband.

Figure 5.23 right shows circuit behavior with a comparable, yet fixed linear load (i.e., R = 60 kΩ, C = 212 pF) as a reference.

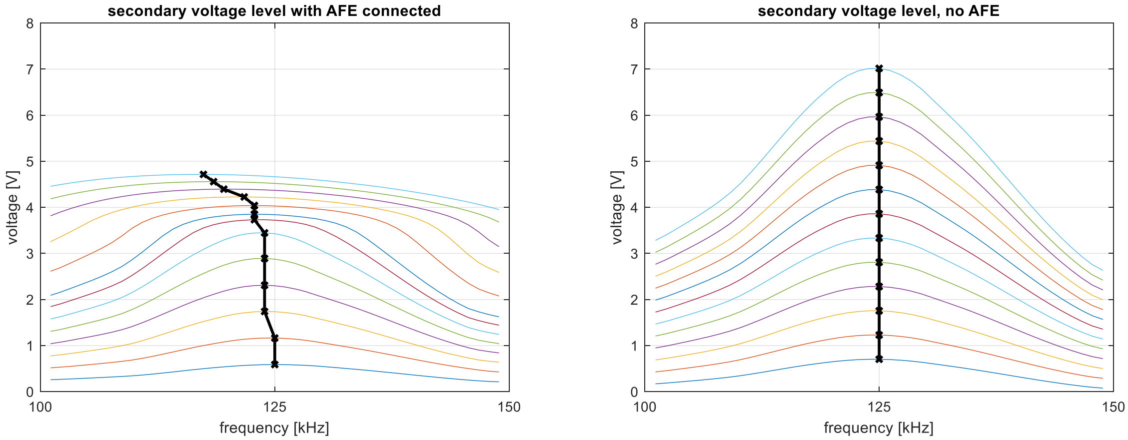

Figure 5.23 Simulated secondary voltage U_s with (left) and without AFE circuit (right), U_{src} = [1..10.3] V

These phenomena – peak shift, bandwidth increase and magnitude decrease need to be regarded in a target application. Their presence, for example, can degrade the overall figure of merit of magnetically coupled coils operating in resonance [202]. Under certain conditions, however, the existing nonlinearities can provide additional benefits in coupling compensation, as presented below.

Further studies of nonlinear resonance

The nonlinear resonance indicated from the above evaluations can be considered in a slightly broader context. As the AFE circuits can differ, their specific non-linearity type can result in a difficult-to-locate phenomenon during measurements either simulations. Therefore, proper recognition of circuit's behavior can help select the correct identification and verification methods.

Taking the equation (176) describing a secondary side of the magnetic link and rewriting it here for clarity, it shows:

$$\frac{d^2 i_s}{dt^2} L_s C + \frac{di_s}{dt}(R_{ss}C + GL_s) + i_s(GR_{ss} + 1) + \frac{d^2 i_p}{dt^2} MC + \frac{di_p}{dt} GM = 0. \qquad (101)$$

The components, including derivatives of current i_p can be regarded as excitation source reflected from the primary side, following the presence of the mutual coupling M. Although, it is not a pure harmonic source; however, with a dominance of strong i_p current such simplification is acceptable. The coefficients applicable to current i_s are split as linear factors (i.e., attenuation and dumping factors δ and α, respectively), and a nonlinear function $f_{nl}(.)$ summarizing circuit nonlinearities. It results in a more generalized equation (assuming $L_s C \neq 0$) as:

$$\ddot{I}_s + \delta \dot{I}_s + \alpha I_s + f_{nl}\left(\dot{I}_s, I_s\right) = f_{exc}(\omega t)\,, \tag{102}$$

where f_{exc} is a harmonic excitation of angular frequency ω.

With an assumption of 3rd power as a dominant nonlinearity (scaled by β factor) and cosine excitation (with magnitude ξ), the above equation takes the known form of a forced Duffing oscillator [203], as:

$$\ddot{I}_s + \delta \dot{I}_s + \alpha I_s + \beta I_s^3 = \xi cos(\omega t)\,. \tag{103}$$

Such nonlinearity type was observed in various circuits [180, 204], and has been analyzed already in details [205]. Although this work aims not to analyze Duffing's oscillator behavior, that phenomenon can appear crucial for a comparable class of nonlinear circuits being frequency modulated. Therefore, Figure 5.24 summarizes the effect of β within the range [-0.02 .. 0.02], considered for a normalized angular frequency ω = [0.5 .. 1.5] - only as an illustrative example. The responses are scaled vs. peak value under a pure linear condition (i.e., β = 0) and using δ = 0.05, α = 1, ξ = 0.2.

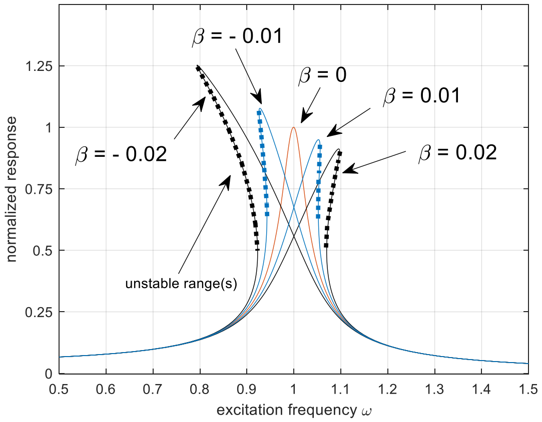

Figure 5.24 Effect of β factor in Duffing oscillator

It is characteristic that peak value can reach a higher level than a pure linear condition, which is visible for $\beta < 0$ (i.e., softening condition [203]). This observation suggests the possible use of the cubic nonlinearity for compensation of mutually linked circuits, detuned from an optimal state by position change of the coupled coils. In practice, the variation of a coupling factor k can be compensated in both directions within a specific range. Recent works considering the efficiency of wireless power transfer (WPT) highlighted this topic [202, 204], which can be assumed as a starting point for further studies.

Chapter summary

This chapter introduced nonlinear models of the AFE circuit, not yet presented in the literature in a described context. The existing works have limited the identified equivalent impedance only to correlate it with the actual disturbance level. This evaluation goes a step further – it allows predicting the level of introduced disturbances using the proposed gray-box and black-box models.

The first of it consists of nonlinear resistance and capacitance equivalent components and is described by nonlinear differential equations. That form provides an intuitive link between the measured data and the model parameters and, therefore, is easy to use and apply to any similar class of circuits. Despite its simple structure, the proposed model supports the accurate representation of spurs' magnitude and phase under each operating condition, including low, high, and overdrive excitation. The proposed model also supports the typical solving methods, of which the harmonic balance is identified as highly efficient.

The above model also provides the capability to estimate the resulting accuracy of spurs magnitude and phase, using the known accuracy of the measured impedance. The provided methodology confirmed a high correlation between the measurements and the Monte Carlo simulations.

The second model, using the polyharmonic distortion concept, introduces a new approach in analyzing the low-frequency circuits. It proposes to apply a formal X-parameters-based description to the definition of introduced disturbances, employing the one-port structure. Using it, the direct mapping of measured harmonics is possible, together with their exact correlation with the excitation level. Therefore, the proposed model supports a broad class of nonlinear circuits, and which is also essential – can be analyzed using industry-standard tools (like ADS or AWR).

Using the well-recognized behavior of the AFE model, the complete structure of the magnetic link was analyzed in the second part of this chapter. Employing the coil equivalent models and the mutual coupling data, it was possible to obtain the planar map of nonlinear disturbances related to the actual locations of the coils. The resulting data allowed defining the coils' positions, in which the level of introduced disturbances stays within the pre-defined limits. In addition, such analysis, not yet previously reported, can serve as a tool in defining design constraints, which are addressed in the following chapter.

Concluding this chapter, the related phenomena were also highlighted as resulting from the presence of the nonlinear circuit within a magnetic link. Thus, based on the nonlinear resonance effect, the directions for future studies were presented.

END OF CHAPTER 5

6 Evaluation of radiated disturbances in automotive setups

The following overview summarizes the methodology of determining radiated disturbances introduced by the nonlinear circuits considered in previous chapters. It starts with a short description of the low-frequency environment and resulting simplifications.

A typical measurement setup compliant with the CISPR 25 specification [2] and widely used in automotive is presented in the following. On its basis, the role of each component is described, which allows proper recognition of the radiation sources and the associated coupling mechanisms. The rod antenna's behavior is presented in detail, for which the equivalent circuit model is introduced.

Next, the commonly used prediction methods supporting the estimation of radiated emission are shortly presented. On their basis, the method originating from the transmission factor is selected for consecutive evaluations and the estimation of the radiated disturbance level.

The predicted levels of introduced disturbances are then validated in the semi-anechoic absorber lined shielded enclosure (ALSE) chamber using a dedicated measurement setup.

6.1 Estimation of radiated emissions

This section aims to estimate levels of radiated disturbances introduced by coils' current determined in the previous chapter. An efficient method supporting analysis such an EMC-related problem is its separation into three groups [206], which is shown in Figure 6.1.

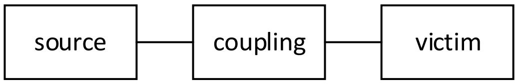

Figure 6.1 Structural view on interference problem

The first group results from characteristics of considered parts (i.e., coils, AFE) and those were analyzed using circuit equations. Supplementary to that, the setup parts (like wires) are recognized as additional sources (or emitters), contributing to the measured level of disturbances.

On the opposite side is a victim (or a receiver), which role during the measurement takes a rod antenna. It is used to capture electromagnetic fields and convert them into a measurable voltage signals.

These two groups of components interact with each other through the coupling mechanisms. It is observed that the placement of setup parts and the orientation of the tested component (i.e., an EUT) significantly affect the antenna's received signal. Proper capturing of those effects is challenging and discussed widely [207-209].

All the abovementioned three groups are discussed below, starting with an overview of the low-frequency environment in which these components operate.

6.1.1 Near-field low-frequency implications

This work considers the low-frequency behavior of magnetically coupled circuits. As a result, all the parts present in the circuit (i.e., coils, AFE) were analyzed regarding their lumped equivalents (as respective R, L, and C components).

A similar approach is applied now in analyzing radiated emission mechanisms. It is a consequence of the frequency range under consideration, assumed as 100 kHz .. 1.8 MHz, with a prime interest in the 125 kHz carrier and its first harmonics. Hence, the physical dimensions of all setup parts (presented in 6.1.2) can be regarded as small (or short) compared to wavelength (i.e., λ_{100kHz} = 3 km, $\lambda_{1.8MHz}$ = 167 m, respectively) and operating in the near-field area.

Therefore, it is valid to consider a cable bundle (i.e., a wiring) and a rod antenna as lumped circuits and neglect any wave effects [9, 210]. This methodology significantly simplifies the following analysis, starting with a review of the measurement setup commonly used in automotive.

6.1.2 CISPR 25 measurement setup

The CISPR 25 specification [2] defines rigorous emission levels of onboard electronics (used on vehicles or boats) to prevent interference with onboard radio receivers. Simultaneously, the measurement methods are recommended to determine reliably introduced disturbances with support of the unified setup.

Automotive setup overview

The sketch of the measurement setup defined by the CISPR 25 [2] and used within 150 kHz .. 30 MHz frequency range is shown in Figure 6.2. It consists of the grounded semi-anechoic chamber ①, internally filled with the absorbing material ②, which primary purpose is to attenuate chamber's reflections at higher frequencies. The flat metal plate ③, located 0.9 m above the floor, emulates the car chassis. This conducting surface is grounded through multiple metal stripes ④, providing low impedance to the reference. The tested EUT ⑤ – in this case, the set of coupled coils and the AFE circuit, is positioned at distance d_h = 0.05 m above the metal plate ③ by a non-conductive separator ⑥ of low permittivity. The EUT is connected through the cable bundle ⑦ of nominal length l_h = 1.5 m with the artificial network (AN) ⑧, providing the known impedance towards the driving circuitry. A rod antenna ⑨ of height h_a = 1 m is located centrally at the distance D = 1 m in front of the setup. In most common configurations, the antenna is followed by a preamplifier of high input impedance located underneath. Amplified signal is supplied to the electromagnetic interference (EMI) receiver ⑩, located outside the chamber. Its primary function is monitoring the voltage level supplied by the rod antenna, which is defined by the antenna factor (AF) from the surrounding *E* and *H* fields.

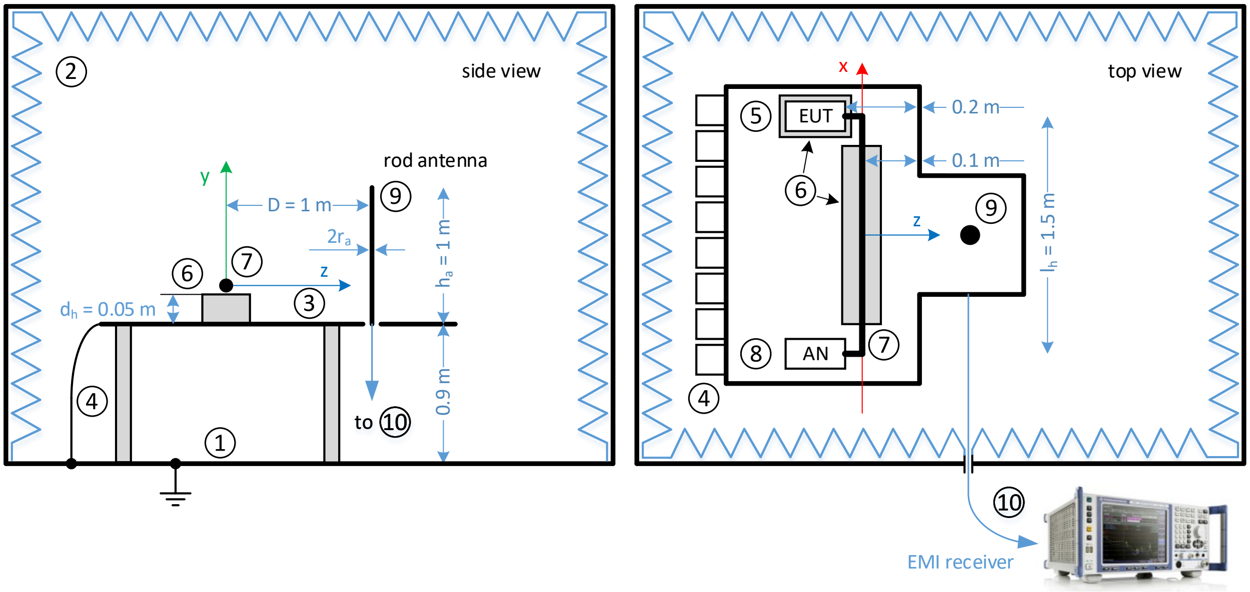

Figure 6.2 Measurement setup in ALSE chamber, according to CISPR 25 [2]

Simulation model

Evaluations completed in this chapter used the simplified 3D model of the CISPR 25 setup, shown in Figure 6.3. It consisted of parts assumed to have significant contributions, which were the air coil (i.e., primary, transmitting, or *Tx*), the ferrite-core coil (i.e., secondary, receiving, or *Rx*), and the wiring in the form of a single wire of radius $r_h = 2$ mm. The short connection from the wiring to the primary coil was neglected. Similarly, the connection from the secondary coil to the AFE circuit was omitted, as both introduce negligible contributions. The nonlinear AFE's behavior was represented by the spectral contents of the coil currents I_p and I_s, identified in chapter 5 (see Figure 5.19). A separator ⑥ was replaced by the air during simulation. Nonetheless, the required distance $d_h = 0.05$ m was still retained by proper positioning of the wiring ⑦ over the grounded metal plane ③. The floor reference was omitted entirely after initial check confirming its negligible impact [7, 211, 212].

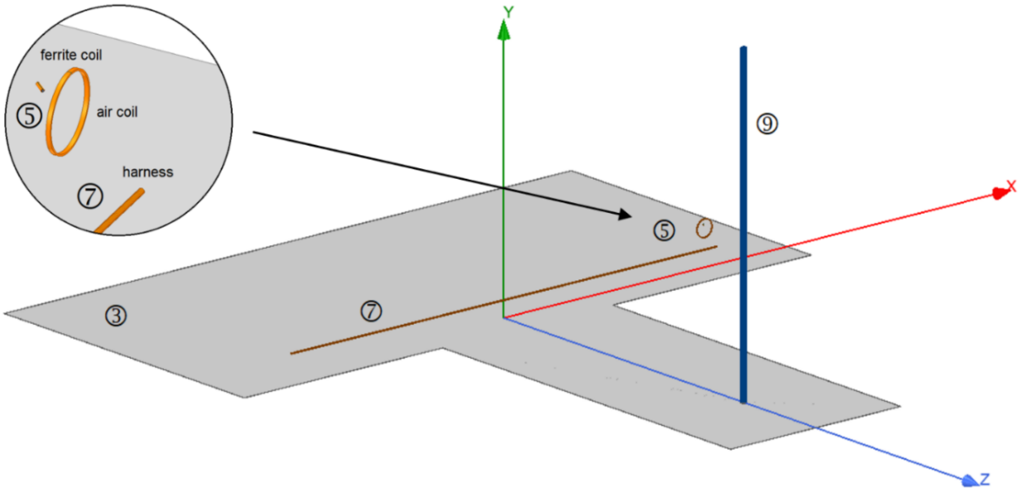

Figure 6.3 Simulation model of CISPR 25 setup employing coils equivalents

During simulations, respective currents and voltages were assigned to given setup parts to obtain impedance data and determine individual couplings with a rod antenna. Simulations also supported the sweeping of model parameters (like a rotation angle of the coil set) and determining their impacts on the resulting field levels.

The first step in estimating the radiated emission is reviewing field sources acting in the measurement setup.

6.1.3 Radiated emission sources

Three components are being recognized as sources of the electromagnetic field. The first two are the primary and secondary coils, creating their time-varying magnetic fluxes excited by the respective currents derived in chapter 5. There are also associated electric fields, which levels are expected low compared to the remaining component. The third source is a wiring supplying the primary coil and, therefore, exciting electric and magnetic fields around the conducting wire. Additionally, the voltages present on the parts are assumed to be significant contributors, which is shown throughout this chapter.

Primary and secondary coil

The familiar approximations of fields of a coil carrying a current I_p [83], reassembled by Mardiguian [206] to more usable forms is presented here on example of the E_φ component of the primary coil as:

$$E_\varphi = \frac{\eta_0 \pi^2 N_p I_p r_p^2}{\lambda^2 D_p} \sqrt{1 + \left(\frac{\lambda}{2\pi D_p}\right)^2} \sin(\theta)\,, \tag{104}$$

where D_p is a distance to the observation point, η_0 is the intrinsic impedance of vacuum, λ is a considered wavelength, and θ represents the observation angle referred to as a coil symmetry axis [83].

The maximum value of E_φ = 59.3 dBμV/m was calculated using primary coil data (described in 2.3.4 and summarized in 8.4), with I_p = 0.1 A, f = 125 kHz, D_p = 1.25 m (resulting from the coil position within the setup). However, even assuming the strongest possible field (i.e., $\sin(\theta) = 1$), it was still nearly 40 dB smaller than the measured level using the configuration from Figure 6.2. Therefore, the other contributions from the remaining setup parts were investigated.

Wiring harness

It is well known that using a differential connection scheme reduces the level of radiated disturbances introduced through the wiring. Typically, such a connection uses dedicated drivers (like in the CAN interface) and operates in a balanced state. A similar driving concept is shown in Figure 4.2, considering the voltage U_{src} as resulting from two sources operating out-of-phase. In this case, the connections with the coil L_p supply differential currents I_p and $-I_p$, reducing radiated disturbances introduced through the wiring. Furthermore, the emission level is lowered by limiting radiating area (i.e., decreasing wire-to-wire distance) and minimizing induced fields (using twisted wires or shielded cables). Oppositely, any mismatch (i.e., imbalance) of wires or circuit components leads to the introduction of a common current I_{cm} or a common voltage V_{cm} to the system [213, 214]. The latter can be intensified in the circuit shown in Figure 4.2, when resonance components (like C_{res}) are located far from the coil (i.e., on the opposite harness end) and their values differ. In that case, a relatively high voltage (see eqn. (36) in chapter 5) from a *hot* coil terminal (in practice, both are hot) is introduced to the wiring, which increases leakage currents.

The presence of a common voltage in a harness can be substituted by a single wire very well [29, 210]. In that case, the V_{cm} can be regarded as a charge distributed on a single conductor located over a ground plane, which correctly describes the radiation mechanism in a low-frequency range [215]. Similarly, the equal currents flowing in the same direction in conductors can be replaced by a single wire with the I_{cm} [216]. Such simplification is possible because the excited fields of individual wires carrying differential currents subtract each other due to opposite directions and, therefore, can be neglected [216]. However, the effects of common currents are summed, which is confirmed in several works [6, 214-219] as dominating radiating mechanism in RF.

Therefore, in this work, a single wire representation of the automotive harness is implemented. Despite only having one wire in a bundle, calling it a *harness* is well established in the industry; hence, this name is also kept here.

The circuit representing common-mode sources is shown in Figure 6.4. Additional measurements can estimate source's voltage V_s and impedance Z_s, yet for the evaluation purposes, it is enough to provide either I_{cm} or V_{cm}. The equivalent load impedance Z_l can be obtained using structural simulation considering the harness as a lumped circuit.

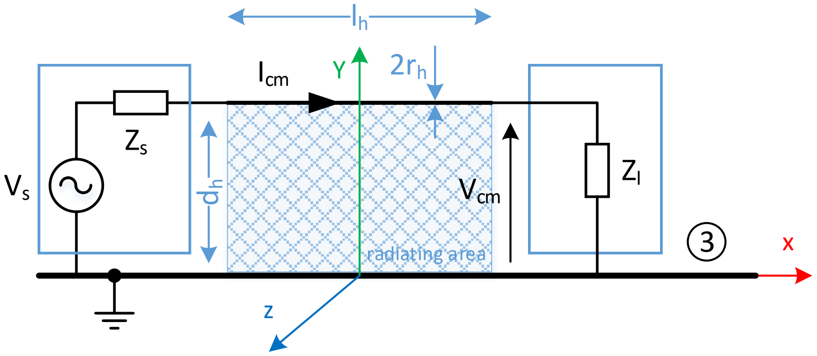

Figure 6.4 Single-wire substitution of a common-mode sources

The current I_{cm} results in an excited magnetic field from the simplified radiating area defined by the harness of length l_h located at a distance d_h above the metal plane. Nevertheless, this effect is negligible due to perpendicular orientation of the emitting circuit towards the rod antenna and the setup symmetry. The more dominant is capacitive coupling with the rod, as explained in the following. Similarly, considering a common voltage V_{cm} leads to electrostatic analysis [215] and assuming quasi-static fields as shown in 6.1.4.

Although measurement of I_{cm} or V_{cm} is possible in the target setup [217, 220, 221], their estimation purely from the schematic is complicated. In typical cases, those sources result from the system parasitic, which do not exist in the idealized circuit. Therefore, they can be deduced only partially, using the MTL theory [222] or imbalance difference [223, 224] method.

6.1.4 Review of prediction methods

Typical methods allowing estimation of electromagnetic fields or their end effects (like a voltage induced in the antenna) are shortly presented here. On their basis, the method originating from the transmission factor is proposed. It allows intuitive localization of coupling mechanisms of the rod antenna with remaining setup parts and is fully supported by the structural simulators.

Quick estimations of the surrounding fields excited by the circuit currents provide fast estimation methods. In typical cases, they are used to swiftly compare obtained results (i.e., analytic, simulated, or measured) with those assumed as typical (or well-known) for a given excitation. A more accurate approach, yet still referencing elementary radiating sources like dipoles or loops, provides the field equations. They are helpful to qualitatively analyze field components and understand mechanisms influencing them from the given setup part. The last referenced method determines relations between disturbance sources and the voltage induced in a rod antenna. Obtained frequency-dependent transmission factors employ actual parameters of all setup parts (like dimensions, materials, positions) and, therefore, are supposed to predict the antenna voltage accurately (i.e., the radiated emission equivalent).

Fast estimation methods

Following [215], the field strength monitored by the EMI receiver can be determined directly from a known common-mode current I_{cm} as:

$$E[dB\mu V/m] = (I_{cm}[dB\mu A] + 8[dB]) \cdot 1[dB\mu V/(dB\mu A \cdot m)]\,, \tag{105}$$

where the current I_{cm} results from measurements or simulations employing a realistic cable model. The free term reflects given setup dimensions (i.e., l_h, d_h, h_a), an intrinsic impedance of vacuum η_0, and mirroring effect, considered as in the mentioned reference [215]). Unfortunately, such a method results in a high uncertainty under low frequencies, easily approaching 40 dB or more [215, 225].

The already mentioned references [206, 216] provide numerous formulae like (104) or (105), supporting a fast estimation of electromagnetic fields. In most cases, they describe scenarios resulting from the worse orientation of the part towards the antenna. For that reason, obtaining such orientation seems to be prime activity during evaluation.

Field equations

Famous formulae (106)..(108) [216] assume a certain level of simplification, resulting from used structures (like loops or wires) and mathematical description (like a series expansion). On their basis, the individual contributions to induced antenna voltage U_a (assumed open circuited) were estimated. Both electric (shown below on the example of the harness) and magnetic fields were considered for completeness, yet as shown later, some interactions can be neglected.

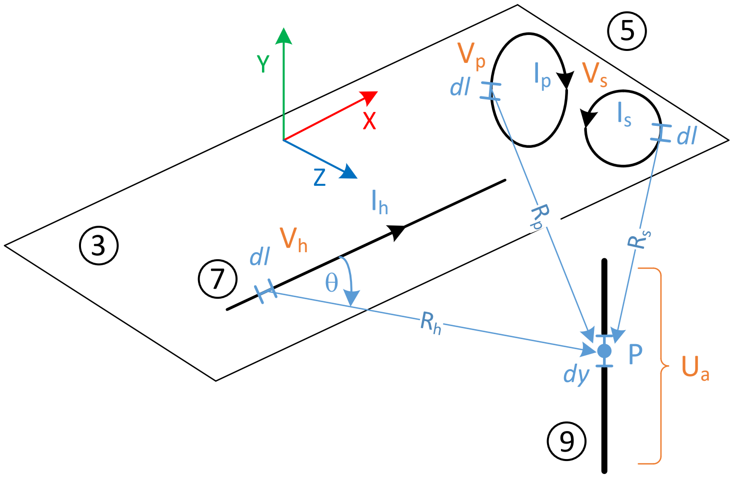

Figure 6.5 Analytical model of antenna coupling

Antenna voltage U_a due to E-field of a harness

The exampled electric field components E_θ, E_{R_h}, E_φ [206] excited by the harmonic current I_h at the observation point P, positioned by a distance R_h from the harness component dl, were calculated in spherical coordinates [216] as:

$$E_\theta = j\eta_0 \frac{kI_h \cdot dl}{4\pi R_h} \sin(\theta) \left(1 + \frac{1}{jkR_h} - \frac{1}{(kR_h)^2}\right) e^{-jkR_h} \,, \tag{106}$$

$$E_{R_h} = \eta_0 \frac{I_h \cdot dl}{2\pi {R_h}^2} \cos(\theta) \left(1 + \frac{1}{jkR_h}\right) e^{-jkR_h} \,, \tag{107}$$

$$E_\varphi = 0 \,, \tag{108}$$

where k is a wave number considered separately for each analyzed frequency.

It is helpful to determine firstly the field resulting from the entire wire length and then integrate it along Y-axis to obtain excited voltage U_a. After leaving only the E_y component, the induced voltage was [211]:

$$U_a = -\int_0^{h_a} E_y dy \,, \tag{109}$$

where integration limits reflected the antenna length and a rod reference.

However, this approach can underestimate the antenna voltage due to the influence of the near metal plane [226]. Therefore, the image theory [206, 226] was applied to account for this effect. The considered field (i.e., vertical and horizontal components) was mirrored at a $-d_h$ distance from the XZ plane and regarded as an additional field source, as shown in Figure 6.6. According to [8, 215], this observation is also valid for the chamber walls, which contribute nonnegligible to the antenna voltage.

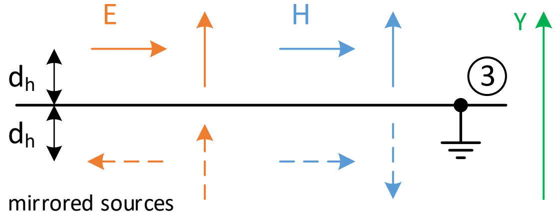

Figure 6.6 Effect of the near metal plane regarding electric and magnetic field components

The determined antenna voltage reflecting original and mirrored sources was converted to the equivalent field strength in the last step, using the antenna factor presented in section 6.1.5. This way, the calculated field can be related to the levels indicated by the EMI receiver.

Transmission factor

The well-established method in predicting radiated emissions is based on the so-called transmission factor [8, 215, 227-230] describing the interactions between the tested component (i.e., its interference source) and the monitoring antenna. Chen [231] analyzed this mechanism by observing the harness current and the voltage at antenna terminals. Similarly, Gao [230] constructed a 3D model to predict the relation between the given circuit's current and a monitoring antenna. Commonly, the scattering **S**-matrix [225, 232] or impedance **Z**-matrix [230] were determined, on which basis the antenna voltage was predicted. That idea implementing the concept of a transmission factor is shown in Figure 6.7.

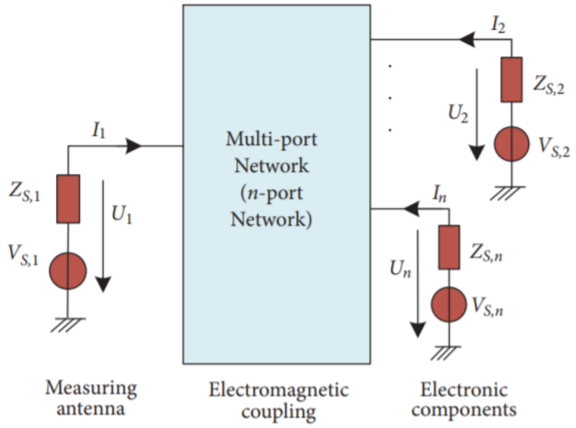

Figure 6.7 Transmission factor concept, following [230]

There is a similarity to the high-level interference model shown in Figure 6.1. In addition, the emission sources can be localized intuitively, which supports efficient verification. This feature was considered when selecting the method for subsequent assessments.

Proposed coupling method

The practical method used to estimate the antenna voltage assumed that the coupling factors could accurately represent interactions between the emission sources and the rod antenna in the low-frequency band. The background for selecting such an approach was the structural model developed in section 3.1.5 and used successfully to determine the mutual inductance between the coils. Furthermore, it was supposed to accurately describe also the coupling with the rod antenna, taking its original form and embedding it into the complete model of the measurement setup shown in Figure 6.3. Consequently, both inductive and capacitive couplings were assessed using simulation features offered by the Ansys Maxwell 3D [39] environment. In this way, the proposed methodology followed a well-established transmission factor method yet implemented the mutual inductance and capacitance concepts instead of scattering matrices.

Hence, the magnetic T_M and capacitive T_C transmission factors are defined, referencing given source current I_x and voltage V_x to the rod antenna output voltage V_{rod} as:

$$T_{Mx} = \frac{V_{rod}}{I_x}, \tag{110}$$

$$T_{Cx} = \frac{V_{rod}}{V_x}, \tag{111}$$

respectively, where V_{rod} is the resulting voltage of the rod antenna (i.e., fields equivalent), and x denotes index of the considered source. These factors are frequency-dependent and determined for a given position of the setup parts.

Notwithstanding the proposed methodology, the analytical and fast estimation methods were also used to compare and adequately reference the obtained results.

Determining of transmission factors starts with the analysis of a rod antenna regarded as a lumped circuit.

6.1.5 Rod antenna

Different antenna types are considered within CISPR 25 setup, depending on the frequency range and the related field polarization. A monopole antenna of only vertical polarization is used for the lowest frequency band – from 150 kHz to 30 MHz. The horizontal component in this band is expected to be small due to the presence of the metal surface [2].

Independently of the dominance of the electric either magnetic field in a tested setup, a measurement of the radiated emission in the LF band requires the antenna in the form of a 1 m long rod. Due to that requirement, it is essential to understand how the antenna captures the surrounding electromagnetic fields.

Rod antenna factor

To define a conversion ratio of given *E* and *H* field intensities to the antenna output voltage, the dedicated calibration procedure specified in CISPR 16-1-4 [233] is used. Following that, the corresponding AF_E and AF_H factors (both frequency-dependent) are identified by the antenna manufacturer as:

$$AF_E = \frac{|E|}{|V_{rod}|}, \tag{112}$$

and

$$AF_H = \frac{|H|}{|V_{rod}|}, \tag{113}$$

where V_{rod} is a voltage induced between antenna terminals, and E and H are the respective fields of a given polarization. However, the AF_H factor for a rod antenna is rarely available and typically as informative value.

In the case of the attached preamplifier, the antenna factor specifies a complete set. Therefore, the denominator in formulae (112) and (113) shall be replaced by the voltage V_a observed on the nominal 50 Ω load (see Figure 6.8 for more details). The exampled active rod antenna like R&S HFH2-Z6 [234] shows AF_E = 10 dB(1/m) and allows accurate measurements (i.e., ± 1 dB) from 9 kHz.

The sensitivity of the rod antenna to the magnetic field is very low compared to its sensitivity to the electric field (a difference is typically - 40 .. - 60 dB). Therefore, understanding the rod antenna behavior needs a deeper review of its parameters.

Equivalence of *E* and *H* fields

Theoretically, it is possible to recalculate field levels using intrinsic impedance of vacuum η_0 defined as:

$$\eta_0 = \frac{|E|}{|H|} = \sqrt{\frac{\mu_0}{\varepsilon_0}} \cong 377\,\Omega\,, \tag{114}$$

yet, in this case, the obtained results are assumed as identified in a far-field region. For example, to get the E-field intensity from the measured H-field, a useful logarithmic form of equations (112) and (113) is typically used, resulting in $|E[dB\mu V/m]| = V_{rod}[dB\mu V] + AF_H[dB(1/m)] + 51.5dB$, where $51.5_{dB} \cong 20log(377)$.

The issue with such recalculation is that the wave impedance in the near-field area is far from the nominal value defined by equation (114) [206], and, in general, is challenging to be captured accurately. To account for that, following [29], the field components need to be considered independently. Therefore, the individual contributions from the setup parts shown in Figure 6.2 can be analyzed concerning inductive and capacitive couplings to predict the level of introduced disturbances. It is possible after exploring the equivalent model of a typical rod antenna.

Rod antenna model

The rod antenna is considered as a conducting straight wire of length h_a and radius r_a, located perpendicularly over a ground plane. Within the frequency range under consideration (see 6.1.1), the antenna is regarded as short compared to the wavelength.

The rod antenna model consists of the reactive X_a and resistive R_a components, which is shown in Figure 6.8. The antenna current I_a (caused by the exciting E and H fields) flows to the input of the following preamplifier circuit, simplified by the impedance Z_{in}. The preamplifier output is loaded with an EMI receiver input. The voltage V_a is regarded as an output of a rod antenna (in practice, *active* rod antenna). It is typically referenced to 1 μV level and expressed in the logarithmic units dBμV.

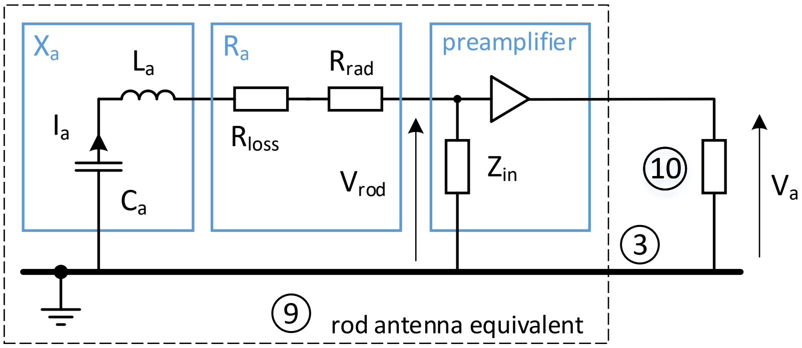

Figure 6.8 The electrical model of a rod antenna with attached preamplifier circuit

A low sensitivity to magnetic fields suggests a capacitive nature of the rod antenna impedance. In a general case, however, it is a complex number, defined as:

$$Z_a = R_a + jX_a \, . \tag{115}$$

The real part R_a consists of a sum of loss and radiation resistances, R_{loss} and R_{rad}, respectively. The imaginary part X_a results from the inductance L_a and capacitance C_a presented by the solid conducting rod above a metal surface (regarded as an infinite ground plane).

The following evaluations consider the frequency range 100 kHz .. 1.8 MHz, which is slightly lowered (compared to specified by CISPR 25) in order to capture effects near the carrier frequency (i.e., 125 kHz). Within this range, the rod impedance data are calculated assuming harmonic operation of the entire system (hence the symbolic notation used).

Resistive losses R_{loss} and R_{rad}

The first component of antenna resistance - R_{loss}, is material and frequency-dependent and can be estimated using the methodology presented in section 2.2.1 assuming skin loss model. Within the analyzed frequency range and taking a typical rod diameter $2r_a = 4$ mm, the resulting R_{loss} is 6.9 .. 28.2 mΩ for copper material.

Following [244], an approximation of radiation resistance, which is valid for antenna length $h_a < 0.14\lambda$, is well approximated by the formula (116):

$$R_{rad} \approx 40\pi^2 \left(\frac{h_a}{\lambda}\right)^2 . \tag{116}$$

The calculated value of R_{rad} is low 0.04 .. 14.2 mΩ and, therefore, it can be neglected similarly as a resistive loss R_{loss} due to a high resistance part of the input impedance Z_{in} (typically 100 kΩ .. 1 MΩ || 10 .. 100 pF [235-237]) of the following preamplifier circuit.

Antenna inductance L_a

The inductance of a wire with a non-negligible diameter can be taken as a partial inductance [238] and specified per unit length. Using the solution presented in [238], the antenna inductance L_a is then:

$$L_a = \frac{\mu_0}{2\pi} \, ln\left(\frac{h_a}{r_a} + \sqrt{\left(\frac{h_a}{r_a}\right)^2 - 1}\right), \tag{117}$$

which gives L_a = 1.1 µH and follows the known relation of 1 µH/m for a straight wire. The knowledge of antenna inductance is essential, as it allows further estimation of a possible mutual coupling with other magnetic components present in the setup. Within a considered frequency range, the antenna represents the inductive reactance X_L = 0.86 .. 15.6 Ω.

Antenna capacitance C_a

Calculation of the antenna capacitance C_a employs model of a straight wire oriented perpendicularly to the ground plane. In [29], it is derived as:

$$C_a = \frac{2\pi\varepsilon_0 h_a}{ln\left(\frac{h_a}{r_a}\right) - 1} \; . \tag{118}$$

For a given antenna dimensions, C_a = 10.6 pF, and it is similar to reported values in related works [7, 29]. Due to a low operating frequency, the capacitive reactance is high: X_C = 8.3 .. 149 kΩ, so it dominates over the remaining impedance components.

A given rod antenna unit needs to be calibrated together with the attached preamplifier as its input capacitance effectively forms a capacitive voltage divider.

Typically, the impedance Z_{in} is not directly specified, and the antenna factor usually contains its effect. Notwithstanding, the following evaluations assumed a fixed value Z_{in} as 100 kΩ || 33 pF as needed to determine the preamplifier input voltage V_{rod}.

Antenna impedance Z_a

Consideration of a rod antenna impedance as a lumped circuit in a low-frequency band, employing the elementary circuit shown in Figure 6.2, results in reducing it to the reactance components as:

$$Z_a \cong \frac{1}{j\omega C_a} + j\omega L_a \; . \tag{119}$$

The resistance R_a is neglected entirely as having no noteworthy impact on the system operation.

The following section analyzes the dominance of inductive or capacitive coupling with the remaining setup parts. The existing sources [29, 231, 232] considered the harness only; therefore, it is valuable to recognize effects related to the coupled coils.

Because of the operation within a near-field area, inductive and capacitive mechanisms are analyzed independently [29].

6.1.6 Coupling consideration

The identified couplings (as mutual inductances and capacitances) of harness and coils with a rod antenna are shown in Figure 6.9 for clarity. The marked numbers reflect the setup parts shown in Figure 6.2.

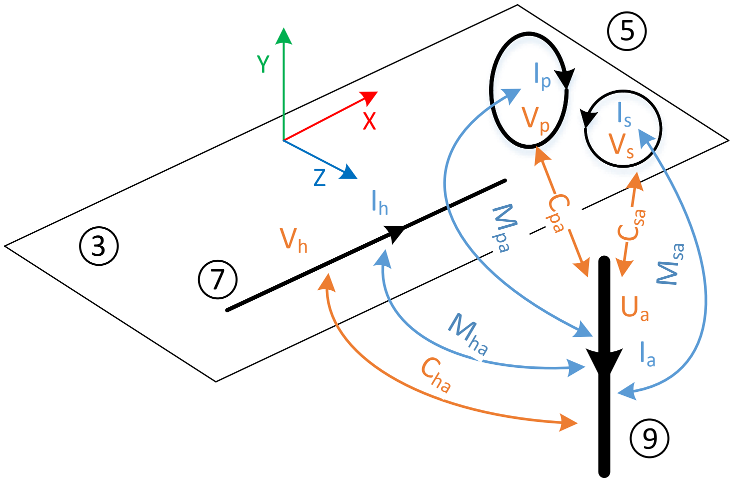

Figure 6.9 Mutual couplings of a harness and coils with a rod antenna

The actual value of each coupling type resulting from the measurement setup is determined using the structural simulator in form of inductance and capacitance matrices [9, 108].

Inductive coupling

Generally, due to relatively low value of antenna inductance L_a = 1.1 µH, low system currents, and a loose coupling (i.e., D = 1 m) to the rest of the setup parts, the interaction from the exciting fluxes is expected to be low. Additionally, the orthogonal and symmetrical orientation of a rod antenna versus harness supposes a low inductive coupling between those parts. Notwithstanding, increasing the operating frequency can lead to a higher induced voltage, as described by formula (120).

Portions of magnetic fluxes passing through the antenna inductance L_a (distributed along a rod) induce the voltage U_a proportional to the circuit current I_x (page 105) and analyzed angular frequency ω. Because of the individual linkages between flux sources and the rod antenna, their impacts can be regarded as mutual inductances M_{ha}, M_{pa}, and M_{sa} for the harness and the primary and secondary coils, respectively. Therefore, the antenna voltage V_{rod} is determined from the circuit shown in Figure 6.10:

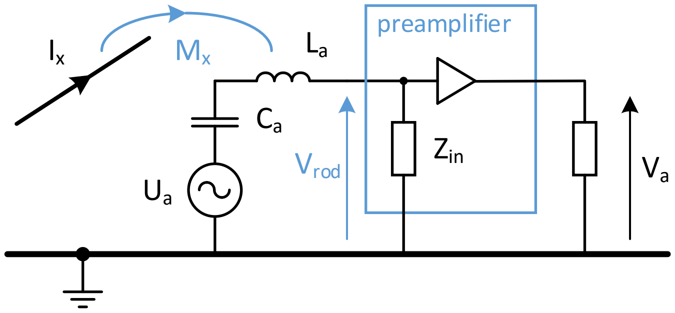

Figure 6.10 Equivalent circuit representing inductive coupling mechanism

and using equations (120)(121) as:

$$U_a = -j\omega M_x I_x \, , \tag{120}$$

$$V_{rod} = \frac{U_a}{\frac{1}{j\omega C_a} + j\omega L_a + Z_{in}} Z_{in} = \frac{-j\omega M_x Z_{in}}{\frac{1}{j\omega C_a} + j\omega L_a + Z_{in}} I_x = T_{Mx} I_x \,, \qquad (121)$$

where the mutual inductance M_x and current I_x represent respective coupled circuit.

Capacitive coupling

With the assumption of nonzero voltage existing on a harness and coils, a time-varying electric field is observed at antenna location as resulting from the charges distributed on these parts. Accordingly, the E-field lines terminated on the charges induced within the rod, effectively created the antenna current I_x. This mechanism, known as a capacitive coupling, is recognized on the antenna side as a presence of the input voltage V_{rod} (resulting from the voltage drop on Z_{in}).

Charges on the harness and coils are considered as voltages [215] V_h, V_p and V_s (referenced to the ground plane) allow the estimation of the antenna voltage V_{rod}, assuming known mutual capacitances C_{ha}, C_{pa}, C_{sa}, and employing coupling scheme shown in Figure 6.11.

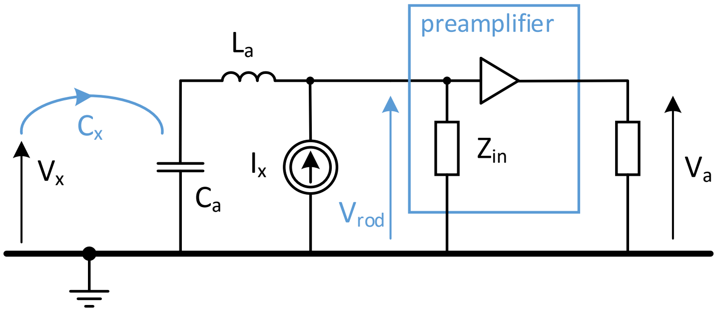

Figure 6.11 Equivalent circuit representing capacitive coupling mechanism

Describing induced current as:

$$I_x = j\omega C_x V_x \,, \qquad (122)$$

the voltage V_{rod} due to capacitive coupling can be deduced as:

$$V_{rod} = \frac{I_x}{\frac{1}{Z_{in}} + \frac{1}{\frac{1}{j\omega C_a} + j\omega L_a}} = \frac{j\omega C_x}{\frac{1}{Z_{in}} + \frac{1}{\frac{1}{j\omega C_a} + j\omega L_a}} V_x = T_{Cx} V_x \,. \qquad (123)$$

Note the V_x and C_x in the above formulae represent the individual capacitive coupling of each contributor defined above, respectively.

Determination of the EUT orientation

The harness location during measurement is fixed and strictly defined by the CISPR 25 standard. Similarly, the tested EUT shall be placed in a predefined area, however, in the orientation resulting in the highest emission level. Fulfilling this requirement can be complicated during a verification phase, requiring multiple measurements in a chamber and resulting in an increased time and cost.

Therefore, having the possibility of determining such a worse position by simulation seems to be very attractive.

The developed model of the monitoring antenna supported this process by estimating such direction of the coil set (i.e., the EUT), in which coupling to the rod showed the highest value. The EUT was rotated around the local Y-axis with a 5-degree step, simultaneously determining coupling values. The definition of the rotation angle θ_{EUT} is shown in Figure 6.12. Although a similar evaluation can be performed over the remaining X and Z axes, it was abandoned due to the construction of the validation stand (see section 6.2.1), allowing rotation only around the Y-axis.

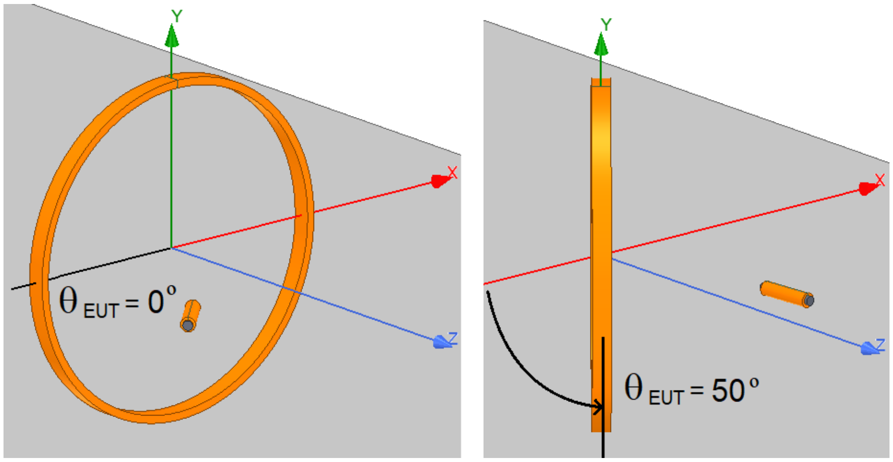

Figure 6.12 The EUT in neutral position (i.e., $\theta_{EUT} = 0$ degree) (left) and the dominating direction at $\theta_{EUT} = 50$ degrees (right)

The interaction with the rod antenna was identified for both inductive and capacitive components and resulted in coupling factors determined for a whole rotation. To adequately capture directions of the strongest coupling, the normalization to the highest values was applied, resulting in data shown in Figure 6.13.

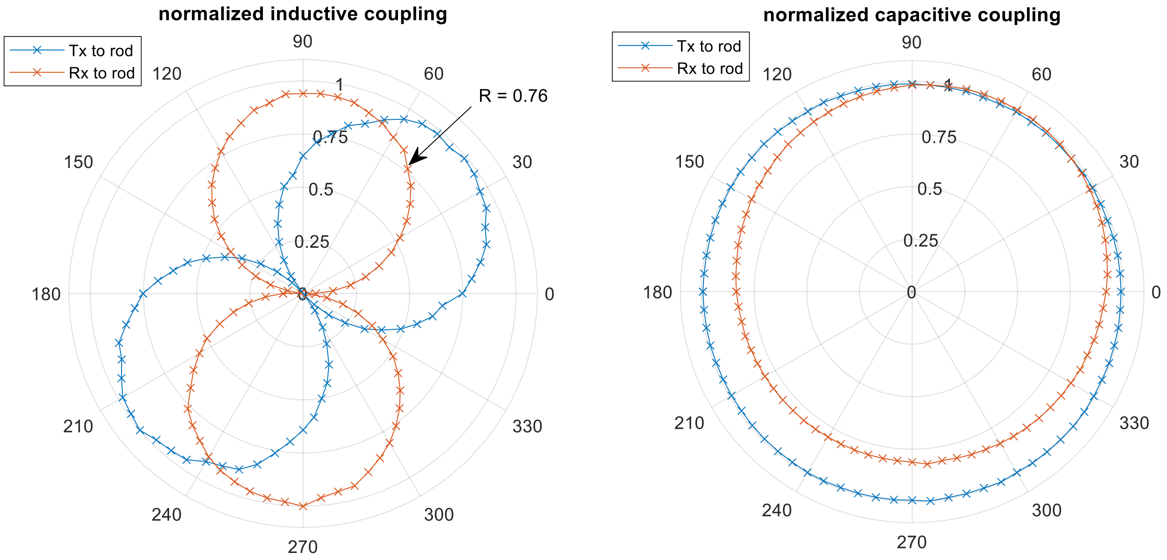

Figure 6.13 Normalized inductive (left) and capacitive (right) couplings of coils with a rod antenna

The inductive coupling shows well-defined directivity, highest between 40 and 55 degrees (either 210 to 230 degrees) for the primary *Tx* coil case. Similarly, coupling with a secondary *Rx* coil indicates peaks between 85 and 95 degrees (either 265 to 275 degrees). Accordingly, the *Tx* coil case's capacitive coupling is nearly constant, yet the *Rx* coil shows a maximum value between 45 and 75 degrees. Therefore, the question arises, which angle shall be selected as a worse condition resulting in the highest voltage induced in the antenna.

To help answering this question, an optimization method is proposed. Knowing respective levels of excitation sources (i.e., V_x and I_x) and using a multivariable optimization scheme employing formulae (121) and (123), the rotation angle can be determined. In this case, the objective function f_{min} being minimized is constructed as:

$$f_{min} = -\left(\sum_x T_{Mx} I_x + \sum_x T_{Cx} V_x\right). \qquad (124)$$

Components in summations reflect contributions defined by formulae (121) and (123), respectively. Using this method, the rotation angle was determined as being close to 53 degrees using equal levels of particular sources (i.e., V_x = 1 V and I_x = 0.1 A).

Alternatively, in a simpler manner, the rotation angle can be selected coarsely as 50 degrees, due to the dominance of the *Tx* coil. Simultaneously, the influence of the *Rx* coil's current can be corrected by the factor resulting from its directivity, in this case, multiplied by ~1.3 (i.e., 1/0.76, as observed in Figure 6.13 left).

Yet another approach proposed Brunett [239] regarding mutual impedance of two coils coupled to a common load. Accordingly, if condition (125) is satisfied (which is the case here), the induced voltages in the antenna are assumed identical using only one or two coils. Therefore, the coupling mechanism can be simplified to the dominant source (in this case, the primary coil). However, the current of the omitted (i.e., secondary) coil shall be reflected in the primary to not lose information of its spectral content.

The formula describing the importance of both sources is [239]:

$$\left(L_p + L_a\right)\left(L_s + L_a\right) \gg M_{ps}^2 , \qquad (125)$$

where M_{ps} (~ 20 μH) is a mutual inductance between primary and secondary coils. The usability of this method is straightforward, as it could further simplify the simulation model.

Concluding this section, the rotation angle equal to 50 degrees was selected to define the EUT orientation, with correction of the secondary coil current. In this case, the influence of a given excitation source (i.e., V_x and I_x) to the radiated emission level can be analyzed using a fixed orientation of coils.

Mutual couplings with a rod antenna

Table 9 shows the respective coupling values obtained for the reference position (i.e., r = 20 mm, a = 28 mm, see Figure 5.22), yet entirely rotated by θ_{EUT} = 50 degrees. Shown capacitances are comparable with ones of relevant works [7, 29], while references to mutual inductances were difficult to locate in literature. Notwithstanding, their effects stay in line with other works [9, 231], claiming the low sensitivity of the rod antennas to magnetic fields. Therefore, these values (together with the remaining couplings between parts and ground) were used for determining levels of radiated emissions.

Table 9 Summary of rod antenna couplings obtained from 3D simulator for rotation angle θ_{EUT} = 50 degrees

Coupling element	**Coupling value**
M_{ha}	0.18 pH
M_{pa}	22.3 nH
M_{sa}	2.95 nH
C_{ha}	0.15 pF / 0.047 pF (cal.)
C_{pa}	0.032 pF
C_{sa}	0.004 pF

The value related to the mutual inductance M_{ha} needs some comment. A change of antenna tilt angle by some degrees along the X-axis dramatically changed that coupling. The slight deviation by only 3 degrees led to a coupling increase by nearly 60 dB (to 0.14 nH). It is equivalent to the ~ 50 mm movement of the antenna end from the nominal position, which is difficult to notice. The remaining couplings showed significantly smaller sensitivities regarding their nominal orientations, estimated as ± 17 % maximum (i.e., + 1.4 / -1.6 dB). Those changes were analyzed by the movement of the individual part by ± 5 mm in X or Z direction, which is an acceptable estimation of the placement repeatability in the laboratory.

Transmission factors

The determined transmission factors T_{Mx} and T_{Cx} are shown in Figure 6.14 left. As supposed, a dominance of the capacitive coupling (represented by the component T_{Cha}) over inductive (i.e., T_{Mha}) is observed for a harness case, which follows the actual observations. Due to negligible contribution (also with a slight tilt), the latter coupling can be assumed negligible in practical cases.

From the other couplings, the one with a primary coil M_{pa} is noticed as dominating others. It is interesting because it may suggest that the magnetic field can determine the overall emission level. However, such an effect is not observed using rod antennas. Therefore, to get a quick impression of the relevance of a given coupling type, the plot of the antenna voltage V_{rod} versus frequency is shown in Figure 6.14 right. The assumed levels of typical excitation sources were the voltages V_x = 1 V and currents I_x = 0.1 A. The summarized inductive and capacitive contributions are shown, together with the total voltage induced in a rod antenna due to both effects. The marked uncertainty area resulted from the assumed placement accuracy of setup parts.

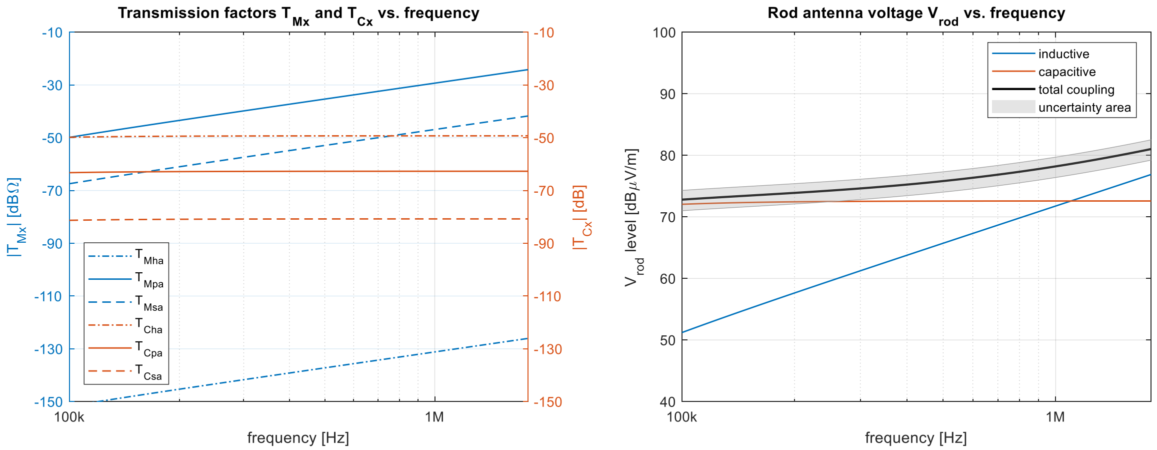

Figure 6.14 Determined nominal transmission factors T_{Mx} and T_{Cx} (left), and induced antenna voltage V_{rod} (right) considering sources as $V_x = 1$ V and $I_x = 0.1$ A

The dominance of the capacitive coupling is noticed, which determines the overall behavior of the rod antenna.

6.1.7 Estimation of radiated emissions

To predict radiated emission level due to known system current I_x, the formulae (126) can be used:

$$E[dB\mu V/m] = T_{Mx}[dB\Omega] + I_x[dB\mu A] + AF_E[dB(1/m)]\,. \tag{126}$$

Similarly, in a case of known common voltage V_x, it is:

$$E[dB\mu V/m] = T_{Cx}[dB] + V_x[dB\mu V] + AF_E[dB(1/m)]\,. \tag{127}$$

Consideration of all sources together requires firstly summation of the relevant effects to obtain induced voltage V_{rod} as:

$$V_{rod} = \sum_x T_{Mx} I_x + \sum_x T_{Cx} V_x\,, \tag{128}$$

and then applying formula (129) to get the equivalent field strength as:

$$E[dB\mu V/m] = V_{rod}[dB\mu V] + AF_E[dB(1/m)]\,. \tag{129}$$

6.2 Disturbance measurement

The validation methodology is presented in this section. The completed measurements aimed to recognize the radiated disturbances introduced from the setup and compare them with the predicted levels. The necessary steps to achieve that are presented below.

6.2.1 Validation in ALSE chamber

The measurement of a weak signal (like a harmonic spur, < -80 dBc) in the presence of a relatively strong carrier current (i.e., 0.1 A) requires the avoidance (or at least significant reduction) of all non-EUT related disturbances. When those signals overlap, the proper recognition of the EUT's harmonics is complicated or even impossible. One method of avoiding that is the appropriate filtering of the excitation signal. It was successfully implemented in chapter 4 for the AFE characterization, and, therefore, it was also reused here.

The physical placement of setup parts added another complication related to the repeatability issues. For example, a slight change of the wire routing introduced measurable (part of dB) effects due to different coupling with the monitoring antenna. Therefore, repeated measurements were completed to indicate the range of possible changes when it was possible.

The measurements started with the preparation of the CISPR 25 compliant setup.

Setup overview

The validation was performed in the ALSE chamber and utilized standard equipment applied for EMC-related tests. The measurement setup employed the circuit shown in Figure 6.15, except the initial verification step, which is explained in the following. The secondary coil with the connected AFE circuit was moved during the validation, yet the harness and the primary coil positions were retained fixed. That helped to reference obtained results with prior simulations properly.

Excitation path

The excitation path consisted initially of the signal generator (SG), type R&S SML01 and the power amplifier (PA), type AR 150A400 (both were used for typical immunity tests in the EMC laboratory). However, due to identified poor signal purity of the given SG type, it was replaced with the unit previously used during AFE characterization (i.e., Keysight 33220A). The role of the artificial network (AN) took the bandpass (BP) filter centered at 125 kHz with the transformer acting as a voltage balun (both have been already used for the AFE characterization). The balun used four identical windings in (1+1):(1+1) topology and supported differential driving of the harness. The 375 kHz notch filter resulted from balun's core 3rd spur, which arose during loading above 0.1 A. Two capacitors $C_{res1,2}$ supported the series resonance with the primary coil L_p. Although their values are expected equal (~3 nF), commonly, only a single part determines the resonance behavior to simplify the overall tuning procedure (however, by the cost of the line unbalance). Therefore, a typical solution implementing $C_{res1} = 1.6$ nF and $C_{res2} = 15$ nF capacitors were used. Additionally, they were intentionally located far from the coil, following a typical configuration adopted in the industry. The above parts (i.e., BP filter, balun, notch filter, capacitors) were put in an aluminum shielding box (shown in Figure 6.16) to reduce coupling with the rest of the setup.

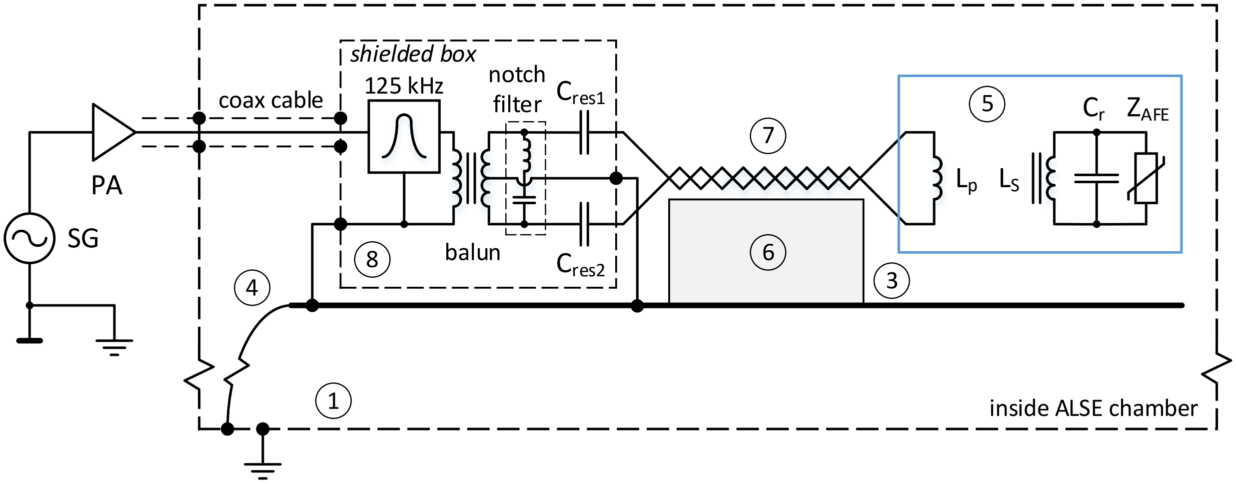

Figure 6.15 Measurement setup used for the measurement of radiated disturbances

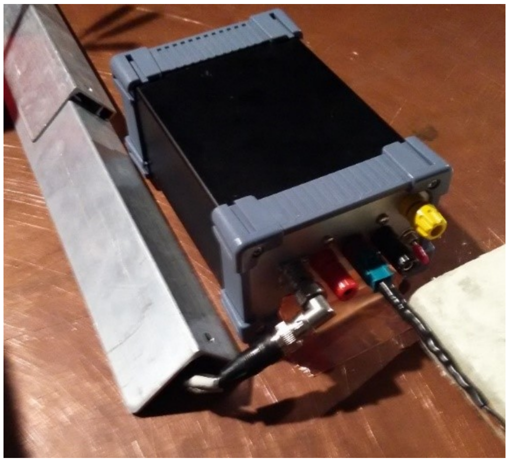

Figure 6.16 Shielded box view

Rotation head with the EUT

The primary and secondary coils were mounted on the measurement stand shown in Figure 6.17 left. It allowed linear positioning of the secondary coil with 1 mm resolution, together with the rotation with 5-degrees steps around the Y-axis. The AFE circuit and the resonance capacitor C_r were located on the small printed circuit board (PCB) of the same kind as used in the serially produced key fob, shown in Figure 6.17 right. Unused parts mounted on the PCB were deactivated by simple cut of their connections.

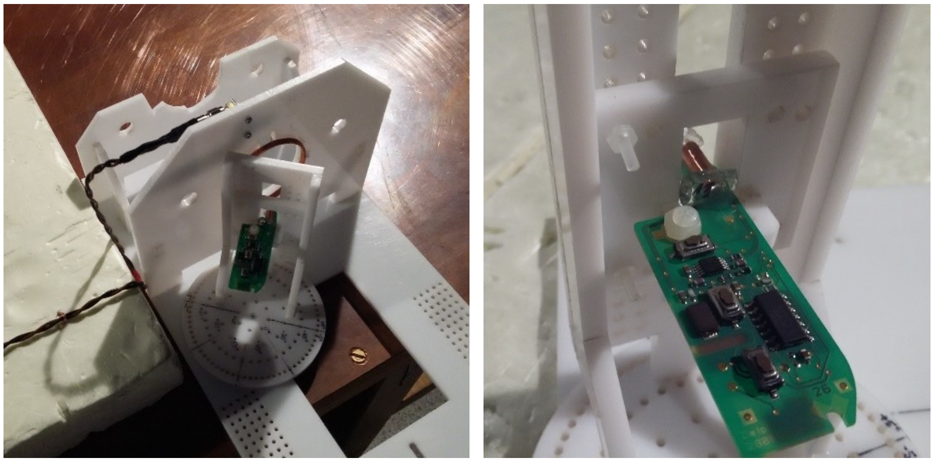

Figure 6.17 The EUT view (left) and the close view on the AFE circuit (right)

Monitoring

The actual level of radiated disturbances was monitored by the R&S ESR7 EMI receiver using the active rod antenna type HFH2-Z6 by R&S, having AF_E =10 dB(1/m). The overall measurement process was controlled by the EMC32 [240] application.

Methodology

The voltage induced in the rod antenna contains contributions from the measurement setup (like the harness) and the nonlinear effects of the AFE circuit introduced through the coupled coils. Additionally, the presence of the SG and the following PA can add their distortions, observed as additional spurs. However, this work aims to predict the disturbances resulting from the AFE and coils' nonlinearities. Therefore, the validation steps shall capture all those phenomena appropriately.

They started with a general check of the monitoring path.

Verification of the monitoring path

Initial part of the checks verifying setup correctness was performed before the subsequent measurements. In the beginning, the chamber's noise floor was determined, shown in Figure 6.18 left. Next, the calibration wire of length 0.5 m was used to excite the expected field strength, monitored by the EMI receiver. Following Annex J of CISPR 25 [2], this verification step should yield field strength as 60 dBμV/m ± 6 dB [241]. The measurement setup was equivalent to the circuit shown in Figure 6.4, assuming $Z_l = Z_s = 50\,\Omega$, $l_h = 0.5$ m, $V_s = 0.2$ V, so $V_h = V_{cm} = 110$ dBμV. The wire was driven directly from the SG, which excluded the need for the harness voltage measurement (the calibrated SG determined known level). Actual data and the predicted level (129) as $E_{[dB\mu V/m]} = T_{ChaCAL[dB]} + V_{h[dB\mu V]} + AF_{E[dB(1/m)]} = 60.3$ dBμV/m are shown in Figure 6.18 right. The calibration factor T_{ChaCAL} for a shorter harness (i.e., 0.5 m) was determined by the simulation as - 59.7 dB @ 125 kHz. The setup view during this step is shown in Figure 6.19.

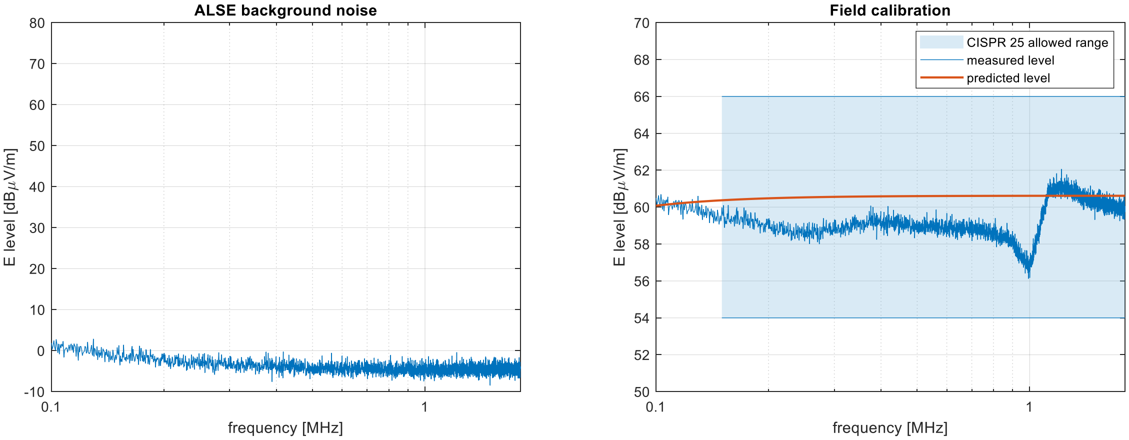

Figure 6.18 ALSE chamber noise floor (left) and the calibration level (right)

Figure 6.19 The setup view during calibration step

The results of both measurements allowed us to correctly verify the spectral purity of the driving source in the next step.

Excitation path spectral purity check

Chapter 4 emphasizes that the SG plays an essential role during the characterization of nonlinear circuits. Together with the PA in the excitation path, they can introduce non-negligible distortions when operating at higher levels. Therefore, it was necessary to verify that under conditions similar to those presented by the closely coupled coils with the attached nonlinear AFE circuit. Such maximum load was estimated from Figure 4.20 for the overdrive condition when the AFE consumed nearly 60 mW of peak power (i.e., 56 mW @ 5.84 V).

The verification utilized the setup shown in Figure 6.15, with the Z_{AFE} replaced by the 620 Ω load resistor. Initially, the complete setup noise floor was rechecked due to adding the PA to the signal path (the calibration step used only the SG). A spur introduced by the PA around 168.5 kHz was noticed, shown in Figure 6.20 left. However, it was excluded from further considerations as not correlated with the EUT's excitation frequency. Next, the gain of the PA was tuned to achieve the primary coil current I_p = 0.1 A peak, measured by the current probe during the uncoupled condition (i.e., without a secondary coil). Finally, Figure 6.20 right shows the highest system-related disturbances localized by a free movement of the secondary coil within the available area. That position was found for a radial displacement (see Figure 3.8 left) at $r = 20$ mm, $a = 2$ mm (i.e., close to the primary coil winding with coaxial orientation) and the rotation angle similar to the one indicated in Figure 6.12 (i.e., ~ 50 degrees).

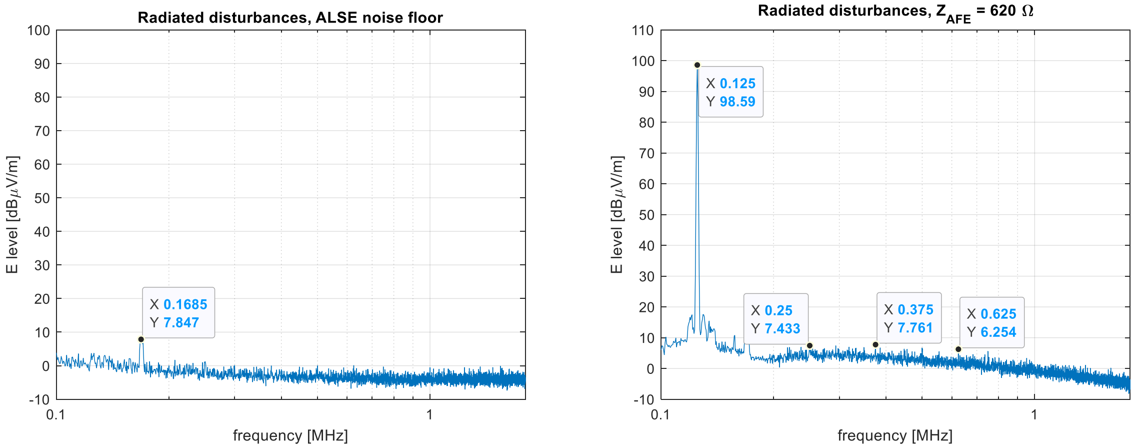

Figure 6.20 ALSE chamber noise floor with the PA present (left) and spectral purity with the 620 Ω load (right)

The harmonic spurs were observed within the recorded spectrum. Even harmonics were attributed to the PA, with a maximum 7.4 dBμV/m @ 250 kHz. The balun introduced odd spurs, with the highest level 7.7 dBμV/m @ 375 kHz. The slightly increased noise floor (by ~ 6 .. 8 dB around considered harmonics) resulted from the PA's distortions introduced through the coax cable to the ALSE chamber. However, all those contributions were insignificant, and the excitation source (i.e., the SG and PA) supported more than 90 dBc of spurious-free operation. Therefore, it was concluded that the level of radiated disturbances from the EUT could be determined reliably.

6.2.2 Results

The measured level of introduced disturbances was referenced to the predicted values, which are shown in Figure 6.21. That was completed for the considered position defined in Figure 6.12 right and the one reflecting the strongest coupling between the coils (identified above).

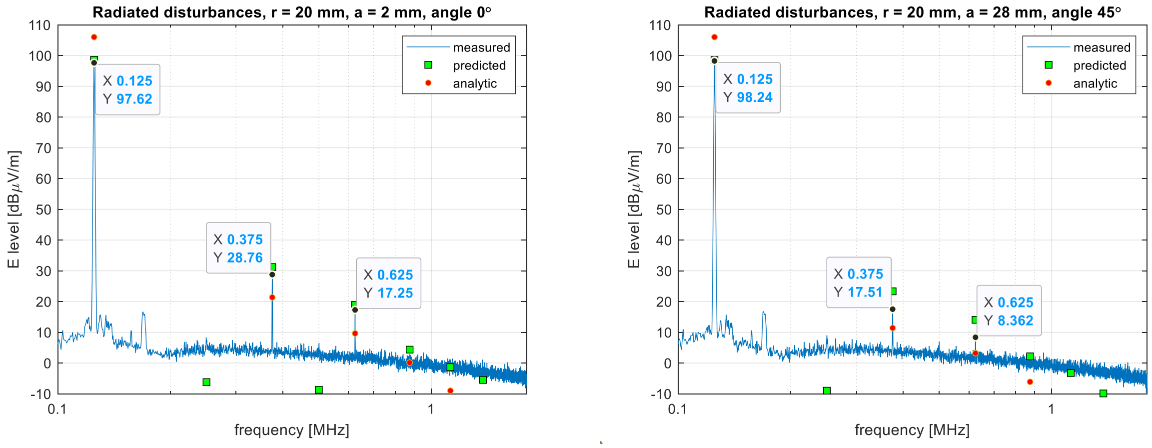

Figure 6.21 Radiated disturbances using $r = 20$ mm, $a = 2$ mm, angular 0 degree (left) and $r = 20$ mm, $a = 28$ mm, angular 45 degrees (right). Both cases reflect $\theta_{EUT} = 50$ degrees.

The coils' currents, voltages, and phase relationships required for a field prediction were determined using the harmonic balance method described in section 5.1.2. The example of such data is shown in Figure 5.20 right in the case of the 3rd harmonic of the secondary coil, which gives - 27.8 dBmA (i.e., 32.2 dBμA) at $r = 20$ mm, $a = 28$ mm. The voltage along the coil (similarly to its current) was assumed constant, which is valid in a low frequency.

The harness current I_{cm} was not measured (the work aims to predict all the contributions), so assumed null. The harness voltage V_{cm} at the carrier frequency was estimated using eqn. (36) from chapter 5, assuming it as a half of that present in the resonance. That supposition was feasible, because unequal values of capacitors C_{res} introduced high unbalance in a harness, even it was driven differentially. For the higher frequencies, the common voltage was determined using simulated couplings and taking the secondary coil's harmonic currents as the excitation sources.

Comparison of estimated disturbances

The results shown in Figure 6.21 represent the similarity between the predicted and measured values. The lowest difference (less than 1 dB) was observed for the carrier signal. For the closest coupling shown in the left picture, the differences were + 2.5 dB and + 1.7 dB for the 3rd and 5th harmonic spurs, respectively. Accordingly, for the second position shown in the right picture, those numbers were + 5.8 dB and + 5.7 dB, respectively. There were no noticeable even harmonics excited by the EUT, as predicted in chapter 5. Therefore, their calculated levels are presented only for evaluation completeness. Similarly, the levels determined by the analytic solution were used only as a quick reference without further consideration of their accuracy.

The overall representation of the radiated disturbances using the transmission factors is satisfactory. The overall emission level from the coil currents and voltages was captured accurately, assuming the achieved 6 dB difference was acceptable. However, the individual contributions were not analyzed during the validation. For example, performing multiple measurements around a considered location can help determine the predicted field's uncertainty (similarly as it was completed in 5.2.5 for the case of complex impedance). For that case, however, the automated positioning of the EUT is required, which can reduce placement uncertainty associated with the manual operation.

Uncertainty estimation

The overall uncertainty of the predicted levels of radiated disturbances contains contributions from the measurement system (i.e., EMI receiver, antenna, cables, current probe, ALSE, etc.) and the uncertainty resulting from the measurement setup, including the EUT. The first part was estimated in the usual way [242] as ± 5 dB, which is the typical range for the verification laboratory, where the validation was conducted. The second part was mostly evaluated using simulated placement sensitivities (determined in 6.1.6 as + 1.4 / - 1.6 dB), while the influence of the coils' equivalents (in 3.1.7 as 2.4 %) can be neglected. However, the harness model substituted by the single wire be regarded as too much simplified. It was observed that its contribution at the carrier frequency was dominant. Although the resulting field was the most accurate at this point, the detailed model can support more accurate estimations at the higher frequencies. This direction should be considered as the goal of future research.

Chapter summary

The new methodology of predicting radiated disturbances from magnetically coupled circuits was proposed in this chapter. It employed the well-established transmission factor concept, yet now using data determined entirely by the structural simulations. The analyzed circuits were modeled as a part of the CISPR 25 compliant measurement setup, commonly referenced in works addressing disturbance measurements in automotive. However, many existing analyses consider only the harness as the predominant radiating source, assuming that other couplings (including magnetic) are negligible. With the presence of the inductive parts acting as radiating components, such supposition is no more valid. Therefore, both the capacitive and inductive couplings with the monitoring rod antenna were investigated in detail.

The rod antenna was considered as a lumped circuit, for which the equivalent impedance model was proposed. It was shown that it allows the accurate representation within the low frequency band considered herein. Furthermore, it was proved by the calibration measurement, confirming sufficient correlation with the predicted level.

The orientation of the tested EUT resulting in the highest coupling with the monitoring antenna was determined by simulation. This necessary step allowed omitting entirely the time-consuming measurements typically performed in the semi-anechoic chamber. Instead, that position was obtained for the EUT as a whole, yet considering coupling directions of each coil. The resulting orientation (as a rotation angle) was determined using the optimization method, taking contributions from relevant voltage and current sources into account.

The validation completed in the ALSE chamber demonstrated comparable levels of radiated disturbances with the predicted values for the carrier and initial odd harmonics. The remaining spurs stayed near the noise floor, similarly to their predicted levels.

The dedicated setup consisting of the rotation head was prepared for measurement purposes, allowing reliable positioning of the EUT. As a result, it was possible to recognize regions resulting in the highest disturbances on its base, which were located close to the coil winding. In those cases, they stayed in line with the predicted areas, determined purely from calculations.

END OF CHAPTER 6

7 Conclusion and outlook

In radiated emission compliance tests of automotive components according to standard CISPR 25, the semi-anechoic ALSE chamber is used. It supports a good correlation with disturbances observed in a vehicle; therefore, it is also used for verifications at the early designing phase. However, the associated development cost is high, and not all manufactures can afford it. In this context, a straightforward alternative method is required to provide a reliable assessment of radiated emission levels.

This thesis focuses on accurately determining radiated disturbances introduced by the nonlinear circuits through the inductively coupled coils. The proposed methodology is comprehensive and supports the necessary steps to establish an appropriate radiation model of a complete system.

The thesis put in this work is confirmed, which allows the use of the proposed methodology of predicting the radiated emission levels within the ± 6 dB limit for the carrier signal and the dominant harmonic spurs within the LF band. Three research questions were also analyzed, each finding proper support in the performed research and obtaining a positive answer.

The developed alternative can be summarized in the following steps.

Firstly, the detailed model of the air and ferrite-core based coils was introduced. It supported the semi-layered winding structure observed in actual inductors. The causes of disordered turns placement were identified as the material and manufacturing capabilities. It was emphasized that the standard estimation formulae showed decreasing accuracy for the higher frequencies and non-ideal windings. To improve the comparability with measurements, the frequency-dependent coil impedance components were determined using structural simulations. That resulted in accurate representation (below 2 %) of the coils, which supported reliable estimation of the mutual inductance in the next step.

The inductive coupling was supposed to determine resulting distortion levels; therefore, it was studied in detail. The practical approaches were analyzed, starting from the analytical methods known from the literature. Initially, the Babic method was incorporated, which described mutual inductance for each considered position of the coupled coils. It was then referenced with the proposed compact coil model, which was used to determine accurately (better than 0.5 % in a case of a ferrite coil) the magnetic field in the proximity. The following measurements confirmed a satisfactory (4 % maximum difference) representation of the inductive coupling mechanism, including frequency dependence in the LF band. Many spatial positions of coils were investigated, including axial, radial, and angular displacement rarely available in the literature. Therefore, the completed evaluation of the mutual inductance can be regarded as the first important contribution of this work.

Capabilities and limitations of the nonlinear low-power characterization have been investigated and discussed within the next major step. First, the existing gap in the available instrumentation was identified in the low-frequency band. Then, the complete solution was proposed to overcome the limitation in the frequency offset measurements of the harmonic spurs (including their phase relations). It employed the two generator-based method of synchronous cancellation of a given harmonic spur. It was supported by the spectrum analyzer operating as a null detector, providing a high dynamic range. The matched four-stage bandpass filter supported the required pure harmonic excitation. The frequency and level-dependent nonlinear characteristics were obtained using the introduced methodology. The relative expanded uncertainty of the proposed solution was estimated as 3.2 % (with the option to improve it further) in the case of the angle measurement, which was found very satisfactory. Developing the complete characterization methodology is regarded then as the second significant contribution of this work. The resulting accurate distortion characteristics of the considered nonlinear AFE circuit maintained the construction of the equivalent model in the next step.

Prediction of harmonic spurs required knowledge of system currents and voltages as the sources of radiated disturbances. Obtaining them utilized the complete model of the magnetic link, thus coil equivalents and the appropriate representation of the circuit nonlinearities. It was managed twofold. The nonlinear AFE model was formulated using the complex impedance form described by differential circuit equations. It contained voltage-dependent capacitive and resistive components, accurately representing operating modes of the considered AFE circuit. This so-called gray-box model supported frequency characteristics (i.e., magnitude and phase) within the whole operating range of the nonlinear component. That modeling approach allowed restoration of the harmonic spurs from the measurements, not only describing circuit operation compared to previous works. Supplementary, the AFE modeling has also been represented by the polyharmonic distortion approach, reflecting the nonlinear part as the one-port device. On its basis, the efficient representation of the low-frequency operation was proposed using the X-parameters. This unique approach helped to describe accurately (limited in practice only by the accuracy of the measurement equipment used) the harmonic spectrum of the nonlinear part. Therefore, it was possible to employ the common RF simulation tools to analyze also the LF parts.

The important topic of uncertainty propagation was considered regarding complex impedance. The long-term measurements referenced to the Monte Carlo simulations showed the comparable (0.9 dBm and - 2º, respectively) spurs magnitude and phase data. That was simultaneously confirmation of the high quality of the proposed model, supporting the reliable determination of the planar map of disturbances.

Three aspects of the real validation in the ALSE chamber have been considered during the last step of analyzing the CISPR 25 environment. Firstly, the appropriate near-field quasi-static methodology was used to simplify the setup parts and reduce them to the forms containing only the harness and coils as radiating components. Secondly, the low-frequency model of the monitoring rod antenna was introduced. On its basis, the individual couplings with the remaining setup parts were determined. That supported estimation of the antenna voltage (hence radiated disturbances) by using the equivalent transmission factor concept. In addition, they were specified for both capacitive and inductive couplings, from which the latter was typically neglected in recent works. However, their presence was vital to determine introduced disturbances accurately. And thirdly, a detailed procedure allowing reliable measurements of the weak distortions was implemented. It was emphasized that the spectral purity of the excitation source plays a significant role during the disturbance measurement process.

There are at least two noticeable scientific findings obtained from this work. First, the assumption of the only dominant role of the automotive harness during the CISPR 25 compliant measurements shall be revised when the magnetic field sources are present. Their importance can increase with a frequency due to the existence of magnetic coupling with the rod antenna. Additionally, multiturn windings can intensify magnetic fields by the factor reflecting their number of turns, which is nonnegligible. The second finding is the possibility of analyzing even complicated nonlinear systems in a low-frequency with support of the relatively simple instrumentation. That observation simultaneously provides a positive answer to the last research question. It was confirmed that the accurate determination of harmonic nonlinearities is possible with the support of the elementary spectrum analyzer and the dedicated circuit embedding the bandpass filter and the low-power transformer.

Analyzing the second research topic addressing coil coupling can conclude that relatively simple forms represented by the circular rings of the rectangular cross-section correctly described the LF operation. Induced voltage determined on their basis accurately predicted the excitation level of the nonlinear part, thus the introduced level of radiated disturbances. Furthermore, the simulation time was significantly reduced due to their optimized forms, which helped perform the evaluations efficiently. Therefore, that research question is also acknowledged.

The last research question put in this work needs a bit more comments. During evaluations in the ALSE chamber, the exact placement of the setup parts played an essential role during the measurements. The small asymmetry of the harness placement, a slight tilt of the rod antenna, or the vertical orientation of the connections to the coils introduced measurable effects on the recorded spectrum. Only the precise parts placement, strictly following the CISPR 25 defined positions, allowed obtaining the data comparable with the simulations reflecting the nominal conditions. The measured disturbances were close to their predicted levels, with differences below 1 dB for carrier cases and the maximum + 5.8 dB for the dominant 3rd spur. The overall extended uncertainty was estimated below ± 6 dB level, which is a highly satisfying result. In that context, the introduced methodology allows the reliable prediction of radiated disturbances, which acknowledges the thesis put in this work. Additionally, it is possible to relatively fast estimate the level of introduced disturbances using the simplified model of the complete measurement setup. Therefore, it can be concluded that the proposed approach fits automotive industry demands.

Independently of the above achievements, a further research is proposed on those topics. In the author's opinion, additional evaluations should concentrate on detailed sensitivity analyses of the measurement setup. The already completed simulations can be supplemented by the measurements with a semi-automatic positioning of the radiating components. That can support obtaining statistical data, hence defining components or their features (like a wire diameter, length or bending angle) with the dominant impact on the monitoring spectrum. Under such circumstances, the prediction accuracy might be increased by optimizing the most sensitive parts acting in the CISPR 25 validation.

The measurement setup used for the nonlinear characterization can also be reconsidered. The already proposed use of a xDSL transformer type can further reduce system nonlinearities due to their highly optimized design. Some initial trials showed promising results, mainly for the higher (i.e., above 0.5 W) loads.

The last idea of this work was to construct a compact module containing all the circuits used for nonlinear measurements. These were the multistage bandpass filter, transformer, power splitter, range resistor, and mode switch. Furthermore, the interface used for measurements of mutual inductance can be added as well. That approach could additionally reduce the overall system noise floor due to omitting modules' interconnections. The author is currently considering that concept as a continuation of this work.

8 Appendix

8.1 Geometry model

Taking Figure 2.4 left as a reference, the position of a given turn can be described as a pair of coordinates a_i and l_i, as shown in Figure 8.1 reflecting A, B, C, D turns. The turns A and C are assumed parts of the lower layer and the turns B and D of the upper one.

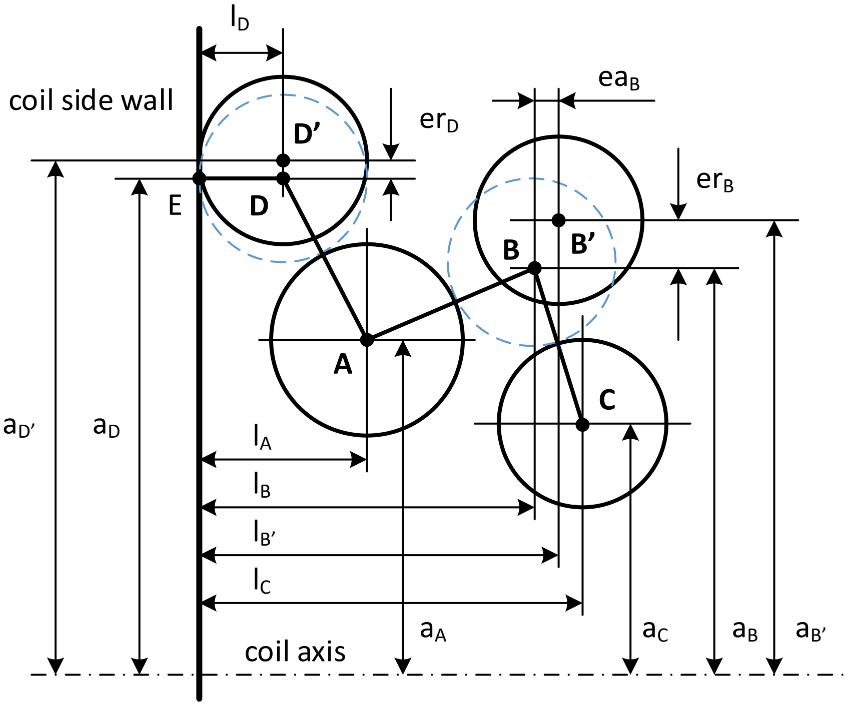

Figure 8.1 Turns' positioning in a coil winding

The virtual 'wound' is explained for two cases, and it starts with the turn B located above any two turns (here A and C). To calculate its initial position (i.e., marked in blue) described by coordinates a_B and l_B, the segments $\overline{AB}$ and $\overline{BC}$ are firstly compared with respective sums of wires' radii as:

$$\begin{cases} \sqrt{(l_B - l_A)^2 + (a_B - a_A)^2} = \dfrac{d_{w,A}}{2} + \dfrac{d_{w,B}}{2} \\ \sqrt{(l_C - l_B)^2 + (a_B - a_C)^2} = \dfrac{d_{w,B}}{2} + \dfrac{d_{w,C}}{2} \end{cases}, \tag{130}$$

with condition $a_B > min(a_A, a_C)$ locating turn B in the upper layer. Next, the relaxation described by the axial ea_B and radial er_B displacements are introduced to the respective coordinate as:

$$a_{B'} = a_B + er_B\,, \tag{131}$$

$$l_{B'} = l_B + ea_B\,. \tag{132}$$

Finally, the distance verification (with the optional correction) is applied (i.e., $\overline{AB'} \geq d_{w,A}/2 + d_{w,B}/2$ and $\overline{B'C} \geq d_{w,B}/2 + d_{w,C}/2$), which avoids overlapping of the winding turns.

The second case reflects the turn D located near the coil side wall. Considering segments $\overline{AD}$, $\overline{DE}$ and respective radii as:

$$\begin{cases} \sqrt{(l_A - l_D)^2 + (a_D - a_A)^2} = \dfrac{d_{w,A}}{2} + \dfrac{d_{w,D}}{2} \\ \sqrt{(l_D - 0)^2 + (a_D - a_D)^2} = \dfrac{d_{w,D}}{2} \end{cases}, \tag{133}$$

with condition $a_D > a_A$, the coordinates a_D and l_D are determined. Similarly to the previous case, the following turn relaxation and distance verification are applied. To evaluate winding behavior near the second side of the coil, the same equation (133) can be used, yet with an update of the coil length l instead of null value.

8.2 Orthogonality of skin and proximity effects

Following [58, 243], the current density $\boldsymbol{J}_z(\rho)$ in the round conductor due to longitudinal magnetic field B_z is determined in the cylindrical coordinate system as:

$$\boldsymbol{J}_z(\rho) = \frac{kB_z}{\mu_0\mu_{cond}} \frac{J_1(k\rho)}{J_0(kr)} \hat{\phi}, \qquad \rho \le r, \tag{134}$$

where J_0 and J_1 are Bessel functions of the first kind, order 0 and 1, respectively. The wave number k of the conductor is calculated as:

$$k = \sqrt{-j\omega\mu_0\mu_{cond}\sigma_{cond}}\,. \tag{135}$$

Accordingly, also following [58, 243], the current density $\boldsymbol{J}(\rho, \phi)$ in the round conductor due to transversal horizontal magnetic field B_x is:

$$\boldsymbol{J}_x(\rho, \phi) = \hat{\boldsymbol{z}} \left[\frac{-2j\omega\sigma_{cond}B_x r}{krJ_1'(kr) + J_1(kr)}\right] J_1(k\rho) sin(\phi), \qquad \rho \le r, \tag{136}$$

where J_1' is derivative of Bessel function of order 1. Similarly, the effect of transversal vertical field B_y is:

$$\boldsymbol{J}_y(\rho, \phi) = \hat{\boldsymbol{z}} \left[\frac{-2j\omega\sigma_{cond}B_y r}{krJ_1'(kr) + J_1(kr)}\right] J_1(k\rho) cos(\phi), \qquad \rho \le r, \tag{137}$$

Due to fields' orthogonality, their effects (i.e., current density distributions) can be summed up to reflect the *eddy currents* effect in a conducting wire, shown in Figure 8.2. As those effects increase with a frequency, the results refer to the highest considered value (i.e., 1.8 MHz) and possible magnetic fields intensities.

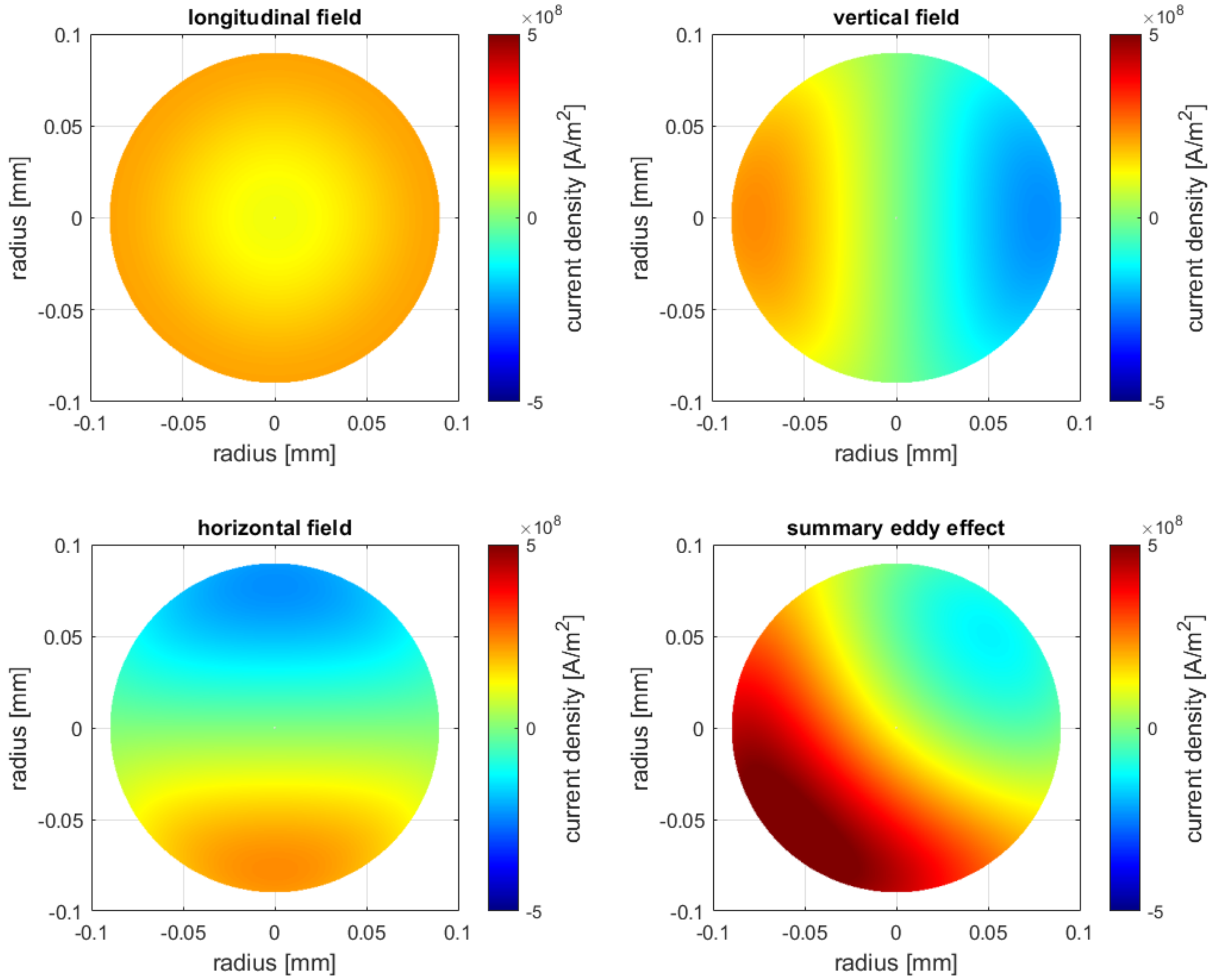

Figure 8.2 Summary of three orthogonal magnetic fields' effects (i.e., longitudinal, vertical and horizontal) in AWG33 copper wire using $B_x = B_y = B_z = 10$ mT and $f = 1.8$ MHz

8.3 Derivation of wire length W_{lcon} formula

Locating coil symmetry axis centrally and perpendicularly to the XY plane (shown in Figure 8.3), the position $P(x, y, z)$ on the given i-th turn can be defined in the Cartesian coordinates as:

$$x(\phi) = a(\phi)cos(\phi)\,, \tag{138}$$

$$y(\phi) = a(\phi)sin(\phi)\,, \tag{139}$$

$$z(\phi) = l_i + \left(\frac{l_{i+1} - l_i}{2\pi}\right)\phi = l_i + \rho\phi\,, \tag{140}$$

where the variable turn radius $a(\cdot)$ is:

$$a(\phi) = a_i + \left(\frac{a_{i+1} - a_i}{2\pi}\right)\phi = a_i + \Delta\phi\,, \tag{141}$$

and ϕ is a rotation angle around the coil symmetry axis.

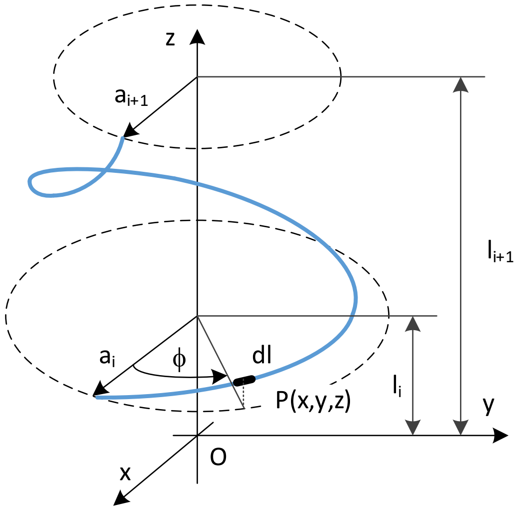

Figure 8.3 Definition of i-th turn length

The length of i-th turn W_{lcon} can be calculated as a sum of dl segments involving complete rotation, thus $\phi = \{0 \,..\, 2\pi\}$. Therefore,

$$W_{lcon} = \int_0^{2\pi} dl d\phi = \int_0^{2\pi} \sqrt{\left(\frac{dx}{d\phi}\right)^2 + \left(\frac{dy}{d\phi}\right)^2 + \left(\frac{dz}{d\phi}\right)^2}\, d\phi \,. \tag{142}$$

Equations (138) to (141) lead to the following derivatives:

$$\frac{da}{d\phi} = \Delta \,, \tag{143}$$

$$\frac{dx}{d\phi} = \Delta\cos(\phi) - (a_i + \Delta\phi)sin(\phi) \,, \tag{144}$$

$$\frac{dy}{d\phi} = \Delta\sin(\phi) + (a_i + \Delta\phi)cos(\phi) \,, \tag{145}$$

$$\frac{dz}{d\phi} = \rho \,. \tag{146}$$

Substituting above derivatives into (142) results in:

$$\begin{aligned} W_{lcon} = & \left[\frac{1}{2\Delta}\Big((\Delta\phi + a_i)\sqrt{\Delta^2(\phi^2+1) + 2\Delta a_i\phi + \rho^2 + {a_i}^2} \right. \\ & \left. + (\Delta^2 + \rho^2)log\left(\sqrt{\Delta^2(\phi^2+1) + 2\Delta a_i\phi + \rho^2 + {a_i}^2} + \Delta\phi + a_i\right)\Big)\right]_0^{2\pi} , \end{aligned} \tag{147}$$

for $\Delta \neq 0$. For the pure helical turn case (i.e., $a_i = a_{i+1}$, thus $\Delta = 0$) the equation (142) reduces to the known Pythagoras' formula as:

$$W_{lcon} = 2\pi\sqrt{\rho^2 + {a_i}^2} \,. \tag{148}$$

Consequently, considering the axial displacement as null (i.e., $l_i = l_{i+1}$, so $\rho = 0$), one may calculate the length of the planar turn, known as the Archimedean spiral. However, this process can be further simplified by integrating (141) in polar coordinates, using infinitesimal arc instead of the straight line segment dl, as:

$$W_{lcon} = \int_0^{2\pi} a(\phi)d\phi = \int_0^{2\pi} (a_i + \Delta\phi)d\phi = 2\pi(a_i + \pi\Delta) = \pi(a_i + a_{i+1}). \qquad (149)$$

8.4 Summary of prototype coils

This section summarizes data collected during the evaluation of the prototype coils.

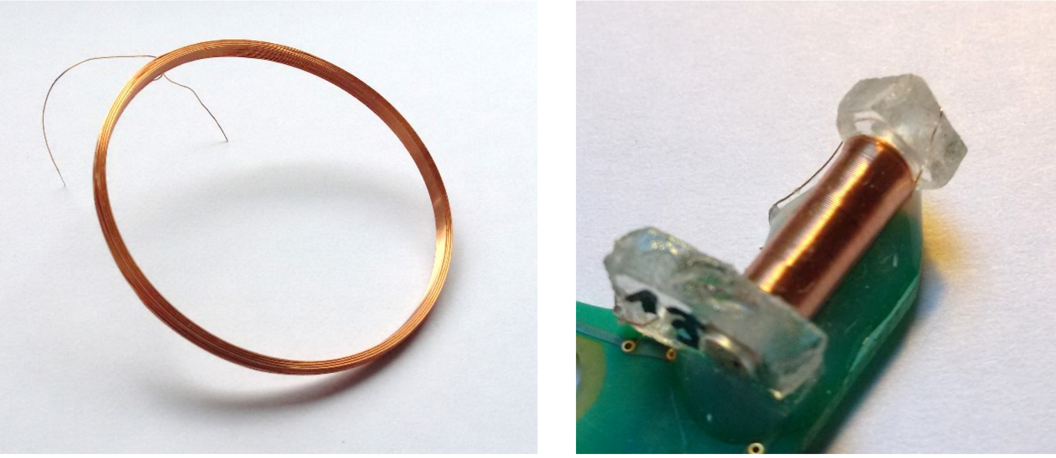

Figure 8.4 Picture of the air coil (left) and ferromagnetic-core coil (right) prototypes

Table 10 and Table 11 show coils' impedance data obtained analytically, being simulated, and measured, for the air coil and the ferrite-core based coil, respectively.

Table 10 Air coil summary

Parameter	**Analytic**		**2D simulation**		**Measured**
	nominal	**disordered**	**nominal**	**disordered**	
Internal self-inductance, L_{INT}, eqn. (15)	0.771 μH	0.775 μH	21.6 μH	20.3 μH	n/a
External self-inductance, L_{EXT}, eqn. (16)	18.74 μH	18.88 μH			
Mutual inductance, L_{MUT}, eqn. (18)	987.3 μH	975.2 μH	984.1 μH	973.4 μH	
Total inductance, L, eqn. (14)	1.0069 mH	0.9949 mH	1.0057 mH	0.9937 mH	0.9968 mH
Resistance, R_{dc}, eqn. (20)	10.39 Ω	10.48 Ω	10.66 Ω	10.76 Ω	10.43 Ω
Capacitance, C, eqn. (23), sim. (24)	48.7 pF	39.2 pF	46.54 pF	20.28 pF	47.4 pF
Resonance frequency, $\omega_{SRF}/2\pi$, eqn. (13)	718.7 kHz	805.91 kHz	735.7 kHz	1.121 MHz	735.5 kHz
Resistance, R_p, eqn. (12)	n/a	n/a	n/a	n/a	88.75 kΩ

Table 11 Ferrite-core coil summary

Parameter	**Analytic**		**2D simulation**		**Measured**
	nominal	**disordered**	**nominal**	**disordered**	
Internal self-inductance, L_{INT}, eqn. (15)	0.145 µH	0.153 µH	1.959 µH	2.005 µH	n/a
External self-inductance, L_{EXT}, eqn. (16)	2.044 µH	2.198 µH			
Mutual inductance, L_{MUT}, eqn. (18)	74.298 µH	81.052 µH	74.153 µH	82.212 µH	
Total inductance, L, eqn. (14), no core	76.488 µH	83.405 µH	76.112 µH	84.217 µH	n/a
Total inductance, with core FF = 19.1, eqn. (30); FF = 21.54, sim. 2D	1.4609 mH	1.593 mH	1.6402 mH	1.814 mH	1.6612 mH
Resistance, R_{dc}, eqn. (20)	10.41 Ω	10.63 Ω	10.53 Ω	10.82 Ω	9.83 Ω
Capacitance, C, eqn. (23), sim. (24)	18.2 pF	12.9 pF	17.21 pF	13.64 pF	15.4 pF
Resonance frequency, $\omega_{SRF}/2\pi$, eqn. (13)	976.05 kHz	1.11 MHz	947.29 kHz	1.018 MHz	994.53 kHz
Resistance, R_p, eqn. (12)	n/a	n/a	n/a	n/a	129.97 kΩ

8.5 Mutual coupling formulae

General formula

With reference to Figure 3.1 and the Babic work [53], the mutual inductance between two coils freely positioned in space is accurately described by equation (28). It is assumed, that the secondary coil is placed in the inclined plane centered at $C(x_c, y_c, z_c)$, whose general equation is:

$$\lambda \equiv\ ax + by + cz\,, \tag{150}$$

where a, b and c are the coefficients of the plane's transformation. The parameters p_1, p_2, p_3 and $\Psi(\cdot)$ of (28) are as follow:

$$p_1 = \frac{\gamma c}{l}, \tag{151}$$

with $\gamma = \frac{y_c}{r_p}$ and $l = \sqrt{a^2 + c^2}$;

$$p_2 = \frac{\beta l^2 + \gamma ab}{lL}, \tag{152}$$

with $\beta = \frac{x_c}{r_p}$ and $L = \sqrt{b^2 + l^2}$;

$$p_3 = \frac{\alpha c}{L}, \tag{153}$$

with $\alpha = \frac{r_s}{r_p}$;

$$\Psi(k) = \left(1 - \frac{k^2}{2}\right) K(k) - E(k)\,, \tag{154}$$

with $k^2 = \frac{4V_0}{A_0 + 2V_0}$.

Denominator of (28) is defined as:

$$\mathrm{V}_0^2 = \beta^2 + \gamma^2 + \alpha^2(l_1 cos^2\phi + l_2 sin^2\phi + l_3 sin2\phi) + 2\alpha(q_1 cos\phi + q_2 sin\phi)\,, \tag{155}$$

with parameters $l_1 = 1 - \frac{b^2c^2}{l^2L^2}$, $l_2 = \frac{c^2}{l^2}$, $l_3 = \frac{abc}{l^2L}$, $q_1 = \frac{\gamma l^2 - \beta ab}{lL}$, and $q_2 = -\frac{\beta c}{l}$.

Finally, the parameter A_0 is defined as:

$$A_0 = 1 + \alpha^2 + \beta^2 + \gamma^2 + \delta^2 + 2\alpha(p_4 cos\phi + p_5 sin\phi), \tag{156}$$

with $\delta = \frac{z_c}{r_p}$, $p_4 = \frac{\gamma l^2 - \beta a - \delta bc}{lL}$, and $p_5 = \frac{\delta a - \beta c}{l}$.

Filamentary formula

Referring to discretized winding shown in Figure 3.7 and [53], the meaning of formula (34) parameters is as follow:

$$M(g,h,p,q) = \frac{\mu_0 r_s(q)}{\pi} \int_0^{2\pi} \frac{(p_1 cos\phi + p_2 sin\phi + p_3)\Psi(k)}{k\sqrt{V_0^3}} d\phi\,, \tag{157}$$

with dependence on g, h, p and q as given below:

$$\alpha = \frac{r_s(q)}{r_p(h)}\,, \beta = \frac{x(p)}{r_p(h)}\,, \gamma = \frac{y(p)}{r_p(h)}, \delta = \frac{z(g,p)}{r_p(h)}\,. \tag{158}$$

Those parameters are defined as:

$$r_p(h) = r_p + \frac{h_p}{2N+1} h\,, \tag{159}$$

$$r_s(q) = r_s + \frac{h_s}{2n+1} q\,, \tag{160}$$

$$x(p) = x_c + \frac{l_s a}{2m+1} p\,, \tag{161}$$

$$y(p) = y_c + \frac{l_s b}{2m+1} p\,, \tag{162}$$

$$z(g,p) = z_c + \frac{l_p}{2S+1} g + \frac{l_s c}{2m+1} p\,. \tag{163}$$

8.6 Magnetic link equations

The primary side's circuit equations including mutual inductance *M* as an equivalent voltage source result with:

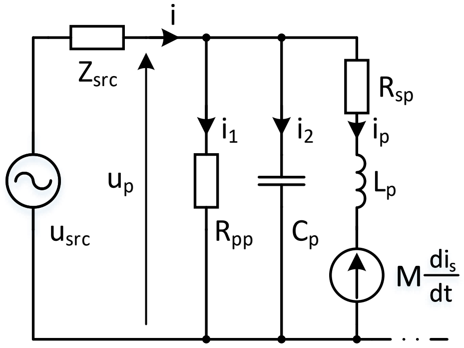

Figure 8.5 The primary side of the circuit

$$u_{src} - Z_{src} i - u_p = 0\,, \tag{164}$$

$$i_1 = \frac{u_p}{R_{pp}} = G_{pp} u_p\,, \tag{165}$$

$$i_2 = C_p \frac{du_p}{dt}\,, \tag{166}$$

$$u_p = R_{sp} i_p + L_p \frac{di_p}{dt} + M \frac{di_s}{dt}\,, \tag{167}$$

$$i = i_1 + i_2 + i_p\,. \tag{168}$$

The secondary side is supplemented by the AFE model from Figure 5.3, describing it as nonlinear resistance and capacitance. The circuit equations are therefore equal to:

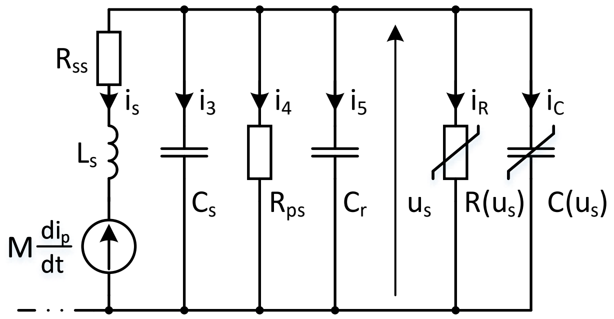

Figure 8.6 The secondary side of the circuit

$$u_s = R_{ss} i_s + L_s \frac{di_s}{dt} + M \frac{di_p}{dt}\,, \tag{169}$$

$$i_3 = C_s \frac{du_s}{dt}\,, \tag{170}$$

$$i_4 = \frac{u_s}{R_{ps}} = G_{ps} u_s\,, \tag{171}$$

$$i_5 = C_r \frac{du_s}{dt}\,, \tag{172}$$

$$i_R = \frac{u_s}{R(u_s)} = G(u_s) u_s\,, \tag{173}$$

$$i_C = C(u_s) \frac{du_s}{dt}\,, \tag{174}$$

$$i_s + i_3 + i_4 + i_5 + i_R + i_C = 0\,. \tag{175}$$

Magnetic link general formula

Putting together formulae (164)..(175) results with the set of nonlinear equations shown below:

$$\begin{cases} u_{src} - \left[\frac{d^2 i_p}{dt^2} R C_p L_p + \frac{di_p}{dt}\left(R G_{pp} L_p + R C_p R_{sp} + L_p\right) + i_p\left(R G_{pp} R_{sp} + R_{sp} + R\right) + \frac{d^2 i_s}{dt^2} R C_p M + \frac{di_s}{dt}\left(R G_{pp} M + M\right)\right] = 0 \\ \frac{d^2 i_s}{dt^2} L_s C + \frac{di_s}{dt}(R_{ss} C + G L_s) + i_s(G R_{ss} + 1) + \frac{d^2 i_p}{dt^2} M C + \frac{di_p}{dt} G M = 0 \\ u_s - R_{ss} i_s + L_s \frac{di_s}{dt} + M \frac{di_p}{dt} = 0 \end{cases}, \tag{176}$$

where G and C are defined for notation simplicity as:

$$G = G_{ps} + G(u_s)\,, \tag{177}$$

$$C = C_s + C_r + C(u_s)\,, \tag{178}$$

and the source impedance Z_{src} is replaced by the system resistance R.

9 References

[1] P. Razmjouei, A. Kavousi-Fard, M. Dabbaghjamanesh, T. Jin and W. Su, "Ultra-Lightweight Mutual Authentication in the Vehicle Based on Smart Contract Blockchain: Case of MITM Attack," *IEEE Sensors Journal,* vol. 21, no. 14, pp. 15839-15848, 2021.

[2] "CISPR 25, Vehicles, boats and internal combustion engines – Radio disturbance characteristics – Limits and methods of measurement for the protection of on-board receivers, Edition 4.0," IEC, 2014.

[3] "CISPR 16-1-1:2019 Specification for radio disturbance and immunity measuring apparatus and methods - Part 1-1: Radio disturbance and immunity measuring apparatus - Measuring apparatus," IEC, 2019.

[4] "FMC1278 Rev. 2 Electromagnetic Compatibility Specification For Electrical/Electronic Components and Subsystems," Ford, 2016.

[5] G. Oleszek, "2D Disturbance Map of Low-Power Front-End Circuits in Low Frequency Band," *Progress In Electromagnetics Research C,* vol. 92, pp. 87-100, 2019.

[6] Z. Chen and S. Frei, "Near-field measurement based prediction of antenna test results below 30 MHz in CISPR 25 setups," *2016 International Symposium on Electromagnetic Compatibility - EMC EUROPE,* pp. 17-22, 2016.

[7] C. Carobbi, "A Circuit Model of the Rod Antenna Automotive and Military Test Setups: Analysis and Interpretation," *2018 IEEE Symposium on Electromagnetic Compatibility, Signal Integrity and Power Integrity (EMC, SI & PI),* pp. 454-459, 2018.

[8] D. Schneider, S. Tenbohlen and W. Köhler, "Untersuchung von Vorhersagemethoden der Abstrahlung bei Komponententests nach CISPR 25," *EMV 2012, Internationale Fachmesse und Kongress für Elektromagnetische Verträglichkeit,* vol. 2012, pp. 263-271, 2012.

[9] S. Frei, R. G. Jobava, D. Karkashadze, A. Gheonjian and E. Yavolovskaya, "Calculation of low frequency EMC problems in large systems with a quasi-static approach," *2004 International Symposium on Electromagnetic Compatibility,* vol. 3, pp. 798-803, 2004.

[10] G. Xie, K. Yang, C. Xu, R. Li and S. Hu, "Digital Twinning Based Adaptive Development Environment for Automotive Cyber-Physical Systems," *IEEE Transactions on Industrial Informatics,* vol. 18, no. 2, pp. 1387-1396, 2022.

[11] G. Oleszek, "Coexistence of the wireless charger and low-power circuit in a car interior," *2021 IEEE 19th International Power Electronics and Motion Control Conference (PEMC),* pp. 237-242, 2021.

[12] G. Oleszek, "RF disturbances from magnetically coupled nonlinear AFE circuit under LF band," in *EPNC 2020 Electromagnetic Phenomena in Nonlinear Circuits : XXVI symposium*, Torino, Italy, 2020.

[13] D. Chen, J. A. Brug and R. B. Goldfarb, "Demagnetizing factors for cylinders," *IEEE Transactions on Magnetics,* vol. 27, no. 4, pp. 3601-3619, 1991.

[14] P. T. Theilmann and P. M. Asbeck, "An Analytical Model for Inductively Coupled Implantable Biomedical Devices With Ferrite Rods," *IEEE Transactions on Biomedical Circuits and Systems,* vol. 3, no. 1, pp. 43-52, 2009.

[15] P. Csurgai and M. Kuczmann, "Coupling Factor Calculation of Low Frequency RFID Systems by the Mutual Inductance Effective Permeability Method," *Acta Technica Jaurinensis,* vol. 6, no. 1, pp. 31-37, 2013.

[16] F. P. Cortes, "A low-power RF/analog front-end architecture for LF passive RFID tags with dynamic power sensing," *2014 IEEE International Conference on RFID (IEEE RFID),* pp. 60-66, 2014.

[17] N. Gvozdenovic, L. W. Mayer and C. F. Mecklenbräuker, "Measurement of harmonic distortions and impedance of HF RFID chips," *8th European Conference on Antennas and Propagation (EuCAP 2014),* pp. 2940-2944, 2014.

[18] N. Gvozdenovic, R. Prestros and C. F. Mecklenbräuker, "HF RFID spiral inductor synthesis and optimization," *2014 International Symposium on Wireless Personal Multimedia Communications (WPMC),* pp. 53-59, 2014.

[19] M. Faifer, C. Laurano, R. Ottoboni, S. Toscani and M. Zanoni, "Harmonic Distortion Compensation in Voltage Transformers for Improved Power Quality Measurements," *IEEE Transactions on Instrumentation and Measurement,* vol. 68, no. 10, pp. 3823-3830, 2019.

[20] M. Gebhart, J. Bruckbauer and M. Gossar, "Chip impedance characterization for contactless proximity personal cards," *2010 7th International Symposium on Communication Systems, Networks & Digital Signal Processing (CSNDSP 2010),* pp. 826-830, 2010.

[21] S. Rizkalla, R. Prestros and C. F. Mecklenbräuker, "Optimal Card Design for Non-Linear HF RFID Integrated Circuits With Guaranteed Standard-Compliance," *IEEE Access,* vol. 6, pp. 47843-47856, 2018.

[22] F. Giannini and G. Leuzzi, Nonlinear Microwave Circuit Design, Chichester: John Wiley & Sons Ltd, 2004.

[23] M. I. Goffioul, P. Wambacq, G. Vandersteen and S. Donnay, "Analysis of nonlinearities in RF front-end architectures using a modified Volterra series approach," *Proceedings 2002 Design, Automation and Test in Europe Conference and Exhibition,* pp. 352-356, 2002.

[24] X. Y. Z. Xiong, L. J. Jiang, J. E. Schutt-Ainé and W. C. Chew, "Volterra Series-Based Time-Domain Macromodeling of Nonlinear Circuits," *IEEE Transactions on Components, Packaging and Manufacturing Technology,* vol. 7, no. 1, pp. 39-49, 2017.

[25] W. R. Jacobs, T. J. Dodd and S. R. Anderson, "Frequency-Domain Analysis for Nonlinear Systems With Time-Domain Model Parameter Uncertainty," *IEEE Transactions on Automatic Control,* vol. 64, no. 5, pp. 1905-1915, 2019.

[26] H. Q. Benedikt and P. J. Tasker, "Nonlinear Data Utilization: From Direct Data Lookup to Behavioral Modeling," *IEEE Transactions on Microwave Theory and Techniques,* vol. 57, no. 6, pp. 1425-1432, 2009.

[27] X. Y. Z. Xiong, L. J. Jiang, J. E. Schutt-Ainé and W. C. Chew, "Blackbox macro-modeling of the nonlinearity based on Volterra series representation of X-parameters," *2014 IEEE 23rd Conference on Electrical Performance of Electronic Packaging and Systems,* pp. 85-88, 2014.

[28] K. Gao, R. Xie and G. Zhang, "Harmonic Analysis of Nonlinear Periodic Network Using the Dynamic Harmonic Domain," *2020 7th International Forum on Electrical Engineering and Automation (IFEEA),* pp. 616-622, 2020.

[29] S. Frei, "Bestimmung der bordnetzgebundenen Störaussendung mit dem kapazitiven Spannungssensor," *GMM-Tagung,* 2005.

[30] "CISPR TR 16-4-1:2009 Specification for radio disturbance and immunity measuring apparatus and methods - Part 4-1: Uncertainties, statistics and limit modelling - Uncertainties in standardized EMC tests," IEC, 2009.

[31] "ISO/IEC GUIDE 98-3:2008 Uncertainty of measurement — Part 3: Guide to the expression of uncertainty in measurement (GUM:1995)," ISO, 2008.

[32] J. Bönig, B. Bickel, M. Spahr, C. Fischer and J. Franke, "Simulation of orthocyclic windings using the linear winding technique," *2015 5th International Electric Drives Production Conference (EDPC),* pp. 1-6, 2015.

[33] P. Stenzel, P. Dollinger, J. Richnow and J. Franke, "Innovative needle winding method using curved wire guide in order to significantly increase the copper fill factor," *2014 17th International Conference on Electrical Machines and Systems (ICEMS),* pp. 3047-3053, 2014.

[34] "Magnet Wire," Cooner Wire, [Online]. Available: https://www.coonerwire.com/magnet-wire/. [Accessed 11 November 2021].

[35] "Cable Dielectric (Insulation)," ATLAS, 2019. [Online]. Available: https://www.atlascables.com/design-insulation.html. [Accessed 11 November 2021].

[36] W. L. Lenders, "The orthocyclic method of coil winding," Philips, 1962.

[37] V. A. Callcut , "Coppers for electrical purposes," *IEE Proceedings A (Physical Science, Measurement and Instrumentation, Management and Education, Reviews),* vol. 133, no. 4, p. 174 – 201, 1986.

[38] F. A. Wolff and J. H. Dellinger, "The electrical conductivity of commercial copper," *Proceedings of the American Institute of Electrical Engineers,* vol. 29, no. 12, pp. 1981-2008, 1910.

[39] *Low Frequency EM Field Simulation,* Ansys Maxwell, 2019.

[40] S. Z. Dabbak, H. A. Illias, B. C. Ang, N. A. Latiff and M. Z. Makmud, "Electrical Properties of Polyethylene/Polypropylene," *Energies,* vol. 11, pp. 1-13, 2018.

[41] "Pitch and Diameter Accuracy in Coil Winding," Engineering by Design, October 2014. [Online]. Available: https://www.ebdesign.com/solutions/pitch-and-diameter-accuracy-in-coil-winding/. [Accessed 09 November 2021].

[42] J. Hagedorn, F. Sell-Le Blanc and J. Fleischer, Handbook of Coil Winding: Technologies for efficient electrical wound products and their automated production, Springer, 2017.

[43] T. Wang, "Influence of Winding Accuracy on Magnetic Field Distribution in YBCO Pancake Coil for Cyclotron Application," *IEEE Transactions on Applied Superconductivity,* vol. 24, no. 3, pp. 1-5, 2014.

[44] S. Takayama, "Influence of Manufacturing Accuracy on Magnetic Field Distribution in Magnet for HTS Rotating Gantry," *IEEE Transactions on Applied Superconductivity,* vol. 26, no. 4, pp. 1-4, 2016.

[45] P. N. Murgatroyd, "The optimal form for coreless inductors," *IEEE Transactions on Magnetics,* vol. 25, no. 3, pp. 2670-2677, 1989.

[46] A. Rikhter and M. Fogler, "Inductor coil of the highest possible Q," *Sci Rep 10,* 2020.

[47] J. Martínez, S. Babic and C. Akyel, "On Evaluation of Inductance, DC Resistance, and Capacitance of Coaxial Inductors at Low Frequencies," *IEEE Transactions on Magnetics,* vol. 50, no. 7, pp. 1-12, 2014.

[48] M. Aghaei and S. Kaboli, "On the Effect of Disorder on Stray Capacitance of Transformer Winding in High-Voltage Power Supplies," *IEEE Transactions on Industrial Electronics,* vol. 64, no. 5, pp. 3608-3618, 2017.

[49] S. Mohsenzade, M. Aghaei and S. Kaboli, "Leakage Inductance Calculation of the Transformers With Disordered Windings," *IEEE Transactions on Plasma Science,* vol. 47, no. 4, pp. 1799-1807, 2019.

[50] C. Snow, "The mutual inductance of two parallel circles," *Bureau of Standards Journal of Research,* vol. 3, no. 2, p. Research Paper 94, 1929.

[51] H. Nagaoka, "The Inductance Coefficients of Solenoids," *Journal of the College of Science, Imperial University,* vol. 27, no. 6, pp. 1-33, 1909.

[52] H. A. Wheeler, "Simple Inductance Formulas for Radio Coils," *Proceedings of the Institute of Radio Engineers,* vol. 16, no. 10, pp. 1398-1400, 1928.

[53] S. Babic, J. Martinez, C. Akyel and B. Babic, "Mutual Inductance Calculation Between Misalignment Coils for Wireless Power Transfer of Energy," *Progress In Electromagnetics Research M,* vol. 38, pp. 91-102, 2014.

[54] K. Fotopoulou and B. W. Flynn, "Wireless Power Transfer in Loosely Coupled Links: Coil Misalignment Model," *IEEE Transactions on Magnetics,* vol. 47, no. 2, pp. 416-430, 2011.

[55] M. Schormans, V. Valente and A. Demosthenous, "Practical Inductive Link Design for Biomedical Wireless Power Transfer: A Tutorial," *IEEE Transactions on Biomedical Circuits and Systems,* vol. 12, no. 5, pp. 1112-1130, 2018.

[56] C. Kuhlmann, S. Draack , T. Viereck , M. Schilling and F. Ludwig, "Modeling the impedance of water-cooled core-less multi-layered solenoid coils for MPI drive field generation," *International Journal on Magnetic Particle Imaging,* vol. 4, no. 1, pp. 1-9, 2018.

[57] H. A. Wheeler, "Formulas for the Skin Effect," *Proceedings of the IRE,* vol. 30, no. 9, pp. 412-424, 1942.

[58] J. Lammeraner and M. Stafl, Eddy Currents, London: Iliffe Books, 1966.

[59] W. R. Smythe, Static and Dynamic Electricity, McGraw-Hill Book Company Inc., 1950.

[60] P. L. Dowell, "Effects of eddy currents in transformer windings," *Proceedings of the Institution of Electrical Engineers,* vol. 113, no. 8, pp. 1387-1394, 1966.

[61] R. P. Wojda and M. K. Kazimierczuk, "Winding Resistance and Power Loss of Inductors With Litz and Solid-Round Wires," *IEEE Transactions on Industry Applications,* vol. 54, no. 4, pp. 3548-3557, 2018.

[62] Y. Yin and L. Li, "Improved method to calculate the high-frequency eddy currents distribution and loss in windings composed of round conductors," *IET Power Electron.,* vol. 10, no. 12, p. 1494–1503, 2017.

[63] X. Nan and C. R. Sullivan, "Simplified high-accuracy calculation of eddy-current loss in round-wire windings," *IEEE 35th Annual Power Electronics Specialists Conference,* vol. 2, pp. 873-879, 2004.

[64] D. Whitman and M. K. Kazimierczuk, "An Analytical Correction to Dowell's Equation for Inductor and Transformer Winding Losses Using Cylindrical Coordinates," *IEEE Transactions on Power Electronics,* vol. 34, no. 11, pp. 10425-10432, 2019.

[65] J. A. Ferreira, "Appropriate modelling of conductive losses in the design of magnetic components," *21st Annual IEEE Conference on Power Electronics Specialists,* pp. 780-785, 1990.

[66] M. K. Kazimierczuk, G. Sancineto, G. Grandi, U. Reggiani and A. Massarini, "High-frequency small-signal model of ferrite core inductors," *IEEE Transactions on Magnetics,* vol. 35, no. 5, pp. 4185-4191, 1999.

[67] Z. Shen, Y. Shen, Z. Qin and H. Wang, "Modeling and Optimization of Displacement Windings for Transformers in Dual Active Bridge Converters," *2018 International Power Electronics Conference (IPEC-Niigata 2018 -ECCE Asia),* pp. 1925-1930, 2018.

[68] Z. Shen and H. Wang, "Parasitics of Orthocyclic Windings in Inductors and Transformers," *IEEE Transactions on Power Electronics,* vol. 36, no. 2, pp. 1994-2008, 2021.

[69] G. S. Dimitrakakis, E. C. Tatakis and E. J. Rikos, "A Semiempirical Model to Determine HF Copper Losses in Magnetic Components With Nonlayered Coils," *IEEE Transactions on Power Electronics,* vol. 23, no. 6, pp. 2719-2728, 2008.

[70] J. Kim and Y. Park, "Approximate Closed-Form Formula for Calculating Ohmic Resistance in Coils of Parallel Round Wires With Unequal Pitches," *IEEE Transactions on Industrial Electronics,* vol. 62, no. 6, pp. 3482-3489, 2015.

[71] C. R. Sullivan, "Computationally efficient winding loss calculation with multiple windings, arbitrary waveforms, and two-dimensional or three-dimensional field geometry," *IEEE Transactions on Power Electronics,* vol. 16, no. 1, pp. 142-150, 2001.

[72] R. Bramanpalli, "Accurate Calculation of AC Losses of Inductors in Power Electronic Applications," *PCIM Europe 2016; International Exhibition and Conference for Power Electronics, Intelligent Motion, Renewable Energy and Energy Management,* pp. 1-8, 2016.

[73] M. J. Jacoboski, A. de Bastiani Lange and M. L. Heldwein, "Closed-Form Solutions for Core and Winding Losses Calculation in Single-Phase Boost PFC Rectifiers," *2019 IEEE 15th Brazilian Power Electronics Conference and 5th IEEE Southern Power Electronics Conference (COBEP/SPEC),* pp. 1-6, 2019.

[74] E. C. Snelling, Soft Ferrites, Second Edition: Properties and Applications 2nd Edition, Butterworth-Heinemann, 1988.

[75] P. Szczerba, S. Ligenza, P. Trojan and C. Worek, "Practical Design Considerations of Inductor AC Resistance Calculation Methods," *2019 20th International Symposium on Power Electronics (Ee),* pp. 1-5, 2019.

[76] C. P. Steinmetz, "On the law of hysteresis," *Proceedings of the IEEE,* vol. 72, no. 2, pp. 197-221, 1984.

[77] G. Durin and S. Zapperi, "The Barkhausen Effect," *Materials Science, Physics,* 2006.

[78] J. Muhlethaler, J. Biela, J. W. Kolar and A. Ecklebe, "Improved Core-Loss Calculation for Magnetic Components Employed in Power Electronic Systems," *IEEE Transactions on Power Electronics,* vol. 27, no. 2, pp. 964-973, 2012.

[79] "Ferroxcube material loss coefficients, Technical Note," FERROXCUBE, 2016.

[80] "3C90 Material specification," FERROXCUBE, 2008.

[81] N. C. Hamilton, "Ferrites: magnetic and electric equivalent circuits and the complex permeability spectra," *Active and Passive RF Devices Seminar,* pp. 1-8, 2016.

[82] C. A. Balanis, Antenna theory: analysis and design, vol. 2, John Wiley & Sons, Inc, 2016.

[83] D. H. Werner, "Exact Expressions for the Total Radiated Power, Radiation Resistance, and Directivity of an Arbitrary Size Uniform Current Elliptical Loop Antenna," *IEEE Transactions on Antennas and Propagation,* vol. 68, no. 9, pp. 6816-6820, 2020.

[84] F. M. Rotella, V. Blaschke and D. Howard, "A broad-band scalable lumped-element inductor model using analytic expressions to incorporate skin effect, substrate loss, and proximity effect," *Digest. International Electron Devices Meeting,* pp. 471-474, 2002.

[85] C. Bednarz, H. Schreiber and M. Leone, "Efficient Multiport Equivalent Circuit for Skin and Proximity Effect in Parallel Conductors With Arbitrary Cross Sections," *IEEE Transactions on Electromagnetic Compatibility,* vol. 60, no. 6, pp. 2053-2056, 2018.

[86] A. Schellmanns, P. Keradec and J. L. Schanen, "Electrical equivalent circuit for frequency dependant impedance: minimum lumped elements for a given precision [SMPS transformer]," *IEEE Industry Applications Conference. Thirty-Fifth IAS Annual Meeting and World Conference on Industrial Applications of Electrical Energy,* vol. 5, pp. 3105-3110, 2000.

[87] F. d. Leon and A. Semlyen, "Time domain modeling of eddy current effects for transformer transients," *IEEE Transactions on Power Delivery,* vol. 8, no. 1, pp. 271-280, 1993.

[88] D. Deswal and F. de León, "Generalized Circuit Model for Eddy Current Effects in Multi-Winding Transformers," *IEEE Transactions on Power Delivery,* vol. 34, no. 2, pp. 638-650, 2019.

[89] W. Cheng, "Frequency Properties of an Air-Cored Coil and Application to Conductivity Measurement," *IEEE Access,* vol. 8, pp. 219802-219809, 2020.

[90] E. B. Rosa and F. W. Grover, "Formulas and Tables for the Calculation of Mutual and Self Inductance," *Bulletin of the Bureau of Standards,* vol. 8, no. 1, 1911.

[91] C. Snow, "A simplified precision formula for the inductance of a helix with corrections for the lead-in wires, RP479," *Bureau of Standards Journal of Research,* vol. 9, pp. 419-426, 1932.

[92] Y. Qiu, Q. Zhang and M. L. Zhang, "Numerical calculation on multi-layers solenoidal coil," *IEEE Transactions on Magnetics,* vol. 29, no. 2, pp. 1434-1437, 1993.

[93] S. R. Khan, S. K. Pavuluri and M. P. Desmulliez, "Accurate Modeling of Coil Inductance for Near-Field Wireless Power Transfer," *IEEE Transactions on Microwave Theory and Techniques,* vol. 66, no. 9, pp. 4158-4169, 2018.

[94] E. Kaverine, S. Palud, F. Colombel and M. Himdi, "Investigation on an Effective Magnetic Permeability of the Rod-Shaped Ferrites," *Progress In Electromagnetics Research Letters,* vol. 65, pp. 43-48, 2017.

[95] J. C. Maxwell, A Treatise on Electricity and Magnetism, London: Oxford University Press, 1873.

[96] C. T. Johnk, Engineering electromagnetic fields and waves, John Willey & Sons Inc., 1988.

[97] B. Liu, R. Ren, F. Wang, D. Costinett and Z. Zhang, "Winding Scheme With Fractional Layer for Differential-Mode Toroidal Inductor," *IEEE Transactions on Industrial Electronics,* vol. 67, no. 2, pp. 1592-1604, 2020.

[98] E. Laveuve, J. Keradec and M. Bensoam, "Electrostatic of wound components: analytical results, simulation and experimental validation of the parasitic capacitance," *Conference Record of the 1991 IEEE Industry Applications Society Annual Meeting,* vol. 2, pp. 1469-1475, 1991.

[99] J. Biela and J. W. Kolar, "Using Transformer Parasitics for Resonant Converters-A Review of the Calculation of the Stray Capacitance of Transformers," *IEEE Transactions on Industry Applications,* vol. 44, no. 1, pp. 223-233, 2008.

[100] A. De Leo and G. Cerri, "A Charge Distribution Based Model for the Evaluation of an Air-Coil Stray Capacitance," *IEEE Transactions on Electromagnetic Compatibility,* vol. 61, no. 5, pp. 1673-1677, 2019.

[101] M.-X. Du, Y. Zhang, H. Wang, Y. Tian, Z. Ouyang and K.-X. Wei, "An Improved Calculation Method for Static Capacitance in Inductor Windings," *Progress In Electromagnetics Research C,* vol. 104, pp. 25-36, 2020.

[102] H. Li and W. M. Rucker, "An Accurate and Efficient Hybrid Method for the Calculation of the Equivalent Capacitance of an Arbitrary-Shaped Coil," *IEEE Transactions on Magnetics,* vol. 52, no. 3, pp. 1-4, 2016.

[103] L. F. d. F. Gutierres and G. Cardoso, "Analytical Technique for Evaluating Stray Capacitances in Multiconductor Systems: Single-Layer Air-Core Inductors," *IEEE Transactions on Power Electronics,* vol. 33, no. 7, pp. 6147-6158, 2018.

[104] A. Massarini, "Analytical Approach to the Calculation of Parasitic Capacitance Between Winding Turns," *2018 IEEE 4th International Forum on Research and Technology for Society and Industry (RTSI),* pp. 1-4, 2018.

[105] H. Zhao et all, "Physics-Based Modeling of Parasitic Capacitance in Medium-Voltage Filter Inductors," *IEEE Transactions on Power Electronics,* vol. 36, no. 1, pp. 829-843, 2021.

[106] Z. Shen, H. Wang, Y. Shen, Z. Qin and F. Blaabjerg, "An Improved Stray Capacitance Model for Inductors," *IEEE Transactions on Power Electronics,* vol. 34, no. 11, pp. 11153-11170, 2019.

[107] F. Salomez, A. Videt and N. Idir, "Semi-Analytical Model of Parasitic Capacitance of Inductor with Conductive Core," *International Exhibition and Conference for Power Electronics, Intelligent Motion, Renewable Energy and Energy Management,* pp. 1-8, 2021.

[108] X. Liu, W. Zhong, H. Cui, P. Lin and D. Xu, "Precise General Modeling of Windings for Wireless Power Transfer," *2019 IEEE Energy Conversion Congress and Exposition (ECCE),* pp. 5337-5343, 2019.

[109] N. Djukic, L. Encica and J. J. Paulides, "Overview of capacitive couplings in windings," *2015 Tenth International Conference on Ecological Vehicles and Renewable Energies (EVER),* pp. 1-11, 2015.

[110] D. Liang, K. Zhang, Q. Jiang and Y. Wang, "A Novel Analytic Method to Calculate the Equivalent Stray Capacitance of the Low-Speed Maglev Train's Suspension Electromagnet," *Energies,* vol. 20, 2020.

[111] Q. Yu and T. W. Holmes, "Stray capacitance modeling of inductors by using the finite element method," *IEEE International Symposium on Electromagnetic Compatability,* vol. 1, pp. 305-310, 1999.

[112] T. Duerbaum and G. Sauerlaender, "Energy based capacitance model for magnetic devices," *Sixteenth Annual IEEE Applied Power Electronics Conference and Exposition,* vol. 1, pp. 109-115, 2001.

[113] M. Aghaei, S. Mohsenzade and S. Kaboli, "On the Calculation of the Leakage Inductance in Transformers With Nonideal Windings," *IEEE Transactions on Power Electronics,* vol. 35, pp. 8460-8471, 2020.

[114] "Prometheus, Klaster obliczeniowy," Akademickie Centrum Komputerowe Cyfronet AGH, 2021. [Online]. Available: https://www.cyfronet.pl/komputery/15207,artykul,prometheus.html. [Accessed 11 November 2021].

[115] L. Deng, P. Wang, X. Li, H. Xiao and T. Peng, "Investigation on the Parasitic Capacitance of High Frequency and High Voltage Transformers of Multi-Section Windings," *IEEE Access,* vol. 8, pp. 14065-14073, 2020.

[116] G. Oleszek, "Estimation of the Operating Range of Automotive Key Fobs during a Radiated Emissions Test under a Low Frequency Band," *2019 MIXDES - 26th International Conference "Mixed Design of Integrated Circuits and Systems,* pp. 350-355, 2019.

[117] F. E. Neumann, "Allgemeine Gesetze der inducirten elektrischen Ströme," *Abhandlungen der Königlichen Akademie der Wissenschaften zu Berlin,* p. 1–87, 1845.

[118] S. Butterworth, "On the coeffcients of mutual induction of eccentric coils," *Philosophical Magazine,* vol. 31, pp. 443-454, 1916.

[119] F. W. Grover, "The Calculation of the Mutual Inductance of Circular Filaments in Any Desired Positions," *Proceedings of the IRE,* vol. 32, no. 10, pp. 620-629, 1944.

[120] M. Soma, D. C. Galbraith and R. L. White, "Radio-Frequency Coils in Implantable Devices: Misalignment Analysis and Design Procedure," *IEEE Transactions on Biomedical Engineering,* Vols. BME-34, no. 4, pp. 276-282, 1987.

[121] K. Fotopoulou and B. W. Flynn, "Wireless Powering of Implanted Sensors using RF Inductive Coupling," *SENSORS,* pp. 765-768, 2006.

[122] X. Zhang, H. Meng, B. Wei, S. Wang and Q. Yang, "Mutual inductance calculation for coils with misalignment in wireless power transfer," *The Journal of Engineering,* vol. 16, no. 3, pp. 1041-1044, 2019.

[123] S. Babic, F. Sirois, C. Akyel and C. Girardi, "Mutual Inductance Calculation Between Circular Filaments Arbitrarily Positioned in Space: Alternative to Grover's Formula," *IEEE Transactions on Magnetics,* vol. 46, no. 9, pp. 3591-3600, 2010.

[124] Y. Yu and Y. Luo, "Inductance calculations for non-coaxial Bitter coils with rectangular cross-section using inverse Mellin transform," *IET Electric Power Applications,* vol. 13, no. 1, pp. 119-125, 2019.

[125] S. Xianjin, L. Guoqiang, Z. Chao, L. Yanhong and X. Xiaoyu, "Analyses of the coupling model combining field and circuit equations based on solenoidal coils for wireless power transfer," *IET Power Electronics,* vol. 13, no. 4, pp. 873-880, 2020.

[126] G. Di Capua, "Mutual Inductance Behavioral Modeling for Wireless Power Transfer System Coils," *IEEE Transactions on Industrial Electronics,* vol. 68, no. 3, pp. 2196-2206, 2019.

[127] R. M. Bozorth, "Demagnetizing Factors of Rods," *Journal of Applied Physics,* vol. 13, no. 5, p. 320, 1942.

[128] J. T. Conway, "Inductance Calculations for Noncoaxial Coils Using Bessel Functions," *IEEE Transactions on Magnetics,* vol. 43, no. 3, pp. 1023-1034, 2007.

[129] W. G. Hurley, M. C. Duffy, J. Zhang, I. Lope, B. Kunz and W. H. Wölfle, "A Unified Approach to the Calculation of Self- and Mutual-Inductance for Coaxial Coils in Air," *IEEE Transactions on Power Electronics,* vol. 30, no. 11, pp. 6155-6162, 2015.

[130] R. A. Schill, "General relation for the vector magnetic field of a circular current loop: a closer look," *IEEE Transactions on Magnetics,* vol. 39, no. 2, pp. 961-967, 2003.

[131] A. Marinescu and I. Dumbravă, "Using VNA for IPT coupling factor measurement," *2016 IEEE International Power Electronics and Motion Control Conference (PEMC),* pp. 1026-1030, 2016.

[132] J. Seon-Jae and D. W. Seo, "Coupling Coefficient Measurement Method with Simple Procedures Using a Two-Port Network Analyzer for a Multi-Coil WPT System," *Energies,* vol. 12, no. 20, pp. 1-10, 2019.

[133] M. Shauber, "Measurement of mutual inductance from the frequency dependence of impedance of AC coupled circuits using a digital dual-phase lock-in amplifier," *American Journal of Physics,* vol. 76, no. 129, 2008.

[134] S. Raju, R. Wu, M. Chan and C. P. Yue, "Modeling of Mutual Coupling Between Planar Inductors in Wireless Power Applications," *IEEE Transactions on Power Electronics,* vol. 29, no. 1, pp. 481-490, 2014.

[135] D. Stahl and W. Mathis, "Coupling aspects between two coils in arbitrary position," *2013 International Conference on Electromagnetics in Advanced Applications (ICEAA),* pp. 1020-1023, 2013.

[136] M. Yang, Y. Wang, X. Zhang and J. Li, "Analysis of Reflected Load Model for Inductively Coupled Power Transfer Systems," *2010 Asia-Pacific Power and Energy Engineering Conference,* pp. 1-4, 2010.

[137] D. M. Beams and S. G. Annam, "Validation of a reflected-impedance design method for wireless power transfer applications," *2012 IEEE 55th International Midwest Symposium on Circuits and Systems (MWSCAS),* pp. 758-761, 2012.

[138] C. C. C. dos Santos, L. J. Ortiz, J. P. Américo and K. S. Linares, "Nonlinear modeling of magnetic materials for electromagnetic devices simulation," *2017 IEEE XXIV International Conference on Electronics, Electrical Engineering and Computing (INTERCON),* pp. 1-4, 2017.

[139] L. G. Petrescu, "Magnetic Properties of Manganese-Zinc Soft Ferrite Ceramic for High Frequency Applications," *Materials,* vol. 12, 2019.

[140] R. Kronberger, A. Geissler and B. Friedmann, "New methods to determine the impedance of UHF RFID chips," *2010 IEEE International Conference on RFID (IEEE RFID 2010),* pp. 260-265, 2010.

[141] J. Essel, D. Brenk, J. Heidrich, R. Weigel and D. Kissinger, "Large-Signal Measurements and Nonlinear Characterization of an Analog Frontend for Passive UHF CMOS RFID Transponders," *IEEE Transactions on Microwave Theory and Techniques,* vol. 61, no. 2, pp. 948-959, 2013.

[142] T. R. Turlington, Behavioral Modeling of Nonlinear RF and Microwave Devices, Artech House, 1999.

[143] J. Balcells, M. Lamich, E. Griful and M. Corbalan, "Influence of data resolution in nonlinear loads model for harmonics prediction," *IECON 2016 - 42nd Annual Conference of the IEEE Industrial Electronics Society,* pp. 6560-6565, 2016.

[144] J. E. Caicedo, A. A. Romero and H. C. Zini, "Frequency domain modeling of nonlinear loads, considering harmonic interaction," *2017 IEEE Workshop on Power Electronics and Power Quality Applications (PEPQA),* pp. 1-6, 2017.

[145] T. Komuro, S. Sobukawa, H. Sakayori, M. Kono and H. Kobayashi, "Total Harmonic Distortion Measurement System of Electronic Devices up to 100 MHz With Remarkable Sensitivity," *IEEE Transactions on Instrumentation and Measurement,* vol. 56, no. 6, pp. 2360-2368, 2007.

[146] T. Sun, F. Xu, J. Lu, Y. Xu and K. Liu, "Novel and simplified passive intermodulation distortion measurement using vector network analyzer," *2014 9th IEEE Conference on Industrial Electronics and Applications,* pp. 1688-1690, 2014.

[147] A. Greer, J. G. Leckey, A. D. Patterson, V. F. Fusco and J. A. Stewart, "A non linear vector corrected measurement system for device and system characterisation," *MTT/ED/AP/LEO Societies Joint,* pp. 14-20, 1997.

[148] K. Kishore and S. A. Akbar, "Evolution of Lock-In Amplifier as Portable Sensor Interface Platform: A Review," *IEEE Sensors Journal,* vol. 20, no. 18, pp. 10345-10354, 2020.

[149] L. Sainz, "Harmonic filter design by the attenuation factor method," *10th International Conference on Harmonics and Quality of Power,* vol. 2, pp. 513-518, 2002.

[150] M. Horibe, "Performance comparisons between impedance analyzers and vector network analyzers for impedance measurement below 100 MHz frequency," *89th ARFTG Microwave Measurement Conference (ARFTG),* pp. 1-4, 2017.

[151] J. Liu, U. Frühauf and A. Schönecker, "Accuracy improvement of impedance measurements by using the self-calibration," *Measurement,* vol. 25, no. 3, pp. 213-225, 1999.

[152] Y. Yang, J. Wang, Z. Gao and Y. Liu, "Accuracy improvement by A three-reference calibration algorithm for a bioimpedance spectrometer," *International Conference on Bioinformatics and Biomedical Technology,* pp. 253-256, 2010.

[153] M. Dutta, A. Rakshit, S. N. Bhattacharyya and J. K. Choudhury, "An application of an LMS adaptive algorithm for a digital AC bridge," *IEEE Transactions on Instrumentation and Measurement,* vol. 36, no. 6, pp. 894-897, 1987.

[154] M. Faifer, C. Laurano, R. Ottoboni, S. Toscani and M. Zanoni, "A Simple Method for Compensating the Harmonic Distortion Introduced by Voltage Transformers," *IEEE 9th International Workshop on Applied Measurements for Power Systems (AMPS),* pp. 1-6, 2018.

[155] R. Stiegler, J. Meyer, J. Kilter and S. Konzelmann, "Assessment of voltage instrument transformers accuracy for harmonic measurements in transmission systems," *17th International Conference on Harmonics and Quality of Power (ICHQP),* pp. 152-157, 2016.

[156] G. A. Kyriazis and M. L. de Campos, "An algorithm for accurately estimating the harmonic magnitudes and phase shifts of periodic signals with asynchronous sampling," *IEEE Transactions on Instrumentation and Measurement,* vol. 54, no. 2, pp. 496-499, 2005.

[157] H. Zhang, Y. Wang, C. Zhu, Y. Mei, T. Xu and F. Lu, "The High Order Harmonic Distortion Phenomenon in the Strongly Coupled IPT System and Its Reduction Method," *IEEE Energy Conversion Congress and Exposition (ECCE),* pp. 4223-4228, 2019.

[158] G. Palumbo and S. Pennisi, "Feedback amplifiers: a simplified analysis of harmonic distortion in the frequency domain," *ICECS 2001. 8th IEEE International Conference on Electronics, Circuits and Systems,* vol. 1, pp. 209-212, 2001.

[159] P. G. Sulzer, "A Note on a Bridged-T Network," *Proceedings of the IRE,* vol. 39, no. 7, pp. 819-821, 1951.

[160] B. Ross, "T-Coils and Bridged-T Networks," in *European IBIS Summit*, Naples, 2011.

[161] A. Cataliotti, V. Cosentino, G. Crotti, D. Giordano, M. Modarres, D. Di Cara, G. Tinè, D. Gallo, C. Landi and M. Luiso, "Metrological performances of voltage and current instrument transformers in harmonics measurements," *2018 IEEE International Instrumentation and Measurement Technology Conference (I2MTC),* pp. 1-6, 2018.

[162] A. Wiliams and F. Taylor, Electronic Filter Design Handbook, Fourth Edition, McGraw-Hill Education, 2006.

[163] H. Meuche and M. Esguerra, "Ferrite cores for xDSL: optimum selection," *Proceedings: Electrical Insulation Conference and Electrical Manufacturing and Coil Winding Conference,* pp. 605-609, 1999.

[164] W. G. Kürten Ihlenfeld and R. T. Vasconcellos, "On the nonlinear voltage dependence of passive electronic components," *29th Conference on Precision Electromagnetic Measurements (CPEM 2014),* pp. 96-97, 2014.

[165] C. Yun, Q. Xinyu and Z. Xiyang, "Measuring Harmonic Distortion Accurately Using Spectrum Analyzer," *2014 Fourth International Conference on Instrumentation and Measurement, Computer, Communication and Control,* pp. 920-923, 2014.

[166] R. Uhl, M. Mirz, T. Vandeplas, L. Barford and A. Monti, "Non-linear behavioral X-Parameters model of single-phase rectifier in the frequency domain," *IECON 2016 - 42nd Annual Conference of the IEEE Industrial Electronics Society,* pp. 6292-6297, 2016.

[167] D. A. Pérez, H. Gietler and H. Zangl, "Automatic Uncertainty Propagation Based on the Unscented Transform," *2020 IEEE International Instrumentation and Measurement Technology Conference (I2MTC),* pp. 1-6, 2020.

[168] J. Verspecht and D. E. Root, "Polyharmonic distortion modeling," *IEEE Microwave Magazine,* vol. 7, pp. 44-57, 2006.

[169] B. Pichler, G. Magerl and H. Arthaber, "A Study on Quadratic PHD Models for Large Signal Applications," *IEEE Transactions on Microwave Theory and Techniques,* vol. 67, no. 7, pp. 2514-2520, 2019.

[170] M. Faifer, C. Laurano, R. Ottoboni, S. Toscani and M. Zanoni, "A Pruning Technique for Volterra Models: Exploiting Knowledge About Input Spectrum," *2020 IEEE International Instrumentation and Measurement Technology Conference (I2MTC),* pp. 1-6, 2020.

[171] S. Srimani, R. Singh, M. K. Parai, K. Ghosh and H. Rahaman, "Distortion Analysis Using Volterra Kernel for Amplifier Circuits," *2019 IEEE International Symposium on Smart Electronic Systems (iSES),* pp. 308-311, 2019.

[172] M. Faifer, C. Laurano, R. Ottoboni, S. Toscani and M. Zanoni, "Behavioral Modeling of an Inductive Voltage Transformer: Comparison Between X-Parameters and Simplified Volterra Approaches," *2019 IEEE International Instrumentation and Measurement Technology Conference (I2MTC),* pp. 1-6, 2019.

[173] T. M. Martín-Guerrero, J. T. Entrambasaguas and C. Camacho-Peñalosa, "Poly-harmonic distortion model extraction in charge-controlled one-port devices," *2017 12th European Microwave Integrated Circuits Conference (EuMIC),* pp. 252-255, 2017.

[174] M. Faifer, C. Laurano, R. Ottoboni, S. Toscani and M. Zanoni, "Behavioral Representation of a Bridge Rectifier Using Simplified Volterra Models," *IEEE Transactions on Instrumentation and Measurement,* vol. 68, no. 5, pp. 1611-1618, 2019.

[175] S. Jinlong, L. Maoliu and W. Zhilu, "Characterization of harmonic distortion and memory effects for RF power amplifiers based on volterra algorithm," *2014 XXXIth URSI General Assembly and Scientific Symposium (URSI GASS),* pp. 1-4, 2014.

[176] L. Manuel, B. Josep, M. Juan, C. Montserrat and G. Eulalia, "Modelling harmonics drawn by nonlinear loads," *2015 9th International Conference on Compatibility and Power Electronics (CPE),* pp. 93-97, 2015.

[177] L. Wang, H. Li, J. Duan and D. Zhang, "A Novel Modeling Method for Nonlinear Magnetic Devices Reflect Magnetic Circuit and Circuit Characteristics," *2018 IEEE International Power Electronics and Application Conference and Exposition (PEAC),* pp. 1-6, 2018.

[178] A. Amini and S. Boumaiza, "Time-invariant behavioral modeling for harmonic balance simulation based on waveform shape maps," *2015 IEEE MTT-S International Conference on Numerical Electromagnetic and Multiphysics Modeling and Optimization (NEMO),* pp. 1-3, 2015.

[179] A. Tag, "Polyharmonic Distortion modeling of RF BAW components," *2015 IEEE MTT-S International Microwave Symposium,* pp. 1-4, 2015.

[180] X. Pang and Y. K. Yong, "Simulation of Nonlinear Resonance, Amplitude–Frequency, and Harmonic Generation Effects in SAW and BAW Devices," *IEEE Transactions on Ultrasonics, Ferroelectrics, and Frequency Control,* vol. 67, no. 2, pp. 422-430, 2020.

[181] M. Faifer, C. Laurano, R. Ottoboni, S. Toscani and M. Zanoni, "Frequency-Domain Nonlinear Modeling Approaches for Power Systems Components—A Comparison," *Energies,* vol. 13, no. 10, 2020.

[182] B. Zhang and et all, "A Study on the Memory Effect of Mixer," *2020 IEEE Radar Conference (RadarConf20),* pp. 1-5, 2020.

[183] P. Roblin, D. E. Root, J. Verspecht, Y. Ko and J. P. Teyssier, "New Trends for the Nonlinear Measurement and Modeling of High-Power RF Transistors and Amplifiers With Memory Effects," *IEEE Transactions on Microwave Theory and Techniques,* vol. 60, no. 6, pp. 1964-1978, 2012.

[184] H. D. Lang and X. Zhang, "The Harmonic Balance Method," 2013.

[185] Z. C. Chen, B. Wang and D. Palanker, "Harmonic-balance circuit analysis for electro-neural interfaces," *Journal of Neural Engineering,* vol. 17, no. 3, pp. 1-18, 2020.

[186] G. Sun, Y. Xu and A. Liang, "The study of nonlinear scattering functions and X-parameters," *2010 International Conference on Microwave and Millimeter Wave Technology,* pp. 1086-1089, 2010.

[187] T. Kato, K. Inoue and D. Kagawa, "Lumped equivalent model synthesis for a passive element with frequency-dependent and/or temperature-dependent characteristics for EMC simulation," *2009 IEEE 6th International Power Electronics and Motion Control Conference,* pp. 963-969, 2009.

[188] M. Krack and J. Groß, Harmonic Balance for Nonlinear Vibration Problems, Cham: Springer International Publishing, 2019.

[189] D. E. Root, J. Verspecht, D. Sharrit, J. Wood and A. Cognata, "Broad-band poly-harmonic distortion (PHD) behavioral models from fast automated simulations and large-signal vectorial network measurements," *IEEE Transactions on Microwave Theory and Techniques,* vol. 53, no. 11, pp. 3656-3664, 2005.

[190] T. m. Martin-Guerrero, J. d. Banos-Polglase, C. Camacho-Penalosa, M. Fernandez-Barciela, D. G. Morgan and P. J. Tasker,, "Frequency domain-based approach for nonlinear quasi-static FET model extraction from large-signal waveform measurements," *2006 European Microwave Integrated Circuits Conference,* pp. 441-444, 2006.

[191] B. Pichler, G. Magerl and H. Arthaber, "A Robust Extraction Technique for Second Order PHD Based Behavioral Models," *2018 International Workshop on Integrated Nonlinear Microwave and Millimetre-wave Circuits (INMMIC),* pp. 1-3, 2018.

[192] Q. Lu, S. Yang, D. Zhang, Y. Fan and E. Li, "X-Parameter Phase and Load of Nonlinear Devices," *2019 12th International Workshop on the Electromagnetic Compatibility of Integrated Circuits (EMC Compo),* pp. 281-283, 2019.

[193] C. Chiu, S. Lin, B. Chen, K. Chen and G. Huang, "Nonlinear behavior characterization of RF active devices using impedance-dependence X-parameters," *2010 Asia-Pacific Microwave Conference,* pp. 2307-2310, 2010.

[194] H. Hsiao, C. Tu and D. Chang, "Non-fifty ohm X-parameter model measurement system for nonlinear amplifier application," *2018 IEEE International Instrumentation and Measurement Technology Conference (I2MTC),* pp. 1-5, 2018.

[195] "PathWave Advanced Design System (ADS)," Keysight Technologies, 2021. [Online]. Available: https://www.keysight.com/zz/en/products/software/pathwave-design-software/pathwave-advanced-design-system.html. [Accessed 11 November 2021].

[196] G. Andíia Vera, Y. Duroc and S. Tedjini, Non-linearities in Passive RFID Systems: Third Harmonic Concept and Applications, Wiley-ISTE, 2018.

[197] G. Andíia Vera, Y. Duroc and S. Tedjini, "Third Harmonic Exploitation in Passive UHF RFID," *IEEE Transactions on Microwave Theory and Techniques,* vol. 63, no. 9, pp. 2991-3004, 2015.

[198] N. Craig, V. Zomorrodian, S. Warren and J. G. Qorvo, "Measurement-based temperature-dependent X-Parameter models from high-power MMIC power amplifiers," *2018 IEEE 19th Wireless and Microwave Technology Conference (WAMICON),* pp. 1-4, 2018.

[199] L. T. Stant, M. J. Salter, N. M. Ridler, D. F. Williams and P. H. Aaen, "Propagating Measurement Uncertainty to Microwave Amplifier Nonlinear Behavioral Models," *IEEE Transactions on Microwave Theory and Techniques,* vol. 67, no. 2, pp. 815-821, 2019.

[200] T. Volk, M. Bhattacharyya, W. Grünwald, L. Reindl and D. Jansen, "Formal Description of Inductive Air Interfaces Using Thévenin's Theorem and Numerical Analysis," *IEEE Transactions on Magnetics,* vol. 50, pp. 1-9, 2014.

[201] K. F. Warnick, R. B. Gottula, S. Shrestha and J. Smith, "Optimizing Power Transfer Efficiency and Bandwidth for Near Field Communication Systems," *IEEE Transactions on Antennas and Propagation,* vol. 61, pp. 927-933, 2013.

[202] O. Abdelatty, X. Wang and A. Mortazawi, "Nonlinear Resonant Circuits for Coupling-Insensitive Wireless Power Transfer Circuits," *IEEE/MTT-S International Microwave Symposium - IMS,* pp. 976-979, 2018.

[203] W. Wawrzynski, "Duffing-type oscillator under harmonic excitation with a variable value of excitation amplitude and time-dependent external disturbances," Nature, Gdynia, 2021.

[204] R. Chai and A. Mortazawi, "A Coupling Factor Independent Wireless Power Transfer System Employing Two Nonlinear Circuits," *2020 IEEE/MTT-S International Microwave Symposium (IMS),* pp. 393-396, 2020.

[205] O. Abdelatty, X. Wang and A. Mortazawi, "Position-Insensitive Wireless Power Transfer Based on Nonlinear Resonant Circuits," *IEEE Transactions on Microwave Theory and Techniques,* vol. 67, no. 9, pp. 3844-3855, 2019.

[206] M. Mardiguian and D. L. Sweeney, Controlling Radiated Emissions by Design 3rd ed., Springer, 2014.

[207] T. Burghart, H. Rossmanith and G. Schubert, "Evaluating the RF-emissions of automotive cable harness," *2004 International Symposium on Electromagnetic Compatibility,* vol. 3, pp. 787-791, 2004.

[208] C. Carobbi and D. Izzo, "Reproducibility of CISPR 25 ALSE Test Method," *2018 IEEE Symposium on Electromagnetic Compatibility, Signal Integrity and Power Integrity (EMC, SI & PI),* pp. 1-49, 2018.

[209] M. Mardiguian, "For a better consistency between EMC tests," *IEEE 1997 International Symposium on Electromagnetic Compatibility. Symposium Record,* pp. 370-373, 1997.

[210] C. Ueda, "Low frequency emission simulation using 3D electromagnetic solver based on CISPR25," *2012 International Symposium on Antennas and Propagation (ISAP),* pp. 704-707, 2012.

[211] R. Azaro and A. Gandolfo, "On the Electric Field Distribution in Radiated Emission Rod Antenna Test Setups: Numerical Analysis and Experimental Validation," *IEEE Transactions on Electromagnetic Compatibility,* vol. 62, no. 4, pp. 1611-1618, 2020.

[212] R. Azaro and A. Gandolfo, "A Detailed Numerical Analysis of the Electric Field Distribution in Rod Antenna Radiated Emission Setups," *2019 IEEE International Symposium on Electromagnetic Compatibility, Signal & Power Integrity (EMC+SIPI),* pp. 537-542, 2019.

[213] S. Saito, Y. Akeboshi and S. Nitta, "A study on the common mode current generated from an AFE of a modem and the magnetic field emitted from signal wires driven by the AFE," *2008 International Symposium on Electromagnetic Compatibility - EMC Europe,* pp. 1-6, 2008.

[214] D. M. Hockanson, J. L. Drewniak, T. H. Hubing, T. P. Van Doren, Fei Sha and M. J. Wilhelm, "Investigation of fundamental EMI source mechanisms driving common-mode radiation from printed circuit boards with attached cables," *IEEE Transactions on Electromagnetic Compatibility,* vol. 38, no. 4, pp. 557-56, 1996.

[215] H. Hackl and B. Auinger, "Calculation of very near field radiated emission of a straight cable harness," *2016 12th Conference on Ph.D. Research in Microelectronics and Electronics (PRIME),* pp. 1-4, 2016.

[216] C. R. Paul and D. R. Bush, "Radiated Emissions from Common-Mode Currents," *1987 IEEE International Symposium on Electromagnetic Compatibility,* pp. 1-7, 1987.

[217] N. Kuwabara, T. Matsushima, Y. Fukumoto and H. Okumura, "Characteristics of Radiated Emission by PLC Signal from Three-wire Power Cable," *2019 International Symposium on Electromagnetic Compatibility - EMC EUROPE,* pp. 267-272, 2019.

[218] K. Fu, W. Chen and S. Lin, "A General Transformer Evaluation Method," *Energies,* vol. 12, pp. 1-21, 2019.

[219] J. Jia, D. Rinas and S. Frei, "Predicting the Radiated Emissions of Automotive Systems According to CISPR 25 Using Current Scan Methods," *IEEE Transactions on Electromagnetic Compatibility,* vol. 58, no. 2, pp. 409-418, 2016.

[220] F. Anemiya, N. Kuwabara and T. Ideguchi, "Method for Estimating Electromagnetic Interference due to Unbalance in Telecommunications Line," *The Institute of Electronics, Information and Communication Engineers,* Vols. E75-B, no. 3, pp. 141-147, 1992.

[221] T. Takahashi, L. Niu and T. Hubing, "Estimation of common mode current on coaxial cable with twisted wire pair," *2014 International Symposium on Electromagnetic Compatibility,* pp. 553-556, 2014.

[222] M. D'Amore, M. S. Sarto and A. Scarlatti, "Theoretical analysis of radiated emission from modal currents in multiconductor transmission lines above a lossy ground," *IEEE International Symposium on Electromagnetic Compatibility. Symposium Record,* vol. 2, pp. 729-734, 2000.

[223] L. Niu and T. H. Hubing, "Rigorous Derivation of Imbalance Difference Theory for Modeling Radiated Emission Problems," *IEEE Transactions on Electromagnetic Compatibility,* vol. 57, no. 5, pp. 1021-1026, 2015.

[224] C. Su and T. H. Hubing, "Calculating Radiated Emissions Due to I/O Line Coupling on Printed Circuit Boards Using the Imbalance Difference Method," *IEEE Transactions on Electromagnetic Compatibility,* vol. 54, no. 1, pp. 212-217, 2012.

[225] H. Hackl, G. Winkler and B. Deutschmann, "Simulation of radiated emission during the design phase based on scattering parameter measurement," *2015 10th International Workshop on the Electromagnetic Compatibility of Integrated Circuits (EMC Compo),* pp. 228-231, 2015.

[226] M. C. Di Piazza, A. Ragusa, G. Tine and G. Vitale, "A model of electromagnetic radiated emissions for dual voltage automotive electrical systems," *2004 IEEE International Symposium on Industrial Electronics,* vol. 1, pp. 317-322, 2004.

[227] W. T. Smith and R. K. Frazier, "Prediction of anechoic chamber radiated emissions measurements through use of empirically-derived transfer functions and laboratory common-mode current measurements," *1998 IEEE EMC Symposium. International Symposium on Electromagnetic Compatibility,* vol. 1, pp. 387-392, 1998.

[228] D. Schneider, M. Böttcher, B. Schoch, S. Hurst, S. Tenbohlen and W. Köhler, "Transfer functions and current distribution algorithm for the calculation of radiated emissions of automotive components," *2013 International Symposium on Electromagnetic Compatibility,* pp. 443-448, 2013.

[229] D. Schneider, M. Beltle, M. Siegel, S. Tenbohlen and W. Köhler, "Radiated Emissions of an Electric Drive System Estimated on a Bench Using Disturbance Currents and Transfer Functions," *IEEE Transactions on Electromagnetic Compatibility,* vol. 57, no. 3, pp. 311-321, 2015.

[230] F. Gao, C. Ye, Z. Wang and X. Li, "Improvement of Low-Frequency Radiated Emission in Electric Vehicle by Numerical Analysis," *Journal of Control Science and Engineering,* vol. 2018, 2018.

[231] C. Chen, "Predicting vehicle-level radiated EMI emissions using module-level conducted EMIs and harness radiation efficiencies," *2001 IEEE EMC International Symposium. Symposium Record. International Symposium on Electromagnetic Compatibility,* vol. 2, pp. 1146-1151, 2001.

[232] G. Li, "Estimating the radiated emissions from cables attached to a switching power supply in a MIL-STD 461 test," *2013 IEEE International Symposium on Electromagnetic Compatibility,* pp. 626-631, 2013.

[233] "CISPR 16-1-4:2019 Specification for radio disturbance and immunity measuring apparatus and methods - Part 1-4: Radio disturbance and immunity measuring apparatus - Antennas and test sites for radiated disturbance measurements," IEC, 2019.

[234] "R&S HFH2-Z6E Active Rod Antenna," Rohde&Schwarz,, HF – VHF/UHF – SHF Antennas, Catalog 2020/2021, pp. 58-59, 2021.

[235] W. Martinsen, "A High Performance Active Antenna for the High Frequency Band," Australian Government - Department of Defence, Defence Science and Technology Group, 2018.

[236] F. S. Colligan, "An "E" Field Rod Antenna and Preamplifier for A.M. Field Strength Measurements," *IEEE Transactions on Broadcasting,* Vols. BC-26, no. 4, pp. 93-98, 1980.

[237] H. W. Gaul, "Electromagnetic modeling and measurements of the 104 cm rod and biconical antenna for radiated emissions testing below 30 MHz," *2013 IEEE International Symposium on Electromagnetic Compatibility,* pp. 434-438, 2013.

[238] C. R. Paul, "The Concept of Partial Inductance," *Inductance: Loop and Partial,* pp. 195-245, 2010.

[239] J. D. Brunett, V. V. Liepa and D. L. Sengupta, "Extrapolating near-field emissions of low-frequency loop transmitters," *IEEE Transactions on Electromagnetic Compatibility,* vol. 47, no. 3, pp. 635-641, 2005.

[240] *R&S EMC32 measurement software,* Rohde & Schwarz, 2020.

[241] A. M. Silaghi, R. A. Aipu, A. De Sabata and F. Alexa, "Absorber Lined Shielded Enclosure Chamber Validation," *2018 International Symposium on Electronics and Telecommunications (ISETC),* pp. 1-6, 2018.

[242] S. Jayashankar, "A detailed test method for measuring radiated spurious emissions by signal substitution and the effect of relevant source parameters," *2002 IEEE International Symposium on Electromagnetic Compatibility,* vol. 1, pp. 509-514, 2002.

[243] J. R. Nagel, "Induced Eddy Currents in Simple Conductive Geometries: Mathematical Formalism Describes the Excitation of Electrical Eddy Currents in a Time-Varying Magnetic Field," *IEEE Antennas and Propagation Magazine,* vol. 60, no. 1, pp. 81-88, 2018.

[244] A. Negut, “Ultra short multiband AM/FM/DAB active antennas for automotive applications,” Materials Science, Engineering, 2011